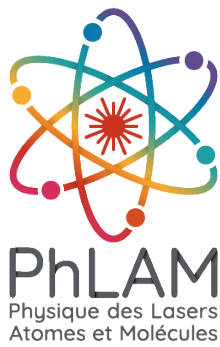




Université
de Lille



Manipulation and Characterization of Multimode Quantum Light in Photonic Systems

Manipulation et Caractérisation de la Lumière Quantique Multimode dans les Systèmes Photoniques

Doctoral Thesis/Thèse de doctorat de l'Université de Lille
préparée au PhLAM

École doctorale n°104 Sciences de la Matière, du Rayonnement et de
l'environnement (SMRE)
Spécialité de doctorat: Milieux dilués et Optique Fondamentale (DS2)

Thèse présentée et soutenue à Villeneuve d'Ascq, le 20 Décembre 2024, par

BAKHAO DIOUM

Composition du Jury :

Nicolas Treps PR, Université Pierre et Marie Curie (Laboratoire Kastler Brossel)	Président
Germán de Valcarcel PR, University of Valencia (Departamento de Óptica)	Rapporteur
Pérola Milman DR, Université Paris Cité (Matériaux et Phénomènes Quantiques)	Rapporteuse
Carlos Navarrete-Benlloch PI, University of Valencia (Optics and Optometry and Vision Sciences)	Examineur
Majid Taki PR, Université de Lille (DYSCO)	Directeur de thèse
Giuseppe Patera MCF, Université de Lille (Systèmes Quantiques)	Co-directeur de thèse

Thèse de doctorat

Abstract

This thesis advances multimode quantum optics through two major theoretical and practical contributions.

First, we introduce temporal cavities as a novel approach to temporal mode filtering, leveraging space-time duality principles to translate spatial mode-cleaning cavity principles to the temporal domain. Unlike existing approaches, this filter operation does not rely on nonlinear interactions or phase matching, preserves the carrier frequency, and maintains the temporal mode structure intact. We demonstrate practical implementation feasibility using electro-optic time lenses and diffraction gratings, with comprehensive parameter optimization strategies for both classical and quantum applications.

Second, we address fundamental limitations in quantum state detection through interferometers with memory effect (IME). We establish new criteria for predicting hidden squeezing directly from system parameters and develop novel smooth decomposition methods for implementing frequency-dependent unitaries. These innovations enable perfect mode-matching for states exhibiting complex spectral features and morphing supermodes, which are more common than previously recognized in cavity-based quantum systems. The effectiveness of our approach is demonstrated through detailed case studies of optical parametric oscillator configurations.

Keywords quantum optics, multimode, temporal cavities, interferometers with memory effect, hidden squeezing, temporal mode filtering, frequency combs, smooth decomposition, measurement, quantum state detection, homodyne detection, cavity quantum optics, frequency-dependent unitaries, morphing supermodes, time lens,

Contents

General Introduction	1
1 Quantum Optics Fundamentals	9
1.1 The quantum Harmonic Oscillator	10
1.1.1 Classical Harmonic Oscillator	11
1.1.2 Quantum Harmonic Oscillator	12
1.1.3 Discrete States	13
1.1.4 Continuous States	14
1.1.5 The EPR Paradox and Quantum Entanglement	19
1.2 Quantization of the Electromagnetic field	21
1.2.1 The analytical Electromagnetic signal	21
1.2.2 The electromagnetic wave nature of light	22
1.2.3 Mode of Electromagnetic fields and mode basis	24
1.2.4 Quantization of the EM field in the basis of TPW	29
1.2.5 Basis Change	33
1.2.6 Paraxial optics and transverse modes	35
1.2.7 Quantization in an optical cavity	38
1.2.8 Particular examples of cavities	42
1.3 Multimode Gaussian States	47
1.3.1 Phase Space Description	48
1.3.2 Gaussian States	51
1.3.3 Gaussian Unitaries and the symplectic group	53

1.3.4	Symplectic representation of linear optics operations	57
1.3.5	Bloch-Messiah Decompostion	63
1.4	Quantum Theory of open cavities	66
1.4.1	The open cavity model	66
1.4.2	Heisenberg picture approach: The quantum Langevin equation	69
1.4.3	Open Cavity output	73
1.4.4	Time Correlation Matrix	75
1.5	Measurement techniques	80
1.5.1	Ideal Photodetection	81
1.5.2	Quadrature measurements	83
1.5.3	Measurement of a Fixed Quadrature : Homodyne Detection	85
1.5.4	Heterodyne Detection	90
1.5.5	Multimode Synodyne Detection	93
2	Temporal Cavities as temporal mode filters	97
2.1	Space-time duality and Temporal Imaging	99
2.1.1	Space-time duality	99
2.1.2	Temporal ABCD matrix formalism	105
2.1.3	Photonic Components	115
2.1.4	Time lens	116
2.1.5	Diffraction gratings	121
2.2	Temporal cavity	128
2.2.1	From mode cleaner cavity to temporal cavity	129
2.2.2	Eigenvalue and Eigenmode conditions	131
2.2.3	Input-output relations	133
2.2.4	Application of temporal cavities in communication protocols	140
2.2.5	Cavity Characterisation: Figures of merit	142
2.2.6	Intrinsic Losses and Compromises	145
2.2.7	Parameter choice	148
2.2.8	Experimental feasibility	149

3	Generalized quantum mode-matching through interferometry with memory	157
3.1	Quadratic Hamiltonian in cavity quantum optics	159
3.1.1	Quadratic Hamiltonian evolution in cavity	159
3.1.2	Resolution of the Hamiltonian Problem	162
3.1.3	Analytic Bloch-Messiah Decomposition	167
3.1.4	Spectral covariance matrix of the multimode state	172
3.1.5	Hidden squeezing	174
3.2	Conditions for a spectral covariance matrix	180
3.2.1	Framework	181
3.2.2	Boundaries to complex spectral covariance matrices	183
3.2.3	Case studies	187
3.3	Achieving generalized quantum mode-matching	192
3.3.1	Implementing the interferometer with memory effect	199
3.3.2	Smooth two-mode decomposition	200
3.3.3	Smooth single-mode decomposition	206
3.4	Measuring morphing supermodes	211
3.4.1	Optimization strategy	211
3.4.2	Single-mode OPO	218
3.4.3	Two-mode OPO	225
3.4.4	Four-mode OPO	237
3.4.5	Scaling and losses	241
	Conclusion and Perspectives	249
A	Frequency comb formalism	255
A.0.1	Round Trip Analysis	256
A.0.2	Propagation through D_1	257
A.0.3	Propagation through the time lens	258
A.0.4	Propagation through D_2	260
A.0.5	Final Round Trip Analysis	261
A.0.6	Round Trip Condition	261

B Two-mode smooth decomposition algorithms	263
C Supplemental details on IME	265
C.1 Recycling IME cavities	265
C.2 Morphing supermodes of four mode OPOs	268
C.3 Optimal parameters of the four modes OPOs	268

List of Figures

1.1	Phase space sketch of a coherent and squeezed state	15
1.2	Transverse Hermite-Gaussian mode	27
1.3	Temporal modes	28
1.4	Frequency combs temporal modes	28
1.5	Mode cleaner cavity	43
1.6	Illustration of Bloch-Messiah decomposition	64
1.7	Open cavity model	66
1.8	Schematic of ideal single-mode detection	81
1.9	Principle of homodyne detection	85
1.10	Principle of heterodyne detection	90
1.11	Principle of synodyne detection	93
2.1	Spatial mode cleaner cavity translation	100
2.2	Spatial and Temporal Gaussian Pulses	102
2.3	Diffraction gratings	122
2.4	Grating pairs in Treacy configuration	125
2.5	Grating pairs in Treacy vs Martinez configuration	128
2.6	Train of Pulse decomposition	131
2.7	Schematic of a temporal cavity	134
2.8	Temporal cavity resonances	135
2.9	Different schematic of a temporal cavity	136
2.10	Temporal cavities for quantum communication	141

2.11	Characterisation of the temporal cavity resonances	142
2.12	Temporal cavities with losses	146
2.13	Constraints on low loss	149
2.14	Resonances at square	151
2.15	Resonances at the first stage for cascaded temporal cavities	152
2.16	Resonances at the second stage for cascaded temporal cavities	153
2.17	Constraints on high loss	154
2.18	EOPM time lens aperture	155
2.19	Resonances at circle	156
3.1	Conditions for a real-valued spectral covariance matrix	184
3.2	SFWM main and parasitic processes	189
3.3	Squeezing spectrum with and without parasitic processes vs HD	190
3.4	Generalized quantum mode-matching through IME	193
3.5	Smooth two-mode decomposition	200
3.6	Smooth decomposition method for triangular decomposition: nulling order	205
3.7	Smooth decomposition method for rectangular decomposition: nulling order	205
3.8	Smooth single mode decomposition	207
3.9	Output transfer function and spectral covariance of single mode OPOs	220
3.10	Squeezing levels and morphing supermodes of single mode OPOs	221
3.11	Measurement of squeezing level of a single mode OPO using HD and IME	222
3.12	Comparison between optimal squeezing and squeezing measured via HD and IME for single-mode OPO 5% below threshold	222
3.13	Comparison between optimal squeezing and squeezing measured via HD and IME for single-mode OPO 50% below threshold	223
3.14	Comparison between optimal squeezing and squeezing measured via HD and IME for single-mode OPO 5% below threshold	224
3.15	HD vs IME scheme for two-mode OPO	226
3.16	Output spectral covariances of two-mode OPOs	227

3.17 Squeezing levels and morphing supermodes of two-mode OPOs 7% below threshold	229
3.18 Squeezing levels and morphing supermodes of two-mode OPOs 43% below threshold	230
3.19 Comparison between optimal squeezing $d_1^{-2}(\omega)$ and squeezing measured via HD and IME for two-mode $\chi^{(3)}$ -based OPO 7% below threshold	232
3.20 Comparison between optimal squeezing $d_2^{-2}(\omega)$ and squeezing measured via HD and IME for two-mode $\chi^{(3)}$ -based OPO 7% below threshold	233
3.21 Overlap between generalized LO and morphing supermodes	234
3.22 HD vs IME scheme for four-mode OPO	237
3.23 Output spectral covariances of four-mode OPOs	238
3.24 Comparison between squeezing measured via HD with and without IME for two configurations of four-mode OPO	239
3.25 Input-output quadratures for the lossy IME	242
3.26 Loss scaling	247
A.1 Fields for frequency comb modes calculations	255
C.1 Two-mode OPO recycling IME	265
C.2 Four-mode OPO recycling IME	266
C.3 Morphing supermodes of the four modes OPO configuration at 7% below threshold	267
C.4 Morphing supermodes of the four modes OPO configuration at 100% below threshold	270

List of Tables

2.1	Mapping between Spatial and Temporal Parameters	102
2.2	Comparison of Spatial and Temporal Domain Parameters	104
2.3	Comparison of Space and Time Optical Elements	115
2.4	Comparison between Treacy and Martinez Configurations	128

General Introduction

The foundations of quantum mechanics and its interpretation can be traced back to 1927, during the fifth Solvay Conference, where Einstein first questioned the quantum mechanical uncertainty principle. In 1935, Einstein, Podolsky and Rosen pointed out the paradoxical fact that for a special class of states, say entangled, quantum theory could predict correlations stronger than the ones predictable by any other theory obeying "local realism" and this led them to conclude that quantum theory was incomplete [1]. In 1964, J. S. Bell derived his well-known inequalities which fix an upper limit to the strength of correlations for theories obeying local realism and permitted to test experimentally quantum theory [2]. After 1964, an increasing number of experimental tests supported the consistency of quantum entanglement, culminating in the groundbreaking experiments by Alain Aspect [3], John Clauser [4] and Anton Zeilinger [5], who were awarded the 2022 Nobel Prize in Physics for their pioneering work in quantum entanglement and Bell test experiments. This fundamental understanding laid the groundwork for what is called the Second Quantum Revolution, where quantum effects are not just observed but actively controlled and harnessed for practical applications. This new era, transforming quantum phenomena into revolutionary technologies has led to entangled states being recognized as the primary resource in quantum communication protocols (QIP) and quantum information science.

Building upon this foundation, the manipulation of quantum states of light has evolved in a vast and diverse landscape encompassing discrete variable states like polarization-entangled photon pairs to states exhibiting nonclassicality in the continuous variable (CV) regime [6, 7]. The latter, of particular relevance to this thesis, is at the heart of many protocols for the processing of quantum information such as quantum computation via cluster states [8, 9], quantum metrology [10] and quantum communication [11, 12]. In particular Gaussian CV states have

been effectively employed in quantum teleportation [13, 6], cryptography [14, 15, 12], and computation [16, 17, 8, 7] due to their mathematical simplicity with the existence of well-established theoretical tools to describe their properties [12, 7]. Single and multimode Gaussian states can be generated and manipulated experimentally in a variety of physical systems, ranging from light fields to atomic ensembles [13, 18].

However, the practical implementation of these quantum protocols faces a fundamental challenge rooted in quantum mechanics itself. The intrinsic statistical behaviour of light, arising from its quantum nature, induces fluctuations which degrade the precision of measurements. These fluctuations are unavoidable even when all other classical sources of noise have been cancelled and are usually referred to as shot-noise. While the shot-noise represents the standard quantum limit for individual quadrature measurements, the Heisenberg uncertainty principle imposes a fundamental constraint only on the product of the variances of two conjugate observables (i.e., two field quadratures). This means that the fluctuations of one observable can be reduced below the shot-noise provided that, at the same time, the noise on the conjugate observable is enhanced. Such states are called squeezed states of light and they were introduced during the late 1970s and mid-1980 [19, 20], as states capable of circumventing quantum mechanical limits on measurement precision performed with coherent light, showing the possibility of manipulating quantum fluctuations and paving the way for advancements beyond the standard quantum limit.

These states found their way into the new century thanks to their widely proven applications in ultra-precise metrology such as gravitational wave detection [21, 22, 23, 24], quantum sensing [25]) or beam displacements [26, 27], as well as in a wide range of quantum computing algorithms [12, 28, 29, 30], where the highest-quality entangled states known to date are currently obtained by mixing squeezed beams with linear optics [13, 31]. The generation and manipulation of these non-classical states of light, however, requires precise control over light-matter interactions and careful management of optical modes, something optical cavities excel at for modern quantum optics experiments.

Resonant cavities play a crucial role in optics and photonics in generating and manipulating these quantum states by enabling precise control of light at specific frequencies or wavelengths. These cavities are typically designed to confine light within a bounded region, allowing

it to interact with matter or other optical elements in a controlled manner. The ability to enhance optical power and matter-light interactions, as well as to impose a defined mode structure on the electromagnetic field, makes optical cavities essential in many applications in optics. This enhanced field strength enables for more efficient coupling of light with atoms, molecules, quantum dots, or other nanoscale materials, leading to enhanced spectroscopic sensitivity and stronger light-matter interactions. Employed as add-drop (de-)multiplexers, they are integral to current telecommunications technologies for routing information encoded in the Fourier basis of monochromatic spectral modes. In astronomy, their use as light accumulators improves the sensitivity of gravitational wave detection; as filters, they enable the precise calibration of spectrographs for observing exoplanets [32, 33].

While optical cavities excel at manipulating light on the Fourier basis, quantum optics has revealed the importance of alternative modal decompositions. Since the foundational work of Titulaer and Glauber in 1966 [34], it has been understood that the electromagnetic field can be quantized, not just with monochromatic modes, but using any complete set of modes such as temporal modes(TM) [35, 36]. TMs are orthogonal broadband wavepackets of light, forming a family over which any pulse can be decomposed. Thus, they represent an alternative to the usual Fourier basis, in particular, because they offer several advantages for communication and metrology. In fiber-based communication, TM encodings remain orthogonal throughout propagation as they are uniformly affected by dispersion. This enables avoiding cross-talk that constrains data rates and transmission distances, limiting overall performance when employing Fourier modes. In metrology, mode-selective measurements in the TM basis lead to space-time positioning and clock synchronisation potentially reaching the yoctosecond range [37] and allows to elude Rayleigh's curse in the estimation of separations in time and frequency well below the spread of the source light [38]. Developing TM-selective measurements would significantly enhance the ability to identify and mitigate noise in pulsed laser systems, as these systems exhibit noise patterns corresponding to the TM basis [39]. Despite mode-selective techniques have been developed in the last few years such as, for example, the quantum pulse gate (QPG) [40, 41, 42, 43, 44, 45, 46], to date, an approach to implement a genuine filter, which would sort TMs while maintaining their carrier frequency as well as their original shape (in time or frequency domain), has not been shown. Optical cavities, for example, cannot distinguish

between different linear combinations of monochromatic modes when operating outside their natural Fourier basis.

Beyond the challenge of mode filtering, resonant cavities present another fundamental aspect in quantum optics that requires careful consideration. When these cavities are used to generate quantum states - whether in optical parametric oscillators (OPOs), optomechanical systems, gravitational interferometers, or more broadly in open quantum systems such as cavity-based quantum optics - they exhibit distinctive temporal characteristics that set them apart from freely propagating fields. In these systems, the quantum dynamics evolves at frequencies much slower than optical frequencies, typically on the order of the cavity resonance width. This temporal evolution manifests in the interaction picture through slowly-varying boson field operators, whose properties must be captured through a correlation matrix [47] that depends on two different times t and t' . For stationary-in-time systems, the correlation matrix depends only on the time difference $t - t'$. For such systems, one can introduce its Fourier transform that depends only on one frequency ω [47], their spectral covariance matrix. This object describes the frequency-dependent quantum correlations between the spectral components of amplitude and phase quadratures of single or multimode states. While in the literature this matrix is generally assumed to be real [48, 49, 50, 51, 52, 53], recent research reveals that scenarios leading to complex spectral covariances [54].

For the characterisation of these non-classical states, measurement, given its projective nature, is a valuable tool for the preparation of these quantum states or their evolution in measurement-based approaches to quantum computation. For example, at the output of a pulsed parametric down-conversion, the signal can be decomposed into several orthogonal squeezed modes known as temporal modes (TM). Matching the local oscillator (LO), of say a homodyne detection (HD) measurement, to a specific modal component of this beam enables access to the pure state carried by that mode and reliable measurement of its squeezing level. On the other side, when the LO is not matched to a specific TM of this beam, it behaves as a filter, leading to quadrature measurement involving all the modal content that overlaps with the LO. HD capabilities have been also extended to hybrid regimes by including a weak local oscillator and photon counting detection. This broadens HD's range of applications, leveraging the advantages of both the CV and discrete variables (DV) regimes.

QIP protocols based on HD operate effectively in many cases, but there are more common scenarios than previously thought where HD is inefficient. Recent studies in the field of integrated quantum photonics have drawn attention to the dissipative dynamics of nonlinear $\chi^{(3)}$ -based microresonators. They revealed a broader category of multimode Gaussian states characterized by two distinctive features: (i) "hidden squeezing" and (ii) "morphing supermodes". "Hidden squeezing" was first explored and explained in several works by Barbosa *et al.* [55, 56]. It is known that the squeezing of a single beam of light actually involves two-mode squeezing correlations between sideband modes symmetric with respect to the carrier. In many situations, an effective single-mode description can be applied, but this holds true only when the noise spectral power between these modes is identical. Conversely, a two-mode description becomes necessary, and in such cases, HD lacks the necessary degrees of freedom to detect the correlations between them and reconstruct the complete information. Current research shows that even for devices integrated on-chip, their complex dynamics revealed that these unbalanced quantum states are more common than believed. Previous analysis of the quantum properties of these quantum states completely ignored these features because the covariance matrix was defined as real. It was shown in [57, 54] that the output of these devices presents indeed a spectral unbalance, or, in our language, a spectral covariance matrix that is complex. "Morphing supermodes" are the normal modes that decouple the system dissipative dynamics, mapping the output multimode CV entangled state into a collection of independent squeezed states that exhibit frequency-dependent coefficients (typically varying at the scale of the cavity bandwidth). A morphing behaviour of the normal modes generalizes for multimode beams a quite common phenomenon in nonlinear optical cavities. The most simple examples are given by a detuned single-mode degenerate optical parametric oscillator (DOPO) [58, 59] and optomechanical cavities [60, 61, 62] where, at the output, optimal squeezing is found in a frequency-dependent quadrature that varies at scales of the cavity bandwidth. While these frequency dependent features exist in some systems, they are also wanted resources for example in Fabry-Perot cavities that have been considered in order to produce frequency-dependent squeezed states or frequency-dependent LO for the purpose of improving the sensitivity of the current generation of gravitational waves interferometers [21, 24]. These interferometers exhibit a sensitivity curve constrained by phase noise at low frequencies and intensity noise at high

frequencies. To enhance their performance, the frequency-dependent passive transformation induced by an empty cavity can be employed to manipulate an input frequency-independent squeezed state.

States presenting these hidden squeezing and morphing supermodes features are expected to be ubiquitously generated not only in microring resonators but also in a wide range of physical systems, including optomechanical systems, four-wave mixing (FWM) in atomic ensembles, semiconductor microcavities, and quantum cascade lasers [54]. It was demonstrated that both aspects can be reduced to a mode-matching problem and that achieving perfect matching through HD is not possible.

The contributions of this thesis advance the field of temporal mode manipulation and quantum state detection through two significant developments. The first major contribution introduces the concept of a "temporal cavity" [63] as an innovative approach to temporal mode (TM) filtering. An ideal TM sorter should separate the targeted TM from the other modes avoiding overlapping with other components and – for quantum applications – with efficiency close 100%. The temporal cavity design emerges from the principles of space-time duality [64], leveraging the formal analogy between spatial and temporal degrees of freedom in optical beam propagation. One of the most fascinating results yielded by this analogy is the time lens, a device that mimics, in the time domain, the effect of thin lenses on spatial images, by imprinting a parabolic time-dependent phase on an optical pulse. Time lenses have been implemented with deterministic linear electro-optic phase modulation [65, 66, 67, 68, 69] or non-linear optical processes [70, 71, 72, 73, 74, 75] and have recently been adopted for manipulation of pulses in discrete [76, 77, 67, 78, 79, 80] or in continuous [81, 82, 83, 84] variables for photonic quantum information processing. A temporal cavity is obtained by using the temporal analogue of a spatial-mode cleaning cavity, whose eigenvectors are Hermite-Gaussian transverse modes, with mode-dependent reflection and transmission coefficients.

The second major contribution targets the general case of multimode homodyne measurements. We introduce an approach that extends HD capabilities to both frequency-dependent observables and their hidden correlations by using "interferometers with memory effect" (IME) [85]. The theoretical framework introduces a sophisticated structure combining cavity dynamics with frequency conversion terms. The IME architecture serves as a bridge between the generation

of non-classical state stage and homodyne detection (HD), offering enhanced mode-matching capabilities allowing to deal with both hidden squeezing and morphing supermodes. This was achieved through the introduction of new smooth single- and two-mode decomposition that allows the decomposition of any arbitrary frequency-dependent unitary into a network of basic single-, and two-mode photonic components with specific architectures. These new decompositions allow us to map the implementation of the IME to a network of coupled-cavity arrays.

To establish a connection between a cavity-based system's parameters and ensure an appropriate choice for the need of IMEs in the context of hidden squeezing, we introduce precise criteria on these system's physical parameters to determine whether the corresponding spectral covariance matrix is real or complex [86]. These criteria allow for the prediction of the nature of the Gaussian state solely from the system's interaction parameters without the necessity of fully characterizing the spectral covariance matrix or the complete quantum state reconstruction. As a consequence, our results allow the appropriate choice of measurement strategies for better characterization and exploitation of these quantum states.

Chapter 1 establishes the theoretical fundamentals of quantum optics, beginning with the quantum harmonic oscillator and its transition from classical to quantum mechanics and then progressing to the quantization of electromagnetic fields. The chapter delves into multimode Gaussian states, exploring phase space descriptions and Gaussian unitaries. The latter sections address practical quantum optics, covering open cavity theory, quantum Langevin equations, and various measurement techniques from homodyne to synodyne detection.

Chapter 2 develops the concept of temporal cavities through space-time duality principles and temporal ABCD matrix formalism. Building on the analogy between spatial and temporal degrees of freedom in optical propagation, we introduce temporal cavities as a novel approach to temporal mode filtering. The chapter characterizes these devices through eigenvalue conditions and input-output relations, examining implementation strategies with diffraction gratings and time lenses and addressing current limitations, practical challenges and optimization requirements.

Chapter 3 introduces interferometry with memory effect (IME), a novel detection scheme that extends homodyne detection's capabilities to measure both frequency-dependent observables and hidden correlations in quantum states, Starting with quadratic Hamiltonians in cavity quan-

tum optics, we establish criteria for predicting hidden squeezing from system parameters and develop smooth decomposition methods for implementing frequency-dependent unitaries. The chapter demonstrates IME's effectiveness through detailed case studies of optical parametric oscillator configurations, from single-mode to four-mode systems, providing a comprehensive analysis of performance and scaling.

Chapter 1

Quantum Optics Fundamentals

Contents

1.1	The quantum Harmonic Oscillator	10
1.1.1	Classical Harmonic Oscillator	11
1.1.2	Quantum Harmonic Oscillator	12
1.1.3	Discrete States	13
1.1.4	Continuous States	14
1.1.5	The EPR Paradox and Quantum Entanglement	19
1.2	Quantization of the Electromagnetic field	21
1.2.1	The analytical Electromagnetic signal	21
1.2.2	The electromagnetic wave nature of light	22
1.2.3	Mode of Electromagnetic fields and mode basis	24
1.2.4	Quantization of the EM field in the basis of TPW	29
1.2.5	Basis Change	33
1.2.6	Paraxial optics and transverse modes	35
1.2.7	Quantization in an optical cavity	38
1.2.8	Particular examples of cavities	42
1.3	Multimode Gaussian States	47

1.1. THE QUANTUM HARMONIC OSCILLATOR

1.3.1	Phase Space Description	48
1.3.2	Gaussian States	51
1.3.3	Gaussian Unitaries and the symplectic group	53
1.3.4	Symplectic representation of linear optics operations	57
1.3.5	Bloch-Messiah Decomposition	63
1.4	Quantum Theory of open cavities	66
1.4.1	The open cavity model	66
1.4.2	Heisenberg picture approach: The quantum Langevin equation	69
1.4.3	Open Cavity output	73
1.4.4	Time Correlation Matrix	75
1.5	Measurement techniques	80
1.5.1	Ideal Photodetection	81
1.5.2	Quadrature measurements	83
1.5.3	Measurement of a Fixed Quadrature : Homodyne Detection	85
1.5.4	Heterodyne Detection	90
1.5.5	Multimode Synodyne Detection	93

1.1 The quantum Harmonic Oscillator

The quantum harmonic oscillator (HO) stands as one of the most fundamental systems in quantum mechanics. Beyond its role in describing mechanical oscillations, it provides the mathematical framework needed to understand quantum electromagnetic fields. In particular, in the next section, we show that the electromagnetic field can be seen as a collection of harmonic oscillators. This section develops the formalism from classical to quantum descriptions of the HO, introducing key concepts like creation and annihilation operators, coherent states, and squeezed states. These tools will prove essential in our subsequent treatment of electromagnetic field quantization.

This section follows the formalism presented in Dr. Carlos Navarrete-Benlloch's lecture notes on Introduction to Quantum Optics [87] and his PhD manuscript [88].

1.1.1 Classical Harmonic Oscillator

The classical Harmonic Oscillator (HO) is a fundamental concept in physics that can be approached from both Newtonian and Hamiltonian perspectives. Consider the one-dimensional model: a particle with mass m at equilibrium when $x = 0$. When displaced from this position, a restoring force $F = -kx$, proportional to the displacement x , acts on the particle, where k is the spring constant. Applying Newton's second law yields the equation of motion $F = m \frac{d^2x}{dt^2} = -kx$. Given initial conditions $x(0) = x_0$ and $\frac{dx}{dt}(0) = v_0$, the solution to this differential equation is: $x(t) = x_0 \cos(\omega t) + \frac{v_0}{\omega} \sin(\omega t)$, where $\omega = \sqrt{\frac{k}{m}}$ represents the angular frequency of oscillation. Writing the solution in the form

$$x(t) = \sqrt{x_0^2 + \frac{v_0^2}{\omega^2}} \cos\left(\omega t - \arctan\left(\frac{v_0}{\omega x_0}\right)\right), \quad (1.1)$$

we can see that the particle oscillates between $\pm \sqrt{x_0^2 + \frac{v_0^2}{\omega^2}}$ with a period of $\frac{2\pi}{\omega}$.

From the Hamiltonian mechanics formalism, we define generalized coordinates of position $q = x$ and momenta $p = m \frac{dx}{dt}$. The potential energy of the system is given by $V(x) = \frac{1}{2}kx^2$. Combining this with the kinetic energy, we can write the Hamiltonian:

$$H = \frac{p^2}{2m} + \frac{1}{2}m\omega^2 q^2. \quad (1.2)$$

The canonical equations of motion in the Hamiltonian framework write:

$$\frac{dq}{dt} = \frac{\partial H}{\partial p} = \frac{p}{m} \quad (1.3)$$

$$\frac{dp}{dt} = -\frac{\partial H}{\partial q} = -m\omega^2 q. \quad (1.4)$$

With initial condition $(x_0, \frac{v_0}{\omega})$, these equations yield the phase space trajectory

$$\left(q, \frac{p}{m\omega}\right) = \left(x_0 \cos(\omega t) + \frac{v_0}{\omega} \sin(\omega t), \frac{v_0}{\omega} \cos(\omega t) - x_0 \sin(\omega t)\right). \quad (1.5)$$

This trajectory forms a circle in phase space $q^2 + \frac{p^2}{m^2\omega^2} = R^2$ with radius $R = \sqrt{x_0^2 + \frac{v_0^2}{\omega^2}}$. The system returns to its initial state at times $t_n = \frac{2\pi n}{\omega}$, where n is any non-negative integer.

1.1. THE QUANTUM HARMONIC OSCILLATOR

This description can be further condensed using a complex normal variable:

$$q(t) + i\frac{p(t)}{m\omega} = Re^{i\varphi(t)} \quad (1.6)$$

whose amplitude remains constant, while the phase $\varphi(t)$ decreases linearly with time according to $\varphi(t) = \varphi(0) - \omega t$.

1.1.2 Quantum Harmonic Oscillator

In quantum mechanics, the harmonic oscillator serves as a classic example of a system described by an infinite-dimensional Hilbert space. To understand this, we examine the eigenstates of its Hamiltonian operator, expressed similarly to the classical Hamiltonian as in Eq. (3.148):

$$\hat{H} = \frac{\hat{p}^2}{2m} + \frac{1}{2}m\omega^2\hat{q}^2 \quad (1.7)$$

Here, \hat{q} and \hat{p} represent respectively the position and momentum operators and obey the fundamental commutation relation: $[\hat{q}, \hat{p}] = i\hbar$. For convenience, we introduce dimensionless versions of these operators, known as the \hat{x} and \hat{y} quadratures, using the uncertainties in position and momentum for the oscillator's ground state, often referred to as zero-point fluctuations $\left(\sqrt{\frac{\hbar}{2m\omega}}, \sqrt{\frac{\hbar m\omega}{2}}\right)$:

$$\hat{x} = \frac{\hat{q}}{\sqrt{\frac{\hbar}{2m\omega}}} \quad \text{and} \quad \hat{y} = \frac{\hat{p}}{\sqrt{\frac{\hbar m\omega}{2}}} \quad (1.8)$$

These quadratures satisfy the modified commutation relation $[\hat{x}, \hat{p}] = 2i$. This leads to the uncertainty principle for these quadratures

$$\Delta\hat{x}\Delta\hat{y} \geq 1. \quad (1.9)$$

Using these quadratures, we can rewrite the Hamiltonian as:

$$\hat{H} = \frac{\hbar\omega}{4}(\hat{x}^2 + \hat{y}^2). \quad (1.10)$$

1.1. THE QUANTUM HARMONIC OSCILLATOR

To analyze the eigensystem of this Hamiltonian, we introduce the annihilation (\hat{a}) and creation (\hat{a}^\dagger) operators, defined as $\hat{a} = \hat{x} + i\hat{y}$ and $\hat{a}^\dagger = \hat{x} - i\hat{y}$, satisfying the commutation relation $[\hat{a}, \hat{a}^\dagger] = 1$. We can express the Hamiltonian in terms of these operators:

$$\hat{H} = \hbar\omega \left(\hat{a}^\dagger \hat{a} + \frac{1}{2} \right), \quad (1.11)$$

introducing the number operator $\hat{n} = \hat{a}^\dagger \hat{a}$, which plays a crucial role in understanding the energy spectrum of the quantum harmonic oscillator, since finding the eigensystem of the system's Hamiltonian comes back to finding the eigensystem of the number operator.

1.1.3 Discrete States

To determine the eigensystem of \hat{n} , we consider its properties:

Property 1.1.1. Positivity: For any state $|\psi\rangle$, $\langle \psi | \hat{n} | \psi \rangle \geq 0$, implying that all eigenvalues n are non-negative.

Property 1.1.2. Ladder structure: Using the commutation relations $[\hat{n}, \hat{a}] = -\hat{a}$ and $[\hat{n}, \hat{a}^\dagger] = \hat{a}^\dagger$, we find that $\hat{a}|n\rangle$ and $\hat{a}^\dagger|n\rangle$ are eigenstates of \hat{n} with eigenvalues $n - 1$ and $n + 1$, respectively.

These properties lead to several important conclusions with well-known proofs:

- The spectrum of \hat{n} consists of non-negative integers: $n \in \{0, 1, 2, \dots\}$.
- There exists a ground state $|0\rangle$ satisfying $\hat{a}|0\rangle = 0$.
- The set of eigenstates $\{|n\rangle\}$ form an orthonormal basis: $\langle n | m \rangle = \delta_{nm}$.

The action of the creation and annihilation operators on these states is given by:

$$\hat{a}|n\rangle = \sqrt{n}|n-1\rangle \quad \text{and} \quad \hat{a}^\dagger|n\rangle = \sqrt{n+1}|n+1\rangle. \quad (1.12)$$

These relations have profound physical implications:

- Energy quantization: The energy eigenvalues are $E_n = \hbar\omega(n + \frac{1}{2})$, where n represents the number of excitations or quanta.
- Discrete spectrum: Only specific, equally spaced energy levels are allowed, separated by $\hbar\omega$.

1.1. THE QUANTUM HARMONIC OSCILLATOR

- Zero-point energy: Even in the ground state ($n = 0$), the oscillator possesses a non-zero energy of $\frac{\hbar\omega}{2}$.

The states $|n\rangle$ are called number states or Fock states, characterized by a definite number of excitations ($\Delta n = 0$). The state $|0\rangle$ is referred to as the vacuum state, representing the lowest energy configuration of the oscillator.

This discrete nature of the energy spectrum and the existence of a non-zero ground state energy are notable quantum features, marking a significant departure from the classical description of the harmonic oscillator.

1.1.4 Continuous States

Unlike the number operator \hat{n} , the quadrature operators \hat{x} and \hat{y} possess continuous spectra. For the position quadrature \hat{x} , we denote its eigenvectors by $|x\rangle$ with corresponding eigenvalues $x \in \mathbb{R}$: $\hat{x}|x\rangle = x|x\rangle$. The continuous nature of \hat{x} 's spectrum can be demonstrated using the relation:

$$e^{i\frac{y}{2}\hat{y}}\hat{x}e^{-i\frac{y}{2}\hat{y}} = \hat{x} + y, \quad (1.13)$$

coming from the Baker-Campbell-Hausdorff lemma :

$$e^{\hat{A}}\hat{B}e^{-\hat{A}} = \sum_{n=0}^{\infty} \frac{1}{n!} [\hat{A}, [\hat{A}, \dots [\hat{A}, \hat{B}] \dots]]_n, \quad (1.14)$$

where we have chosen $\hat{A} = i\frac{y}{2}\hat{y}$ and $\hat{B} = \hat{x}$.

This implies that if $|x\rangle$ is an eigenvector of \hat{x} with eigenvalue x , then $e^{-i\frac{y}{2}\hat{y}}|x\rangle$ is also an eigenvector of \hat{x} with eigenvalue $x + y$ for any real number y . Consequently, the spectrum of \hat{x} spans the entire real line. Similar results hold for the momentum quadrature \hat{y} , with eigenvectors $|y\rangle$ and eigenvalues $y \in \mathbb{R}$: $\hat{y}|y\rangle = y|y\rangle$.

It's important to emphasize that these results are not exclusive to the harmonic oscillator. Rather, they stem from the fundamental canonical commutation relations and thus apply universally to any quantum system. It's also important to note that these eigenvectors while forming a continuous basis of the Hilbert space (with Dirac normalization $\langle x|y\rangle = \delta(x - y)$), are not

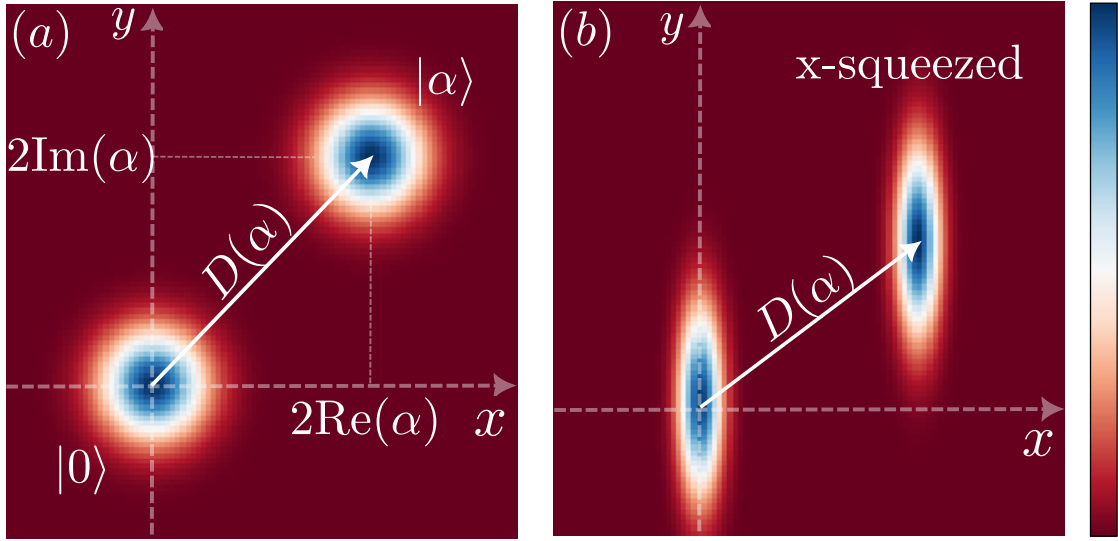


Figure 1.1: (a) Phase space sketch of a coherent state obtained from displaced vacuum state, (b) x-Squeezed state obtained from displaced vacuum squeezed state.

physically realizable states due to their non-normalizability.

Before discussing more specific continuous states of the HO, it's important to introduce the broader class of Gaussian states, which play a crucial role in quantum optics and quantum information theory. Gaussian states are completely characterized by their first and second moments. These states maintain their Gaussian character under linear transformations and measurements, making them particularly useful for theoretical analysis and experimental implementations.

Coherent States

We define minimum uncertainty states, states verifying the equality of the uncertainty principle for their quadratures in Eq. (1.9): $\Delta\hat{x}\Delta\hat{y} = 1$. Among these minimum uncertainty states, coherent states represent the simplest type of Gaussian states, introduced by Roy J. Glauber [89] to explain the quantum properties of laser light. It consists of the simplest Gaussian state, vacuum, transformed by the simplest type of Hamiltonian, one that is linear in the quadratures, as shown in Fig. 1.1. These states, as we will show in the next subsection, allow us to bridge the gap between quantum and classical descriptions of the harmonic oscillator.

We define coherent states as displaced vacuum states $|\alpha\rangle = \hat{D}(\alpha)|0\rangle$ where $\hat{D}(\alpha)$ is the

1.1. THE QUANTUM HARMONIC OSCILLATOR

displacement operator:

$$\hat{D}(\alpha) = \exp(\alpha\hat{a}^\dagger - \alpha^*\hat{a}). \quad (1.15)$$

Here, $\alpha = \frac{x+iy}{2}$ is a complex parameter. Some key properties of coherent states include:

- They are right eigenstates of the annihilation operator with complex eigenvalues: $\hat{a}|\alpha\rangle = \alpha|\alpha\rangle$.
- Consequently, using the displacement operator, they are also left eigenstates of the creation operator: $\langle\alpha|\hat{a}^\dagger = \alpha^*\langle\alpha|$.

Regarding the displacement operator:

- As its name suggests, it transforms the creation and annihilation operators as $\hat{D}^\dagger(\alpha)\hat{a}\hat{D}(\alpha) = \hat{a} + \alpha$ and $\hat{D}^\dagger(\alpha)\hat{a}^\dagger\hat{D}(\alpha) = \hat{a}^\dagger + \alpha^*$.
- It equivalently transforms the quadratures as: $\hat{D}^\dagger(\alpha)\hat{x}\hat{D}(\alpha) = \hat{x} + 2\text{Re}(\alpha)$ and $\hat{D}^\dagger(\alpha)\hat{y}\hat{D}(\alpha) = \hat{y} + 2\text{Im}(\alpha)$, effectively inducing a displacement in the Phase-space as shown in Fig. 1.1a.
- The displacement therefore, as for any Gaussian state, displaces the mean vector of $2(\text{Re}(\alpha), \text{Im}(\alpha)^T)$ in the phase-space but leaves the variances unchanged.

Coherent states as a bridge between Quantum and Classical Physics

The classical and quantum formalisms of the harmonic oscillator appear strikingly different at first glance. Classically, the oscillator can possess any positive energy value and follows a well-defined trajectory in phase space. In contrast, quantum mechanics allows only discrete energy values and introduces position and momentum uncertainties that preclude well-defined trajectories. Coherent states, however, provide means to reconcile these seemingly contradictory descriptions.

The key to this reconciliation lies in examining the quantum predictions for measurement statistics. We seek a quantum state that yields statistics closely matching classical expectations. Coherent states with large amplitudes ($|\alpha| \gg 1$) fulfil this requirement, as we will show.

1.1. THE QUANTUM HARMONIC OSCILLATOR

Consider a coherent state $|\alpha\rangle$ at $t = 0$, evolving under the harmonic oscillator Hamiltonian. The time-evolved state is given by:

$$|\psi(t)\rangle = e^{-i\omega t \hat{n}} |\alpha\rangle = \sum_{n=0}^{\infty} e^{-|\alpha|^2/2} \frac{\alpha^n}{\sqrt{n!}} e^{-in\omega t} |n\rangle = |e^{-i\omega t} \alpha\rangle. \quad (1.16)$$

This remains a coherent state with a time-dependent amplitude $\alpha(t) = e^{-i\omega t} \alpha$, which equals the expectation value of the annihilation operator, $\langle \hat{a}(t) \rangle = \alpha(t)$. This evolution mirrors exactly the classical solution in the complex representation in Eq. (1.6).

Moreover, the uncertainty in any quadrature \hat{x}_ϕ remains constant: $\Delta x_\phi(t) = 1$. As $|\alpha|$ increases, the signal-to-noise ratio $\frac{|\alpha|}{\Delta x}$ grows, approaching infinity as $|\alpha|$ increases to infinity. Thus, for large amplitudes, quantum noise becomes negligible compared to classical noise sources, effectively recovering the classical trajectory.

The energy quantization issue can also be addressed using coherent states. The ratio of energies between consecutive number states is:

$$\frac{E_{n+1}}{E_n} = \frac{n + 3/2}{n + 1/2}. \quad (1.17)$$

As n increases, this ratio approaches unity, making the discrete nature of the energy spectrum less perceptible. Coherent states with $|\alpha| \gg 1$ project onto high-order number states with a narrow Poisson distribution centred at $\langle \hat{N} \rangle = |\alpha|^2$ and width $\Delta N = |\alpha|$:

$$|\alpha\rangle = e^{-|\alpha|^2/2} \sum_{n=0}^{\infty} \frac{\alpha^n}{\sqrt{n!}} |n\rangle = \sum_{n=0}^{\infty} e^{-|\alpha|^2/2} \frac{\alpha^n}{\sqrt{n!}} |n\rangle. \quad (1.18)$$

This distribution effectively smooths out the discrete energy levels, yielding a continuous spectrum.

Squeezed States

In quantum sensing applications, harmonic oscillators are often used to detect signals encoded as phase or amplitude modulations. While coherent states provide a balanced uncertainty in both quadratures $\Delta \hat{x}_\phi = \Delta \hat{y}_\phi = 1$, they still suffer from quantum noise limitations. This

1.1. THE QUANTUM HARMONIC OSCILLATOR

noise, rooted in vacuum fluctuations, can mask weak signals and limit measurement precision. Squeezed states offer a solution to this problem by redistributing the uncertainty between quadratures. Consider a state where $\Delta\hat{x}_\phi \ll 1$ and $\Delta\hat{y}_\phi \gg 1$ while still satisfying the uncertainty principle $\Delta\hat{x}_\phi\Delta\hat{y}_\phi \geq 1$, as depicted in Fig. 1.1.b for the case of $\phi = 0$. Such a state allows for more precise measurements in the squeezed quadrature $\Delta\hat{x}_\phi$ at the expense of increased uncertainty in the orthogonal quadrature $\Delta\hat{y}_\phi \gg 1$.

Formally, we define a squeezed state as one in which a particular quadrature \hat{x}_ϕ has an uncertainty below the vacuum level $\Delta\hat{x}_\phi < 1$.

A special class of squeezed states are those that satisfy the equality in the uncertainty relation for all quadratures $\Delta\hat{x}_\phi\Delta\hat{y}_\phi = 1$ for all ϕ . These minimum uncertainty squeezed states can be generated using the squeezing operator:

$$\hat{S}(\zeta) = \exp\left(\frac{\zeta^*}{2}\hat{a}^2 - \frac{\zeta}{2}\hat{a}^{\dagger 2}\right), \quad (1.19)$$

where $\zeta = re^{i\theta}$ is the complex squeezing parameter, associated with the Hamiltonian of the form :

$$\hat{H} = \frac{i\hbar}{2}(\zeta^*\hat{a}^2 - \zeta\hat{a}^{\dagger 2}). \quad (1.20)$$

The action of the squeezing operator on the annihilation operator is given by:

$$\hat{S}^\dagger(\zeta)\hat{a}\hat{S}(\zeta) = \hat{a} \cosh r - e^{i\theta}\hat{a}^\dagger \sinh r. \quad (1.21)$$

In terms of quadratures, this transformation becomes:

$$\hat{S}^\dagger(\zeta)\hat{x}_{\theta/2}\hat{S}(\zeta) = e^{-r}\hat{x}_{\theta/2}, \quad \hat{S}^\dagger(\zeta)\hat{y}_{\theta/2}\hat{S}(\zeta) = e^r\hat{y}_{\theta/2}, \quad (1.22)$$

where $\hat{x}_\psi = \cos(\psi)\hat{x} + \sin(\psi)\hat{y}$ and $\hat{y}_\psi = \hat{x}_{\psi+\frac{\pi}{2}}$ for any angle ψ . When applied to the vacuum state for example, this transformation produces a state with $\Delta\hat{x}_{\theta/2} = e^{-r}$ and $\Delta\hat{y}_{\theta/2} = e^r$.

Thus, the squeezing operator creates a minimum uncertainty squeezed state, reducing the uncertainty in one quadrature below the vacuum level while increasing it in the orthogonal

quadrature, all while maintaining the minimum uncertainty product.

1.1.5 The EPR Paradox and Quantum Entanglement

The year 1935 marked a pivotal moment in quantum physics when Einstein, Podolsky, and Rosen introduced a groundbreaking thought experiment that challenged the foundations of quantum mechanics. Their analysis centred on a unique quantum state exhibiting perfect correlations between two particles' position and momentum measurements. This led to a fundamental dilemma: either quantum mechanics permits instantaneous non-local effects between distant particles, or the theory is inherently incomplete.

The possibility of quantum mechanical incompleteness suggests the necessity of additional "hidden" variables governed by classical probability distributions. However, Bell's theoretical work in 1964 [2], followed by numerous experimental validations [3, 90, 91, 92], definitively demonstrated that local hidden variable models cannot adequately explain quantum mechanical phenomena. This revelation established quantum mechanics as an inherently non-local theory, with entangled states serving as crucial resources in quantum information processing.

To recognize quantum correlations, we describe Quantum Non-Demolition (QND) measurements [93]. A QND measurement involves performing a measurement on a first system that is highly correlated with a second system, enabling information extraction from the latter without perturbation. When the quadratures \hat{x}_1 and \hat{x}_2 of two distinguishable electromagnetic field modes are perfectly correlated, a QND measurement allows us to determine the expectation value of \hat{x}_2 without uncertainty by measuring the first quadrature. The QND measurement estimator is characterized by the conditional variance of \hat{x}_2 :

$$\langle \Delta^2(\hat{p}_2|\hat{p}_1) \rangle = \langle \Delta^2\hat{p}_2 \rangle - \frac{\langle \delta\hat{p}_1 \delta\hat{p}_2 \rangle^2}{\langle \Delta^2\hat{p}_1 \rangle} \quad (1.23)$$

where $\delta\hat{p}_i = \hat{p}_i - \langle \hat{p}_i \rangle$. When $\langle \Delta^2(\hat{p}_2|\hat{p}_1) \rangle$ falls below the shot-noise limit, this indicates the presence of quantum correlations between the two modes, confirming the QND nature of the measurement.

Now, consider two spatially separated particles with position and momentum operators denoted as $\hat{x}_1, \hat{y}_1, \hat{x}_2$, and \hat{y}_2 . The original EPR argument demonstrates that perfect correlations

1.1. THE QUANTUM HARMONIC OSCILLATOR

between these operators lead to a paradoxical situation: measuring \hat{x}_1 determines particle 2's position without interaction, implying a reality element for 2's position. Similar logic applies to momentum measurements, contradicting the quantum mechanical uncertainty principle.

The theoretical framework was later extended to continuous-variable optical systems. Reid's formulation [94] demonstrates that EPR correlations can manifest even with non-maximal correlations between conjugate quadratures of optical modes. The paradox emerges when:

$$\langle \Delta^2(\hat{x}_2|\hat{x}_1) \rangle \langle \Delta^2(\hat{p}_2|\hat{p}_1) \rangle < 1. \quad (1.24)$$

A bipartite quantum system described by density matrix $\hat{\rho}$ exhibits inseparability when it cannot be expressed as:

$$\hat{\rho} \neq \sum_i p_i \hat{\rho}_1^i \otimes \hat{\rho}_2^i \quad (1.25)$$

where $\hat{\rho}_1^i$ and $\hat{\rho}_2^i$ represent individual mode density matrices with probabilities p_i .

To discuss the connection between squeezing and entanglement, we consider a 50/50 beam splitter mixing two modes. The transformation equations are:

$$\hat{a}^{(+)} = \frac{\hat{a}_1 + \hat{a}_2}{\sqrt{2}} \quad (1.26)$$

$$\hat{a}^{(-)} = \frac{\hat{a}_1 - \hat{a}_2}{\sqrt{2}} \quad (1.27)$$

The quadrature variances for sum and difference modes are:

$$\langle \Delta^2 \hat{p}^{(-)} \rangle = \langle \Delta^2(\hat{p}_1 - \hat{p}_2) \rangle \quad (1.28)$$

$$\langle \Delta^2 \hat{x}^{(+)} \rangle = \langle \Delta^2(\hat{x}_1 + \hat{x}_2) \rangle \quad (1.29)$$

For EPR-correlated modes, both $\langle \Delta^2(\hat{p}_1 - \hat{p}_2) \rangle$ and $\langle \Delta^2(\hat{x}_1 + \hat{x}_2) \rangle$ approach zero, resulting in squeezed sum and difference modes. Conversely, EPR-correlated states can be generated by combining two squeezed modes at a 50/50 beam splitter.

1.2 Quantization of the Electromagnetic field

The main goal of this section is to provide an introduction to the quantization of the electromagnetic field, focusing on the concept of modes and their application in describing optical beams. The section starts by explaining the concept of the analytical signal, which allows for a complex representation of electromagnetic fields. It then discusses the quantization of the field in different mode bases, including travelling plane waves (TPW) and transverse modes like Hermite-Gauss (HG) modes, which are more suitable for describing real-world optical beams. Finally, the section introduces optical cavities and their use in confining light and briefly mentions the quantization process within a cavity.

For more details, the reader is invited to check multiple lecture notes and books [95, 7, 96, 87] that use the same approach.

1.2.1 The analytical Electromagnetic signal

Consider a real vector field $\vec{E}(\vec{r}, t)$, where \vec{r} denotes the position vector and t represents time. The Fourier transform of this field can be expressed mathematically as:

$$\vec{E}(\vec{r}, t) = \frac{1}{\sqrt{2\pi}} \int_{-\infty}^{\infty} \tilde{\vec{E}}(\vec{r}, \omega) e^{-i\omega t} d\omega. \quad (1.30)$$

A key property of this transform comes from the real nature of \vec{E} . Specifically, the Fourier transform exhibits a conjugate symmetry, which can be demonstrated as follows:

$$\begin{aligned} \vec{E}(\vec{r}, \omega) &= \frac{1}{\sqrt{2\pi}} \int_{-\infty}^{\infty} \tilde{\vec{E}}(\vec{r}, t) e^{i\omega t} dt \\ \vec{E}^*(\vec{r}, \omega) &= \frac{1}{\sqrt{2\pi}} \left[\int_{-\infty}^{\infty} \tilde{\vec{E}}(\vec{r}, t) e^{i\omega t} dt \right]^* \\ &= \frac{1}{\sqrt{2\pi}} \int_{-\infty}^{\infty} \tilde{\vec{E}}^*(\vec{r}, t) e^{-i\omega t} dt \\ &= \frac{1}{\sqrt{2\pi}} \int_{-\infty}^{\infty} \tilde{\vec{E}}(\vec{r}, t) e^{-i\omega t} dt \\ \vec{E}^*(\vec{r}, \omega) &= \vec{E}(\vec{r}, -\omega). \end{aligned} \quad (1.31)$$

1.2. QUANTIZATION OF THE ELECTROMAGNETIC FIELD

This conjugate symmetry in Eq. (1.31) introduces redundancy in the Fourier decomposition. To eliminate this redundancy, we introduce the complex field, defined as:

$$\vec{E}^{(+)}(\vec{r}, t) = \frac{1}{\sqrt{2\pi}} \int_0^\infty \tilde{\vec{E}}(\vec{r}, \omega) e^{-i\omega t} d\omega. \quad (1.32)$$

This formulation selectively incorporates only the positive frequency components of the spectrum, effectively addressing the redundancy issue. The original real vector field can be reconstructed from this complex field using the relation:

$$\vec{E}(\vec{r}, t) = \vec{E}^{(+)}(\vec{r}, t) + \vec{E}^{(-)}(\vec{r}, t). \quad (1.33)$$

Here, $\vec{E}^{(-)}(\vec{r}, t)$ is equivalent to $\vec{E}^{(+)*}(\vec{r}, t)$. It's worth noting that for free electromagnetic fields, which lack static components, the lower integration limit at $\omega = 0$ does not pose computational difficulties or divergence issues.

1.2.2 The electromagnetic wave nature of light

The conceptualization of light as an electromagnetic phenomenon represents a pivotal development in the history of physics. This understanding emerged gradually, beginning with Michael Faraday's mid-19th-century observations of the interaction between light and magnetic fields. Faraday's work hinted at a profound connection between optics and electromagnetism, suggesting that light might propagate as an electromagnetic disturbance without requiring a medium.

The mathematical foundation for this idea was later established by James Clerk Maxwell in his comprehensive theory of electromagnetism [97]. Maxwell's work predicted electromagnetic waves travelling at a speed consistent with measurements of light's velocity. Heinrich Hertz's subsequent experimental confirmation of these waves in the 1880s solidified the electromagnetic theory of light [98].

The foundation of electromagnetic theory lies in Maxwell's equations, which describe the behaviour of electric and magnetic fields. These equations, reformulated by Oliver Heaviside [99] in the vector calculus form we use today, consist of four fundamental relations. The homoge-

1.2. QUANTIZATION OF THE ELECTROMAGNETIC FIELD

neous Maxwell equations are:

$$\operatorname{div} \vec{B} = 0 \quad \overrightarrow{\operatorname{rot}} \vec{E} = -\frac{1}{c^2} \frac{\partial \vec{B}}{\partial t} \quad (1.34)$$

while the inhomogeneous Maxwell equations take the form:

$$\operatorname{div} \vec{E} = \frac{\rho}{\varepsilon_0} \quad \overrightarrow{\operatorname{rot}} \vec{B} = \mu_0 \varepsilon_0 \frac{\partial \vec{E}}{\partial t} + \mu_0 \vec{j}. \quad (1.35)$$

Here, $\rho(\vec{r}, t)$ and $\vec{j}(\vec{r}, t)$ represent charge density and current distribution, respectively, while ε_0 and μ_0 denote the electric permittivity and magnetic permeability of vacuum.

In the absence of sources ($\rho = 0$ and $\vec{j} = \vec{0}$), these equations simplify to:

$$\operatorname{div} \vec{E} = 0 \quad c^2 \overrightarrow{\operatorname{rot}} \vec{B} = \frac{\partial \vec{E}}{\partial t}, \quad (1.36)$$

where $c = \frac{1}{\sqrt{\varepsilon_0 \mu_0}}$ represents the speed of light in vacuum.

The homogeneous equations allow for the derivation of fields from scalar and vector potentials:

$$\vec{B} = \overrightarrow{\operatorname{rot}} \vec{A} \quad \vec{E} = -\overrightarrow{\operatorname{grad}} \phi - \frac{\partial \vec{A}}{\partial t}, \quad (1.37)$$

These potentials exhibit gauge invariance under the transformations:

$$\vec{A} \rightarrow \vec{A} + \overrightarrow{\operatorname{grad}} \Lambda \quad \phi \rightarrow \phi - \frac{\partial \Lambda}{\partial t}, \quad (1.38)$$

where $\Lambda(\vec{r}, t)$ is an arbitrary function. Incorporating these potentials into the inhomogeneous equations yields:

$$\begin{aligned} (c^2 \vec{\Delta} - \frac{\partial^2}{\partial t^2}) \vec{A} &= \frac{\partial}{\partial t} \overrightarrow{\operatorname{grad}} \phi + c^2 \overrightarrow{\operatorname{grad}} (\operatorname{div} \vec{A}), \\ \vec{\Delta} \phi + \frac{\partial}{\partial t} \operatorname{div} \vec{A} &= 0. \end{aligned} \quad (1.39)$$

1.2. QUANTIZATION OF THE ELECTROMAGNETIC FIELD

By adopting the Coulomb gauge ($\text{div } \vec{A} = 0$) and therefore $\phi = 0$, these equations simplify to:

$$\left(\vec{\Delta} - \frac{1}{c^2} \frac{\partial^2}{\partial t^2}\right) \vec{A} = 0. \quad (1.40)$$

This wave equation for the vector potential components, in conjunction with the Coulomb condition, reduces the system to two degrees of freedom from the previous six.

In general, many different solutions are possible for this wave equation. They are coined spatiotemporal modes that adhere to the slowly varying envelope approximation and satisfy temporal orthonormality conditions over an integration time T that exceeds all other relevant timescales in the problem. They are determined by boundary conditions. In many optical systems, these solutions can be represented as $\vec{\varepsilon} A(\vec{r}, t)$, where $\vec{\varepsilon}$ is a constant unit vector and $A(\vec{r}, t)$ is a scalar function. This scalar approximation is applicable when the system exhibits symmetry for both independent components of the vector potential.

Seeking separable solutions of the form $\vec{A}(\vec{r}, t) = u(\vec{r})\vec{A}(t)$, we find that the spatial component must satisfy the Helmholtz equation:

$$\vec{\Delta} u(\vec{r}) + k^2 u(\vec{r}) = 0, \quad (1.41)$$

with k^2 as a separation constant. The solutions to this equation, subject to appropriate boundary conditions, constitute the spatial modes of the system. These modes $\{u_n(\vec{r})\}$, corresponding to the eigenfunctions of the Laplacian operator Δ , are fundamental to the quantization of the electromagnetic field.

1.2.3 Mode of Electromagnetic fields and mode basis

Building upon our discussion of electromagnetic waves, we now turn our attention to the concept of electromagnetic field modes. An electromagnetic field mode is characterized as a normalized vector field $\vec{u}_0(\vec{r}, t)$ that satisfies Maxwell's equations in vacuum. This field must satisfy the following wave equation and divergence condition:

$$\left(\vec{\Delta} - \frac{1}{c^2} \frac{\partial^2}{\partial t^2}\right) \vec{u}_0(\vec{r}, t) = 0 \quad \text{and} \quad \text{div } \vec{u}_0(\vec{r}, t) = 0. \quad (1.42)$$

1.2. QUANTIZATION OF THE ELECTROMAGNETIC FIELD

Furthermore, it must meet a normalization criterion at any given time t :

$$\frac{1}{V} \int_V d^3r |\vec{u}_0(\vec{r}, t)|^2 = 1. \quad (1.43)$$

In this context, V denotes the encompassing volume containing the entire physical system. From one mode satisfying these conditions, it's possible to construct an orthonormal mode basis $\{\vec{u}_m(\vec{r}, t)\}$. This basis serves as a powerful tool for decomposing any solution of Maxwell's equations, with $\hat{u}_0(\vec{r}, t)$ as its initial element. An alternative approach to generating a mode basis involves imposing specific boundary conditions on Maxwell's equation solutions, such as those encountered in resonator systems.

For our analysis, we consider fields confined within a finite spatial volume V . This constraint leads to a discrete basis, indexed by a set of integers collectively denoted as m . Under these conditions, any complex field $\vec{E}^{(+)}(\vec{r}, t)$ can be expressed as a superposition of these modes:

$$\vec{E}^{(+)}(\vec{r}, t) = \sum_m \mathcal{E}_m \vec{u}_m(\vec{r}, t). \quad (1.44)$$

The orthonormality of this basis is ensured by the following conditions:

$$\frac{1}{V} \int_V d^3r \vec{u}_m^*(\vec{r}, t) \cdot \vec{u}_n(\vec{r}, t) = \delta_{mn}. \quad (1.45)$$

Here, δ_{mn} represents the Kronecker delta function, which equals 1 when $m = n$ and 0 otherwise. In this formulation, \mathcal{E}_m represents the complex amplitudes associated with each mode, fully characterizing the EM field.

The modal decomposition of the electric field in Eq; (1.44), as presented in the previous section, can be reinterpreted in the context of a Hilbert space. In this formalism, a given solution of Maxwell's equations $\vec{E}^{(+)}(\vec{r}, t)$ can be represented as a vector in a Hilbert space, which we call the modal space. We denote this with a vector representation:

$$\vec{E} = \sum_m \mathcal{E}_m \vec{u}_m. \quad (1.46)$$

Here, \vec{u}_m represents a unit vector in the modal space, corresponding to a column vector of

1.2. QUANTIZATION OF THE ELECTROMAGNETIC FIELD

zeros with a 1 at the m th position. Consequently, \vec{E} can be expressed as the column vector $(\mathcal{E}_1, \mathcal{E}_2, \dots)^T$, where T denotes the transpose operation in the modal Hilbert space.

Consider a unitary transformation U ($UU^\dagger = U^\dagger U = \mathbb{I}$) with complex components U_{nm} . We can define a new set of modal vectors:

$$\vec{v}_n = \sum_{m=1}^N U_{nm} \vec{u}_m. \quad (1.47)$$

It can be demonstrated that these vectors form another complete set of orthonormal modal vectors, satisfying the condition $\vec{v}_n^\dagger \cdot \vec{v}_{n'} = \delta_{nn'}$. Consequently, any electromagnetic field can be expressed in this new basis:

$$\vec{E}^{(+)}(\vec{r}, t) = \sum_n \mathcal{V}_n \vec{v}_n(\vec{r}, t). \quad (1.48)$$

This mathematical approach to modes offers considerable flexibility in choosing the unitary transformation U and, by extension, the mode basis.

Plane Waves

Our first analysis focused on fields that are superpositions of plane waves with wave vectors close to a mean value \vec{k}_0 (paraxial approximation) and frequencies near a central frequency $\omega_0 = c|\vec{k}_0|$ (narrowband approximation). Assuming \vec{k}_0 is parallel to the z-axis, we can express the electric field as:

$$\vec{E}^{(+)}(\vec{r}, t) = e^{i(k_0 z - \omega_0 t)} \sum_m \mathcal{C}_m \vec{u}_m(\vec{r}, t) \quad (1.49)$$

In this expression, $e^{i(k_0 z - \omega_0 t)}$ represents a carrier wave, while $\vec{u}_m(\vec{r}, t)$ are envelope functions for different modes. These envelope functions vary slowly compared to the rapid oscillations of the carrier wave, both in space (relative to the wavelength) and in time (relative to the optical period). While plane wave modes are commonly used due to their mathematical simplicity, they often lack physical realism. Other mode bases may better suit specific light sources or optical systems.

1.2. QUANTIZATION OF THE ELECTROMAGNETIC FIELD

To simplify our analysis further, we'll consider only those unitary modal transformations that can be separated into transverse and longitudinal components. We can then write :

$$\vec{u}_m(\vec{r}, t) = \vec{u}_{i,p,r}(\vec{r}, t) = \vec{\epsilon}_i u_p^{(T)}(x, y, z) u_r^{(L)}(t, z), \quad (1.50)$$

where, $\vec{\epsilon}_i$ ($i = 1, 2$) represents one of two orthogonal polarization unit vectors in the (x, y) plane. The function $u_p^{(T)}$ describes the transverse (spatial) part of the mode, while $u_r^{(L)}$ represents its longitudinal (temporal) part. For the spatial mode basis, we can employ any set of orthonormal

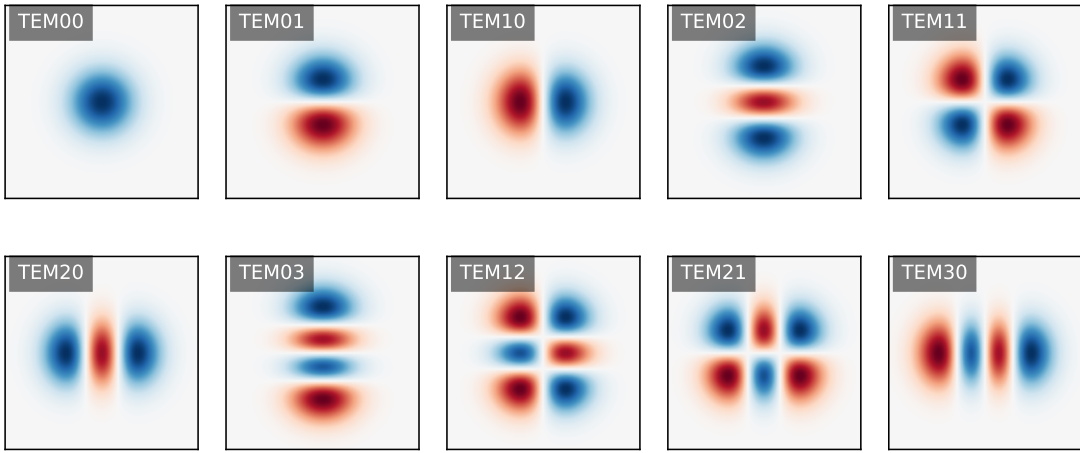


Figure 1.2: 10 first transverse Hermite-Gaussian spatial modes.

functions $u_p(x, y)$ in the transverse plane, provided they satisfy the paraxial approximation by varying slowly over distances comparable to the wavelength. The full spatial mode functions $u_p^{(T)}(x, y, z)$ can be derived from their values at $z = 0$ using the Huygens-Fresnel principle to account for diffraction effects. An example consists of Spatial Hermite-Gauss modes, which are well-suited for beams produced in cavities with spherical mirrors. We plot in Fig. 1.2, the 10 first HG modes. The temporal mode basis can be constructed using any set of functions $u_r(t, z)$ that adhere to the slowly varying envelope approximation and satisfy temporal orthonormality conditions over an integration time T that exceeds all other relevant timescales in the problem. The longitudinal mode functions can take the form $u_r^{(L)}(t, z) = u_r(\tau)$, where $\tau = t - z/c$, describing pulses that propagate undistorted at the speed of light along the z -axis. Examples include Temporal (Fig. 1.3) or frequency Hermite-Gauss modes, which provide a convenient

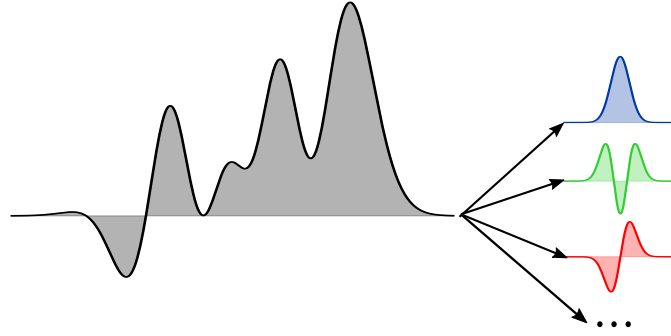


Figure 1.3: An ultrafast pulse decomposed into an orthogonal basis of Hermite Gaussian temporal modes.

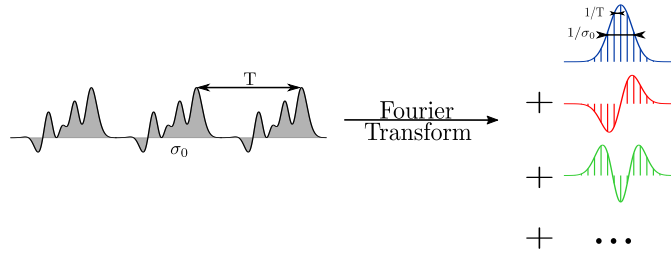


Figure 1.4: Decomposition of a train of pulses into an orthogonal basis of trains of Hermite Gaussian (HG) pulses whose Fourier transform are HG frequency comb modes.

orthogonal basis for light pulses of various temporal or spectral shapes and Hermite-Gaussians frequency combs modes, which can be represented either as a superposition of equally spaced monochromatic waves in the frequency domain or as a train of identical, equally spaced pulses in the time domain (Fig. 1.2).

This formulation allows us to treat polarization, spatial, and temporal effects independently, which is a consequence of our simplifying assumptions. This approach is particularly useful when examining optical phenomena where the temporal characteristics of the light do not significantly influence its spatial distribution, or conversely, when spatial diffraction effects have minimal impact on the temporal profile of light pulses.

When we're dealing with a single temporal mode $u_0^{(L)}(t, z)$, the electric field can be written as:

$$\vec{E}^{(+)}(\vec{r}, t) = \vec{e}_0 e^{i(k_0 z - \omega_0 t)} u_0^{(L)}(t, z) \sum_p \mathcal{E}_p u_p^{(T)}(\vec{r}) \quad (1.51)$$

1.2. QUANTIZATION OF THE ELECTROMAGNETIC FIELD

This allows us to define a transverse electric field:

$$E_T^{(+)}(x, y, z) = \sum_p \mathcal{E}_p u_p^{(T)}(x, y, z) \quad (1.52)$$

Conversely, for a single spatial mode $u_0^{(T)}(\vec{r})$, we can express the electric field as:

$$\vec{E}^{(+)}(\vec{r}, t) = \vec{\epsilon}_0 e^{-i\omega_0 t} u_0^{(T)}(\vec{r}) \sum_r \mathcal{E}_r u_r^{(L)}(t, z) \quad (1.53)$$

This leads to a definition of the temporal or longitudinal field:

$$E_L^{(+)}(t, z) = \sum_r \mathcal{E}_r u_r^{(L)}(t, z) \quad (1.54)$$

1.2.4 Quantization of the EM field in the basis of TPW

In this subsection, we're interested in an electromagnetic system enclosed within a cubic volume (V) with side length L . For any complex field $A^{(+)}(\vec{r}, t)$ within this volume, we can define its spatial Fourier components as:

$$\vec{A}_\ell^{(+)}(t) = \frac{1}{(\sqrt{2\pi L})^3} \int_{(V)} d^3r \vec{A}^{(+)}(\vec{r}, t) \cdot \vec{\epsilon}_\ell e^{-i\vec{k}_\ell \cdot \vec{r}}. \quad (1.55)$$

This decomposition enables us to express the complex vector field as a discrete sum of travelling plane waves:

$$\vec{A}^{(+)}(\vec{r}, t) = \sum_\ell \vec{A}_\ell^{(+)}(t) \vec{\epsilon}_\ell e^{i\vec{k}_\ell \cdot \vec{r}}. \quad (1.56)$$

The index ℓ represents a set of four integers (n_x, n_y, n_z, s) and define the components of the wave vector \vec{k}_ℓ : $k_{x,\ell} = n_x \frac{2\pi}{L}$, $k_{y,\ell} = n_y \frac{2\pi}{L}$ and $k_{z,\ell} = n_z \frac{2\pi}{L}$. The index $s = 1, 2$ denotes two orthogonal polarization unit vectors $\vec{\epsilon}_1$ and $\vec{\epsilon}_2$, which are perpendicular to \vec{k}_ℓ . These polarization vectors may be complex to accommodate circular polarizations.

The time evolution of the Fourier components is governed by the wave equation, Eq. (1.40)

1.2. QUANTIZATION OF THE ELECTROMAGNETIC FIELD

which in this representation takes the form :

$$\frac{d^2 \vec{A}_\ell^{(+)}}{dt^2} + \omega_\ell^2 \vec{A}_\ell^{(+)} = \vec{0}. \quad (1.57)$$

where $\omega_\ell = c \|\vec{k}_\ell\|$ represents the angular frequency of each mode. This represents the equation of motion of the harmonic oscillator, with a little difference, we cannot interpret the $\vec{A}_\ell^{(+)}$ as modal amplitudes since they are complex.

Given that $\vec{A}^{(+)}(\vec{r}, t)$ encompasses only positive frequencies, the solution takes the form:

$$\vec{A}_\ell^{(+)}(t) = \vec{A}_\ell e^{-i\omega_\ell t}, \quad (1.58)$$

where \vec{A}_ℓ is a time-independent complex vector. This leads to a first-order differential equation for the time evolution:

$$i \frac{d}{dt} \vec{A}_\ell^{(+)}(t) = \omega_\ell \vec{A}_\ell^{(+)}(t), \quad (1.59)$$

reminiscent of the Schrödinger equation.

The complex electric and magnetic fields can be expressed in terms of these Fourier components:

$$\vec{E}^{(+)}(\vec{r}, t) = -i \sum_\ell \omega_\ell \vec{A}_\ell^{(+)}(t) \vec{\varepsilon}_\ell e^{i\vec{k}_\ell \cdot \vec{r}}, \quad (1.60)$$

$$\vec{B}^{(+)}(\vec{r}, t) = i \sum_\ell \vec{k}_\ell \times \vec{\varepsilon}_\ell \vec{A}_\ell^{(+)}(t) e^{i\vec{k}_\ell \cdot \vec{r}}. \quad (1.61)$$

The total energy H of the free electromagnetic field is given by the volume integral:

$$H = \varepsilon_0 \int_{(V)} d^3r (\vec{E}^2(\vec{r}, t) + c^2 \vec{B}^2(\vec{r}, t)). \quad (1.62)$$

Utilizing the expressions for $\vec{E}^{(+)}$ and $\vec{B}^{(+)}$ in Eqs. (1.60) and (1.61), this energy can be rewritten

1.2. QUANTIZATION OF THE ELECTROMAGNETIC FIELD

as:

$$H = 2\varepsilon_0 L^3 \sum_{\ell} \omega_{\ell}^2 |\vec{A}_{\ell}^{(+)}|^2 \quad (1.63)$$

This formulation reveals a crucial property: the energy of the free electromagnetic field can be expressed as a sum of independent contributions from each mode. The excitation amplitude of each mode is proportional to $|\vec{A}_{\ell}^{(+)}|^2$. The travelling plane wave (TPW) modes thus serve to diagonalize the energy of the system, establishing themselves as the natural eigenmodes for the free electromagnetic field.

Let us introduce, For the free electromagnetic field, the real and imaginary parts of the complex field $\vec{A}_{\ell}^{(+)}(t)$:

$$\vec{A}_{\ell}^{(+)}(t) = \vec{A}_{q,\ell}(t) + i\vec{A}_{p,\ell}(t), \quad (1.64)$$

which allows us to express the energy as:

$$H = 2\varepsilon_0 L^3 \sum_{\ell} \omega_{\ell}^2 (\vec{A}_{q,\ell}^2 + \vec{A}_{p,\ell}^2). \quad (1.65)$$

In the process of quantizing the electromagnetic field, we must identify the canonical conjugate quantities and establish the appropriate commutation relations. This approach parallels the quantization procedure for the quantum harmonic oscillator in Subsection 1.1.2. Let us consider a classical system characterized by dynamical variables $\{q_i(t), p_i(t)\}$ ($i = 1 \dots n$), with energy given by the Hamiltonian $H(q_1, p_1, \dots, q_n, p_n)$. These variables are canonical conjugates when the system's evolution follows the Hamilton-Jacobi equations:

$$\frac{d}{dt} q_i = \frac{\partial H}{\partial p_i}, \quad \frac{d}{dt} p_i = -\frac{\partial H}{\partial q_i}. \quad (1.66)$$

The quantization procedure associates these classical, time-dependent variables with Hermitian, time-independent operators $\{\hat{q}_i, \hat{p}_i\}$ that satisfy the commutation relations:

$$[\hat{q}_i, \hat{p}_j] = i\hbar\delta_{i,j}. \quad (1.67)$$

1.2. QUANTIZATION OF THE ELECTROMAGNETIC FIELD

From the time evolution equation (1.59), we derive:

$$\frac{d}{dt} \vec{A}_{p,\ell} = \omega_\ell \vec{A}_{q,\ell} = \frac{1}{4\varepsilon_0 L^3 \omega_\ell} \frac{\partial H}{\partial \vec{A}_{q,\ell}}, \quad (1.68)$$

$$\frac{d}{dt} \vec{A}_{q,\ell} = -\omega_\ell \vec{A}_{p,\ell} = -\frac{1}{4\varepsilon_0 L^3 \omega_\ell} \frac{\partial H}{\partial \vec{A}_{p,\ell}}. \quad (1.69)$$

These equations are of the Hamiltonian form in Eq. (1.66), allowing us to identify the canonical conjugate quantities: $q_i \leftrightarrow 2\sqrt{\varepsilon_0 L^3 \omega_\ell} \vec{A}_{q,\ell}$ and $p_i \leftrightarrow 2\sqrt{\varepsilon_0 L^3 \omega_\ell} \vec{A}_{p,\ell}$.

We now associate these classical quantities with time-independent observables $\hat{A}_{x,\ell}$ and $\hat{A}_{y,\ell}$ that obey the commutation relations:

$$[2\sqrt{\varepsilon_0 L^3 \omega_\ell} \hat{A}_{x,\ell}, 2\sqrt{\varepsilon_0 L^3 \omega_\ell} \hat{A}_{y,\ell'}] = i\hbar \delta_{\ell,\ell'}. \quad (1.70)$$

This leads to the fundamental commutation relation:

$$[\hat{A}_{x,\ell}, \hat{A}_{y,\ell'}] = \frac{i\hbar}{4\varepsilon_0 L^3 \omega_\ell} \delta_{\ell,\ell'}. \quad (1.71)$$

Introducing the non-Hermitian operator $\hat{A}_\ell = \hat{A}_{x,\ell} + i\hat{A}_{y,\ell}$, we obtain:

$$[\hat{A}_\ell, \hat{A}_{\ell'}^\dagger] = \frac{\hbar}{2\varepsilon_0 L^3 \omega_\ell} \delta_{\ell,\ell'}. \quad (1.72)$$

Defining:

$$\hat{a}_\ell = \sqrt{\frac{2\varepsilon_0 L^3 \omega_\ell}{\hbar}} \hat{A}_\ell, \quad (1.73)$$

we recover the familiar commutation relation for harmonic oscillators: $[\hat{a}_\ell, \hat{a}_{\ell'}^\dagger] = \delta_{\ell,\ell'}$.

The complex vector potential operator can then be expressed from Eqs. (1.56) and (1.58) as:

$$\hat{A}^{(+)}(\vec{r}, t) = \sum_{\ell} \sqrt{\frac{\hbar}{2\varepsilon_0 \omega_\ell L^3}} \hat{a}_\ell \vec{\varepsilon}_\ell e^{i(\vec{k}_\ell \cdot \vec{r} - \omega_\ell t)}, \quad (1.74)$$

and the Hamiltonian of the quantized field takes the form:

$$\begin{aligned}
 \hat{H} &= 2\varepsilon_0 L^3 \sum_{\ell} \omega_{\ell}^2 (\hat{A}_{q\ell}^2 + \hat{A}_{p\ell}^2) \\
 &= \varepsilon_0 L^3 \sum_{\ell} \omega_{\ell}^2 (\hat{A}_{\ell} \hat{A}_{\ell}^{\dagger} + \hat{A}_{\ell}^{\dagger} \hat{A}_{\ell}) \\
 \hat{H} &= \sum_{\ell} \frac{\hbar \omega_{\ell}}{2} (\hat{a}_{\ell} \hat{a}_{\ell}^{\dagger} + \hat{a}_{\ell}^{\dagger} \hat{a}_{\ell}). \tag{1.75}
 \end{aligned}$$

This Hamiltonian represents an assembly of independent quantum harmonic oscillators, where the position and momentum analogues are the real and imaginary parts of the spatial Fourier component \vec{A}_{ℓ} of the complex vector potential $\vec{A}^{(+)}(\vec{r}, t)$.

1.2.5 Basis Change

While the Travelling Plane Wave (TPW) basis has served us well due to its mathematical simplicity and connection to spatial Fourier transforms, it lacks physical realism as it assumes uniform field amplitude throughout the entire volume $V = L^3$. We will now explore alternative bases that may offer more physically intuitive representations but first let's define this notion of basis change.

Consider a unitary transformation applied to the set of TPW creation operators, yielding a new set of operators $\{\hat{b}_m^{\dagger}\}$:

$$\hat{b}_m^{\dagger} = \sum_{\ell} U_{m\ell} \hat{a}_{\ell}^{\dagger} \tag{1.76}$$

Here, $U_{m\ell}$ represents an element of a unitary matrix \mathbf{U} as we introduced in Eq. (1.47) for the mode basis. The corresponding annihilation operator is given by:

$$\hat{b}_m = \sum_{\ell} U_{m\ell}^{\dagger} \hat{a}_{\ell} = \sum_{\ell} U_{\ell m}^{-1} \hat{a}_{\ell} \tag{1.77}$$

1.2. QUANTIZATION OF THE ELECTROMAGNETIC FIELD

One can verify that these new operators obey the standard commutation relation:

$$[\hat{b}_m, \hat{b}_{m'}^\dagger] = \sum_{\ell, \ell'} U_{m\ell}^\dagger U_{m'\ell'} [\hat{a}_\ell, \hat{a}_{\ell'}^\dagger] = \sum_{\ell} U_{m\ell}^\dagger U_{m'\ell} = \delta_{m,m'} \quad (1.78)$$

This demonstrates that $\{\hat{b}_m\}$ constitute a new set of annihilation operators for independent harmonic oscillators, preserving the fundamental nature of our bosonic operators.

By inverting the transformation, we can express the original operators in terms of the new ones:

$$\hat{a}_\ell = \sum_m U_{m\ell} \hat{b}_m \quad (1.79)$$

Substituting this into our previous expression for the complex field operator Eq. (1.74), we obtain:

$$\hat{A}^{(+)}(\vec{r}) = \sum_m \hat{b}_m \vec{v}_m(\vec{r}) \quad (1.80)$$

where the new mode functions $\vec{v}_m(\vec{r})$ are given by:

$$\vec{v}_m(\vec{r}) = \sum_{\ell} \sqrt{\frac{\hbar}{2\varepsilon_0 L^3 \omega_\ell}} U_{m\ell} \vec{\varepsilon}_\ell e^{i(\vec{k}_\ell \cdot \vec{r} - \omega_\ell t)} \quad (1.81)$$

The set $\{\vec{v}_m\}$ forms a new basis for decomposing complex fields, with each \vec{v}_m describing the spatial mode associated with the annihilation operator \hat{b}_m . It's important to note that this basis is generally not orthonormal due to the frequency-dependent factor $\sqrt{\omega_\ell}$ in the coefficient. However, when the modes are composed only of spectral components centred reasonably around the central carrier frequency, the modes can be considered orthogonal.

While the field operator transforms straightforwardly, the Hamiltonian Eq. (1.75) is not invariant under these general unitary transformations. It takes the form:

$$\hat{H} = \sum_{m,m'} E_{m,m'} \hat{b}_m^\dagger \hat{b}_{m'} \quad (1.82)$$

This indicates that the new modes are not necessarily decoupled in energy and may not be eigenmodes of the radiation field Hamiltonian. The coupling terms $E_{m,m'}$ for $m \neq m'$ represent

interactions between different modes in this new basis.

We can, however, construct a special class of unitary transformations that preserve the eigenmode structure. Consider a transformation that only mixes modes of equal frequencies:

$U_{m\ell} = 0$ if $\omega_\ell \neq \omega_m$. Under this constraint, the field operator takes the form:

$$\hat{A}^{(+)}(\vec{r}) = \sum_m \sqrt{\frac{\hbar}{2\varepsilon_0\omega_m}} \hat{b}_m \vec{v}_m(\vec{r}) \quad (1.83)$$

where the new mode functions are:

$$\vec{v}_m(\vec{r}) = \sum_\ell \sqrt{\frac{1}{L^3}} U_{m\ell} \vec{\varepsilon}_\ell e^{i(\vec{k}_\ell \cdot \vec{r} - \omega_\ell t)} \quad (1.84)$$

These \vec{v}_m form an orthonormal basis satisfying:

$$\int_{(V)} d^3r \vec{v}_m(\vec{r}) \cdot \vec{v}_{m'}^*(\vec{r}) = \delta_{m,m'} \quad (1.85)$$

and

$$\sum_m \vec{v}_m(\vec{r}) \cdot \vec{v}_m^*(\vec{r}') = \delta(\vec{r} - \vec{r}'). \quad (1.86)$$

This transformation preserves the number of photons at each frequency and leaves the Hamiltonian invariant. The new modes are decoupled and represent new eigenmodes of the radiation field.

Practical examples of such eigenmode bases include Hermite-Gauss modes such as in Fig. 1.2, which are particularly useful for describing light beams in the paraxial approximation.

1.2.6 Paraxial optics and transverse modes

While the plane wave decomposition provided a useful mathematical framework, it has limitations in describing real-world optical scenarios due to the infinite transverse extent of plane waves. In this section, we introduce an alternative set of modes that more accurately represent the finite nature of real electromagnetic fields. These modes are particularly relevant to the

optical systems we will explore throughout this thesis and have the added advantage of being experimentally realizable in laboratory settings.

Optical Beams and the Paraxial Approximation

In contrast to the plane wave basis discussed earlier, we now focus on optical beams - light propagating nearly along a specific direction, which we designate as the z axis. The vector potential of such a beam can be expressed as:

$$\vec{A}(\vec{r}, t) = \int dk_z \tilde{A}(k_z, \vec{r}_\perp, z, t) \exp(ik_z z) \quad (1.87)$$

where $\vec{r}_\perp = (x, y)$ represents the transverse coordinates, and $\tilde{A}(k_z, \vec{r}_\perp, z, t)$ is an amplitude that varies slowly compared to $|k_z|$ both longitudinally $|\partial_z^2 \tilde{A}| \ll |k_z \partial_z \tilde{A}| \ll k_z^2 |\tilde{A}|$ and transversely $|\vec{\nabla}_\perp \cdot \tilde{A}| \ll |k_z \tilde{A}|$, where $\vec{\nabla}_\perp = (\partial_x, \partial_y)$. These conditions define paraxial waves. Under these assumptions, the polarization properties of $\tilde{A}(k_z, \vec{r}_\perp, z, t)$ decouple from the spatiotemporal aspects, allowing us to work within the scalar approximation. We seek solutions of the form $\vec{E}(k_z) \mathcal{A}(k_z, t) u(k_z, \vec{r}_\perp, z) \exp(ik_z z)$.

The function $u(k_z, \vec{r}_\perp, z)$ satisfies the paraxial wave equation:

$$(2ik_z \partial_z + \nabla_\perp^2) u(k_z, \vec{r}_\perp, z) = 0. \quad (1.88)$$

This equation has a unique solution when the transverse structure of $u(k_z, \vec{r}_\perp, z)$ is specified at a plane $z = z_0$:

$$u(k_z, \vec{r}_\perp, z) = -\frac{ik_z}{2\pi(z-z_0)} \int_{\mathbb{R}^2} d^2 \vec{r}'_\perp u(k_z, \vec{r}'_\perp, z_0) \exp\left[-\frac{ik_z}{2(z-z_0)} (\vec{r}_\perp - \vec{r}'_\perp)^2\right]. \quad (1.89)$$

This integral form describes how the transverse pattern of an optical beam evolves due to diffraction as it propagates along the z -axis.

A special set of solutions to the paraxial equation maintains its transverse shape during

1.2. QUANTIZATION OF THE ELECTROMAGNETIC FIELD

propagation, changing only in scale and phase:

$$u(k_z, \vec{r}_\perp, z) = \sigma(z) \exp[i\gamma(\vec{r}_\perp, z)] u[k_z, \sigma(z)\vec{r}_\perp, z_0]. \quad (1.90)$$

Their explicit form depends on the chosen coordinate system. The fundamental transverse mode, which is the same in any coordinate system, has a Gaussian form $u(k_z, \vec{r}_\perp, z_0) = u_0 \exp\left[i\frac{k_z \vec{r}_\perp^2}{2q(z_0)}\right]$. Here, $q(z)$ is the complex q-parameter of the beam, typically expressed as:

$$\frac{1}{q(z)} = \frac{1}{R(z)} + i\frac{2}{k_z w^2(z)}. \quad (1.91)$$

where $R(z)$ is the curvature radius and $w(z)$ is the spot size of the mode. Introducing this decomposition into the ansatz Eq. (1.90), we obtain:

$$u(k_z, \vec{r}_\perp, z) \exp(ik_z z_0) = u_0 \exp\left[-\frac{\vec{r}_\perp^2}{w^2(z_0)}\right] \exp\left[ik_z \left(z_0 + \frac{\vec{r}_\perp^2}{2R(z_0)}\right)\right]. \quad (1.92)$$

After applying the paraxial propagator, this transverse pattern evolves to:

$$u(k_z, \vec{r}_\perp, z) = \frac{u_0}{w(z)} \exp\left[i\frac{k_z \vec{r}_\perp^2}{2q(z)} + i\psi(z)\right] \quad (1.93)$$

where: $q(z) = q(z_0) + z - z_0$ and $\psi(z) = \arg\left[1 + \frac{z - z_0}{q(z_0)}\right]$.

Conventionally, we choose the reference plane $z_0 = 0$ as the plane where the wavefront is flat, i.e., $R(z_0 = 0) = \infty$ and denote $\omega(z_0 = 0)$ as ω_0 . With this choice, we obtain:

$$w^2(z) = w_0^2 \left[1 + \left(\frac{z}{z_R}\right)^2\right], \quad (1.94)$$

$$R(z) = z \left[1 + \left(\frac{z_R}{z}\right)^2\right], \quad (1.95)$$

$$\psi(z) = -\arctan\left(\frac{z}{z_R}\right) \in \left[-\frac{\pi}{2}, \frac{\pi}{2}\right]. \quad (1.96)$$

Here, $z_R = \frac{k_z w_0^2}{2}$ is the Rayleigh length (which can be negative when k_z is negative), and $\Psi(z)$ is known as the Gouy phase.

1.2. QUANTIZATION OF THE ELECTROMAGNETIC FIELD

This pattern $u(k_z, \vec{r}_\perp, z)$ relates to $u(k_z, \vec{r}_\perp, z_0)$ in the form of Eq. (1.89), confirming its nature as a transverse mode. This is called the fundamental transverse mode. Other transverse modes have a similar Gaussian structure but are modulated by additional transverse functions.

In Cartesian coordinates, the transverse modes are known as Hermite-Gauss (HG) or TEM_{mn} modes:

$$H_{mn}(k_z, \vec{r}_\perp, z) = \frac{1}{\sqrt{2^{m+n-1} \pi m! n! w(z)}} H_m \left[\frac{\sqrt{2}x}{w(z)} \right] H_n \left[\frac{\sqrt{2}y}{w(z)} \right] \exp \left[ik_z \frac{x^2 + y^2}{2q(z)} + i(1 + m + n)\psi(z) \right] \quad (1.97)$$

where $H_m(x)$ are Hermite polynomials $H_m(x) = (-1)^m \exp(x^2) \frac{d^m}{dx^m} \exp(-x^2)$ and m and n are the horizontal and vertical indices of the mode, respectively. These modes form an orthonormal and complete set in the transverse plane:

$$\int_{\mathbb{R}^2} d^2 \vec{r}_\perp H_{mn}^*(k_z, \vec{r}_\perp, z) H_{m'n'}(k_z, \vec{r}_\perp, z) = \delta_{mm'} \delta_{nn'} \quad \forall z, \quad (1.98)$$

and

$$\sum_{m,n} H_{mn}^*(k_z, \vec{r}'_\perp, z) H_{mn}(k_z, \vec{r}_\perp, z) = \delta^2(\vec{r}_\perp - \vec{r}'_\perp) \quad \forall z. \quad (1.99)$$

This formalism provides a powerful tool for describing realistic optical beams and forms the foundation for understanding more complex optical phenomena in subsequent chapters.

Other sets of transverse modes include Laguerre-Gauss (LG) modes and Hybrid Laguerre-Gauss modes.

1.2.7 Quantization in an optical cavity

An optical cavity is essentially a sophisticated mirror arrangement that forms an interferometer. It's designed to create a specific path length for light to travel. When light completes a round trip within the cavity and its phase aligns perfectly (a multiple of 2π), we get what's called constructive interference. This results in a boost in optical intensity at the cavity's outputs, a state we refer to as resonance between the light and the cavity. Conversely, when the light and cavity

are out of sync, we see destructive interference, and the light simply bounces back off the input mirror.

You can observe these resonance effects by tweaking either the light's frequency or the cavity's length. As you do so, you'll notice intensity peaks that signal resonance. These peaks are spaced out in a predictable way - in terms of frequency, they're separated by the inverse of the round-trip time, while in terms of length, they're spaced by the wavelength λ .

While electromagnetic field quantization in optical cavities is the goal of this section, we focus on the classical foundation: determining cavity modes through geometric optics and ABCD formalism as they will be relevant in Chapter 2 of this thesis. These modes serve as the basis for field quantization, which we use in Chapter 2 for the quantum treatment of a novel type of cavities introduced. For a complete description of electromagnetic field quantization in optical cavities such as the ones we describe in this section, we refer to these resources [88, 100].

Geometrical Optics in Optical Cavities

Optical cavities, at their core, consist of two opposing spherical mirrors forming a linear resonator. These structures excel at trapping light, allowing it to oscillate between the mirrors. We'll examine the conditions necessary for effective light confinement.

In the geometrical optics framework, applicable when the Fresnel number $F = d^2/\lambda l$ is large (where d is the beam's transverse size, λ the wavelength and l the propagation distance), we visualize the beam as a collection of collimated rays. At any longitudinal position z , a ray is characterized by:

$$\vec{v}(z) = \begin{bmatrix} r(z) \\ \theta(z) \end{bmatrix}. \quad (1.100)$$

Here, $r(z)$ denotes the ray's distance from the z -axis, and $\theta(z)$ is its angle with this axis, termed transverse position and inclination respectively. Optical elements' effects on the beam are de-

1.2. QUANTIZATION OF THE ELECTROMAGNETIC FIELD

scribed by ABCD matrices:

$$M = \begin{bmatrix} A & B \\ C & D \end{bmatrix}. \quad (1.101)$$

This matrix transforms an input ray $\vec{v}(z_{in}) = \begin{bmatrix} r_{in} \\ \theta_{in} \end{bmatrix}$ to:

$$\vec{v}(z_{out}) = M\vec{v}(z_{in}) = \begin{bmatrix} Ar_{in} + B\theta_{in} \\ Cr_{in} + D\theta_{in} \end{bmatrix} \quad (1.102)$$

For example, for free-space propagation over distance l :

$$M_{prop} = \begin{bmatrix} 1 & l \\ 0 & 1 \end{bmatrix}. \quad (1.103)$$

A spherical interface with curvature radius R between media of refractive indices n_1 and n_2 also has the following ABDC matrix:

$$M_{interface} = \begin{bmatrix} 1 & 0 \\ \frac{n_1 - n_2}{n_2 R} & \frac{n_1}{n_2} \end{bmatrix}. \quad (1.104)$$

From these, we derive ABCD matrices for lenses and mirrors:

$$M_{lens} = \begin{bmatrix} 1 & 0 \\ -\frac{1}{f} & 1 \end{bmatrix}, \quad M_{mirror} = \begin{bmatrix} 1 & 0 \\ -\frac{2}{R} & 1 \end{bmatrix}, \quad (1.105)$$

with f as lens focal length and R as mirror curvature radius.

For any ABCD matrix M that describes the transformation between two planes with refractive indices n_{in} and n_{out} , a fundamental property holds: $\det(M) = \frac{n_{in}}{n_{out}}$. This relationship can be derived by considering that any complex optical system can be decomposed into a series of simpler elements, each represented by either a propagation matrix (as in Eq. (1.103)) or a

1.2. QUANTIZATION OF THE ELECTROMAGNETIC FIELD

refraction matrix (as in Eq. (1.104)) and that the determinant of the overall system matrix is equal to the product of the determinants of these individual element matrices.

Because as we mentioned earlier, transverse modes maintain their shape through ABCD systems, a mode with initial q -parameter $q(z_{in})$ and Gouy phase $\psi(z_{in})$ through an optical system characterized by its ABCD matrix, will transform into the exact same mode such that:

$$\begin{aligned} q(z_{out}) &= \frac{Aq(z_{in}) + B}{Cq(z_{in}) + D}, \\ \psi(z_{out}) &= \psi(z_{in}) - \arg \left[A + \frac{|B|}{q(z_{in})} \right]. \end{aligned} \quad (1.106)$$

In an optical cavity, a ray $\vec{v}(z_0) = \begin{bmatrix} r_{in} \\ \theta_{in} \end{bmatrix}$ at reference plane $z = z_0$ undergoes a roundtrip transformation:

$$M_{\text{Loop}} = \begin{bmatrix} A_{\text{Loop}} & B_{\text{Loop}} \\ C_{\text{Loop}} & D_{\text{Loop}} \end{bmatrix}. \quad (1.107)$$

After N roundtrips, using Sylvester theorem applied to the N' 'th power of a 2×2 matrix with determinant one:

$$\vec{v}_N(z_0) = M_{\text{Loop}}^N \vec{v}(z_0) = \frac{1}{\sin \phi} \begin{bmatrix} A_{\text{Loop}} \sin N\phi - \sin[(N-1)\phi] & B_{\text{Loop}} \sin N\phi \\ C_{\text{Loop}} \sin N\phi & D_{\text{Loop}} \sin N\phi - \sin(N-1)\phi \end{bmatrix} \vec{v}(z_0) \quad (1.108)$$

where $\cos \theta = (A_{\text{Loop}} + D_{\text{Loop}})/2$.

For cavity confinement, θ must be real, leading to the stability condition:

$$-1 < \frac{A_{\text{Loop}} + D_{\text{Loop}}}{2} < 1. \quad (1.109)$$

Else the trigonometric functions of θ become hyperbolic, leading to divergent ray coordinates. This also could be found by looking at the characteristic equation of the cavity $\lambda^2 - \text{Tr}(M_{\text{total}})\lambda + 1 = 0$ that we solve for λ s with no-nonpositive modulus to ensure stability. This condition,

independent of the reference plane choice, defines a stable optical cavity. The trace of the roundtrip matrix remains constant regardless of the chosen reference plane.

1.2.8 Particular examples of cavities

Let's consider a basic linear cavity. Imagine two flat mirrors facing each other, separated by a distance L . For a plane wave with wavelength λ , you would expect resonances when the round-trip length ($2L$) is a whole number multiple of the wavelength λ . However, this setup isn't practical in the real world because it's not geometrically stable - a real laser beam would eventually spread out too much.

To create a stable cavity, we need at least one optical element with a finite focal length to handle Gaussian modes. Typically, we use concave mirrors for this, as they can counteract the beam's natural tendency to diverge over multiple round trips.

As a Gaussian beam travels, it picks up an interesting phase shift known as the Gouy phase. This phenomenon was first noticed back in 1890 by Louis Georges Gouy [101], a French physicist who observed it in thermal light passing through a focal point. For a laser mode of order N , the Gouy phase $\psi_N(z)$ is given by: $\psi_N(z) = (N + 1) \tan^{-1}(z/z_R)$ [100]. Here, z is measured from the beam's waist, and z_R (the Rayleigh length) equals $\pi w_0^2/\lambda$. This phase shift causes a slight displacement ε_N in where the resonance peaks occur, compared to what you would expect with plane waves. So, for the N th-order mode, resonances happen when the round-trip length is $2L = p\lambda + \varepsilon_N$, where p is an integer.

In a cavity with one flat mirror and one concave mirror spaced L apart, the Gouy phase accumulated over a round trip gives us: $\varepsilon_N = (N + 1) \frac{\lambda}{\pi} \tan^{-1}(L/z_R)$. Notice how ε_N grows linearly with N . This creates a regular spacing between resonant peaks for different mode orders.

Interestingly, cavities with an odd number of mirrors, like triangular cavities, behave differently from those with an even number. In even-mirror cavities, all modes of a given order N accumulate the same total phase in a round trip. But in odd-mirror cavities, some modes can pick up extra phase shifts. This peculiarity allows triangular cavities to distinguish between certain modes, like TEM_{01} and TEM_{10} . Their resonance peaks end up separated by half the distance

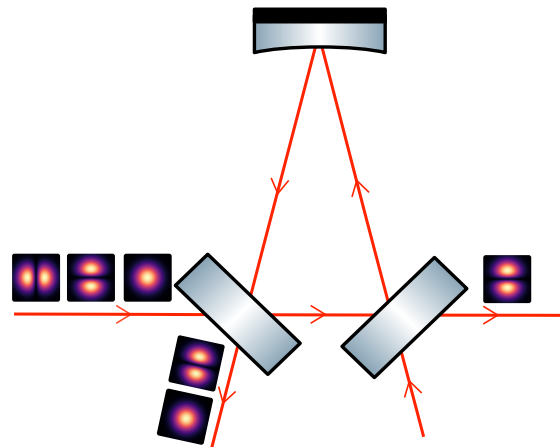


Figure 1.5: **Mode cleaner cavity:** When a paraxial monochromatic beam with a specific transverse-mode distribution impinges on a spatial-mode cleaner that is tuned on a particular transverse mode, the desired mode is transmitted while the rest of the modal content is reflected.

between consecutive TEM_{00} peaks [102]. In frequency terms, that's half a free spectral range (FSR), or $\frac{\lambda}{2}$ in terms of total cavity length.

Particular case of mode cleaner cavities

A triangular resonator is an optical cavity configuration that supports Hermite-Gaussian (HG) modes. This resonator consists of three mirrors arranged in a triangular geometry, enabling the confinement and propagation of light within the cavity. The analysis of such a resonator involves understanding the mode structure, stability conditions, and the behaviour of the electromagnetic fields within the cavity and it is the basis of widely known and used mode-cleaner cavities as shown in Fig. 1.5.

To determine the stability conditions and the complex cavity eigenmodes of the triangular resonator, we employ the ABCD matrix formalism. This approach allows us to model the optical elements and free-space propagation within the resonator systematically.

We use the powerful ABCD matrix formalism we developed in earlier top describe the propagation of Gaussian beams through optical systems. For the triangular resonator, the optical path consists of:

1. Passage through coupler r_1 .

1.2. QUANTIZATION OF THE ELECTROMAGNETIC FIELD

2. Free-space propagation over a distance L_1 .
3. Passage through coupler r_2 .
4. Free-space propagation over a distance L_2 .
5. Reflection from a spherical mirror with radius of curvature R .
6. Free-space propagation over a distance L_3 .

The total propagation length in a round trip is given by: $L_1 + L_2 + L_3 = L_{\text{Loop}}$. The ABCD matrices for these elements are:

$$M_{\text{free}}(L) = \begin{pmatrix} 1 & L \\ 0 & 1 \end{pmatrix}, M_{\text{mirror}} = \begin{pmatrix} 1 & 0 \\ -\frac{2}{R} & 1 \end{pmatrix} \quad (1.110)$$

The total ABCD matrix M_{total} for one round trip in the resonator is the product of the individual matrices in the order of propagation. Note that the couplers r_1 and r_2 affect the field amplitudes but do not alter the ABCD matrices, which are concerned with the ray optics. Thus, the ABCD matrix sequence is:

$$M_{\text{total}} = M_{\text{free}}(L_3) \cdot M_{\text{mirror}} \cdot M_{\text{free}}(L_2) \cdot M_{\text{free}}(L_1) \quad (1.111)$$

Doing the multiplication and simplifying the elements:

$$M_{\text{total}} = \begin{pmatrix} A_{\text{Loop}} & B_{\text{Loop}} \\ C_{\text{Loop}} & D_{\text{Loop}} \end{pmatrix} = \begin{pmatrix} 1 - \frac{2L_3}{R} & L_{\text{Loop}} \left(1 - \frac{2L_3}{R} \right) + L_3 \\ -\frac{2}{R} & 1 - \frac{2L_2}{R} - \frac{2L_1L_2}{R} \end{pmatrix}. \quad (1.112)$$

The stability of the resonator is determined by the trace of the total ABCD matrix. For a resonator to support stable modes, the following condition must be satisfied:

$$-2 < \text{Tr}(M_{\text{total}}) < 2 \quad (1.113)$$

1.2. QUANTIZATION OF THE ELECTROMAGNETIC FIELD

Calculating the trace yield:

$$\text{Tr}(M_{\text{total}}) = \left(1 - \frac{2L_3}{R}\right) + \left(1 - \frac{2L_2}{R} - \frac{2L_1L_2}{R}\right) = 2 - \frac{2(L_2 + L_3)}{R} - \frac{2L_1L_2}{R} \quad (1.114)$$

and applying the stability condition gives:

$$-2 < 2 - \frac{2(L_2 + L_3)}{R} - \frac{2L_1L_2}{R} < 2. \quad (1.115)$$

Solving both inequalities and combining the results, the stability condition is:

$$0 < L_2 + L_3 + L_1L_2 < 2R. \quad (1.116)$$

This condition ensures that the resonator supports confined modes without divergent beam propagation.

The eigenmodes of the resonator are determined by solving the characteristic equation derived from the ABCD matrix. The characteristic equation is: $\lambda^2 - \text{Tr}(M_{\text{total}})\lambda + 1 = 0$. Substituting the trace, we get:

$$\lambda^2 - \left(2 - \frac{2(L_2 + L_3)}{R} - \frac{2L_1L_2}{R}\right)\lambda + 1 = 0. \quad (1.117)$$

Solving for λ using the quadratic formula:

$$\lambda = \frac{\text{Tr}(M_{\text{total}}) \pm \sqrt{\text{Tr}(M_{\text{total}})^2 - 4}}{2} \quad (1.118)$$

For stable resonators(Eq. (1.116)), the discriminant $\Delta = \text{Tr}(M_{\text{total}})^2 - 4$ is negative.

The modes of the resonator can be described by the electric field distribution $U(\vec{r})$, where $\vec{r} = (x, y)$ represents the transverse coordinates. For HG modes, the field distribution is given by:

$$U_{in}(\vec{r}) = A_{mn} H_m \left(\frac{\sqrt{2}x}{w_0} \right) H_n \left(\frac{\sqrt{2}y}{w_0} \right) \exp \left(-\frac{x^2 + y^2}{w_0^2} \right) = U_{mn}(\vec{r}), \quad (1.119)$$

where A_{mn} is the amplitude coefficient, H_m and H_n are Hermite polynomials of order m and n ,

1.2. QUANTIZATION OF THE ELECTROMAGNETIC FIELD

respectively and w_0 is the beam waist.

After n round trips within the resonator, the field distribution evolves as:

$$U_n(\vec{r}) = t_1(r_1 r_2)^n A_{mn} H_m \left(\frac{\sqrt{2}x}{w_0} \right) H_n \left(\frac{\sqrt{2}y}{w_0} \right) e^{-jknL_{\text{Loop}}} e^{j(m+n+1)\psi(nL_{\text{Loop}})} \quad (1.120)$$

where t_1 is the transmission coefficient of coupler r_1 and r_1 and r_2 are the reflection coefficients of the couplers. $\psi(z)$ represents the Gouy phase given by Eq. (1.106). The total field within the resonator is the sum of all round-trip contributions:

$$U_{\text{tot}} = \sum_{n=0}^{+\infty} U_n = \frac{t_1 U_{\text{in}}}{1 - r_1 r_2 \exp \left[j \left[-kL_{\text{Loop}} + (m+n+1)\psi(L_{\text{Loop}}) \right] \right]} \quad (1.121)$$

The transmission coefficient T can be written as:

$$T = \frac{\mathcal{T}_{\text{max}}}{1 + \mathcal{F}^2 \sin^2 \left(\frac{kL_{\text{Loop}}}{2} - \frac{(m+n+1)\psi(L_{\text{Loop}})}{2} \right)} \quad (1.122)$$

It is expressed as a function of the finesse \mathcal{F} and the maximum transmission \mathcal{T}_{max} :

$$\mathcal{F} = \frac{\pi \sqrt{r_1 r_2}}{1 - r_1 r_2} \quad (1.123)$$

$$\mathcal{T}_{\text{max}} = \frac{r_1 r_2}{(1 - r_1 r_2)^2}. \quad (1.124)$$

The triangular cavity's ability to distinguish between transverse modes with the same $m+n$ arises from its geometric configuration, which introduces mode-dependent phase shifts and frequency splitting. Specifically, modes like TE_{01} and TE_{10} have the same $m+n=1$, but their different spatial distributions interact uniquely with the cavity's asymmetry. This leads to slight differences in their resonant frequencies, allowing the cavity to differentiate between them based on their distinct transmission peaks. In the triangular geometry, the asymmetric path lengths and coupler placements result in different Gouy phases for modes with identical $m+n$, thereby lifting the degeneracy. Consequently, TE_{01} and TE_{10} modes resonate at slightly different frequencies, enhancing the cavity's capability to selectively amplify or suppress specific modes. This is true for odd numbers of cavities [102].

Quantization in optical cavities

As discussed previously, the quantization of electromagnetic fields in optical cavities builds upon the understanding of cavity modes. In this section, while we establish the classical foundation using geometric optics and ABCD formalism to determine these modes, a groundwork that is particularly relevant for Chapter 2, where we employ these results to develop a quantum treatment of novel cavity configurations. While we focus here on the classical description, comprehensive treatments of electromagnetic field quantization for the example of optical cavities we considered, can be found in [88, 100].

1.3 Multimode Gaussian States

To introduce the section on multimode Gaussian states, we remind the discussion we had in Subsection 1.1.4 on continuous variable (CV) systems. These are systems whose relevant degrees of freedom are associated with operators having continuous spectra. An example of a multimode case of a bosonic CV system is a quantized field, such as the electromagnetic field. Such a system can be modelled as a collection of non-interacting quantum harmonic oscillators with different frequencies, each referred to as a mode. To simplify our discussion, we will focus on systems with a discrete number of modes (e.g., an optical cavity), each with one spatial dimension.

Here, we adopt the formalism developed by Adesso et al. [7] and the reader is advised to refer to [103, 104] for a different or a more detailed treatment.

An N -mode CV system is described by a Hilbert space $\mathcal{H} = \bigotimes_{m=1}^N \mathcal{H}_m$, where each \mathcal{H}_m is an infinite-dimensional space associated with a single mode. The Hamiltonian for such a system can be expressed as:

$$\hat{H} = \sum_{m=1}^N \hat{H}_m = \sum_{m=1}^N \hbar\omega_m \left(\hat{a}_m^\dagger \hat{a}_m + \frac{1}{2} \right), \quad (1.125)$$

where \hat{a}_m and \hat{a}_m^\dagger are the annihilation and creation operators for the m -th mode with frequency ω_m . These operators, we remind, obey the commutation relations:

$$[\hat{a}_m, \hat{a}_n^\dagger] = \delta_{mn}, \quad [\hat{a}_m, \hat{a}_n] = [\hat{a}_m^\dagger, \hat{a}_n^\dagger] = 0. \quad (1.126)$$

We define quadrature operators analogous to position and momentum for each mode as we did in Subsection 1.1.2 for the HO: $\hat{x}_m = \frac{\hat{a}_m + \hat{a}_m^\dagger}{\sqrt{2}}$ and $\hat{y}_m = -i\frac{\hat{a}_m - \hat{a}_m^\dagger}{\sqrt{2}}$ with $[\hat{x}_m, \hat{y}_n] = i\delta_{mn}$. For compact notation, we introduce the vector of quadrature operators:

$$\hat{R} = (\hat{x}_1, \dots, \hat{x}_N | \hat{y}_1, \dots, \hat{y}_N)^\top. \quad (1.127)$$

This allows us to express the commutation relations as: $[\hat{R}_m, \hat{R}_n] = i\Omega_{mn}$, where Ω is the symplectic form:

$$\Omega = \begin{pmatrix} 0 & I_N \\ -I_N & 0 \end{pmatrix}, \quad (1.128)$$

where I_N is the $N \times N$ identity matrix and Ω verifying $\Omega^\top = -\Omega = \Omega^{-1}$.

1.3.1 Phase Space Description

We previously discussed in Subsection 1.1.4 when talking about continuous variables quantum states that position and momentum observables lack common eigenstates, and their eigenvectors don't represent physically realizable states of the Harmonic Oscillator. Consequently, these observables cannot have definite values simultaneously. Instead, for a given state characterized by its density operator $\hat{\rho}$, we can only provide probability density functions $\langle x | \hat{\rho} | x \rangle$ and $\langle y | \hat{\rho} | y \rangle$ that govern the measurement statistics of these observables. This implies that well-defined trajectories in phase space don't exist quantum mechanically, as position and momentum are always subject to quantum fluctuations.

This leads us to a natural question: Is it possible to describe quantum mechanics using a probability distribution in phase space that essentially blurs classical trajectories? The answer is nuanced, as quantum noise exhibits more intricate characteristics than its classical counterpart.

1.3. MULTIMODE GAUSSIAN STATES

Let's introduce the probability distribution $W_\rho(\vec{r})$ as in the lecture notes [87], where $\vec{r} = (x|y)^\top$ encapsulates all phase-space variables, and the subscript denotes the corresponding quantum state $\hat{\rho}$. We construct this distribution to yield the position and momentum probability density functions as its marginals:

$$\langle x|\hat{\rho}|x\rangle = \int_{\mathbb{R}} dy W_\rho(\vec{r}), \quad (1.129)$$

and

$$\langle y|\hat{\rho}|y\rangle = \int_{\mathbb{R}} dx W_\rho(\vec{r}). \quad (1.130)$$

These conditions uniquely define $W_\rho(\vec{r})$, known as the Wigner function.

To facilitate the analysis, let us stick to the single mode case where the quadrature vector writes $\hat{R} = (\hat{x}, \hat{y})^\top$ and we introduce the following concepts:

- We define the displacement operator, reminiscent of the one defined for coherent states Eq. (2.56) :

$$\hat{D}(\vec{r}) = \exp\left(\frac{i}{2}\hat{R}^\top\Omega\vec{r}\right) = \exp\left(\frac{i}{2}(y\hat{x} - x\hat{y})\right). \quad (1.131)$$

- The quantum characteristic function is given by:

$$\chi_\rho(\vec{s}) = \text{tr}\{\hat{\rho}\hat{D}(\vec{s})\} = \langle\hat{D}(\vec{s})\rangle. \quad (1.132)$$

The Wigner function is then defined as the Fourier transform of the characteristic function:

$$W_\rho(\vec{r}) = \int_{\mathbb{R}^2} \frac{d^2s}{(4\pi)^2} e^{-\frac{i}{2}\vec{r}^\top\Omega\vec{s}} \chi_\rho(\vec{s}). \quad (1.133)$$

This function exhibits several crucial properties, whose proofs can be found in [88, 87]:

1. It yields the correct marginals as defined in Equations 1.129 and 1.130.
2. It is real-valued throughout the whole phase space.

1.3. MULTIMODE GAUSSIAN STATES

3. It is normalized: $\int_{\mathbb{R}^2} d^2r W_\rho(\vec{r}) = 1$.
4. For orthogonal pure states $\hat{\rho}_1$ and $\hat{\rho}_2$, the overlap between their corresponding Wigner functions writes :

$$\int_{\mathbb{R}^2} d^2r W_{\rho_1}(\vec{r}) W_{\rho_2}(\vec{r}) = 0. \quad (1.134)$$

This mathematical relationship reveals a crucial aspect of the Wigner function: it must exhibit negative values in certain regions of phase space. If it were non-negative everywhere, the integral of the product of two Wigner functions would always yield a positive result. Consequently, the Wigner function deviates from the classical notion of a probability density function, highlighting its unique quantum nature.

5. The Wigner function is bounded and can always be visualized in phase space:

$$\int_{\mathbb{R}^2} d^2r W_\rho^2(\vec{r}) = \frac{1}{4\pi} \text{tr}\{\hat{\rho}^2\} \leq \frac{1}{4\pi}. \quad (1.135)$$

The upper bound of $\frac{1}{4\pi}$ stems from the property $\text{tr}\{\hat{\rho}^2\} \leq 1$, which holds for all density operators due to their positive eigenvalues being constrained to values less than or equal to unity. This constraint ensures that the Wigner function remains finite throughout phase space, enabling its visualization and analysis without encountering divergences.

6. It uniquely determines the quantum state:

$$\hat{\rho} = \int_{\mathbb{R}^2} \frac{d^2s}{4\pi} \hat{D}^\dagger(\vec{s}) \chi_\rho(\vec{s}). \quad (1.136)$$

This property shows the equivalence between the Wigner function (or its characteristic function) and the quantum state itself. By encapsulating all the information contained in the state $\hat{\rho}$, the Wigner function serves as an alternative, phase-space representation of quantum states, offering a complementary perspective to traditional quantum mechanical formalisms.

These properties reveal that the Wigner function closely resembles a probability density function

in phase space, with the crucial distinction of potentially taking negative values. This negativity is fundamental, indicating that quantum mechanics cannot be fully simulated using classical means. While not a true probability density function, the Wigner function serves as an invaluable tool for visualizing quantum fluctuations in phase space. Many experimentally accessible states of the harmonic oscillator exhibit positive Wigner functions, allowing us to apply classical probability theory intuition to quantum fluctuations in these cases. The appearance of negativities serves as a clear indicator of genuine quantum phenomena.

1.3.2 Gaussian States

Gaussian states are frequent in quantum physics laboratories. They can be generated and manipulated experimentally in a variety of physical systems, ranging from light fields to atomic ensembles [13, 18]. They encompass a wide range of important quantum states, including coherent states (such as those produced by lasers), thermal states (emitted by black body sources), and even the vacuum state. The defining characteristic of a Gaussian state is that its characteristic functions (Eq. (1.139)) and quasiprobability distributions (Eqs. (1.129) and (1.130)) are Gaussian functions in the quantum phase space. For pure states, this property also manifests as a Gaussian wavefunction in the quadrature (position or momentum) basis [105].

A key feature of Gaussian states is that they are fully characterized by their first and second moments. The first moment vector \vec{d} of a state is defined as: $\vec{d} = \langle \hat{\vec{R}} \rangle$, while the second order moments form the covariance matrix $\sigma = (\sigma_{ij})$, given by:

$$\sigma = \frac{1}{2} \langle \hat{\vec{R}} \hat{\vec{R}}^\top + (\hat{\vec{R}} \hat{\vec{R}}^\top)^\top \rangle - \langle \hat{\vec{R}} \rangle \langle \hat{\vec{R}} \rangle \quad (1.137)$$

and equivalently

$$\sigma_{ij} = \frac{1}{2} \langle \hat{R}_i \hat{R}_j + \hat{R}_j \hat{R}_i \rangle - \langle \hat{R}_i \rangle_\rho \langle \hat{R}_j \rangle, \quad (1.138)$$

with $\hat{\vec{R}}$ the quadrature vector (Eq. (1.127)) and the expectation value taken in regards to the state $\hat{\rho}$: $\langle \hat{A} \rangle = \langle \hat{A} \rangle_\rho = \text{Tr}[\hat{\rho} \hat{A}]$ where \hat{A} is any operator.

The covariance matrix σ is a real, symmetric, positive definite matrix. For N -mode Gaus-

1.3. MULTIMODE GAUSSIAN STATES

sian states ρ , both the characteristic and Wigner functions have Gaussian forms, completely determined by \vec{d} and σ :

$$\chi_\rho(\vec{\xi}) = e^{-\frac{1}{4}\vec{\xi}^T \Omega \sigma \Omega^T \vec{\xi} - i(\Omega \vec{d})^T \vec{\xi}}, \quad (1.139)$$

$$W_\rho(\vec{x}) = \frac{1}{\pi^N} \frac{1}{\sqrt{\det(\sigma)}} e^{-(\vec{x}-\vec{d})^T \sigma^{-1} (\vec{x}-\vec{d})}, \quad (1.140)$$

where $\vec{\xi}$ and $\vec{X} \in \mathbb{R}^{2N}$.

Coherent states, which we introduced earlier in Subsection 1.1.4, are examples of Gaussian states. For a single-mode coherent state $|\alpha\rangle$, the first moments and covariance matrix:

$$\vec{d} = \sqrt{2} \begin{pmatrix} \text{Re}(\alpha) \\ \text{Im}(\alpha) \end{pmatrix}, \quad \sigma = I. \quad (1.141)$$

Particularly, the covariance matrix for a coherent state is the identity matrix, regardless of the coherent parameter α . We show that in Subsection 1.4.4 for the simplest coherent state. This reflects the fact that coherent states are states of minimum Heisenberg uncertainty $\Delta \hat{x} \Delta \hat{y} = 1$, where we remind that $\Delta(\hat{A}) = \langle \hat{A}^2 \rangle - \langle \hat{A} \rangle^2$ is the variance of an observable \hat{A} for a given state ρ .

Coherent states are not the only states we reviewed that saturate the uncertainty relation. Squeezed states, we mentioned in Subsection 1.1.4, also maintain this property while allowing for unbalanced variances on the two canonical quadratures for each mode. The most general Gaussian pure state $|\psi\rangle$ of a single mode is a displaced squeezed state, obtained by applying both the displacement operator $\hat{D}(\alpha)$ (Eq. (1.131)) and the single-mode squeezing operator $\hat{S}(\zeta)$ to the vacuum state: $|\psi_{\alpha,\zeta}\rangle = \hat{D}(\alpha)\hat{S}(\zeta)|0\rangle$. Pure single-mode Gaussian states are thus fully specified by their displacement vector $\alpha \in \mathbb{C}$, squeezing degree $s \in \mathbb{R}^+$, and squeezing phase $\theta \in [0, 2\pi]$: $|\psi_{\alpha,\zeta}\rangle \equiv |\psi_{\alpha,s,\theta}\rangle$.

Despite the infinite dimension of the associated Hilbert space, an arbitrary Gaussian state $\hat{\rho}$ can be completely described (up to local unitary operations) by its $2N \times 2N$ covariance matrix σ . The physical validity of a covariance matrix is ensured by the condition: $\sigma + i\Omega \geq$

0. This inequality, which is a consequence of the uncertainty principle in its strong Robertson–Schrödinger form [106, 107], is necessary and sufficient for σ to describe a physical Gaussian state [108, 109], and is necessary (but not sufficient) for non-Gaussian states.

1.3.3 Gaussian Unitaries and the symplectic group

Building upon our discussion of Gaussian states, we now explore how unitary transformations are represented in this framework. This leads us to the concept of Gaussian unitaries. In the Hilbert space, unitary transformations on Gaussian states map to real symplectic transformations in phase space, affecting both the first and second moments:

$$\hat{\rho}' = \hat{U}\hat{\rho}\hat{U}^\dagger \Rightarrow \begin{cases} \vec{d}' = S\vec{d}, \\ \sigma' = S\sigma S^\top. \end{cases} \quad (1.142)$$

Here, S represents a symplectic matrix corresponding to the action of \hat{U} on $\hat{\rho}$. This elegant transformation rule applies exclusively to unitaries with exponents at most quadratic in the mode operators $\{\hat{a}_m, \hat{a}_m^\dagger\}$. Such transformations preserve the Gaussian nature of states, as higher-order terms would influence moments beyond the second order.

To fully grasp these symplectic transformations, we must venture into symplectic geometry, a field deeply rooted in classical mechanics but with profound quantum implications [110, 103, 111, 104].

The real symplectic group denoted $\text{Sp}(2N, \mathbb{R})$, is defined by the group of real matrices satisfying the condition: $S\Omega S^\top = \Omega$, where Ω is the symplectic form. More explicitly: $\text{Sp}(2N, \mathbb{R}) = \{S \in \mathbb{R}^{2N \times 2N} | S\Omega S^\top = \Omega\}$. Symplectic matrices are square ($2N \times 2N$), invertible, and have determinant $+1$. Given our quadrature operator arrangement, we can decompose a symplectic matrix into blocks:

$$S = \begin{pmatrix} S_1 & S_2 \\ S_3 & S_4 \end{pmatrix}, \quad (1.143)$$

where S_1, S_2, S_3, S_4 are $N \times N$ submatrices that must satisfy certain conditions derived from the

1.3. MULTIMODE GAUSSIAN STATES

defining symplectic relation $S\Omega S^T = \Omega$: both $S_1 S_2^T$ and $S_3 S_4^T$ must be symmetric and $S_1 S_4^T - S_2 S_3^T = I_N$. These conditions ensure that S preserves the symplectic structure.

An important result in symplectic geometry is the Williamson theorem, which states that any symmetric positive-definite matrix can be diagonalized via a symplectic transformation [112]. This theorem is instrumental in finding the symplectic eigenvalues of a Gaussian state's covariance matrix:

Theorem 1.3.1 (Williamson Theorem). *For any $2N \times 2N$ positive-definite matrix σ , there exists $S \in Sp(2N, \mathbb{R})$ such that:*

$$\sigma = S \begin{pmatrix} \Lambda & 0 \\ 0 & \Lambda \end{pmatrix} S^T, \quad (1.144)$$

where Λ is the $N \times N$ submatrix that represents the symplectic spectrum associated with σ .

Sometimes alternative representations are used in different quadrature bases involving different arrangements of the quadrature operators. For example, let's consider an alternative representation on a different basis :

$$\hat{R}' = \begin{pmatrix} \hat{x}_1 \\ \vdots \\ \hat{x}_N \\ \hat{y}_1 \\ \vdots \\ \hat{y}_N \end{pmatrix} \equiv T \begin{pmatrix} \hat{x}_1 \\ \hat{y}_1 \\ \vdots \\ \hat{x}_N \\ \hat{y}_N \end{pmatrix}. \quad (1.145)$$

Here, $T = (T_{ij})$ is a basis-changing matrix with elements: $T_{ij} = \delta_{i,2j-1} + \delta_{i+2N,2j}$ for $i, j = 1, \dots, 2N$. This rearrangement leads to a block form for the symplectic form and symplectic matrices:

$$\Omega' = \bigoplus_{k=1}^N \omega, \quad \omega = \begin{pmatrix} 0 & 1 \\ -1 & 0 \end{pmatrix} \quad (1.146)$$

and

$$S' = \begin{pmatrix} s_{11} & s_{12} & \cdots & s_{1N} \\ s_{21} & s_{22} & \ddots & \vdots \\ & & & s_{NN} \end{pmatrix} \quad (1.147)$$

where the 2×2 sub-block s_{mn} represents the transformation between the modes m and n . In this representation, the Williamson normal form of a covariance matrix σ can be expressed as:

$$\sigma = S \bigoplus_{k=1}^N \begin{pmatrix} d_k & 0 \\ 0 & d_k \end{pmatrix} S^\top. \quad (1.148)$$

An alternative representation, known as the complex form of $\text{Sp}(2N, \mathbb{R})$ [113], can be obtained by transforming from the quadrature operators \hat{x}_j, \hat{y}_j to the mode operators $\hat{a}_j, \hat{a}_j^\dagger$. This transformation is given by: $\hat{\xi} = L\hat{R}'$:

$$\hat{\xi} = \begin{pmatrix} \hat{a}_1 \\ \vdots \\ \hat{a}_N \\ \hat{a}_1^\dagger \\ \vdots \\ \hat{a}_N^\dagger \end{pmatrix} = L \begin{pmatrix} \hat{x}_1 \\ \vdots \\ \hat{x}_N \\ \hat{y}_1 \\ \vdots \\ \hat{y}_N \end{pmatrix} \quad (1.149)$$

where the basis-changing matrix L is defined as:

$$L = \frac{1}{\sqrt{2}} \begin{pmatrix} I_N & iI_N \\ I_N & -iI_N \end{pmatrix} \quad (1.150)$$

In this complex representation, any matrix S in the quadrature basis transforms as $S \rightarrow S_\xi = LSL^\dagger$. This transformation leads to the following expressions for the symplectic form and sym-

plectic matrices:

$$\Omega_\xi = -iK, \quad K = \begin{pmatrix} I_N & 0 \\ 0 & -I_N \end{pmatrix}, \quad S_\xi = \begin{pmatrix} S_{\xi 1} & S_{\xi 2} \\ S_{\xi 2}^* & S_{\xi 1}^* \end{pmatrix}. \quad (1.151)$$

In this complex form, the defining symplectic relation becomes $S_\xi K S_\xi^\dagger = K$, where the transposition operation in the quadrature basis is replaced by Hermitian conjugation. This leads to the following conditions for S_ξ to be symplectic: $S_{\xi 1} S_{\xi 1}^\dagger - S_{\xi 2} S_{\xi 2}^\dagger = I$ and $S_{\xi 1} S_{\xi 2}^\dagger = (S_{\xi 1} S_{\xi 2}^\dagger)^\dagger$.

The Williamson normal form in the complex representation is given by:

$$\sigma_\xi = S_\xi \begin{pmatrix} \Lambda_\xi & 0 \\ 0 & \Lambda_\xi \end{pmatrix} S_\xi^\dagger, \quad (1.152)$$

where σ_ξ is the complex form of the covariance matrix, defined in terms of the mode operators as:

$$\sigma_\xi = \langle \hat{\xi} \hat{\xi}^\dagger + (\hat{\xi} \hat{\xi}^\dagger)^\dagger \rangle - 2\langle \hat{\xi} \rangle \langle \hat{\xi}^\dagger \rangle, \quad (1.153)$$

such that

$$(\sigma_\xi)_{ij} = \langle \hat{\xi}_i \hat{\xi}_j^\dagger + \hat{\xi}_i^\dagger \hat{\xi}_j \rangle - 2\langle \hat{\xi}_i \rangle \langle \hat{\xi}_j^\dagger \rangle. \quad (1.154)$$

In this complex form, the symplectic spectrum of a covariance matrix can be computed using: $\Lambda_\xi = \text{Eig}^+(K\sigma_\xi)$, where Eig^+ denotes the positive eigenvalues.

The complex form covariance matrix can be obtained from its quadrature counterpart σ using the transformation with Eq. (1.150), resulting in the block form:

$$\sigma_\xi = \begin{pmatrix} \sigma_{\xi 1} & \sigma_{\xi 2} \\ \sigma_{\xi 2}^* & \sigma_{\xi 1}^* \end{pmatrix}, \quad (1.155)$$

with $\sigma_{\xi 1}^\dagger = \sigma_{\xi 1}$ and $\sigma_{\xi 2}^\dagger = \sigma_{\xi 2}$, ensuring that σ_ξ is hermitian : $\sigma_\xi^\dagger = \sigma_\xi$.

1.3.4 Symplectic representation of linear optics operations

Linear optics forms the backbone of many quantum optical experiments [95], primarily due to the challenges in achieving high-order non-linear effects on single modes or interactions between multiple modes simultaneously. The unitary transformations in linear optics are characterized by exponents that are quadratic in the field operators: $\hat{U} = e^{-i\frac{\hat{H}}{\hbar}}$, where the Hamiltonian \hat{H} takes the most general quadratic form:

$$\hat{H} = \hbar \sum_{m,n} G_{m,n} \hat{a}_m^\dagger \hat{a}_n + \frac{\hbar}{2} \sum_{m,n} [F_{m,n} \hat{a}_m^\dagger \hat{a}_n^\dagger + \text{H.c.}]. \quad (1.156)$$

We've omitted linear terms as they can be absorbed by local displacements. In this expression, the matrix F is a complex symmetric matrix $F = F^T$, while G is a Hermitian complex matrix, verifying $G = G^\dagger$. We will discuss later on what these matrices represent in different scenarios.

Using the Baker-Campbell-Hausdorff lemma and more particularly its extended form the Hadamard lemma:

$$e^{\hat{A}} \hat{X} e^{-\hat{A}} = \sum_{n=0}^{\infty} \frac{1}{n!} [\hat{A}, [\hat{A}, \dots [\hat{A}, \hat{X}] \dots]]_n, \quad (1.157)$$

we obtain:

$$\hat{U} \hat{\xi} \hat{U}^\dagger = e^{-i\frac{\hat{H}}{\hbar}} \hat{\xi} e^{i\frac{\hat{H}}{\hbar}} = S_\xi \hat{\xi}, \quad (1.158)$$

showing the correspondence between unitary transformations and symplectic matrices, where $S_\xi = e^{-iM} = e^{-iKH}$ and M writes:

$$M = \begin{pmatrix} G & F \\ -F^* & -G^* \end{pmatrix} = \begin{pmatrix} I_N & 0 \\ 0 & -I_N \end{pmatrix} \begin{pmatrix} G & F \\ F^* & G^* \end{pmatrix} = KH. \quad (1.159)$$

H is a Hermitian matrix known as bosonic Bogoliubov-de Gennes (BdG) Hamiltonian related to the Hamiltonian operator through the following $\hat{H} = \hbar(\hat{\xi}^\dagger)^\top H \hat{\xi}$.

1.3. MULTIMODE GAUSSIAN STATES

Proof. To demonstrate the correspondence between unitary transformations and symplectic matrices, we'll use the Baker-Campbell-Hausdorff lemma in Eq. (1.157). Applying this to our case, with $\hat{A} = -i\frac{\hat{H}}{\hbar}$ and $\hat{X} = \hat{a}_k$ or \hat{a}_k^\dagger , we get:

$$e^{-i\frac{\hat{H}}{\hbar}} \hat{a}_k e^{i\frac{\hat{H}}{\hbar}} = \sum_{n=0}^{\infty} \frac{(-i)^n}{n!} \left[\frac{\hat{H}}{\hbar}, \left[\frac{\hat{H}}{\hbar}, \dots \left[\frac{\hat{H}}{\hbar}, \hat{a}_k \right] \dots \right] \right]_n, \quad (1.160)$$

$$e^{-i\frac{\hat{H}}{\hbar}} \hat{a}_k^\dagger e^{i\frac{\hat{H}}{\hbar}} = \sum_{n=0}^{\infty} \frac{(-i)^n}{n!} \left[\frac{\hat{H}}{\hbar}, \left[\frac{\hat{H}}{\hbar}, \dots \left[\frac{\hat{H}}{\hbar}, \hat{a}_k^\dagger \right] \dots \right] \right]_n. \quad (1.161)$$

Let's evaluate the first-order commutator for \hat{a}_k :

$$\left[\frac{\hat{H}}{\hbar}, \hat{a}_k \right] = \sum_{m,n} G_{mn} [a_m^\dagger a_n, \hat{a}_k] + \frac{1}{2} \sum_{m,n} \{F_{mn} [a_m^\dagger a_n^\dagger, \hat{a}_k] + F_{mn}^* [a_n a_m, \hat{a}_k]\} \quad (1.162)$$

$$= \sum_{m,n} G_{mn} [a_m^\dagger, \hat{a}_k] a_n + \frac{1}{2} \sum_{m,n} \{F_{mn} a_m^\dagger [a_n^\dagger, \hat{a}_k] + F_{mn}^* [a_n, \hat{a}_k] a_m\} \quad (1.163)$$

$$= \sum_{m,n} -G_{mn} a_n \delta_{mk} + \frac{1}{2} \sum_{m,n} -F_{mn} [a_n^\dagger \delta_{mk} + a_m^\dagger \delta_{nk}] \quad (1.164)$$

$$\left[\frac{\hat{H}}{\hbar}, \hat{a}_k \right] = -\sum_m (G_{km} \hat{a}_m + F_{km} \hat{a}_m^\dagger). \quad (1.165)$$

Similarly, for \hat{a}_k^\dagger :

$$\left[\frac{\hat{H}}{\hbar}, \hat{a}_k^\dagger \right] = \sum_m (G_{mk}^* \hat{a}_m^\dagger + F_{km}^* \hat{a}_m) \quad (1.166)$$

We can express these compactly using vector notation:

$$\left[\frac{\hat{H}}{\hbar}, \vec{\xi} \right] = -M \hat{\xi}, \quad \text{where } M = \begin{pmatrix} G & F \\ -F^* & -G^* \end{pmatrix}. \quad (1.167)$$

Now, let's consider the second-order commutator:

$$\left[\frac{\hat{H}}{\hbar}, \left[\frac{\hat{H}}{\hbar}, \hat{\xi} \right] \right] = \left[\frac{\hat{H}}{\hbar}, -M \hat{\xi} \right] = -M \left[\frac{\hat{H}}{\hbar}, \hat{\xi} \right] = M^2 \hat{\xi} \quad (1.168)$$

1.3. MULTIMODE GAUSSIAN STATES

By induction, we can show that the n -th order commutator is:

$$\left[\frac{\hat{H}}{\hbar}, \left[\frac{\hat{H}}{\hbar}, \dots \left[\frac{\hat{H}}{\hbar}, \hat{\xi}\right] \dots\right]\right]_n = (-1)^n M^n \hat{\xi} \quad (1.169)$$

Substituting this back into the Baker-Campbell-Hausdorff expansion:

$$e^{-i\frac{\hat{H}}{\hbar}} \hat{\xi} e^{i\frac{\hat{H}}{\hbar}} = \sum_{n=0}^{\infty} \frac{(-i)^n}{n!} M^n \hat{\xi} = e^{-iM} \hat{\xi} \quad (1.170)$$

This demonstrates that the unitary transformation $e^{-i\frac{\hat{H}}{\hbar}}$ on the operators $\vec{\xi}$ corresponds to the symplectic transformation $S_{\xi} = e^{-iM}$ in phase space. \square

These Bogoliubov transformations in Eq. (1.171) map linear combinations of field operators to other linear combinations.

Let us remind the commutation relations for the mode operators $[\hat{\xi}_m, \hat{\xi}_n^{\dagger}] = K_{mn}$. The unitarity of \hat{U} imposes conditions on S_{ξ} to preserve commutation relations: $S_{\xi} K S_{\xi}^{\dagger} = K$, which is the definition the complex form of $Sp(2N, \mathbb{R})$ in the $\hat{\xi}$ basis.

Proof. We can go further and for unitaries expressible as a single exponential, we can derive the following unique correspondence between quadratic unitary operators and symplectic matrices:

$$\hat{U} = e^{-i\hat{\xi}^{\dagger} \cdot H \cdot \hat{\xi}} \rightarrow S_{\xi} = e^{-iKH}. \quad (1.171)$$

\square

Passive and active transformations

The symplectic group $Sp(2N, \mathbb{R})$ consists of real $2N \times 2N$ matrices S that satisfy the condition $S\Omega S^T = \Omega$, where Ω is the symplectic form defined earlier. This non-compact group contains the orthogonal group $SO(2N)$ as a maximal compact subgroup. Symplectic matrices with determinant +1 form a connected subgroup of $Sp(2N, \mathbb{R})$.

Passive transformations are those that preserve the mean energy of the system, characterized by $\text{Tr } \sigma$, when acting on the covariance matrix σ by congruence. These include operations such as phase shifters and beam splitters. In contrast, active transformations, generated by symmetric operators, do not preserve the system's energy and include operations like single-mode and two-mode squeezing.

Let's examine some standard symplectic matrices S associated with key linear optics transformations:

Phase shift

A single-mode rotation by an angle $\phi/2$ in phase space is represented by the unitary operator $\hat{U} = \exp(\frac{i}{\hbar} \frac{\phi}{2} \hat{a}_k^\dagger \hat{a}_k)$ for mode k . The corresponding symplectic transformation $R(\phi)$ in the quadrature basis is:

$$R(\phi) = \begin{pmatrix} \cos(\frac{\phi}{2}) & -\sin(\frac{\phi}{2}) \\ \sin(\frac{\phi}{2}) & \cos(\frac{\phi}{2}) \end{pmatrix} \quad (1.172)$$

Proof. Defining the hamiltonian from the unitary evolution $\hat{H} = -\frac{\phi}{2} \hat{a}_k^\dagger \hat{a}_k$ for and matching it to the expression in Eq. (1.156), we can deduce that $G = -\frac{\phi}{2}$. This yield a M matrix:

$$M = \begin{pmatrix} -\frac{\phi}{2} & 0 \\ 0 & \frac{\phi}{2} \end{pmatrix} \quad (1.173)$$

Recalling Eqs. (1.171), (3.14) and (1.150), we can write:

$$R(\phi) = L^\dagger e^{-iKH} L \quad (1.174)$$

$$= \begin{pmatrix} \frac{1}{\sqrt{2}} & \frac{1}{\sqrt{2}} \\ \frac{-i}{\sqrt{2}} & \frac{i}{\sqrt{2}} \end{pmatrix} \begin{pmatrix} e^{i\phi/2} & 0 \\ 0 & e^{-i\phi/2} \end{pmatrix} \begin{pmatrix} \frac{1}{\sqrt{2}} & \frac{i}{\sqrt{2}} \\ \frac{1}{\sqrt{2}} & \frac{-i}{\sqrt{2}} \end{pmatrix} \quad (1.175)$$

$$= \begin{pmatrix} \cos(\frac{\phi}{2}) & -\sin(\frac{\phi}{2}) \\ \sin(\frac{\phi}{2}) & \cos(\frac{\phi}{2}) \end{pmatrix}. \quad (1.176)$$

□

Beam Splitter Operation

The beam splitter is a fundamental component in quantum optics, representing an ideal (phase-free) unitary operation. Its action on two modes i and j can be expressed as:

$$\begin{cases} \hat{a}'_i = \hat{a}_i \cos \phi - \hat{a}_j \sin \phi \\ \hat{a}'_j = \hat{a}_i \sin \phi + \hat{a}_j \cos \phi \end{cases}. \quad (1.177)$$

This passive transformation is characterized by its transmissivity τ , which relates to the rotation angle ϕ in phase space through $\tau = \cos^2(\phi)$. A notable example is the balanced 50:50 beam splitter, where $\tau = 1/2$ and $\phi = \pi/4$.

In the symplectic formalism, using the process we used for the phase shift operation, the beam splitter transformation is represented by the matrix:

$$BS(\phi) = \begin{pmatrix} \cos(\phi) & -\sin(\phi) & 0 & 0 \\ \sin(\phi) & \cos(\phi) & 0 & 0 \\ 0 & 0 & \cos(\phi) & -\sin(\phi) \\ 0 & 0 & \sin(\phi) & \cos(\phi) \end{pmatrix}. \quad (1.178)$$

Proof. This symplectic representation encapsulates the beam splitter's action on the quadrature operators of the two involved modes, preserving the Gaussian nature of input states. \square

Single-Mode Squeezing Operation

The single-mode squeezing operation shows an active transformation. It's described by the unitary operator $\hat{S}_k(re^{i\theta})$ (Eq. (1.19)), where r represents the squeezing magnitude, θ the squeezing angle and k the number of squeezing modes. In this case, $k = 1$. In the symplectic formalism, using Eqs. (1.19), (1.20) and (1.21), this operation is represented by the matrix:

$$S_1(r, \theta) = \begin{pmatrix} \cosh(r) + \cos(\theta) \sinh(r) & \sin(\theta) \sinh(r) \\ \sin(\theta) \sinh(r) & \cosh(r) - \cos(\theta) \sinh(r) \end{pmatrix}. \quad (1.179)$$

For $\theta = 0$, this simplifies to:

$$S_1(r, 0) = \begin{pmatrix} e^r & 0 \\ 0 & e^{-r} \end{pmatrix}. \quad (1.180)$$

This operation, when $s > 0$, reduces the momentum variance exponentially while increasing the position variance. The case $\theta = \pi/2$ reverses this effect, squeezing the position quadrature instead.

Two-mode squeezing

Similarly, this active transformation, important for creating CV entanglement, is described by the unitary $\hat{U}_{i,j}(r) = \exp[r(\hat{a}_i^\dagger \hat{a}_j^\dagger - \hat{a}_i \hat{a}_j)]$ and has the symplectic representation:

$$S_2(r) = \begin{pmatrix} \cosh r & \sinh r & 0 & 0 \\ \sinh r & \cosh r & 0 & 0 \\ 0 & 0 & \cosh r & -\sinh r \\ 0 & 0 & -\sinh r & \cosh r \end{pmatrix}. \quad (1.181)$$

Proof.

□

Mode-wise squeezing

To generalize the previous example, we turn into the class of mode-wise squeezing. This type of transformation is characterized by a particular form of the Hamiltonian, in Eq. (1.156) where F is diagonal and writes: $F = \text{diag}\{r_1, \dots, r_n\}$, containing real squeezing parameters r_1, \dots, r_n and G is null.

It's worth noting that while we could consider complex parameters $\xi_k = r_k e^{i\phi_k}$, as we did for the single mode squeezing case and the phase $e^{i\phi_k}$ will act as a passive Gaussian unitary transformation. To maintain a clear distinction between transformation classes, we focus on real squeezing parameters r_k . Moreover, the sign of r_k can be absorbed into the phase, so we typically consider non-negative values for r_1, \dots, r_n .

In mode-wise squeezing, each field mode, represented by the operator $\hat{\xi}$, undergoes squeezing according to its corresponding parameter in R . The complex symplectic matrix for this transformation takes the form:

$$S_{\xi} = \exp \begin{pmatrix} 0 & F \\ F & 0 \end{pmatrix} = \begin{pmatrix} \cosh(F) & \sinh(F) \\ \sinh(F) & \cosh(F) \end{pmatrix}. \quad (1.182)$$

The unitary operator corresponding to this transformation can be expressed as:

$$\hat{U} = \exp \left(\hat{\xi}^{\dagger} \begin{pmatrix} 0 & -\frac{1}{2}F \\ \frac{1}{2}F & 0 \end{pmatrix} \hat{\xi} \right) = e^{-\frac{r_1}{2}(\hat{a}_1^{\dagger 2} - \hat{a}_1^2)} \dots e^{-\frac{r_N}{2}(\hat{a}_N^{\dagger 2} - \hat{a}_N^2)}. \quad (1.183)$$

This decomposition illustrates that mode-wise squeezing can be understood as a series of single-mode squeezing operations applied independently to each mode.

1.3.5 Bloch-Messiah Decomposition

We now turn our attention to a crucial decomposition in multimode quantum optics: the Bloch-Messiah decomposition (BMD). This decomposition provides a powerful tool for understanding and implementing any Gaussian unitary transformations in terms of simpler, physically realizable operations.

The Bloch-Messiah decomposition states that any Gaussian unitary S transformation can be decomposed into two passive transformations and one mode-wise squeezing transformation [113, 114, 115]:

$$S = \begin{pmatrix} U & 0 \\ 0 & U^* \end{pmatrix} \exp \begin{pmatrix} 0 & D \\ D & 0 \end{pmatrix} \begin{pmatrix} V & 0 \\ 0 & V^* \end{pmatrix}^{\dagger} = \mathbb{U} \mathbb{D} \mathbb{V}, \quad (1.184)$$

where U and V are unitary matrices, and D is a diagonal matrix with non-negative entries. This decomposition was originally introduced by Bloch and Messiah for fermionic systems [116] and later extended to bosonic systems [117]. The physical interpretation of this decomposition is profound: it demonstrates that any Gaussian unitary transformation can be realized through

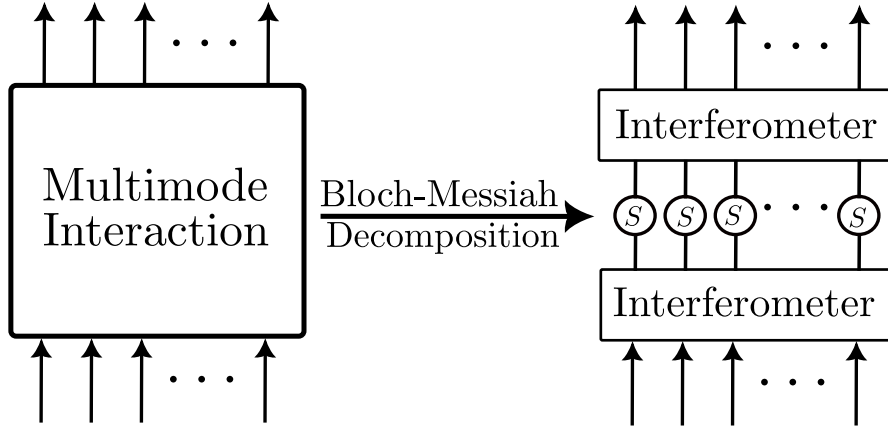


Figure 1.6: **Illustration of Bloch-Messiah decomposition** of a multimode interaction (gaussian unitary) into an input linear multiport \mathbb{V} followed by single mode squeezers \mathbb{D} and an output linear multiport \mathbb{U} .

a sequence of two multiport interferometers (represented by \mathbb{U} and \mathbb{V}) and a set of single-mode squeezers (represented by R). This concept is illustrated in Fig. 1.6. More explicitly, the symplectic transformation is related to Bloch-Messiah decomposition through the following:

$$S = \begin{pmatrix} S_1 & S_2 \\ S_2^* & S_1^* \end{pmatrix} = \begin{pmatrix} U \cosh(D)V^\dagger & U \sinh(D)V^\top \\ U^* \sinh(D)V^\dagger & U^* \cosh(D)V^\top \end{pmatrix}. \quad (1.185)$$

This formulation, used by Braunstein [114], clearly shows how the passive transformations (U and V) and the active squeezing operations in (D) combine to produce the overall Gaussian unitary. The dimensionality of the symplectic group, as revealed by this decomposition, is $2N^2 + N$, which accounts for the two passive transforms and the mode-wise squeezing operations.

Interestingly, the Bloch-Messiah decomposition can be reduced to a Takagi decomposition [118], a variant of singular value decomposition for complex symmetric matrices [119]. For a complex symmetric matrix $M = M^\top \in \mathbb{C}^{N \times N}$, the Takagi decomposition states:

$$M = PD'P^\top \quad (1.186)$$

where D' is a diagonal semi-definite matrix and P is unitary .

By setting $M = S_1 S_2^\top$, we can derive the Bloch-Messiah decomposition from the Takagi

decomposition using the following expression:

$$\begin{aligned}
 U &= P, \\
 D &= \frac{1}{2} \operatorname{arcsinh}(2D'), \\
 V &= S_{\xi 1}^\dagger P \left[\cosh \left(\frac{1}{2} \operatorname{arcsinh}(2D') \right) \right]^{-1} = S_{\xi 1}^\dagger P [\cosh(D)]^{-1}.
 \end{aligned} \tag{1.187}$$

This connection to the Takagi decomposition provides a practical method for implementing the Bloch-Messiah decomposition, which will be of practical interest in Chapter 3.

Multimode squeezing

To explore an application of the powerful tool of the Bloch-Messiah decomposition, we can now explore multimode squeezing within the framework of symplectic matrix formalism. This approach allows us to understand more complex squeezing operations that involve multiple modes simultaneously.

In the case of multimode squeezing, we consider a free Hamiltonian \hat{H}_0 and an interaction Hamiltonian of the form in Eq. (1.156) where $G = 0$ and F is, we remind, complex symmetric matrix ($F = F^T$) that is not necessarily diagonal. The corresponding Gaussian unitary operator takes the form:

$$\hat{U} = \exp \left[\frac{1}{2} \left(\hat{\tilde{a}}^T F^* \hat{\tilde{a}} - \hat{\tilde{a}}^\dagger F \hat{\tilde{a}}^{\dagger T} \right) \right], \tag{1.188}$$

where $\hat{\tilde{\xi}} = (\hat{\tilde{a}} | \hat{\tilde{a}}^\dagger)$ where $\hat{\tilde{a}} = (\hat{a}_1, \dots, \hat{a}_n)^T$. This expression bears a formal resemblance to the squeezing operators we encountered earlier.

It's important to note that when F contains only diagonal elements, this operator describes mode-wise squeezing, as we discussed in previous sections. However, the power of this formulation becomes apparent when F is non-diagonal, allowing for more complex squeezing operations that involve interactions between different modes.

Interestingly, even in the case of a non-diagonal F , we can always reframe the operation in terms of mode-wise squeezing by choosing an appropriate mode basis. This insight comes from applying the Bloch-Messiah decomposition to this class of operators, where the symplectic

transformation takes on the form of Eq. (1.184), where $U = V$ is related intimately to the Takagi decomposition of the matrix $F = URU^T$.

1.4 Quantum Theory of open cavities

In this section, we explore cavity-based open quantum models, building upon our previous discussion of electromagnetic field quantization within a closed optical cavity. We now extend our analysis to more realistic scenarios where optical cavities have at least one partially transmitting mirror. This configuration allows for the injection of light into the cavity and the observation of intracavity processes through the emitted light. We follow the formalism in [87] that we extend to the multimode case.

We begin by developing a model for an open cavity with a single partially transmitting mirror. From this foundation, we derive the evolution equations for the intracavity field in the Heisenberg.

1.4.1 The open cavity model

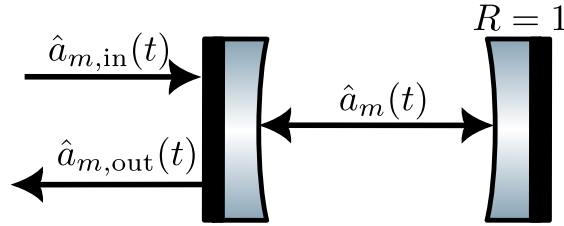


Figure 1.7: **Open cavity model:** each mode (here only one) couples to the environment via a semi-transparent mirror interface. The environmental modes exist as a continuous spectrum, which can be conceptualized as an extended resonator sharing the semi-transparent mirror but extending infinitely in one direction.

From previous sections, we start with the field vector operator defined as:

$$\hat{E}^{(+)}(\vec{r}, t) = i \sum_m \mathcal{E}'_m \hat{a}_m \vec{u}_m(\vec{r}, t) \quad (1.189)$$

where $\mathcal{E}'_m = \sqrt{\frac{\hbar\omega_m}{2\varepsilon_0 LS}}$ and we have considered the longitudinal modes of an optical cavity $\vec{\mathcal{E}}_m e^{i(k_m z - \omega_m t)}$ of length L and section S . The corresponding potential vector operator is given

by:

$$\hat{A}^{(+)}(\vec{r}, t) = \sum_m \mathcal{E}_m \hat{a}_m \vec{\epsilon}_m e^{i(k_m z - \omega_m t)}, \quad (1.190)$$

where $\mathcal{E}_m = \sqrt{\frac{\hbar}{2\varepsilon_0 \omega_m L S}}$.

In this model, each cavity mode of index m couples to a set of external modes through the partially transmitting mirror, which matches the cavity mode in polarization and transverse shape. We represent them as modes of auxiliary cavities ($\sum_{m'}$) of length L_{ext} that share the partially transmitting mirror with the real cavity but have their second mirrors at infinity.

The field corresponding to this auxiliary cavity for mode m can be expressed as:

$$\hat{A}_{\text{ext}}^{(+)}(\vec{r}, t) = \sum_m \left[\lim_{L_{\text{ext}} \rightarrow \infty} \sum_k \mathcal{E}_k \hat{a}_{\text{ext},k}(t) \vec{\epsilon}_k e^{i(k_k(z-L) - \omega_k t)} \right] \quad \text{with } L \leq z \leq L + L_{\text{ext}}. \quad (1.191)$$

Here, the boson external operators satisfy the usual commutation relations $[\hat{a}_{\text{ext},k}(t), \hat{a}_{\text{ext},k'}^\dagger(t)] = \delta_{kk'}$, and $\omega_{k'} = \frac{\pi c}{L} k'$. As the auxiliary cavity length approaches infinity, the longitudinal modes become infinitely dense in frequency space. This allows us to replace the sum over m with an integral:

$$\lim_{L \rightarrow \infty} \sum_k = \frac{L}{\pi c} \int d\omega, \quad (1.192)$$

and the Kronecker delta converges to a Dirac delta $\lim_{L \rightarrow \infty} \delta_{kk'} = \frac{\pi c}{L} \delta(\omega - \omega')$, where the term $\frac{\pi c}{L}$ is for normalization ensuring $\lim_{L_{\text{ext}} \rightarrow \infty} \sum_{k'=1}^{\infty} \delta_{kk'} = 1$. Even though going as high $\omega \rightarrow \infty$ makes no physical sense, it is irrelevant to our description, since we will see that only frequencies around the transitions of the cavity Hamiltonian will effectively play a non-negligible role.

We define new continuous boson operators:

$$\hat{a}_{\text{ext},m}(\omega) = \sqrt{\frac{L}{\pi c}} \lim_{L \rightarrow \infty} \hat{b}_m, \quad (1.193)$$

which satisfy $[\hat{a}_{\text{ext},m}(\omega), \hat{a}_{\text{ext},m'}^\dagger(\omega')] = \delta(\omega - \omega') \delta_{mm'}$. The vector potential of the field outside the

1.4. QUANTUM THEORY OF OPEN CAVITIES

cavity can now be written as:

$$\hat{A}_{\text{ext}}^{(+)}(\vec{r}, t) = \sum_m \int d\omega \mathcal{E}(\omega) \hat{a}_{\text{ext},m}(\omega) \vec{\epsilon}(\omega) e^{i[k(\omega)z - \omega t]}, \quad (1.194)$$

with $\mathcal{E}(\omega) = \sqrt{\frac{\hbar}{2\pi c \epsilon_0 \omega S}}$. It is crucial to emphasize that the frequency dependence of the continuous annihilation operators does not represent a Fourier transform of the time-dependent operators. Instead, it serves as a label for the available external electromagnetic modes, analogous to the discrete index m used for the cavity with finite length.

The free evolution of the cavity mode and external modes is governed by the Hamiltonian $\hat{H}_0 = \hat{H}_{\text{cav}} + \hat{H}_{\text{ext}}$, where:

$$\hat{H}_{\text{cav}} = \sum_m \hbar \omega_m \hat{a}_m^\dagger \hat{a}_m + \hat{H}_I \quad \text{and} \quad \hat{H}_{\text{ext}} = \sum_m \int d\omega \hbar \omega \hat{a}_{\text{ext},m}^\dagger(\omega) \hat{a}_{\text{ext},m}(\omega). \quad (1.195)$$

Here, \hat{H}_I represents any additional intracavity processes we choose to include, such as those described in Eq. (1.156) for example.

The coupling between the cavity and external modes through the mirror is described by a beam-splitter Hamiltonian:

$$\hat{H}_I = i\hbar \sum_m \int d\omega T_m(\omega) [\hat{a}_{\text{ext},m}^\dagger(\omega) \hat{a}_m - \hat{a}_m^\dagger \hat{a}_{\text{ext},m}(\omega)]. \quad (1.196)$$

This form can be justified through various considerations. Mirrors are typically constructed from dielectrics operating in the linear regime to avoid altering the fundamental properties of light. Consequently, we anticipate the mirror's contribution to the Hamiltonian to be quadratic in annihilation and creation operators. Terms like $\hat{a}_{\text{ext},m}^\dagger(\omega) \hat{a}_m^\dagger$ are excluded as they would necessitate an energy $\hbar(\omega_c + \omega)$ from an unspecified source. This formulation aligns with the classical behaviour of mirrors and beam splitters, which split incident beams into reflected and transmitted components while preserving spatiotemporal properties and conserving total intensity.

The parameters $T_m(\omega)$ depend on the mirror's transmissivity for each mode and satisfy $T_m^2(\omega) \ll \omega_m$ for optical frequencies. Assuming only frequencies near the cavity frequencies contribute significantly (resonant interaction), we can approximate $T_m(\omega) = \sqrt{\frac{\gamma_m}{\pi}}$, where γ_m

is the mode-dependent, ω -independent damping rates. This allows us to write the interaction Hamiltonian:

$$\hat{H}_I = i\hbar \sum_m \sqrt{\frac{\gamma_m}{\pi}} \int_{-\infty}^{+\infty} d\omega [\hat{a}_{\text{ext},m}^\dagger(\omega) \hat{a}_m - \hat{a}_m^\dagger \hat{a}_{\text{ext},m}(\omega)] \quad (1.197)$$

This model forms the basis for our analysis of the open cavity. In the following sections, we will now derive reduced evolution equations for the intracavity mode in the Heisenberg picture.

1.4.2 Heisenberg picture approach: The quantum Langevin equation

In the Heisenberg picture, we derive the N set of equations of motion for the annihilation operators:

$$\frac{d\hat{a}_m}{dt} = -i\omega_m \hat{a}_m + \left[\hat{a}_m, \frac{\hat{H}_I}{i\hbar} \right] - \sqrt{\frac{\gamma}{\pi}} \int_{-\infty}^{+\infty} d\omega \hat{a}_{\text{ext}}(\omega), \quad (1.198)$$

$$\frac{\partial \hat{a}_{\text{ext},m}(\omega, t)}{\partial t} = -i\omega \hat{a}_{\text{ext},m}(\omega) + \sqrt{\frac{\gamma_m}{\pi}} \hat{a}_m. \quad (1.199)$$

The formal integration of Eq. (1.199) yield:

$$\hat{a}_{\text{ext},m}(\omega, t) = \hat{a}_{\text{ext},m}^0(\omega) e^{-i\omega(t-t_0)} + \sqrt{\frac{\gamma_m}{\pi}} \int_{t_0}^t dt' e^{i\omega(t'-t)} \hat{a}_m(t'), \quad (1.200)$$

where $\hat{a}_{\text{ext},m}^0(\omega)$ represents the external annihilation operators at the initial time t_0 . Putting this solution in Eq. (1.198) leads to:

$$\begin{aligned} \frac{d\hat{a}_m}{dt} = & -i\omega_m \hat{a}_m + \left[\hat{a}_m, \frac{\hat{H}_I}{i\hbar} \right] \\ & - \sqrt{\frac{\gamma_m}{\pi}} \left(\int_{-\infty}^{+\infty} d\omega \hat{a}_{\text{ext},m}^0(\omega) e^{-i\omega(t-t_0)} + \sqrt{\frac{\gamma_m}{\pi}} \int_{t_0}^t dt' \int_{-\infty}^{+\infty} d\omega e^{i\omega(t'-t)} \hat{a}_m(t') \right). \end{aligned} \quad (1.201)$$

We consider the following identities:

$$\int_{-\infty}^{+\infty} d\omega e^{i\omega(t'-t)} = \delta(t' - t) \quad \text{and} \quad \int_{t_0}^t dt' \delta(t' - t) \hat{a}(t') = \frac{\hat{a}_m(t)}{2}, \quad (1.202)$$

Proof. To support this property, let's consider the following property :

$$\int_{t_0}^{t_2} dt' f(t') \delta(t' - t_1) = f(t_1) \quad \text{for } t_0 < t_1 < t_2. \quad (1.203)$$

Using the natural property of integrals:

$$\int_{t_0}^{t_2} dt' f(t') \delta(t' - t_1) = \int_{t_0}^{t_1} dt' f(t') \delta(t' - t_1) + \int_{t_1}^{t_2} dt' f(t') \delta(t' - t_1) \quad (1.204)$$

. For this expression to be independent of the function and integration limits, we must choose:

$$\int_{t_0}^{t_1} dt' f(t') \delta(t' - t_1) = \int_{t_1}^{t_2} dt' f(t') \delta(t' - t_1) = f(t_1)/2 \quad (1.205)$$

. which aligns with our chosen interpretation when $t_1 = t_0$ and $t_2 = t$ in Eq. (1.202). \square

Introducing also the input operator as the inverse Fourier transform of the external annihilation operators :

$$\hat{b}_{\text{in},m}(t) = -\frac{1}{\sqrt{2\pi}} \int_{-\infty}^{+\infty} d\omega e^{-i\omega t} \hat{a}_{\text{ext},m}^0(\omega), \quad (1.206)$$

which satisfies the commutation relations $[\hat{b}_{\text{in},m}(t), \hat{b}_{\text{in},m'}^\dagger(t')] = \delta(t-t')\delta_{mm'}$ and $[\hat{b}_{\text{in},m}(t), \hat{b}_{\text{in},m'}(t')] = [\hat{b}_{\text{in},m}^\dagger(t), \hat{b}_{\text{in},m'}^\dagger(t')] = 0$, the resulting evolution equation for the intracavity mode is:

$$\frac{d\hat{a}_m}{dt} = -(\gamma_m + i\omega_m)\hat{a}_m + \left[\hat{a}_m, \frac{\hat{H}_I(t)}{i\hbar} \right] + \sqrt{2\gamma} \hat{b}_{\text{in},m}(t), \quad (1.207)$$

known as quantum Langevin equations, with the $b_{\text{in},m}(t)$ acting as input quantum noise terms.

We can consider different configurations for this quantum noise. When the external modes are initially in the vacuum state, since they verify the properties: $\langle \hat{a}_{\text{ext},m}^0(\omega) \rangle = 0$, $\langle \hat{a}_{\text{ext},m}^0(\omega) \hat{a}_{\text{ext},m}^0(\omega') \rangle = 0$ and $\langle \hat{a}_{\text{ext},m}^{0\dagger}(\omega) \hat{a}_{\text{ext},m}^0(\omega') \rangle = 0$, we can derive the following first and second order moments:

$$\langle \hat{b}_{\text{in},m}(t) \rangle = \langle \hat{b}_{\text{in},m}^\dagger(t) \hat{b}_{\text{in},m'}(t') \rangle = 0, \quad (1.208)$$

$$\langle \hat{b}_{\text{in},m}(t) \hat{b}_{\text{in},m'}^\dagger(t') \rangle = \delta(t-t')\delta_{mm'}, \quad (1.209)$$

1.4. QUANTUM THEORY OF OPEN CAVITIES

For a laser injection with monochromatic frequencies $\omega_{L,m}$ for example, we have: $\langle \hat{a}_{\text{ext},m}^0(\omega) \rangle = \alpha_m \delta(\omega - \omega_{L,m})$ and $\langle \hat{a}_{\text{ext},m}^{0\dagger}(\omega) \hat{a}_{\text{ext},m}^0(\omega') \rangle = |\alpha_{L,m}|^2 \delta(\omega - \omega_{L,m}) \delta(\omega' - \omega_{L,m})$, where $\alpha_{L,m}$ is the amplitudes of the monochromatic modes :

$$\hat{A}_L^{(+)}(t) = \sum_m \mathcal{E}_m \alpha_m \vec{\epsilon}_m e^{-i\omega_{L,m}t}. \quad (1.210)$$

We define in this case a new input operator $\hat{a}_{\text{in},m}(t) = \hat{b}_{\text{in},m}(t) - \langle \hat{b}_{\text{in},m}(t) \rangle$ which satisfies vacuum correlations in Eq. (1.208).

The N -quantum Langevin equations become:

$$\frac{d\hat{a}_m}{dt} = \sqrt{\frac{\gamma_m}{\pi}} \alpha_m e^{-i\omega_{L,m}t} - (\gamma_m + i\omega_m) \hat{a}_m + \left[\hat{a}_m, \frac{\hat{H}_I(t)}{i\hbar} \right] + \sqrt{2\gamma_m} \hat{a}_{\text{in},m}(t). \quad (1.211)$$

A convenient transformation is a change of basis of each mode's reference frame to the rotating frame of the corresponding laser mode: $\hat{a}_m \rightarrow \hat{a}_m e^{i\omega_{L,m}t}$, where the quantum Langevin equations in Eq. (1.211) become :

$$\frac{d\hat{a}_m}{dt} = \sqrt{\frac{\gamma_m}{\pi}} \alpha_m - (\gamma_m - i\Delta_m) \hat{a}_m + \left[\hat{a}_m, \frac{\hat{H}_I(t)}{i\hbar} \right] + \sqrt{2\gamma_m} \hat{a}_{\text{in},m}(t), \quad (1.212)$$

where $\Delta_m = \omega_{L,m} - \omega_m$ correspond to the detunings from cavity resonances and the input noise terms have suffered the transformations $\hat{a}_{\text{in},m}(t) \rightarrow \hat{a}_{\text{in},m}(t) e^{i\omega_{L,m}t}$. Eq. (1.212) can be condensed in a singular vectorial quantum Langevin equation that writes :

$$\frac{d\hat{\xi}(t)}{dt} = \hat{A}_d(t) - (\Gamma - i\mathbb{D}) \hat{\xi}(t) + \left[\hat{\xi}(t), \frac{\hat{H}_I(t)}{i\hbar} \right] + \sqrt{2\Gamma} \hat{\xi}_{\text{in}}(t), \quad (1.213)$$

where $\vec{A}_d(t) = (\sqrt{\frac{\gamma_1}{\pi}} \alpha_1 e^{-i\omega_{L,1}t}, \dots, \sqrt{\frac{\gamma_N}{\pi}} \alpha_{L,N} e^{-i\omega_{L,N}t} |H.c.)^\top$ is the (coherent) driving term. It is equivalent to adding a time-dependent term $\hat{H}_d(t) = i\hbar \sum_m \sqrt{\frac{\gamma_m}{\pi}} (\alpha_m \hat{a}^\dagger e^{-i\omega_{L,m}t} - \alpha_m^* \hat{a} e^{i\omega_{L,m}t})$, to the intracavity Hamiltonian \hat{H}_I while considering the external modes to be in vacuum. Both $\Gamma = \text{diag}\{\gamma_1, \dots, \gamma_N | \gamma_1, \dots, \gamma_N\}$ and $\mathbb{D} = \text{diag}\{\Delta_1, \dots, \Delta_N | -\Delta_1, \dots, -\Delta_N\}$ are $2N \times 2N$ diagonal matrix, respectively accounting for the damping rates and the detunings from cavity resonances and $\hat{\xi}_{\text{in}}(t) = (\hat{a}_{\text{in},1}(t), \dots, \hat{a}_{\text{in},N}(t) | \hat{a}_{\text{in},1}^\dagger(t), \dots, \hat{a}_{\text{in},N}^\dagger(t))^\top$ the vector of input bosonic

modes entering the system through losses.

Eq. (1.213) can be simplified even further by absorbing the detuning terms into the intracavity Hamiltonian since it corresponds to a Hamiltonian in the form: $\hat{H}_\Delta = -\hbar \sum_m \Delta_m \hat{a}_m^\dagger \hat{a}_m$. It becomes

$$\frac{d\hat{\xi}(t)}{dt} = \hat{\mathcal{A}}_d(t) - \Gamma \hat{\xi}(t) + \left[\hat{\xi}(t), \frac{\hat{H}_I(t)}{i\hbar} \right] + \sqrt{2\Gamma} \hat{\xi}_{\text{in}}(t). \quad (1.214)$$

A particular example of intracavity Hamiltonian that will be relevant to this thesis is the nonlinear dynamics of a system of N bosons that can be linearized around a stable classical steady-state solution. We previously introduced this Hamiltonian in Eq. (1.156) as the most general quadratic Hamiltonian and we remind that \hat{H}_I writes :

$$\hat{H}_I = \hbar \sum_{m,n} G_{m,n} \hat{a}_m^\dagger \hat{a}_n + \frac{\hbar}{2} \sum_{m,n} [F_{m,n} \hat{a}_m^\dagger \hat{a}_n^\dagger + \text{H.c.}], \quad (1.215)$$

where F and G are $N \times N$ complex matrices describing respectively pair-production processes and mode-hopping processes. If we consider the input quantum noise modes to be in vacuum, Eq. (1.214) can be rewritten as:

$$\frac{d\hat{\xi}(t)}{dt} = -(\Gamma + iM) \hat{\xi}(t) + \sqrt{2\Gamma} \hat{\xi}_{\text{in}}(t), \quad (1.216)$$

where the intracavity interaction matrix M is defined as Eq. (3.14) in Subsection 1.3.4.

Proof. *Starting with the Hamiltonian:*

$$\hat{H}_I = \hbar \sum_{m,n} G_{m,n} \hat{a}_m^\dagger \hat{a}_n + \frac{\hbar}{2} \sum_{m,n} [F_{m,n} \hat{a}_m^\dagger \hat{a}_n^\dagger + \text{H.c.}], \quad (1.217)$$

we calculate the commutator $[\hat{\xi}, \hat{H}_I]$ as we did in Proof 1.3.4 and we find that $[\hat{\xi}, \hat{H}_I] = i\hbar M \hat{\xi}$. We remind that $\hat{\xi} = (\hat{a}_1, \dots, \hat{a}_N | \hat{a}_1^\dagger, \dots, \hat{a}_N^\dagger)^\top$ and M is the $2N \times 2N$ matrix:

$$M = \begin{pmatrix} G & F \\ -F^* & -G^* \end{pmatrix}. \quad (1.218)$$

Substituting $[\hat{\xi}, \hat{H}_I]$ into the quantum Langevin in Eq. (1.214), we get :

$$\frac{d\hat{\xi}(t)}{dt} = \hat{A}_d(t) - \Gamma\hat{\xi}(t) - iM\hat{\xi}(t) + \sqrt{2\Gamma}\hat{\xi}_{in}(t). \quad (1.219)$$

For the case of vacuum input noise (i.e., $\hat{A}_d(t) = 0$), this simplifies to:

$$\frac{d\hat{\xi}(t)}{dt} = -(\Gamma + iM)\hat{\xi}(t) + \sqrt{2\Gamma}\hat{\xi}_{in}(t). \quad (1.220)$$

□

Using the change of basis with Eq. (1.150), these quantum Langevin equations in Eq. (1.220) transform in the quadrature basis $\hat{R}(t)$ we introduced earlier into :

$$\frac{d\hat{R}(t)}{dt} = (-\Gamma + \mathcal{M})\hat{R}(t) + \sqrt{2\Gamma}\hat{R}_{in}(t) \quad (1.221)$$

where

$$\mathcal{M} = L^\dagger(-iM)L = \left(\begin{array}{c|c} \text{Im}[G + F] & \text{Re}[G - F] \\ \hline -\text{Re}[G + F] & -\text{Im}[G + F]^\top \end{array} \right). \quad (1.222)$$

1.4.3 Open Cavity output

We now move into the analysis of the emitted radiation from open quantum optical systems. Beyond the internal dynamics of cavities, we shift in the perspective of the emitted light out of the cavity since that's what we are able to measure and harness for practical applications. We will show the input-output relations of the cavities, which is the relationship between the output field and the internal system operators, which we've previously characterized using quantum Langevin equations. Furthermore, we'll examine advanced techniques for measuring and characterizing the output field such as HD and other techniques.

To begin our analysis, let's consider the output field associated with multiple modes of our previous open cavity. We can express the vector potential of the field emerging from the cavity (propagating along the positive z direction) similarly to the external field of the cavity as in

Eq. (1.191):

$$\hat{A}_{\text{out}}^{(+)}(\vec{r}, t) = \sum_m \mathcal{E}_m \vec{\varepsilon}_m \hat{a}_{\text{out},m}(t) e^{i[k_m z - \omega_m t]}. \quad (1.223)$$

where we have considering a typically narrowband response of the cavity around the resonance frequencies ω_m , allowing us to approximate the slowly varying envelopes $\mathcal{E}(\omega)$ and $\vec{\varepsilon}(\omega)$ by their values at the cavity frequencies ω_m .

Now, we want to express $\hat{a}_{\text{out},m}(t)$ in terms of the initial field and the intracavity dynamics. For that, we can adopt a similar approach to the one used for solving the equation of motions in Eqs (1.198) and (1.199), but using the final conditions (output) instead of the initial conditions (input). Instead of integrating Eq. (1.199) from t_0 to t , let's integrate it from t to t_1 , where $t_1 > t$:

$$\hat{a}_{\text{ext},m}(\omega, t) = \hat{a}_{\text{ext},m}(\omega, t_f) e^{-i\omega(t-t_f)} - \sqrt{\frac{\gamma_m}{\pi}} \int_t^{t_f} dt' e^{i\omega(t'-t)} \hat{a}_m(t'). \quad (1.224)$$

Substituting Eq. (1.224) into Eq. (1.198) we get:

$$\begin{aligned} \frac{d\hat{a}_m}{dt} = & -i\omega_m \hat{a}_m + \left[\hat{a}_m, \frac{\hat{H}_I}{i\hbar} \right] \\ & - \sqrt{\frac{\gamma_m}{\pi}} \left(\int_{-\infty}^{+\infty} d\omega \hat{a}_{\text{ext},m}(\omega, t_f) e^{-i\omega(t_f-t)} - \sqrt{\frac{\gamma_m}{\pi}} \int_t^{t_f} dt' \int_{-\infty}^{+\infty} d\omega e^{i\omega(t'-t)} \hat{a}_m(t') \right). \end{aligned} \quad (1.225)$$

Using the same development as previously, and defining the output operators:

$$\hat{b}_{\text{out},m}(t) = \frac{1}{\sqrt{2\pi}} \int_{-\infty}^{+\infty} d\omega e^{-i\omega(t_1-t)} \hat{a}_{\text{ext},m}(\omega, t_1), \quad (1.226)$$

we arrive at the N time-reversed Langevin equations :

$$\frac{d\hat{a}_m}{dt} = -(\gamma_m + i\omega_m) \hat{a}_m + \left[\hat{a}_m, \frac{\hat{H}_I(t)}{i\hbar} \right] - \sqrt{2\gamma_m} \hat{b}_{\text{out},m}(t). \quad (1.227)$$

Now, subtracting the quantum Langevin equations (1.207) from their time-reversed version, we

obtain the following input-output relations:

$$\hat{b}_{\text{out},m}(t) = \hat{b}_{\text{in},m}(t) + \sqrt{2\gamma_m} \hat{a}_m(t). \quad (1.228)$$

This relation shows how the output field is composed of the input field and the field leaking out of the cavity. It provides a crucial link between the intracavity dynamics and the observable output, allowing us to infer information about the cavity state from measurements of the emitted light. In the case where we have vacuum input for example, Eqs. (1.228) can be written in a vectorial way in the basis of mode operators as $\hat{\xi}_{\text{out}}(t) + \hat{\xi}_{\text{in}}(t) = \sqrt{2\Gamma} \hat{\xi}(t)$, where we have defined $\hat{\xi}_{\text{out}}(t)$ as we previously defined $\hat{\xi}_{\text{in}}(t)$ in previous sections. These input-output relations also write in the quadratures basis : $\hat{R}_{\text{in}}(t) + \hat{R}_{\text{out}}(t) = \sqrt{2\Gamma} \hat{R}(t)$.

1.4.4 Time Correlation Matrix

To simultaneously describe the statistical properties of all field quadratures, one important tool is the covariance matrix. Since the field inside the cavity is not directly accessible, we do not study the associated covariance matrix. We instead define it for the input operators $\hat{R}_{\text{in}}(t)$ and the output operators $\hat{R}_{\text{out}}(t)$. Note that the operators are defined for each time; therefore, a time dependence must be included in the covariance matrix. Such an object is known in the literature as a time-correlation matrix [47].

In this section, we will give its definition and properties.

Definition

The correlation matrix for Gaussian states is given by:

$$\sigma(t, t') = \frac{1}{2} \langle \delta \hat{R}(t) \delta \hat{R}^\top(t') + [\delta \hat{R}(t') \delta \hat{R}^\top(t)]^\top \rangle, \quad (1.229)$$

where $\delta \hat{R}(t) = \hat{R}(t) - \langle \hat{R}(t) \rangle$ and $\langle \hat{R}(t) \rangle$ is the mean quadrature vector. For Gaussian states with zero mean values $\langle \hat{R}(t) \rangle \approx 0$, the statistical properties are fully captured by:

$$\sigma(t, t') = \frac{1}{2} \langle \hat{R}(t) \hat{R}^\top(t') + [\hat{R}(t') \hat{R}^\top(t)]^\top \rangle. \quad (1.230)$$

We define the coefficients of the covariance matrix as:

$$\sigma_{mn}(t, t') = \frac{1}{2} \langle \hat{R}_m(t) \hat{R}_n(t') + \hat{R}_n(t') \hat{R}_m(t) \rangle, \quad (1.231)$$

where m and n are the mode labels.

For a discrete set of modes, the correlation matrix must be symmetric under the exchange of any two mode labels $m \rightleftharpoons n$. In our case, we also have a continuous index "t", representing time. Therefore, the correlation matrix $\sigma(t, t')$ must be symmetric under the exchange $(m, t) \rightleftharpoons (n, t')$ for it to represent a physical state.

For stationary processes, where the correlation matrix depends only on $\tau = |t' - t|$, we can define its Fourier transform. We write it as $\sigma(\omega)$. The Wiener-Khintchine theorem links the Fourier transform of the autocorrelation function of a random variable to its noise spectrum (power spectral density). The Fourier transform of the correlation matrix is therefore an essential tool for spectral analysis of electric field fluctuations.

Taking the Fourier transform element-wise:

$$\begin{aligned} \sigma_{m,n}(\omega) &= \int d\tau e^{i\omega\tau} \sigma_{m,n}(\tau) \\ &= \int d\tau e^{i\omega\tau} \left[\int \frac{d\omega'}{\sqrt{2\pi}} e^{i\omega'\tau} \sigma_{m,n}(\omega, \omega') \right] \\ &= \int d\omega' \left[\int \frac{d\tau}{\sqrt{2\pi}} e^{i(\omega+\omega')\tau} \right] \sigma_{m,n}(\omega, \omega') \\ &= \int d\omega' \delta(\omega + \omega') \sigma_{m,n}(\omega, \omega') \\ \sigma_{m,n}(\omega) &= \sigma_{m,n}(\omega, -\omega), \end{aligned} \quad (1.232)$$

yields the following spectral covariance matrix:

$$\sigma(\omega) = \frac{1}{2} \langle \hat{R}(\omega) \hat{R}^\top(-\omega) + [\hat{R}(-\omega) \hat{R}^\top(\omega)]^\top \rangle. \quad (1.233)$$

$\sigma(\omega)$ encodes crucial information about the frequency-dependent quantum correlations and is constructed from the spectral quadrature operators $\hat{R}(\omega)$ which are defined as the Fourier trans-

forms of their temporal counterparts:

$$\hat{\tilde{R}}(\omega) = \int \frac{dt}{\sqrt{2\pi}} e^{-i\omega t} \hat{\tilde{R}}(t). \quad (1.234)$$

Properties

Let's look at the elementary properties of the covariance matrix and its repercussion on the frequency domain.

- Reality

As long as the quadrature operators are indeed observables, by definition it is obvious that the covariance matrix is real:

$$\forall t, t', \sigma(t, t') \in M_{N,N}(\mathbb{R}) \quad (1.235)$$

What is the equivalent property in the frequency domain?

For that, we have to consider the properties of the spectral quadratures. While the temporal quadratures are Hermitian and obey the standard commutation relations $[\hat{R}(t), \hat{R}(t')] = i\Omega\delta(t - t')$, one can show that the spectral quadratures only need to be skew-hermitian from their very definition:

$$\begin{aligned} [\hat{\tilde{R}}(\omega)]^\dagger &= \left[\int \frac{dt}{\sqrt{2\pi}} e^{-i\omega t} \hat{\tilde{R}}(t) \right]^\dagger \\ &= \int \frac{dt}{\sqrt{2\pi}} e^{i\omega t} \hat{\tilde{R}}^\dagger(t) \\ &= \int \frac{dt}{\sqrt{2\pi}} e^{i\omega t} \hat{\tilde{R}}(t) \\ [\hat{\tilde{R}}(\omega)]^\dagger &= \hat{\tilde{R}}(-\omega), \end{aligned} \quad (1.236)$$

in order to ensure the hermicity of their temporal counterparts.

As a result, the spectral operators verify the following commutation relation $[\hat{\tilde{R}}(\omega), \hat{\tilde{R}}^\dagger(\omega')] = i\Omega\delta(\omega + \omega')$, confirming their no commutation at ω and $-\omega$ allowing coupling between the sidebands $\hat{\tilde{R}}(\omega)$ and $\hat{\tilde{R}}(-\omega)$ [56, 120].

Proof.

$$\begin{aligned}
 [\hat{R}(\omega), \hat{R}^\dagger(\omega')] &= \int \frac{dt_1}{\sqrt{2\pi}} e^{-i\omega t_1} \int \frac{dt_2}{\sqrt{2\pi}} e^{-i\omega' t_2} [\hat{R}(t_1), \hat{R}^\dagger(t_2)] \\
 &= i\Omega \int \frac{dt_1}{\sqrt{2\pi}} \int \frac{dt_2}{\sqrt{2\pi}} e^{-i(\omega t_1 + \omega' t_2)} \delta(t_1 - t_2) \\
 &= i\Omega \int \frac{dt_1}{\sqrt{2\pi}} e^{-i(\omega + \omega') t_1}, \\
 [\hat{R}(\omega), \hat{R}^\dagger(\omega')] &= i\Omega \delta(\omega + \omega').
 \end{aligned} \tag{1.237}$$

□

Using the identity $\langle \hat{\mathbf{A}} \rangle^* = \langle \hat{\mathbf{A}}^\dagger \rangle$ for any operator vector $\hat{\mathbf{A}}$, one can show that $\langle \hat{R}(\omega) \hat{R}^\dagger(-\omega) \rangle^* = \langle [\hat{R}(\omega) \hat{R}^\dagger(-\omega)]^\dagger \rangle$, and consequently $\langle \hat{R}(\omega) \hat{R}^\dagger(-\omega) \rangle^* = \langle \hat{R}(-\omega) \hat{R}^\dagger(\omega) \rangle$ using Eq. (1.236).

Therefore, writing the complex conjugate of the spectral covariance using Eq. (1.233):

$$\sigma^*(\omega) = \frac{1}{2} \langle \hat{R}(-\omega) \hat{R}^\dagger(\omega) + [\hat{R}(\omega) \hat{R}^\dagger(-\omega)]^\dagger \rangle, \tag{1.238}$$

one can see that it obeys the conjugate symmetry property

$$\forall \omega, \sigma^*(\omega) = \sigma(-\omega) \tag{1.239}$$

This also shows that $\sigma(\omega)$ can in the most general case be complex-valued, which as we will show later have implementations of the detection states.

- **Hermicity**

As we previously mentioned, the covariance matrix $\sigma(t, t')$ must be symmetric under the exchange $(m, t) \rightleftharpoons (n, t')$ for it to represent a physical state : $\sigma_{mn}(t, t') = \sigma_{mn}(t', t)$.

The stationarity hypothesis is expressed as $\sigma(t, t') = \sigma(t - t') = \sigma(\tau)$. Thus $\sigma_{mn}(t - t') = \sigma_{nm}(t' - t) = \sigma_{mn}^\top(- (t - t'))$ We can therefore conclude that thanks to stationarity :

$$\forall \tau, \sigma^\top(\tau) = \sigma(-\tau). \tag{1.240}$$

Using that transposition commutes with the Fourier transform, and that the Fourier trans-

form of $t \mapsto f(-t)$ is $\omega \mapsto \tilde{f}(-\omega)$, we obtain the equivalent in frequencies:

$$\forall \omega, \sigma^T(\omega) = \sigma(-\omega). \quad (1.241)$$

Combining Eqs. (1.241) and (1.239), we can confirm the hermicity of the spectral covariance matrix.

Example : covariance matrix of Vacuum

As an example, let's express the correlation matrix and spectral covariance matrix for an input field $\sigma_{\text{in}}(t, t')$ consisting solely of vacuum. Using the bosonic commutation relations and the definition of the annihilation and creation operators, we can write that :

$$\langle [a_{in,i}(t), a_{in,j}^\dagger(t')] \rangle = \langle a_{in,i}(t) a_{in,j}^\dagger(t') \rangle - \underbrace{\langle a_{in,j}^\dagger(t') a_{in,i}(t) \rangle}_0 = \delta_{ij} \delta(t - t'), \quad (1.242)$$

where the expectation value is taken in in vacuum state $|0\rangle$ and used the definition of the zero value of the photon number operator in vacuum $\langle 0 | a_{in,j}^\dagger(t') a_{in,i}(t) | 0 \rangle = 0$. The following expectation value forms the basis for calculating the correlation matrix elements:

$$\langle x_{in,i}(t) x_{in,j}(t') \rangle = \langle y_{in,i}(t) y_{in,j}(t') \rangle = \frac{1}{2} \delta_{ij} \delta(t - t'), \quad (1.243)$$

$$\langle x_{in,i}(t) y_{in,j}(t') \rangle = -\langle y_{in,i}(t) x_{in,j}(t') \rangle = \frac{i}{2} \delta_{ij} \delta(t - t'). \quad (1.244)$$

Proof.

$$\begin{aligned} \langle x_{in,i}(t) x_{in,j}(t') \rangle &= \frac{1}{2} \langle (a_{in,i}^\dagger(t) + a_{in,i}(t))(a_{in,j}^\dagger(t') + a_{in,j}(t')) \rangle \\ &= \frac{1}{2} \langle a_{in,i}^\dagger(t) a_{in,j}^\dagger(t') + a_{in,i}^\dagger(t) a_{in,j}(t') + a_{in,i}(t) a_{in,j}^\dagger(t') + a_{in,i}(t) a_{in,j}(t') \rangle \\ &= \frac{1}{2} \langle a_{in,i}(t) a_{in,j}^\dagger(t') \rangle \quad (\text{only this term survives in vacuum}) \\ \langle x_{in,i}(t) x_{in,j}(t') \rangle &= \frac{1}{2} \delta_{ij} \delta(t - t'). \end{aligned} \quad (1.245)$$

Similarly

$$\langle y_{in,i}(t)y_{in,j}(t') \rangle = \frac{1}{2}\delta_{ij}\delta(t-t'). \quad (1.246)$$

$$\begin{aligned} \langle x_{in,i}(t)y_{in,j}(t') \rangle &= \frac{i}{2} \langle (a_{in,i}^\dagger(t) + a_{in,i}(t))(a_{in,j}^\dagger(t') - a_{in,j}(t')) \rangle \\ &= \frac{i}{2} \langle a_{in,i}^\dagger(t)a_{in,j}^\dagger(t') - a_{in,i}^\dagger(t)a_{in,j}(t') + a_{in,i}(t)a_{in,j}^\dagger(t') - a_{in,i}(t)a_{in,j}(t') \rangle \\ &= \frac{i}{2} \langle a_{in,i}(t)a_{in,j}^\dagger(t') \rangle \quad (\text{only this term survives in vacuum}) \\ \langle x_{in,i}(t)y_{in,j}(t') \rangle &= \frac{i}{2}\delta_{ij}\delta(t-t'). \end{aligned} \quad (1.247)$$

Similarly

$$\langle y_{in,i}(t)x_{in,j}(t') \rangle = \frac{1}{2}\delta_{ij}\delta(t-t') \quad (1.248)$$

□

We can then gather these in the covariance matrix which is expressed as: $\sigma_{in}(t, t') = \frac{1}{2}\delta(t - t')\mathbb{I}$, where \mathbb{I} is a $2N \times 2N$ identity matrix. Using the stationarity condition, we can write this covariance matrix and its Fourier transform as:

$$\sigma_{in}(\tau) = \frac{1}{2}\mathbb{I}\delta(\tau) \quad \text{with} \quad \sigma_{in}(\omega) = \frac{1}{\sqrt{2\pi}} \int_{-\infty}^{+\infty} e^{-i\omega\tau} \sigma_{in}(\tau) = \frac{1}{2\sqrt{2\pi}}\mathbb{I}. \quad (1.249)$$

1.5 Measurement techniques

In this section, we want to compare different measurement schemes of field quadratures in optical systems employing diverse experimental approaches. They are all fundamentally rooted in interferometric methods and share a common principle: they transform phase-sensitive measurements into detectable photon counts, where photodetectors measure the incoming light's power allowing to quantify all possible quadrature components of the optical field.

1.5.1 Ideal Photodetection

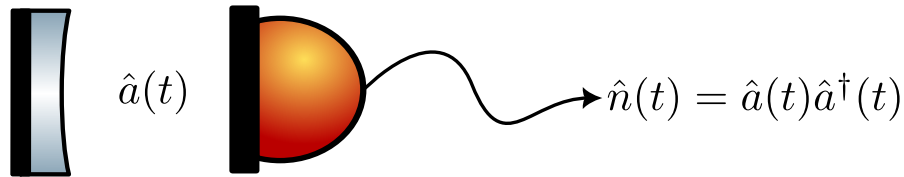


Figure 1.8: Schematic of ideal single-mode detection by Mollow [121].

Photodetection is the most fundamental measurement technique for light. As we shall see with some particular examples (homodyne detection), any other scheme used for measuring different properties of light makes use of photodetection as a part of it.

This technique is based on the photoelectric effect or variations of it. The idea is that when the light beam that we want to detect impinges a metallic surface, it is able to release some of the bound electrons of the metal, which are then collected by an anode. The same happens if light is incident on a semiconductor surface, though in this case instead of becoming free, valence electrons are promoted to the conduction band. The most widely used metallic photodetectors are known as photomultiplier tubes, while those based on semiconducting films are the so-called avalanche photodiodes. In both cases, each photon is able to create one single electron, whose associated current would be equally difficult to measure by electronic means; for this reason, each photoelectron is accelerated towards a series of metallic plates at increasing positive voltages, releasing then more electrons which contribute to generating a measurable electric pulse, the photopulse.

It is customarily said that counting photopulses is equivalent to counting photons, and hence, photodetection is equivalent to a measurement of the number of photons in the light field. This is a highly idealized situation.

Consider the following model for a perfectly efficient detection scheme. A single-mode field with boson operators \hat{a}, \hat{a}^\dagger initially in some state $\hat{\rho}$ is kept in continuous interaction with a photodetector during a time interval T . The intuitive picture of such a scenario is shown in Fig. 1.8: a cavity formed by the photodetector itself and an extra perfectly reflecting mirror contains a single mode. By developing a microscopic model of the detector and its interaction with the light mode, Mollow was able to show that the probability of generating n photoelectrons (equivalently,

1.5. MEASUREMENT TECHNIQUES

the probability of observing n photopulses) during the time interval T is given by [121]:

$$p_n = \left\langle \frac{1}{n!} (1 - e^{-\kappa T})^n (\hat{a}^\dagger \hat{a})^n \exp\left(- (1 - e^{-\kappa T}) \hat{a}^\dagger \hat{a}\right) \right\rangle, \quad (1.250)$$

where the expectation value has to be evaluated in the initial state $\hat{\rho}$ of the light mode, and κ is some parameter accounting for the light–detector interaction. Using the operator identity $: e^{-(1-e^{-\kappa T})\hat{a}^\dagger \hat{a}} := e^{-\kappa T \hat{a}^\dagger \hat{a}}$ [122], and the help of the number state basis $\{|n\rangle\}_{n \in \mathbb{N}}$, it is straightforward to get:

$$p_n = \sum_{m=n}^{\infty} \langle n | \hat{\rho} | n \rangle \frac{m!}{n!(m-n)!} (1 - e^{-\kappa T})^n e^{-\kappa T(m-n)} \xrightarrow{T \gg \kappa^{-1}} \langle n | \hat{\rho} | n \rangle. \quad (1.251)$$

Hence, for large enough detection times, the number of observed pulses follows the statistics of the number of photons. In other words, this ideal photodetection scheme is equivalent to measuring the number operator $\hat{a}^\dagger \hat{a}$ as already commented.

Even though the output of the photodetectors can take only integer values (number of recorded photopulses), they can be arranged to approximately measure the quadratures of light, which we remind are continuous observables.

Electronic noise, particularly Johnson-Nyquist noise, presents significant challenges in photodetection systems by establishing critical power boundaries for effective measurement. The system faces a dual constraint: a lower threshold determined by electronic noise levels, and an upper limit set by detector saturation. When operating near the lower boundary, which typically occurs around hundreds of microwatts in optical systems, the signal risks being overwhelmed by electronic noise. While balanced photodetection techniques can help address electronic noise issues, these methods only capture second-order field characteristics [123], limiting their utility. At the upper end of the measurement range, PIN photodiodes experience high-frequency response saturation around tens of milliwatts, though their low-frequency response remains functional. Creating measurement systems that maintain linearity across this wide operating range (spanning two orders of magnitude) demands sophisticated circuit design. Such systems require regular calibration using coherent state references to ensure measurement accuracy and reliability across the entire operational range [124].

1.5.2 Quadrature measurements

The technique of direct measurement faces two significant constraints in quantum optical systems. First, it can only access one specific combination of quadratures at a time, restricting the completeness of the measurement. Second, the method requires high-intensity light fields with non-zero mean values, making it unsuitable for measuring certain quantum states like vacuum, thermal, or squeezed states where the average field amplitude is zero.

In practice, to overcome these limitations and analyze for example multimode squeezed light to observe noise reduction, interferometric techniques utilizing an optical reference field as a local oscillator (LO) where the LO is shaped to correspond to the quadrature one wishes to observe. These interferometric detection techniques, such as HD, form a broad class of measurement schemes allowing the measurement of specific quadratures $\hat{R}(t)$ by shaping the LO (we call here $\vec{Q}(t)$) to match desired measurement quadrature, whether fixed or time-dependent.

Here, we want to treat the general case accounting for this class of measurement, to link the fluctuations of the quadrature measurement $\vec{Q}(t)$ to the correlation matrix (Subsection 1.4.4). We will later give form to this LO for different detection techniques such as standard homodyne/heterodyne/synodyne detection. We put a particular interest in the quadrature measurement in the frequency domain.

For now, in this general scenario, the photocurrent operator, which is the projection of the LO vector on the quadrature vector can write $\hat{i}(t) = \vec{Q}^T(t)\hat{R}(t)$. Its Fourier transform writes:

$$\hat{i}(\omega) = \int d\omega' \vec{Q}^T(\omega - \omega') \hat{R}(\omega'). \quad (1.252)$$

Since, we want to characterize the most general quadrature measurement in frequency, meaning the local oscillator (in frequency) will be frequency-shaped to the desired spectral quadrature we want to measure: we want to have the product

$$\hat{i}(\omega) = \vec{Q}^T(\omega) \hat{R}(\omega). \quad (1.253)$$

While one can notice that this spectral photocurrent in Eq. (1.253) is not always hermitian, something that's quite counterintuitive, we want to remind that while the temporal photocurrent

1.5. MEASUREMENT TECHNIQUES

$\hat{i}(t)$ is an observable and therefore $\langle \hat{i}(t) \rangle$ is real, its Fourier transform is not necessarily an observable and $\langle \hat{i}(\omega) \rangle$ can be complex-valued.

Through the Wiener-Khinchin theorem when we consider stationary processes, we can relate the spectrum of quantum noise that we call the noise spectral power to the Fourier transform of the autocorrelation function $\langle \hat{i}(t)\hat{i}(t + \tau) \rangle$. To evaluate this autocorrelation function and relate it to the correlation matrix of the system, let us consider a first identity :

$$\langle \hat{i}(t)\hat{i}(t + \tau) \rangle = \langle \hat{i}(t + \tau)\hat{i}(t) \rangle. \quad (1.254)$$

Proving this identity can be trivial in the case where the photocurrent is stationary something we are not sure about for now. To help, let us evaluate the commutation relation between the photocurrent at different times.

$$[\hat{i}(t), \hat{i}(t + \tau)] = \vec{Q}(t) [\hat{\vec{R}}(t), \hat{\vec{R}}(t + \tau)] \vec{Q}(t) \quad (1.255)$$

$$= \vec{Q}(t) [\Omega \delta(\tau)] \vec{Q}(t) \quad (1.256)$$

$$= \vec{Q}(t) \Omega \vec{Q}(t + \tau) \delta(\tau) \quad (1.257)$$

$$[\hat{i}(t), \hat{i}(t + \tau)] = 0. \quad (1.258)$$

Eq. (1.126) shows that the photocurrent at different times always commutes, therefore the identity in Eq. (1.254) still stands regardless of whether the LO vector is stationary or not. We can then write :

$$\langle \hat{i}(t)\hat{i}(t + \tau) \rangle = \langle \hat{i}(t + \tau)\hat{i}(t) \rangle, \quad (1.259)$$

$$\langle \hat{i}(t)\hat{i}(t + \tau) \rangle = \frac{1}{2} \langle \hat{i}(t)\hat{i}(t + \tau) + \hat{i}(t + \tau)\hat{i}(t) \rangle. \quad (1.260)$$

We can now evaluate the two-time autocorrelation function $\langle \hat{i}(t)\hat{i}(t + \tau) \rangle$:

$$\langle \hat{i}(t)\hat{i}(t + \tau) \rangle = \frac{1}{2} \langle \vec{Q}^T(t) \hat{\vec{R}}(t) \hat{\vec{R}}^T(t + \tau) \vec{Q}(t + \tau) + \vec{Q}^T(t + \tau) \hat{\vec{R}}(t + \tau) \hat{\vec{R}}^T(t) \vec{Q}(t) \rangle \quad (1.261)$$

The following proof is much cleaner when using the sum of elements \sum_{ij} , but I choose to keep

it in a more compact form.

Eq. (1.261) confirms that the autocorrelation function of the photocurrent is not stationary because the local oscillator is time-dependent. In this case, we need to be careful when it comes to writing the noise spectral power which will involve multiple convolution functions.

We insist again for a proper spectral quadratures measurement scheme as in Eq. (1.262): again for a proper spectral detection scheme, we want:

$$\Sigma(\omega) = \vec{Q}^T(\omega)\sigma(\omega)\vec{Q}(\omega) \quad (1.262)$$

While depending on the nature of the LO, the spectral photocurrent can be hermitian (or not) and correspond to measurable observable (or not), the noise spectral power is always hermitian. That is why this observable is the one that we will focus more on in terms of interpretation of the measurement outcome of a chosen detection scheme since it does correspond to the measured quantity for this type of detection. And as for any measurable quantity, the noise spectral power is real and always positive. (We show the proof of this in Chapter 3)

1.5.3 Measurement of a Fixed Quadrature : Homodyne Detection

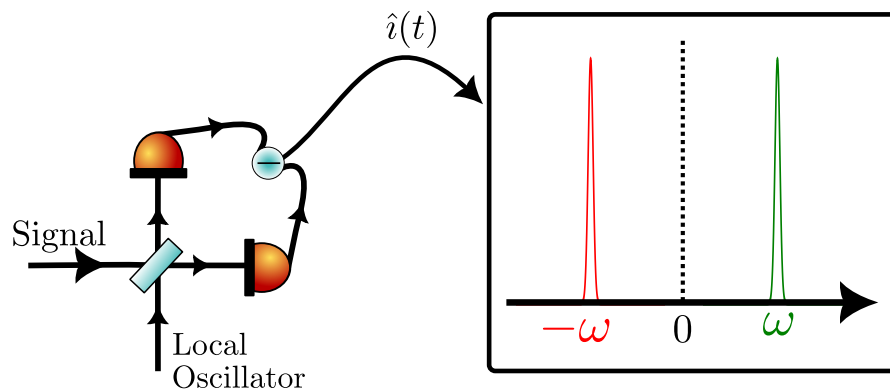


Figure 1.9: **Principle of homodyne detection:** a stationary continuous field is detected by homodyne measurements and the resulting photocurrent is a superposition of spectral components at opposite sideband frequencies. (*left*) homodyne detection, (*right*) balanced homodyne detection. Frequency axis is such that the signal carrier ω_0 is located at 0.

One way to ensure that the noise spectral power from the photocurrent in Eq. (1.252) has the form in Eq. (1.262) and ensure proper spectral quadratures detections is by using for Q to be

a real-valued vector. We show in this subsection that this corresponds to standard Homodyne detection (HD).

Homodyne measurement is a fundamental technique that extracts quadrature information from fields, serving as the foundation of coherent detection in physics and engineering while playing a vital role in quantum information processing. This technique enables various quantum applications, including non-classical squeezing measurements [125], quantum state tomography [126, 127, 128], generation of non-classical states [129], quantum teleportation [130, 13, 131], quantum key distribution, and quantum computing [114, 132]. The process involves comparing the optical signal to a strong and coherent quadrature reference (LO), with the specific quadrature axis selected through LO phase tuning. At its core, a homodyne detector requires an external LO and a field multiplier. In the radio-frequency (RF) domain, this is achieved by directly multiplying the input radio-wave and the LO using an RF frequency mixer. However, optical implementations differ since direct frequency mixers are not available for light; instead, the technique relies on a beam splitter to combine the optical input and LO, utilizing square-law photo-detectors nonlinear electrical response as field multipliers to generate electronic signals proportional to the measured \hat{x} and \hat{y} quadrature.

While standard homodyne detection offers quadrature measurements, its performance can be compromised by noise in the local oscillator. This limitation led to the development of a more robust technique: balanced homodyne detection [133, 134]. The basic scheme is shown in Fig. 1.9b. The mode we want to measure is mixed in a beam splitter with another mode, called the local oscillator, which is in a coherent state $|\alpha_{\text{LO}}\rangle$. When the beam splitter is 50/50 the homodyne scheme is said to be balanced.

We define our fields:

- Field of an N -mode boson operator (Narrowband) of carrier ω_0

$$E^{(+)}(t) = \sum_{m=1}^N \hat{a}_m(t) e^{-i\omega_m t} = e^{i\omega_0 t} \hat{A}(t) = e^{i\omega_0 t} \sum_{m=1}^N \hat{a}_m(t) e^{-i(\omega_m - \omega_0)t} \quad (1.263)$$

1.5. MEASUREMENT TECHNIQUES

- A Local Oscillator (reference beam) of the same carrier

$$E_{LO}^{(+)}(t) = \sum_{m=1}^N \hat{a}_{LO,m}(t) e^{-i\omega_m t} = e^{i\omega_0 t} \hat{A}_{LO}(t) = e^{i\omega_0 t} \sum_{m=1}^N \hat{a}_{LO,m}(t) e^{-i(\omega_m - \omega_0)t} \quad (1.264)$$

with $\hat{a}_{LO,m}^\dagger(t) |\alpha_{LO,m}\rangle = \alpha_m |\alpha_{LO,m}\rangle$. We define the photocurrent for this case as :

$$\hat{i}(t) = \int_{T_{det}} dt \left\langle \hat{E}_{LO}^{(+)}(t) \hat{E}^{(-)}(t) + \hat{E}^{(-)}(t) \hat{E}_{LO}^{(+)}(t) \right\rangle \quad (1.265)$$

$$\hat{i}(t) = \int_{T_{det}} dt \sum_{m,n} \alpha_m^* \hat{a}_n(t) e^{i(\omega_m - \omega_n)t} + \text{H.c.} \quad (1.266)$$

The detection time is usually in the order of nanoseconds (T_{det}). Considering, for example, in the case of a microring resonator, the characteristic time of the slowly varying envelope $T_{\hat{a}_n(t)}$ is in the order of microseconds (1/10 MHz):

$$\Delta\omega = |\omega_m - \omega_n| \approx |m - n| \Omega_{FSR} \leq \Omega_{FSR}, \quad (1.267)$$

where Ω_{FSR} is in the order of 100s of THz corresponding to the characteristic time $T_{\Omega_{FSR}}$ in the order of femtoseconds.

Now comparing the characteristic times:

$$T_{\hat{a}_n(t)} \ll T_{det} \Rightarrow \hat{a}_n(t) \approx \hat{a}_n \quad (1.268)$$

$$T_{\Omega_{FSR}} \ll T_{det} \Rightarrow \int_{T_{det}} dt \approx \int_{-\infty}^{\infty} dt \quad (1.269)$$

The Photocurrent operator then writes:

$$\hat{i}(t) \propto \sum_{m,n} \left[\alpha_m^* \hat{a}_n(t) \int dt e^{i(\omega_m - \omega_n)t} + \text{H.c.} \right] \quad (1.270)$$

$$\propto \sum_{m,n} [\alpha_m^* \hat{a}_n(t) \delta(\omega_m - \omega_n) + \text{H.c.}] \quad (1.271)$$

$$\hat{i}(t) \propto \sum_m [\alpha_m^* \hat{a}_m(t) + \alpha_m \hat{a}_m^\dagger(t)]. \quad (1.272)$$

Let's take a moment here to underline the nature of the LO, relevant for most of the detection

1.5. MEASUREMENT TECHNIQUES

schemes we are going to be discussing. Let's consider the decomposition $\alpha_m = |\alpha_m|e^{i\phi_m}$, then we can photocurrent as

$$\hat{i}(t) \propto \sum_m |\alpha_m| [\hat{a}_m(t)e^{-i\phi_m} + \hat{a}_m^\dagger(t)e^{i\phi_m}] \propto \sum_m |\alpha_m|^2 x_m^{\phi_m}(t). \quad (1.273)$$

We can show that the first and second-order moments of this operator can be written as

$$\langle \hat{i}(t) \rangle = \sum_m |\alpha_m| \langle \hat{x}_m^{\phi_m}(t) \rangle, \quad (1.274)$$

$$\langle \delta \hat{i}(t) \rangle = \sum_m |\alpha_m|^2 \left(\langle (\hat{x}_m^{\phi_m}(t))^2 \rangle + \frac{\langle \hat{a}_m^\dagger \hat{a}_m \rangle}{|\alpha_m|^2} \right) \equiv \sum_m |\alpha_m|^2 \langle (\hat{x}_m^{\phi_m}(t))^2 \rangle, \quad (1.275)$$

where we have simplified the Eq. (1.275) in the limit of strong local oscillator limit $|\alpha_m|^2 \gg \langle \hat{a}_m^\dagger \hat{a}_m \rangle$. The photocurrent of the homodyne scheme has a direct relation with the means and the variances of the quadratures $\hat{x}_m^{\phi_m}(t)$, and therefore to their quantum statistics.

Coming back to Eq. (1.272), we can related it to the quadratures modes (Eq. (1.127))

$$\hat{i}(t) \propto \sum_m [\text{Re}(\alpha_m)\hat{x}_m(t) + \text{Im}(\alpha_m)\hat{y}_m(t)] \quad (1.276)$$

Meaning you as we predicted, we can write the photocurrent as the projection of quadrature vectors in a real vector \vec{Q} : $\hat{i}(t) = \vec{Q}^\top \hat{\vec{R}}(t)$ as in Eq. (1.253) with

$$\hat{\vec{R}}(t) = \left(\hat{x}_1(t), \dots, \hat{x}_N(t) | \hat{y}_1(t), \dots, \hat{y}_N(t) \right)^\top \quad (1.277)$$

and

$$\vec{Q} = \left(\text{Re}(\alpha_1), \dots, \text{Re}(\alpha_N) | \text{Im}(\alpha_1), \dots, \text{Im}(\alpha_N) \right)^\top. \quad (1.278)$$

Here, as a particular case of Eq. (1.253), we have access to a real and stationary local oscillator vector \vec{Q} . From here all the theory we have developed in Subsection 1.5.2 applies, mainly that

we can write the noise spectral power as in Eq. (1.262):

$$\Sigma(\omega) = \int d\omega e^{-i\omega\tau} \vec{Q}^T \sigma(\tau) \vec{Q} \quad (1.279)$$

$$\Sigma(\omega) = \vec{Q}^T \sigma(\omega) \vec{Q}. \quad (1.280)$$

A universally overlooked problem with multimode HD that will be the focus of Chapter 3 is that while the characterisation of frequency-dependent observables involves two-modes, HD is inherently a single-mode measure unable to simultaneously measure complementary quantum correlations within a light field due to its destructive nature. The real and imaginary parts of these quadratures can be described using EPR pairs (Subsection 1.1.5) (\hat{x}_s, \hat{y}_a) and (\hat{x}_a, \hat{y}_s) : $\text{Re}[\hat{x}(\omega)] = \hat{x}_s + \hat{x}_i$ and $\text{Im}[\hat{x}_m(\omega)] = \hat{y}_s - \hat{y}_a$. This limitation means HD cannot provide measurements of both these pairs simultaneously [55, 56]. When measuring therefore the real component, the quantum state is inevitably destroyed during photodetection, making it impossible to subsequently measure the imaginary component. While one might consider splitting the state to perform parallel measurements, this approach introduces unavoidable vacuum noise that compromises the measurement. Therefore, despite the mathematical compatibility of these measurements (as the real and imaginary components commute), the technique can only capture one component per measurement. This limitation can be conceptually compared to an absorptive polarizer in optics, which measures one polarization component while absorbing the orthogonal component, preventing a complete characterization of the polarization state in a single measurement. This phenomenon is termed “hidden squeezing” [54, 86] and requires more advanced detection techniques. We show later this phenomenon is related to the complex nature of the spectral covariance matrix in Eq. (1.233), hence the presence of complex spectral correlations. One other issue we will discuss in Chapter 3 is the case when the interested quadrature (say optimally squeezed quadrature) is frequency dependent. HD with its stationary LO, cannot match the optimally squeezed quadrature across the full spectrum, but only at a single frequency. While the recovery of the full information can be obtained through tomography by scanning the LO phase, this approach is not applicable to QIP and MBQC protocols, where the quantum resource must be accessed in one shot. Such tasks require frequency-dependent quadratures that are known as “morphing supermodes” in highly multimode situations [57].

1.5.4 Heterodyne Detection

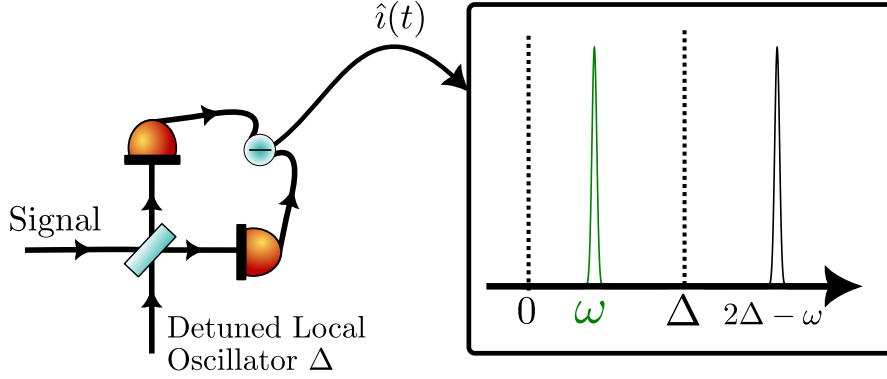


Figure 1.10: **Principle of heterodyne detection:** a stationary continuous field is detected with a local oscillator with an offset Δ from the carrier frequency of the signal. The resulting photocurrent is a superposition of spectral components at ω and $2\Delta - \omega$. Frequency axis is such that the signal carrier ω_0 is located at 0.

Heterodyne detection [135, 136] offers one approach to reveal hidden squeezing. In this technique, the local oscillator (LO) frequencies are deliberately detuned from the carrier frequency, with the offset being substantially larger than the signal frequencies of interest. This allows for the detection and characterization single-mode frequency components with otherwise hidden squeezing effects.

We define our fields, considering the heterodyne detection case where a signal and a local oscillator field with different carrier frequencies are mixed in a BS.

- Field of an N -mode boson operator (Narrowband)

$$E^{(+)}(t) = e^{-i\omega_0 t} \hat{A}(t) := e^{-i\omega_0 t} \sum_{m=1}^N \hat{a}_m(t) e^{-i(\omega_m - \omega_0)t} \quad (1.281)$$

- Local Oscillator (reference beam)

$$E_{LO}^{(+)}(t) = e^{-i\omega_{LO} t} \hat{A}_{LO}(t) := e^{-i\omega_{LO} t} \sum_{m=1}^N \hat{a}_{LO,m}(t) e^{-i(\omega_m - \omega_{LO})t} \quad (1.282)$$

with $\hat{a}_{LO,m}^\dagger(t) |\alpha_{LO,m}\rangle = \alpha_m |\alpha_{LO,m}\rangle$.

When mixing these fields in a beam splitter, we get the sum and the difference fields characterized by $\hat{A}_\pm(t) = \frac{1}{\sqrt{2}} (A(t) \pm A_{LO}(t))$.

1.5. MEASUREMENT TECHNIQUES

The photocurrent in the case writes:

$$\hat{i}(t) = \int_{T_{det}} dt \left(\hat{N}_+(t) - \hat{N}_-(t) \right), \quad (1.283)$$

with $\hat{N}_i(t) = \langle \hat{A}_i^\dagger(t) \hat{A}_i(t) \rangle$, the photonnumber operator for the corresponding i field. We can write these photon number operators as :

$$\hat{N}_\pm = \frac{1}{\sqrt{2}} \left\langle N(t) + N_{LO}(t) \pm \hat{A}^\dagger(t) \hat{A}_{LO}(t) \pm \hat{A}_{LO}^\dagger(t) \hat{A}(t) \right\rangle \quad (1.284)$$

Therefore the photocurrent writes:

$$\hat{i}(t) = \int_{T_{det}} dt \left\langle \hat{A}_{LO}^\dagger(t) \hat{A}(t) + \hat{A}^\dagger(t) \hat{A}_{LO}(t) \right\rangle \quad (1.285)$$

$$\hat{i}(t) = \int_{T_{det}} dt \sum_{m,n} \alpha_m^* \hat{a}_n(t) e^{i(\omega_m - \omega_n + \omega_0 - \omega_{LO})t} + \text{H.c.} \quad (1.286)$$

If I call $\Delta = \omega_{LO} - \omega_0$, we can write :

$$\hat{i}(t) = \int_{T_{det}} dt e^{-i\Delta t} \sum_{m,n} \alpha_m^* \hat{a}_n(t) e^{i(\omega_m - \omega_n)t} + \text{H.c.} \quad (1.287)$$

The detection time is usually in the order of nanoseconds (T_{det}).

If we consider the characteristic time of $e^{i\Delta t}$ to be much smaller than the detection time, we can consider it almost constant. Therefore, we can write the photocurrent as :

$$\hat{i}(t) = e^{-i\Delta t} \int_{T_{det}} dt \sum_{m,n} \alpha_m^* \hat{a}_n(t) e^{i(\omega_m - \omega_n)t} + \text{H.c.} \quad (1.288)$$

Considering, for example, in the case of a microring resonator, the characteristic time of the slowly varying envelope $T_{\hat{a}_n(t)}$ is in the order of microseconds (1/10 MHz).

$$\Delta\omega = |\omega_m - \omega_n| \approx |m - n| \Omega_{FSR} \leq \Omega_{FSR}, \quad (1.289)$$

where Ω_{FSR} is in the order of 100s of THz corresponding to the characteristic time $T_{\Omega_{FSR}}$ in the order of femtoseconds.

1.5. MEASUREMENT TECHNIQUES

Now comparing the characteristic times:

$$T_{\hat{a}_n(t)} \ll T_{det} \Rightarrow \hat{a}_n(t) \approx \hat{a}_n \quad (1.290)$$

$$T_{\Omega_{FSR}} \ll T_{det} \Rightarrow \int_{T_{det}} dt \approx \int_{-\infty}^{\infty} dt \quad (1.291)$$

These considerations allow us to write the photocurrent as :

$$\hat{i}(t) \propto \sum_{m,n} \left[e^{-i\Delta t} \alpha_m^* \hat{a}_n(t) \int dt e^{i(\omega_m - \omega_n)t} + \text{H.c.} \right] \quad (1.292)$$

$$\propto \sum_{m,n} \left[e^{-i\Delta t} \alpha_m^* \hat{a}_n(t) \delta(\omega_m - \omega_n) + \text{H.c.} \right] \quad (1.293)$$

$$\hat{i}(t) \propto \sum_m \left[e^{-i\Delta t} \alpha_m^* \hat{a}_m(t) + e^{i\Delta t} \alpha_m \hat{a}_m^\dagger(t) \right] \quad (1.294)$$

We can write the spectral photocurrent as the “Fourier transform” of the temporal photocurrent. Using the property of modulation of the Fourier transform $\text{TF}[e^{\pm i\Delta t} \hat{a}(t)](\omega) = \hat{a}(\omega \mp \Delta)$, the spectral photocurrent writes

$$\hat{i}(\omega) = \sum_m \left[\alpha_m^* \text{TF}[e^{-i\Delta t} \hat{a}_m(t)](\omega) + \alpha_m \text{TF}[e^{-i\Delta t} \hat{a}_m^\dagger(t)](\omega) \right] \quad (1.295)$$

$$= \sum_m \left[\alpha_m^* \hat{a}_m(\omega + \Delta) + \alpha_m \hat{a}_m^\dagger(\omega - \Delta) \right] \quad (1.296)$$

$$\hat{i}(\omega) = \sum_m \left[\alpha_m^* \hat{a}_m(\Delta + \omega) + \alpha_m [\hat{a}_m(\Delta - \omega)]^\dagger \right] \quad (1.297)$$

So compared to Homodyne detection which attempts to probe spectral components at opposite sideband frequency $\pm\omega$ (in respect to the signal carrier), heterodyne detection instead measures two spectral components symmetric with respect to the detuning between the signal and the LO: $\Delta \pm \omega$. (Fig. 1.10)

Heterodyne detection is used to detect a single spectral component, say at $\pm\omega$ (something HD is incapable of doing). This is possible when we choose a detuning Δ much larger than the typical bandwidth of the signal $|\Delta| \gg \Delta\omega_0$. In that case, the relevant sideband frequencies that we wish to detect are much smaller than the detuning $|\omega| \ll |\Delta|$. We can see it by writing the

spectral photocurrent at $\Delta \mp \omega$.

$$\hat{i}(\Delta - \omega) = \sum_m \left[\alpha_m^* \hat{a}_m(2\Delta - \omega) + \alpha_m [\hat{a}_m(\omega)]^\dagger \right] \quad (1.298)$$

$$\hat{i}(\Delta + \omega) = \sum_m \left[\alpha_m^* \hat{a}_m(2\Delta + \omega) + \alpha_m [\hat{a}_m(-\omega)]^\dagger \right] \quad (1.299)$$

which corresponds to choosing the electronic frequency of the heterodyne photocurrent at $\Delta \pm \omega$. However as seen by Eq. (1.299), this is possible at the cost of the presence of vacuum fields at $2\Delta \pm \omega$. Therefore heterodyne detection admits additional vacuum noise from frequencies that do not contain any signal [137, 133, 138]. This additional noise prevents the heterodyne signal from reaching noise levels below that of homodyne detection, even after accounting for hidden squeezing.

1.5.5 Multimode Synodyne Detection

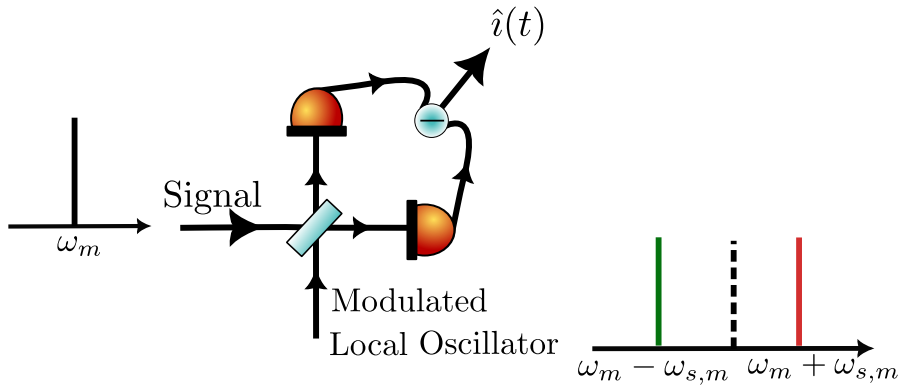


Figure 1.11: **Principle of synodyne detection:** a stationary continuous field is detected with a two-color LO oscillator.

A more elegant solution to hidden squeezing exists through synodyne detection (SD) [139], which effectively addresses hidden squeezing without introducing the additional vacuum noise that is inherent to heterodyne detection. This approach was proposed by Buchmann *et al.* in [139] for the detection of single-mode ponderomotive squeezing and is able to deal with hidden squeezing. We extend this theory to the multimode case of detection.

1.5. MEASUREMENT TECHNIQUES

Let us consider, as introduced in [139](for single mode case) the case of a modulated LO:

$$\hat{E}_{\text{LO}}(t) = i \sum_{m=1}^N \alpha_m(t) e^{-i\omega_m t} + \text{H.c.} \quad (1.300)$$

with the decomposition of $\alpha_m(t)$ (modulation of the complex envelope)

$$\alpha_m(t) = \alpha_m^- e^{i\omega_{s,m} t} + \alpha_m^+ e^{-i\omega_{s,m} t}, \quad (1.301)$$

implying the final of the LO field :

$$\hat{E}_{\text{LO}}^{(+)}(t) = i \sum_m \alpha_m^- e^{-i(\omega_m - \omega_{s,m})t} + \alpha_m^+ e^{i(\omega_m + \omega_{s,m})t} \quad (1.302)$$

This gives a multimode two-tone LO characterized by $(\alpha_m^-, \alpha_m^+ \in \mathbb{C})$ compared to the multimode one-tone LO of HD. We can write the photocurrent as we did for the homodyne detection:

$$\hat{i}(t) = \int_{T_{\text{det}}} dt \sum_{m,n} \alpha_m^*(t) \hat{a}_n(t) e^{i(\omega_m - \omega_n)t} + \text{H.c.} \quad (1.303)$$

Using the same hypothesis that leads to EQUATION and considering again the case of strong LO, the photocurrent operator transforms to:

$$\hat{i}(t) \propto \sum_{m,n} \left[\alpha_m^*(t) \hat{a}_n(t) \int dt e^{i(\omega_m - \omega_n)t} + \text{H.c.} \right] \quad (1.304)$$

$$\propto \sum_{m,n} [\alpha_m^*(t) \hat{a}_n(t) \delta(\omega_m - \omega_n) + \text{H.c.}] \quad (1.305)$$

$$\hat{i}(t) \propto \sum_m [\alpha_m^*(t) \hat{a}_m(t) + \alpha_m(t) \hat{a}_m^\dagger(t)] \quad (1.306)$$

$$\propto \sum_m \left[\text{Re}(\alpha_m(t)) \hat{x}_m(t) + \text{Im}(\alpha_m(t)) \hat{y}_m(t) \right] \quad (1.307)$$

Meaning you can write the photocurrent as the projection of quadrature vectors in a real vector:

$\hat{i}(t) = \vec{Q}^T(t) \hat{\vec{R}}(t)$ with

$$\vec{Q}(t) = \left(\text{Re}[\alpha_1(t)], \dots, \text{Re}[\alpha_N(t)] \mid \text{Im}[\alpha_1(t)], \dots, \text{Im}[\alpha_N(t)] \right)^T. \quad (1.308)$$

The elements of $\vec{Q}(t)$ are characterized as follow:

$$\begin{aligned}\operatorname{Re}(\alpha_m(t)) &= \frac{1}{2} [\alpha_m(t) + \alpha_m^*(t)] \\ &= \frac{1}{2} [(\alpha_m^- + \alpha_m^{*+})e^{i\omega_{s,m}t} + (\alpha_m^+ + \alpha_m^{*-})e^{-i\omega_{s,m}t}] \\ \operatorname{Re}(\alpha_m(t)) &= \frac{1}{\sqrt{2}} \alpha_m^X e^{i\omega_{s,m}t} + H.c.,\end{aligned}\tag{1.309}$$

and

$$\begin{aligned}\operatorname{Im}(\alpha_m(t)) &= \frac{1}{2i} [\alpha_m(t) - \alpha_m^*(t)] \\ &= \frac{1}{2i} [(\alpha_m^- - \alpha_m^{*+})e^{i\omega_{s,m}t} + (\alpha_m^+ - \alpha_m^{*-})e^{-i\omega_{s,m}t}] \\ \operatorname{Im}(\alpha_m(t)) &= \frac{1}{\sqrt{2}} \alpha_m^Y e^{i\omega_{s,m}t} + H.c.\end{aligned}\tag{1.310}$$

$$\begin{aligned}\operatorname{Re}[\alpha_m(t)] &= \frac{1}{\sqrt{2}} \alpha_m^X e^{-i\omega_{s,m}t} + H.c., \\ \operatorname{Im}[\alpha_m(t)] &= \frac{1}{\sqrt{2}} \alpha_m^Y e^{-i\omega_{s,m}t} + H.c.,\end{aligned}\tag{1.311}$$

with $\alpha_m^X = \frac{1}{\sqrt{2}} (\alpha_m^+ + \alpha_m^{-*})$ and $\alpha_m^Y = \frac{1}{\sqrt{2}i} (\alpha_m^+ - \alpha_m^{-*})$.

Some important conditions are: α_m^+ and α_m^- must be complex and $|\alpha_m^X|^2 + |\alpha_m^Y|^2 = 1$. While our two-tone LO presents a non-stationary, inducing a nonreal quadrature measurement in the temporal quadrature basis, something very peculiar happens when going in the Fourier basis. Considering the following Fourier transform identity $\operatorname{TF}[e^{\pm i\omega_{s,m}t} X_\phi(t)](\omega) = X_\phi(\omega \mp \omega_{s,m})$, the Fourier transform of the different elements of $\vec{Q}(t)$ write :

$$\begin{aligned}\operatorname{TF}[\operatorname{Re}[\alpha_m(t)]] &= \frac{1}{\sqrt{2}} [\alpha_m^X \delta(\omega - \omega_{s,m}) + \alpha_m^{X*} \delta(\omega + \omega_{s,m})] \\ \operatorname{TF}[\operatorname{Im}[\alpha_m(t)]] &= \frac{1}{\sqrt{2}} [\alpha_m^Y \delta(\omega - \omega_{s,m}) + \alpha_m^{Y*} \delta(\omega + \omega_{s,m})]\end{aligned}\tag{1.312}$$

1.5. MEASUREMENT TECHNIQUES

We can therefore write the Fourier transform of the photocurrent operator:

$$\begin{aligned}
 \hat{i}(\omega) &= \frac{1}{\sqrt{2}} \sum_m \alpha_m^X \delta(\omega - \omega_{s,m}) \otimes \hat{X}_m(\omega) + \alpha_m^{X*} \delta(\omega + \omega_{s,m}) \otimes \hat{X}_m(\omega) \\
 &\quad \alpha_m^Y \delta(\omega - \omega_{s,m}) \otimes \hat{Y}_m(\omega) + \alpha_m^{Y*} \delta(\omega + \omega_{s,m}) \otimes \hat{Y}_m(\omega), \\
 \hat{i}(\omega) &= \frac{1}{\sqrt{2}} \sum_m \alpha_m^X \hat{X}_m(\omega - \omega_{s,m}) + \alpha_m^{X*} \hat{X}_m(\omega + \omega_{s,m}) \\
 &\quad \alpha_m^Y \hat{Y}_m(\omega - \omega_{s,m}) + \alpha_m^{Y*} \hat{Y}_m(\omega + \omega_{s,m}). \tag{1.313}
 \end{aligned}$$

We can also write the spectral photocurrent in terms of the spectral quadratures vectors at $\omega \pm \omega_{s,m}$:

$$\hat{i}(\omega) = \frac{1}{\sqrt{2}} \left[\vec{Q}^\top \hat{R}(\omega - \omega_{s,m}) + \vec{Q}^\dagger \hat{R}(\omega + \omega_{s,m}) \right], \tag{1.314}$$

with $\vec{Q} = (\alpha_1^X, \dots, \alpha_N^X, \alpha_1^Y, \dots, \alpha_N^Y)^\top$, which is unitary, complex and stationary.

The noise Spectral Power finally writes:

$$\Sigma(\omega) = \vec{Q}^\top \sigma_{\text{out}}(\omega) \vec{Q}. \tag{1.315}$$

While this detection technique (proven only for the single mode case) allows to overcome the limitations of HD in terms of accessing hidden squeezing without additional noise as in heterodyne detection, the two-tone LO presents suffer from an effective stationary profile that does not solve the problem of frequency-dependent optimal quadrature. Syndodyne detection, as HD and heterodyne detection, will in the best scenario match the desired frequency-dependent quadrature only at one frequency.

Chapter 2

Temporal Cavities as temporal mode filters

Contents

2.1	Space-time duality and Temporal Imaging	99
2.1.1	Space-time duality	99
2.1.2	Temporal ABCD matrix formalism	105
2.1.3	Photonic Components	115
2.1.4	Time lens	116
2.1.5	Diffraction gratings	121
2.2	Temporal cavity	128
2.2.1	From mode cleaner cavity to temporal cavity	129
2.2.2	Eigenvalue and Eigenmode conditions	131
2.2.3	Input-output relations	133
2.2.4	Application of temporal cavities in communication protocols	140
2.2.5	Cavity Characterisation: Figures of merit	142
2.2.6	Intrinsic Losses and Compromises	145
2.2.7	Parameter choice	148

2.2.8 Experimental feasibility 149

Temporal modes (TMs) of optical ultra-short pulses provide a reliable and flexible encoding for photonic non-classical states [36]. Their noiseless manipulation plays an important role in the processing of quantum information and communication networks [140, 141, 142, 69], it is therefore important to have schemes for sorting and distributing them within a network. This would enable the implementation of protocols for multipartite entanglement sharing, quantum teleportation, quantum key distribution [36, 140, 143], as well as for the synthesis of multimode entangled states such as cluster states [144, 17, 145], a fundamental resource for the implementation of a computation model based on projective measurements [146]. An ideal TM sorter should separate the targeted TM mode from the other modes and should avoid overlapping with other components and – for quantum applications – with efficiency close 100%. Mode-selective techniques have been developed in the last few years such as, for example, the quantum pulse gate (QPG) [40, 41, 42, 43]. Whereas these devices have the capability of sorting the modal content of the input while preserving its quantum properties [147], they rely on the use of a reference pump signal in the desired TM and an engineered phase-matching that inherently modifies both the central wavelength and the selected TM mode and that may not be available for arbitrary carrier frequencies. On the other side, it is not known whether the complex approach of multi-stage arbitrary modulations of spectral and temporal phases [44, 46] could provide genuine filtering capability. To date, an approach to implement a genuine filter, which would sort TMs while maintaining their carrier frequency as well as their original shape (in time or frequency domain), has not been shown.

We described in Section 1.2.6 the capability of mode cleaner cavities to sort spatial modes relying on the occurrence of mode-dependent resonances. When a paraxial monochromatic beam impinges on them, its modal content at resonance with the cavity is transferred, while the non-resonant modal content is reflected. A typical design we studied for a spatial-mode cleaner cavity consists of two flat partially reflecting mirrors (the input and output couplers) and one spherical perfectly reflecting mirror arranged in triangular geometry as in Fig. 2.1-a. We observed also in that section that a triangular geometry is not the only possible for implementing a mode-cleaner. For example, linear geometry, with a flat mirror and a spherical mirror, can also be used. However, for this geometry, two drawbacks limit their usefulness as a mode-sorting

device:

- The input and the reflected beams are collinear, thus making it difficult to individually address the reflected beam.
- These cavities present degeneracies for transverse modes that belong to the same family, such as TEM_{01} and TEM_{10} . In general such degeneracies are found for cavities with an even number of spherical elements, while for cavities with an odd number the degeneracy is removed.

The goal in this chapter is to leverage the powerful framework of space-time duality [64] in order to translate the triangular cavity to time domain. We propose the “temporal cavity” [63] as a novel type of device that is able to perform genuine TM filtering.

For more details, the subsection on space-time duality and temporal imaging follows the formalism developed in [148] and [149].

2.1 Space-time duality and Temporal Imaging

2.1.1 Space-time duality

The field of Fourier optics emerged from the recognition that manipulating light in the spatial domain provides powerful solutions for information processing applications []. This foundational understanding led to an even more profound insight: the concept of spacetime duality, which enables the translation of spatial-domain techniques into temporal applications, significantly expanding our capabilities in temporal processing and information characterization [150, 64, 151, 148, 73]. The theoretical underpinning of space-time duality stems from a fundamental equivalence discovered nearly six decades ago [152, 153, 154, 155, 156]: the parallel between electromagnetic beam diffraction and the dispersive propagation of electromagnetic pulses. By leveraging this duality, solutions to spatial diffraction problems can be translated into corresponding solutions for temporal dispersion phenomena.

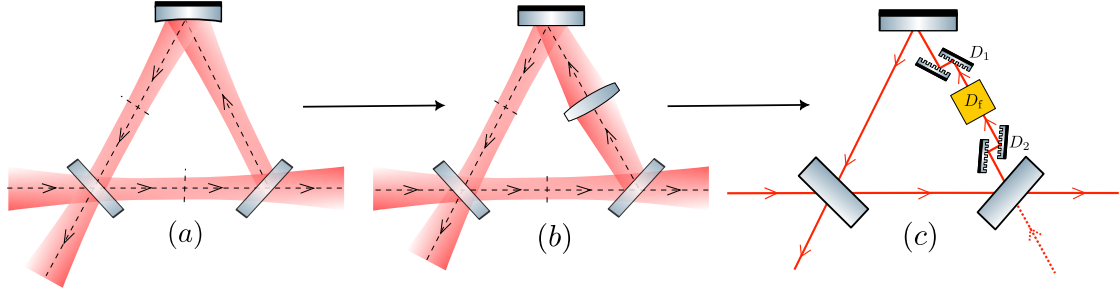


Figure 2.1: **Spatial mode cleaner translation.** (a) Spatial mode-cleaner with spherical mirror, (b) spatial mode-cleaner with a thin lens replacing the spherical mirror, (c) temporal cavity: temporal equivalent of the spatial mode cleaner.

Quantized Field for Diffractive and Dispersive Evolution

We start by introducing the quantized field for both the diffractive and the dispersion evolution. In the quantum description of a monochromatic beam, the positive-frequency part of the electric field operator can be written as

$$\hat{E}'^{(+)}(x, z) = \mathcal{E}'_0 e^{i(k_0 z - \omega_0 t)} \hat{A}'(x, z), \quad (2.1)$$

$$\hat{A}'(x, z) = \sum_{m \in \mathbb{N}} \hat{a}_m u'_m(x, z). \quad (2.2)$$

We assume here a beam propagating along the z direction and having a transverse profile along the x -axis (trivial along y). We show in Section 1.2.6 the case where the transverse plane doesn't have a trivial profile along the y -axis.

Equivalently, in the quantum description of ultra-fast optical pulses, the positive-frequency part of the electric field operator can be written as [96]:

$$\hat{E}^{(+)}(t, z) = \mathcal{E}_0 e^{i(k_0 z - \omega_0 t)} \hat{A}(t, z), \quad (2.3)$$

$$\hat{A}(t, z) = \sum_{m \in \mathbb{N}} \hat{a}_m u_m(t, z). \quad (2.4)$$

Here we assume a pulse propagating along the z and having a trivial profile in the transverse plane (x, y) , i.e. a plane wave.

In both definition in Eqs. (2.1)-(2.4), ω_0 is the carrier, $k_0 = k(\omega_0)$ the propagation constant,

2.1. SPACE-TIME DUALITY AND TEMPORAL IMAGING

$\mathcal{E}_0, \mathcal{E}'_0$, are the single photon amplitudes of the mode m and \hat{a}_m are the annihilation operators satisfying boson commutation relations $[\hat{a}_m, \hat{a}_n^\dagger] = \delta_{m,n}$. The slowly-varying envelope operators $\hat{A}'(x, z), \hat{A}(t, z)$ are each decomposed over a generic orthonormal basis of modal respectively spatial $\{u'_m(x, z)\}_{m \in \mathbb{N}}$ and temporal $\{u_m(t, z)\}_{m \in \mathbb{N}}$ functions.

At the heart of space-time duality lies the mathematical similarity between two key equations. In the spatial domain, the dynamics of a monochromatic beam undergoing one-dimensional diffraction in an isotropic medium is described by:

$$\frac{\partial u'_m}{\partial z}(x, z) = \frac{-j}{2k} \frac{\partial^2 u'_m}{\partial x^2}. \quad (2.5)$$

Analogously, in the temporal domain, the one-dimensional propagation of a pulse in a dispersive medium in the quasi-monochromatic approximation is governed by:

$$\frac{\partial u_m}{\partial z}(\tau, z) = j \frac{\beta_2}{2} \frac{\partial^2 u_m}{\partial \tau^2}. \quad (2.6)$$

where per convenience, we are working in the travelling-wave frame of reference (τ, z) that is propagating with the wave at pulse group velocity where the delayed time is $\tau = t - \beta_1 z$, $\beta_1 = \left(\frac{dk}{d\omega}\right)_{\omega_0} = \frac{1}{v_g}$ is the first-order dispersion parameter, inverse of the group velocity v_g and $\beta_2 = \left(\frac{d^2k}{d\omega^2}\right)_{\omega_0}$ is the group-velocity dispersion (GVD) parameter.

The striking similarity between Eqs. (2.5) and (2.6) forms the basis of space-time duality. It's important to note that both equations represent approximated forms of the wave equation Eq. (1.40). The spatial equation employs the paraxial approximation, assuming slow variation of the field amplitude with z on the scale of a wavelength. Similarly, the temporal equation uses the slowly varying envelope approximation, assuming the amplitude varies slowly with z on the scale of an optical cycle.

By leveraging space-time duality, we can apply well-established spatial-domain techniques to the temporal domain, enabling more powerful approaches to temporal processing and characterization of information. This has led to impressive developments in all-optical signal processing, including temporal Fourier transforms, differentiation, and integration, all achieved using a limited number of active optical components.

2.1. SPACE-TIME DUALITY AND TEMPORAL IMAGING

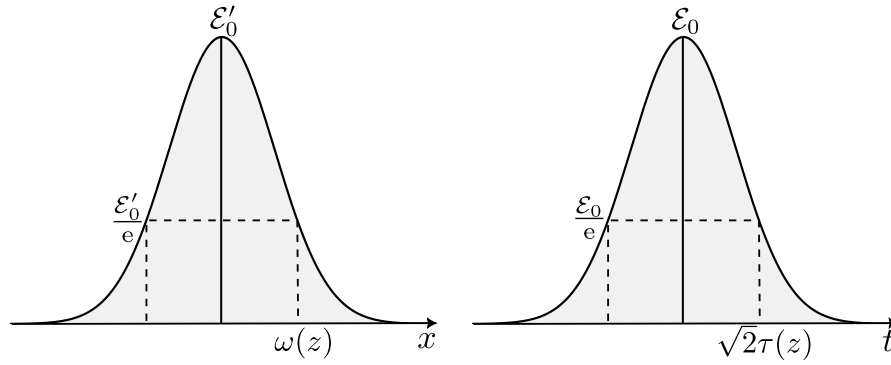


Figure 2.2: **Spatial and Temporal Gaussian Pulses.** Comparison of Gaussian pulses in space and time domains. The left pulse shows the spatial distribution with width $\omega(z)$ corresponding to the beam waist while the right pulse shows the equivalent temporal distribution with width $\sqrt{2}\tau(z)$. Both pulses are normalized to the same peak amplitude, with a characteristic decay marked by the dashed lines.

Spatial Parameters	Equivalence	Temporal Domain Parameters
Traverse spatial parameter x	$x \longleftrightarrow \tau$	Retarded time $\tau = t - \beta_1 z$
Beam waist $w(z)$	$w(z) \longleftrightarrow \sqrt{2} \sigma(z)$	Pulse duration $\sigma(z)$ (Fig. 2.2)
Wavenumber k	$k \longleftrightarrow -\frac{1}{\beta_2}$	Group Velocity dispersion (GVD) β_2
Propagation length z	$z \longleftrightarrow \beta_2 z$	Group delay dispersion (GDD) $\beta_2 z$

Table 2.1: Mapping between Spatial and Temporal Parameters

We can reinforce this duality by making the following coordinate substitutions from both propagation equations in Eqs. (2.1)-(2.4). These substitutions we collected in Table 2.1 map spatial coordinates and wave numbers to their temporal analogues, enabling the translation of spatial equations to the temporal domain.

It is well known, and we have shown that in Section 1.2.6 that a set of possible solutions of the Helmutz Equation Eq. (2.5)) are the orthonormal basis of the HG modes we introduced in Eq. (1.97) which are defined for the case of a single transverse coordinate, up to a normalization constant ϵ'_m :

$$u'_m(x, z) = \epsilon'_m \left[\frac{\omega_0}{\omega(z)} \right] G_m \left(\frac{\sqrt{2}x}{\omega(z)} \right) e^{jk \frac{x^2}{2R(z)}} e^{-j(m+\frac{1}{2})\psi(z)}, \quad (2.7)$$

2.1. SPACE-TIME DUALITY AND TEMPORAL IMAGING

where $G_m(x) = H_m(x)e^{-\frac{x^2}{2}}$ and $H_m(x)$ is the Hermite polynomial of order m . We have also introduced in Eq. (1.91), the definition of the complex beam parameter $q(z)$

$$\frac{1}{q(z)} = \frac{1}{R(z)} - j\frac{\lambda}{\pi w^2(z)} = \frac{1}{R(z)} - j\frac{2}{kw^2(z)}, \quad (2.8)$$

and we remind the definition of the beam waist $w(z)$, the Rayleigh length z_R , the rayon of curvature of the wavefronts $R(z)$ and the Gouy phase $\psi(z)$ (Eqs. (1.94)-(1.96)):

$$w(z) = w_0 \sqrt{1 + \left(\frac{z}{z_R}\right)^2}, \quad (2.9)$$

$$z_R = \frac{\pi w_0^2}{\lambda} = \frac{kw_0^2}{2}, \quad (2.10)$$

$$R(z) = z \left[1 + \left(\frac{z_R}{z}\right)^2 \right], \quad (2.11)$$

$$\psi(z) = -\arctan\left(\frac{z}{z_R}\right) \quad (2.12)$$

where w_0 is the beam waist at $z = 0$ and λ is the wavelength.

Using the transformation in Table 2.1, we can derive a set of solutions for the one-dimensional propagation of a pulse in a dispersive medium (Eq. (2.6) by introducing the temporal equivalent of the complex beam parameter in Eq. (2.8):

$$\frac{1}{q_t(z)} = \frac{1}{\beta_2 R_t(z)} - j\frac{1}{\sigma^2(z)}. \quad (2.13)$$

Since Eq. (2.6) is analogous of the paraxial Helmholtz equation for diffracting beams Eq. (2.5), the orthonormal basis of temporal Hermite-Gauss (HG) functions in Eq. (2.8) is equivalently a possible solution of the dispersion equation. Up to a normalization factor ϵ_m , these solutions read, for $m \in \mathbb{N}$

$$u(t, z) = \epsilon_m \left[\frac{\sigma_0}{\sigma(z)} \right] G_m \left(\frac{t}{\sigma(z)} \right) e^{j\frac{t^2}{2\beta_2 R_t(z)}} e^{-j(m+\frac{1}{2})\psi_t(z)}. \quad (2.14)$$

2.1. SPACE-TIME DUALITY AND TEMPORAL IMAGING

Introducing the temporal phase and its second-time derivative :

$$\phi(t) = \frac{t^2}{2\beta_2 R_t(z)} - (m + \frac{1}{2})\psi_t(z) + \dots (\text{z-dependent term}) \quad (2.15)$$

$$\frac{d^2\phi(t)}{dt^2} = \frac{1}{\beta_2 R_t(z)} = C(z), \quad (2.16)$$

we can express the temporal q parameter and the temporal HG modes in terms of pulse chirp $C(z)$ and pulse duration $\sigma(z)$:

$$\frac{1}{q_t(z)} = C(z) - j \frac{1}{\sigma^2(z)}. \quad (2.17)$$

In the temporal domain, the pulse width $\sigma(z)$, the chirp $C(z)$, the group delay dispersion (GDD) $\beta_2 z$ and the temporal Gouy Phase play similar roles to the spatial beam parameters and are defined as:

$$\sigma(z) = \sigma_0 \sqrt{1 + \left(\frac{\beta_2 z}{\sigma_0^2}\right)^2}, \quad (2.18)$$

$$\frac{1}{C(z)} = \beta_2 z \sqrt{1 + \left(\frac{\sigma_0^2}{\beta_2 z}\right)^2}, \quad (2.19)$$

$$\psi_t(z) = -\arctan\left(\frac{\beta_2 z}{\sigma_0^2}\right). \quad (2.20)$$

We summarize in Table (2.2) the direct correspondence between spatial beam parameters and their temporal counterparts, showing the framework of space-time duality.

Spatial Domain	Correspondance	Temporal Domain
$\frac{\partial A}{\partial z}(x, z) = \frac{-j}{2k} \frac{\partial^2 A}{\partial x^2}$	$x \longleftrightarrow t, k \longleftrightarrow -\frac{1}{\beta_2}$	$\frac{\partial A}{\partial z}(t, z) = j \frac{\beta_2}{2} \frac{\partial^2 A}{\partial t^2}$
Beam waist $w(z)$	$\omega(z) \longleftrightarrow \sqrt{2} \sigma(z)$	Pulse width $\sigma(z)$
Radius of curvature $R(z)$	$\frac{1}{R(z)} \longleftrightarrow C(z)$	Chirp parameter $C(z)$
Gouy phase $\psi(z)$	$\psi(z) \longleftrightarrow \psi_t(z)$	Temporal Gouy Phase $\psi_t(z)$
Complex q parameter $q(z)$	$\frac{1}{R(z)} - j \frac{2}{kw^2(z)} \longleftrightarrow C(z) - j \frac{1}{\sigma^2(z)}$	Temporal q parameter $q_t(z)$

Table 2.2: Comparison of Spatial and Temporal Domain Parameters

2.1.2 Temporal ABCD matrix formalism

Building upon the space-time duality framework introduced earlier, we extend the formalism to encompass basic dispersive photonic components and pulse propagation through these components, using Temporal ABCD matrix formalism. This section presents a unified approach to describe the linear distortion of the pulse envelope in systems composed of concatenated elements that can be characterized within this analogy, referred to as "Gaussian" systems.

The overall system is quantified by multiplying ABCD matrices in the correct sequence, analogous to the spatial case in the paraxial regime [157, 158, 159] in Section 1.2.6, and adapted to the temporal domain [65, 160]. The action of any linear system on the input complex envelope of a short light pulse, $\hat{A}_{\text{in}}(\tau, z)$, can be described as a linear superposition:

$$\hat{A}_{\text{out}}(\tau, z) = \int d\tau' \psi_{\text{in}}(\tau') K(\tau, \tau') \quad (2.21)$$

where the system is defined by the kernel $K(\tau, \tau')$, and $\psi_{\text{out}}(\tau)$ represents the output complex envelope. For Gaussian linear systems, the kernel assumes the form [149]:

$$K(t, t') = \begin{cases} \sqrt{\frac{1}{2\pi B}} \exp \left[\frac{i}{2B} (At'^2 + Dt^2 - 2tt') \right] & \text{if } B \neq 0, \\ \sqrt{\frac{1}{A}} \exp \left[-\frac{iCt^2}{2A} \right] \delta \left(t' - \frac{t}{A} \right) & \text{if } B = 0, \end{cases} \quad (2.22)$$

where the constants A , B , C , and D are the matrix coefficients of the temporal system's ABCD matrix. It's interesting to note that because of the quadratic evolution present in the exponential term, these systems are considered Gaussian.

Similarly to how when a spatial Gaussian beam passes through optical elements, its modifications can be characterised by a linear transformation between the q parameters of the output and input beams characterised by the ABCD matrices of the optical elements, in the time domain, we can treat the propagation of a Hermite-Gaussian pulse by using the transformation between the temporal q parameters from the time domain ABCD matrices of the optical elements. Therefore, similar to in Section 1.2.6, the evolution in Eq. (2.6) can be solved by using the following relation for the temporal q -parameter :

$$q_{\text{out}} = \frac{Aq_{\text{in}} + B}{Cq_{\text{in}} + D}. \quad (2.23)$$

Spectral Dual Formalism

In the realm of temporal optics, there are certain scenarios where the Fourier transform of the envelope, $\hat{A}(\omega, z)$, becomes the primary physical quantity of interest. It's important to note that these two representations are interconnected through a Fourier transform relationship, each containing an equivalent amount of information. Given that linear systems in the time domain exhibit linearity in the frequency domain as well, it becomes advantageous to extend our analysis of Eqs. (2.21) and (2.22) to the dual space. The term "dual" in this context refers to devices that exhibit identical mathematical behaviour but operate in the Fourier domain. This concept can be mathematically expressed as:

$$\hat{A}_{\text{out}}(\omega) = \int d\omega' \hat{A}_{\text{in}}(\omega') \tilde{K}(\omega, \omega') \quad (2.24)$$

where the frequency domain Kernel forms a Fourier transform pair with its time domain counterpart:

$$\tilde{K}(\omega, \omega') = \iint d\tau' d\tau'' K(\tau', \tau'') \exp[i(\omega\tau' - \omega'\tau'')]. \quad (2.25)$$

When considering Gaussian systems specifically, the spectral domain representation also assumes a Gaussian form, mirroring the structure of Eq. (2.22):

$$\tilde{K}(\omega, \omega') = \begin{cases} \sqrt{\frac{i}{2\pi B_\omega}} \exp\left[\frac{-i}{2B_\omega}(A_\omega\omega'^2 + D_\omega\omega^2 - 2\omega\omega')\right] & \text{if } B_\omega \neq 0 \\ \sqrt{\frac{1}{A_\omega}} \exp\left[\frac{-iC_\omega\omega^2}{2A_\omega}\right] \delta(\omega' - \omega/A_\omega) & \text{if } B_\omega = 0. \end{cases} \quad (2.26)$$

The dual coefficients in the frequency domain are intrinsically linked to the matrix parameters A , B , C , and D in the time domain. By incorporating Eq.(2.22) into Eq. (2.25), we derive:

$$\begin{pmatrix} A_\omega & B_\omega \\ C_\omega & D_\omega \end{pmatrix} = \begin{pmatrix} A & B \\ C & D \end{pmatrix}^{-1} = \begin{pmatrix} D & -C \\ -B & A \end{pmatrix}. \quad (2.27)$$

Eqs. (2.26) collectively demonstrate that a Gaussian system's behaviour in the spectral domain is mathematically equivalent to that of a Gaussian system in the temporal domain, with matrix elements provided by the inverse matrix. The full implications of this equivalence will be explored in the next properties.

Properties of temporal ABCD matrices

Below we underline some properties of temporal ABCD matrix systems which are all adapted from their spatial counterparts, but interpreted here in terms of temporal behaviour of photonic components and later on for temporal cavities.

Determinant Condition

Property 2.1.1. *The determinant of an ABCD matrix satisfies $AD - BC = 1$, ensuring the preservation of the canonical commutation relations.*

Temporal Imaging Systems

Property 2.1.2. *When $B = 0$, the Gaussian system conjugates the input and output, resulting in the output intensity being a scaled replica of the input:*

$$I_{out}(\tau, z) = \frac{1}{|A|} I_{in}\left(\frac{\tau}{A}, z\right). \quad (2.28)$$

Proof. *To find the relationship between input and output intensities, consider the complex envelope transformation from Eq. (2.21). With $B = 0$, the kernel from Eq. (2.22) simplifies to:*

$$K(\tau, \tau') = \sqrt{\frac{1}{A}} \exp\left[-\frac{iC\tau^2}{2A}\right] \delta\left(\tau' - \frac{\tau}{A}\right). \quad (2.29)$$

Substituting this into the integral into Eq. (2.21):

$$\hat{A}_{\text{out}}(\tau, z) = \sqrt{\frac{1}{A}} \exp\left[-\frac{iC\tau^2}{2A}\right] \hat{A}_{\text{in}}\left(\frac{\tau}{A}, z\right) \quad (2.30)$$

The intensity is given by the magnitude squared of the complex envelope:

$$I_{\text{out}}(\tau, z) = |\hat{A}_{\text{out}}(\tau, z)|^2 = \left|\sqrt{\frac{1}{A}}\right|^2 \left|\hat{A}_{\text{in}}\left(\frac{\tau}{A}, z\right)\right|^2 = \frac{1}{|A|} I_{\text{in}}\left(\frac{\tau}{A}, z\right) \quad (2.31)$$

Thus, the output intensity is a scaled replica of the input intensity, scaled by the factor $\frac{1}{|A|}$, confirming the property of Temporal Imaging Systems when $B = 0$. \square

Temporal Afocal Systems

Property 2.1.3. Systems with $C = 0$ behave as temporal afocal systems, meaning they do not introduce any quadratic phase modulation to the pulse envelope.

Proof. Consider the ABCD matrix with $C = 0$:

$$\begin{pmatrix} A & B \\ 0 & D \end{pmatrix} \quad (2.32)$$

Substituting into the q -parameter evolution equation:

$$q_{\text{out}} = \frac{Aq_{\text{in}} + B}{D}, \quad (2.33)$$

as we will see there is no dependence on q_{in} in the denominator that could introduce a quadratic phase term.

- Case $B = 0$ The kernel in Eq. (2.22) simplifies to:

$$K(\tau, \tau') = \sqrt{\frac{1}{A}} \delta\left(\tau' - \frac{\tau}{A}\right) \quad (2.34)$$

and the output envelope writes to:

$$\hat{A}_{\text{out}}(\tau, z) = \sqrt{\frac{1}{A}} \hat{A}_{\text{in}}\left(\frac{\tau}{A}, z\right), \quad (2.35)$$

meaning no phase is introduced, particularly no quadratic phase.

- Case : $B \neq 0$

The kernel from Eq. (2.22) is:

$$K(\tau, \tau') = \sqrt{\frac{1}{2\pi B}} \exp\left[\frac{i}{2B} (A\tau'^2 + D\tau^2 - 2\tau\tau')\right] \quad (2.36)$$

Plugging the kernel in Eq.(2.21):

$$\hat{A}_{\text{out}}(\tau, z) = \sqrt{\frac{1}{2\pi B}} \int d\tau' \exp\left[\frac{i}{2B} (A\tau'^2 + D\tau^2 - 2\tau\tau')\right] \hat{A}_{\text{in}}(\tau', z) \quad (2.37)$$

To solve this integral integral, we can approach it by completing the square in the exponent and evaluating the Gaussian integral :

$$A\tau'^2 - 2\tau\tau' = A\left(\tau'^2 - \frac{2\tau}{A}\tau'\right) = A\left(\left(\tau' - \frac{\tau}{A}\right)^2 - \left(\frac{\tau}{A}\right)^2\right). \quad (2.38)$$

Substituting back in the exponential term :

$$\frac{i}{2B} \left[A\left(\left(\tau' - \frac{\tau}{A}\right)^2 - \left(\frac{\tau}{A}\right)^2\right) + D\tau^2 \right] = \frac{iA}{2B} \left(\tau' - \frac{\tau}{A}\right)^2 + \frac{i}{2B} \left(D - \frac{1}{A}\right) \tau^2. \quad (2.39)$$

The integral becomes:

$$\hat{A}_{\text{out}}(\tau, z) = \sqrt{\frac{1}{2\pi B}} \exp\left[\frac{i}{2B} \left(D - \frac{1}{A}\right) \tau^2\right] \int d\tau' \exp\left[\frac{iA}{2B} \left(\tau' - \frac{\tau}{A}\right)^2\right] \hat{A}_{\text{in}}(\tau', z). \quad (2.40)$$

The integral resembles a Gaussian integral of the form:

$$\int_{-\infty}^{\infty} e^{iax^2} dx = \sqrt{\frac{\pi}{-ia}}, \quad (2.41)$$

2.1. SPACE-TIME DUALITY AND TEMPORAL IMAGING

where $a = \frac{A}{2B}$. Applying Eq. (2.41), we get:

$$\int d\tau' \exp \left[\frac{iA}{2B} \left(\tau' - \frac{\tau}{A} \right)^2 \right] = \sqrt{\frac{2\pi B}{iA}}. \quad (2.42)$$

Substituting back into Eq. (2.40), the expression for $\hat{A}_{\text{out}}(\tau, z)$ simplifies to:

$$\hat{A}_{\text{out}}(\tau, z) = \sqrt{\frac{1}{2\pi B}} \cdot \sqrt{\frac{2\pi B}{iA}} \exp \left[\frac{i}{2B} \left(D - \frac{1}{A} \right) \tau^2 \right] \hat{A}_{\text{in}} \left(\frac{\tau}{A}, z \right), \quad (2.43)$$

$$\hat{A}_{\text{out}}(\tau, z) = \frac{1}{\sqrt{iA}} \exp \left[\frac{i}{2B} \left(D - \frac{1}{A} \right) \tau^2 \right] \hat{A}_{\text{in}} \left(\frac{\tau}{A}, z \right). \quad (2.44)$$

When $C = 0$, using the determinant property $AD - BC = 1$ yield $D = \frac{1}{A}$, implying that :

$$\hat{A}_{\text{out}}(\tau, z) = \frac{1}{\sqrt{iA}} \hat{A}_{\text{in}} \left(\frac{\tau}{A}, z \right). \quad (2.45)$$

Thus in both cases when $B = 0$ and $B \neq 0$, the absence of the C term in the ABCD matrix guarantees that the system behaves as a Temporal Afocal System, preserving the phase characteristics of the input pulse envelope without adding any quadratic phase modulation. \square

Spectral Afocal Systems

Property 2.1.4. Combining the two previous properties, and utilizing the spectral formalism developed earlier, any temporal imaging system ($B = 0$) is also a spectral afocal system, and vice versa.

Proof. From the Spectral Dual Formalism, the dual ABCD matrix in the frequency domain is the inverse of the temporal ABCD matrix given by EQUATION. For a Temporal Imaging System, $B = 0$,

$$\begin{pmatrix} A & 0 \\ C & D \end{pmatrix} \quad (2.46)$$

The inverse (dual) matrix becomes:

$$\begin{pmatrix} A_\omega & B_\omega \\ C_\omega & D_\omega \end{pmatrix} = \begin{pmatrix} D & -C \\ 0 & A \end{pmatrix} \quad (2.47)$$

indicating that the spectral dual system has $C_\omega = 0$. Therefore, when $B = 0$ in the temporal domain, the dual system in the spectral domain also satisfies $C_\omega = 0$, classifying it as a Spectral Afocal System. This establishes the equivalence between Temporal Imaging Systems and Spectral Afocal Systems. \square

Spectral Imaging Systems

Property 2.1.5. Conversely, afocal systems ($C = 0$) act as spectral imaging systems, where the output spectrum is a scaled replica of the input's optical spectrum:

$$I_{out}(\omega, z) = \frac{1}{|D|} I_{in}\left(\frac{\omega}{D}, z\right). \quad (2.48)$$

Proof. Consider a temporal Afocal System with $C = 0$:

$$\begin{pmatrix} A & B \\ 0 & D \end{pmatrix} \quad (2.49)$$

Using the Spectral Dual Formalism, the dual ABCD matrix is:

$$\begin{pmatrix} A_\omega & B_\omega \\ C_\omega & D_\omega \end{pmatrix} = \begin{pmatrix} D & 0 \\ -B & A \end{pmatrix} \quad (2.50)$$

Therefore $B_\omega = 0$, classifying the system as a Spectral Imaging System.

Applying the kernel in the spectral domain, the output spectrum is related to the input spectrum by:

$$I_{out}(\omega, z) = \frac{1}{|D|} I_{in}\left(\frac{\omega}{D}, z\right) \quad (2.51)$$

Thus, an Afocal System with $C = 0$ acts as a Spectral Imaging System $B_\omega = 0$, producing a

scaled replica of the input optical spectrum. □

Optical Fourier Transformers

Property 2.1.6. Systems with $A = 0$ function as optical Fourier transformers. In these systems, the output intensity pulse mirrors the optical spectrum of the input pulse, scaled by B :

$$I_{out}(t, z) = \frac{1}{|B|} I_{in}\left(\frac{\omega}{B}, z\right). \quad (2.52)$$

Proof. For an Optical Fourier Transformer, we set $A = 0$, resulting in the matrix,

$$\begin{pmatrix} 0 & B \\ C & D \end{pmatrix} \quad (2.53)$$

and the Kernel (Eq. (2.22)) for the case where $B \neq 0$:

$$K(\tau, \tau') = \sqrt{\frac{1}{2\pi B}} \exp\left[\frac{i}{2B} (D\tau^2 - 2\tau\tau')\right]. \quad (2.54)$$

Substituting the kernel in Eq. (2.21):

$$\begin{aligned} \hat{A}_{out}(\tau, z) &= \sqrt{\frac{1}{2\pi B}} \int d\tau' \exp\left[\frac{i}{2B} (D\tau^2 - 2\tau\tau')\right] \hat{A}_{in}(\tau', z) \\ \hat{A}_{out}(\tau, z) &= \sqrt{\frac{1}{2\pi B}} \exp\left(\frac{iD\tau^2}{2B}\right) \int d\tau' \exp\left(-\frac{i\tau\tau'}{B}\right) \hat{A}_{in}(\tau', z) \end{aligned} \quad (2.55)$$

Recognizing the integral as a Fourier transform of $\hat{A}_{in}(\tau', z)$:

$$\text{TF}\left[\hat{A}_{in}(\tau', z)\right]\left(\omega = \frac{\tau}{B}\right) = \frac{1}{\sqrt{2\pi}} \int d\tau' \exp(-i\omega\tau') \hat{A}_{in}(\tau', z) = \frac{1}{\sqrt{2\pi}} \int d\tau' \exp\left(-\frac{i\tau\tau'}{B}\right) \hat{A}_{in}(\tau', z) \quad (2.56)$$

Thus:

$$\hat{A}_{out}(\tau, z) = \sqrt{\frac{1}{B}} \exp\left(\frac{iD\tau^2}{2B}\right) \text{TF}\left[\hat{A}_{in}(\tau', z)\right]\left(\frac{t}{B}\right). \quad (2.57)$$

2.1. SPACE-TIME DUALITY AND TEMPORAL IMAGING

The optical spectrum $I_{in}(\omega, z)$ of the input pulse is defined as:

$$I_{in}(\omega, z) = \left| \text{TF} \left[\hat{A}_{in}(\tau', z) \right] (\omega) \right|^2 \quad (2.58)$$

Taking the magnitude squared of the output complex envelope:

$$\begin{aligned} I_{out}(\tau, z) &= |\hat{A}_{out}(\tau, z)|^2 = \left| \sqrt{\frac{1}{B}} \exp\left(\frac{iD\tau^2}{2B}\right) \text{TF} \left[\hat{A}_{in}(\tau', z) \right] \left(\frac{\tau}{B}\right) \right|^2 \\ I_{out}(\tau, z) &= \frac{1}{|B|} I_{in}\left(\frac{\omega}{B}\right), \end{aligned} \quad (2.59)$$

indicates that the output intensity $I_{out}(t)$ is a scaled replica of the input optical spectrum $I_{in}(\omega)$, where the scaling factor is $\frac{1}{|B|}$ and the argument is scaled by $\frac{\omega}{B}$. \square

Time-to-Frequency Transformers

Property 2.1.7. By dual analysis, systems with $D = 0$ act as time-to-frequency transformers, where the output optical spectrum is a scaled replica of the input intensity profile:

$$I_{out}(\omega, z) = \frac{1}{|C|} I_{in}\left(\frac{-t}{C}\right). \quad (2.60)$$

Proof. Consider an ABCD matrix with $D = 0$:

$$\begin{pmatrix} A & B \\ C & 0 \end{pmatrix} \quad (2.61)$$

The dual ABCD matrix is:

$$\begin{pmatrix} A_\omega & B_\omega \\ C_\omega & D_\omega \end{pmatrix} = \begin{pmatrix} 0 & -C \\ -B & A \end{pmatrix} \quad (2.62)$$

We can notice that $A_\omega = 0$, meaning that we're in the case of the dual property of the Optical Fourier Transformers. Therefore, the spectral output intensity $I_{out}(\omega, z)$ is a scaled replica of the input optical intensity $I_{in}(t)$, where the scaling factor is $\frac{1}{|B_\omega|}$ and the argument is scaled by $\frac{t}{B_\omega}$.

2.1. SPACE-TIME DUALITY AND TEMPORAL IMAGING

Considering that $B_\omega = -C$, we get :

$$I_{out}(\omega, z) = \frac{1}{|C|} I_{in}\left(\frac{-t}{C}, z\right). \quad (2.63)$$

Thus, when $D = 0$, the system functions as a Time-to-Frequency Transformer, converting the temporal profile of the input intensity into a scaled and inverted optical spectrum. \square

Scaling Systems

Property 2.1.8. Gaussian systems with both $B = 0$ and $C = 0$ perform simultaneous temporal and spectral imaging of the input signal. These scaling systems yield a temporal image of the input's complex field, scaled by the matrix coefficient A :

$$\hat{A}_{out}(\tau, z) = \sqrt{\frac{1}{A}} \hat{A}_{in}\left(\frac{\tau}{A}, z\right). \quad (2.64)$$

Proof. When $B = 0$, we have proven the system can be considered a temporal imaging system. Similarly, when the $C = 0$, the system can be considered a spectral imaging system.

From the proof of the temporal imaging system, we got in the case $B = 0$.

$$\hat{A}_{out}(\tau, z) = \sqrt{\frac{1}{A}} \exp\left[-\frac{iC\tau^2}{2A}\right] \hat{A}_{in}\left(\frac{\tau}{A}, z\right) \quad (2.65)$$

Additionally when $C = 0$,

$$\hat{A}_{out}(\tau, z) = \sqrt{\frac{1}{A}} \hat{A}_{in}\left(\frac{\tau}{A}, z\right) \quad (2.66)$$

\square

General Gaussian Systems

Property 2.1.9. Any Gaussian system with $A \neq 0$ can be decomposed into a combination of three equivalent subsystems: a temporal lens with an equivalent chirping coefficient $-\frac{C}{A}$, a scaling system with an equivalent scaling factor A , A Group Delay Dispersion (GDD) circuit with

an equivalent parameter $\frac{B}{A}$:

$$\begin{pmatrix} A & B \\ C & D \end{pmatrix} = \begin{pmatrix} 1 & 0 \\ \frac{C}{A} & 1 \end{pmatrix} \begin{pmatrix} A & 0 \\ 0 & \frac{1}{A} \end{pmatrix} \begin{pmatrix} 1 & \frac{B}{A} \\ 0 & 1 \end{pmatrix}. \quad (2.67)$$

This decomposition facilitates the design and analysis of complex photonics components by allowing the constituent elements to be treated individually before combining their effects through matrix multiplication.

2.1.3 Photonic Components

Building upon the established temporal ABCD matrix formalism, we will now elucidate the mathematical structure of key devices as highlighted in Table 2.3, crucial for temporal cavities in this thesis.

Space	Time
Diffraction of z $\begin{pmatrix} 1 & z \\ 0 & 1 \end{pmatrix}$	Dispersion of GDD $D = \beta_2 z$ $\begin{pmatrix} 1 & D \\ 0 & 1 \end{pmatrix}$
Thin lens of focal f $\begin{pmatrix} 1 & 0 \\ -\frac{1}{f} & 1 \end{pmatrix}$	time lens of GDD D_f $\begin{pmatrix} 1 & 0 \\ -\frac{1}{D_f} & 1 \end{pmatrix}$

Table 2.3: Comparison of Space and Time Optical Elements

The first elements elucidate the equivalence between diffraction of a monochromatic beam and dispersion on a quasi-monochromatic pulse. In this temporal ABCD formalism, the ABCD matrix M_{disp} for a dispersive propagation through a medium of length d and GVD β_2 is given by

$$M_{\text{disp}} = \begin{pmatrix} 1 & D \\ 0 & 1 \end{pmatrix}, \quad (2.68)$$

where $D = \beta_2 d$ is the GDD. However, it's important to distinguish that while diffraction in spatial optics occurs only for positive wave numbers, the GDD parameter in temporal optics can

assume both positive and negative values, contingent upon the specific material component, waveguide structure, and the carrier frequency of the signal. Using Property 2.1.3, a dispersive propagation through a medium behaves as a temporal afocal system, meaning it preserves the phase characteristic of the input pulse with no added quadratic phase modulation. It equivalently acts, through Property 2.1.5, as a spectral imaging system and inducing a quadratic phase in the spectral domain.

In a similar way, we obtain the ABCD matrix of the dual of the thin lens, M_{TL} of a time lens of focal-GDD D_f :

$$M_{\text{TL}} = \begin{pmatrix} 1 & 0 \\ -1/D_f & 1 \end{pmatrix}. \quad (2.69)$$

Using Property 2.1.2, time lens, we know that a requirement for this device based on the form of its ABCD matrix is to act as a temporal imaging system, inducing additionally a quadratic phase modulation.

Equipped with these few elements we will develop the theory of a temporal cavity. But first, let's give more details about the time lens.

2.1.4 Time lens

The space-time duality extends naturally to optical elements, with time lenses serving as the temporal counterpart to spatial thin lenses. Just as a thin lens imparts a quadratic phase modulation to a beam's spatial profile, a time lens applies a quadratic phase modulation to a temporal waveform. This fundamental analogy forms the basis of temporal imaging systems.

From thin lens to time lens

To better grasp the effects of time lenses, let's exploit again the analogy between diffraction and dispersion. We can examine their impact in their respective Fourier domains. In k -space, the diffraction operator applies a quadratic phase shift to the field: $\phi(k_x) = -\frac{k_x^2 z}{2k}$, where k_x represents the beam's transverse wavenumber, and this phase indicates the beam's divergence along the x -axis.

2.1. SPACE-TIME DUALITY AND TEMPORAL IMAGING

Similarly, in the frequency domain, the dispersion operator imparts a quadratic spectral phase: $\phi(\Omega) = \frac{\beta_2 \Omega^2 z}{2} = \frac{D \Omega^2}{2}$ where Ω denotes the baseband angular frequency.

The impulse response resulting from the diffraction operation can be expressed as:

$$h(x) = h_S \exp\left(\frac{i\pi}{\lambda z} x^2\right) \quad (2.70)$$

where h_s is a constant dependent on the propagation distance z . This response incorporates a quadratic phase shift relative to the spatial parameter x . A thin lens without aberrations, having a focal length f , applies a similar quadratic phase shift to the input electric field:

$$\phi(x) = -\frac{kx^2}{2f} \quad (2.71)$$

A comparable phenomenon occurs when a brief optical pulse traverses a lengthy dispersive medium. The impulse response of the dispersion operator is given by:

$$h_T(\tau) = h_T \exp\left(-\frac{i\tau^2}{2D}\right), \quad (2.72)$$

where h_T is a constant reliant on D . For a short pulse subjected to substantial dispersion, the electric field's phase can be approximated by the quadratic phase in the impulse response. Analogous to the spatial scenario, a temporal equivalent of the thin lens, known as a time lens, can be defined. This time lens imparts a quadratically varying phase shift to the input signal:

$$\phi(\tau) = \frac{\tau^2}{2D_f} \quad (2.73)$$

where D_f represents the focal GDD of the time lens.

This fundamental analysis can be expanded to encompass the broader field of temporal imaging, where spatial imaging systems are adapted into their temporal counterparts [148, 73, 149], enabling the manipulation of intricate optical waveforms. We are not aiming in this thesis at reviewing all of them in this thesis. Instead, we focus on reviewing key components of temporal imaging that can be employed for temporal cavities. Therefore our primary emphasis is on the time lens and its implementation.

Time lens implementations

While time lens-based temporal imaging systems unlock a broader range of possibilities for both temporal and spectral processing of ultrafast waveforms, a crucial first step is the practical implementation of a time lens.

A time lens can be realized by creating a system that applies a temporally quadratic phase shift to the input signal. This necessitates the use of a phase-modulation technique, either electro-optical or all-optical (linear or non-linear). Various time-lens approaches have been demonstrated, each with its own characteristics in terms of processing bandwidth, temporal aperture size, noise and aberration performance, and operating wavelength range. Before going into these methods, it's important to define key parameters that determine a time lens's processing capacity.

For applications in ultra-high-bandwidth signal processing, the most critical characteristic of a time lens is its temporal resolution. To define this parameter, we can draw back to an analogy with the spatial problem of focusing a large Gaussian beam using a thin lens. Consider a lens with focal length f , where the input Gaussian beam waist size is $2w_1$ and the output (focused) beam waist size is $2w_2$. The relationship between these parameters is given by: $w_2 = \frac{\lambda f}{\pi w_1}$. To achieve a smaller output spot size, one must reduce the focal length f and increase the input beam size w_1 . However, the largest input beam size that can be captured is limited by the lens aperture size D .

Applying this analogy to the time domain, we define the resolution of a time lens as the shortest transform-limited Gaussian FWHM pulsewidth $\delta\tau$ that can be generated by compressing a Gaussian pulse. The time-lens aperture length ΔT is defined as the longest Gaussian pulse duration that can be captured. Similar to a spatial Gaussian beam, we can express the temporal resolution of the time lens in terms of its focal group delay dispersion (GDD) and aperture length:

$$\delta\tau = 4 \ln(2) \frac{|D_f|}{\Delta T} \quad (2.74)$$

The time-lens aperture is constrained by two factors.

2.1. SPACE-TIME DUALITY AND TEMPORAL IMAGING

1. First, the phase profile of the time lens must be nearly aberration-free in the region where the profile is quadratic.
2. Second, the amplitude transmission profile of the time lens should ideally be flat across its aperture. Aberrations caused by a non-flat transmission profile are typically easier to correct compared to those resulting from non-quadratic phase terms.

A key figure of merit for a time lens is the ratio between its aperture length and temporal resolution, which indicates the number of temporal features that can be processed:

$$N = \frac{\Delta T}{\delta\tau} = \frac{\Delta T^2}{4 \ln(2) |D_f|} \quad (2.75)$$

This FOM is equivalent to the time-bandwidth product of the time lens. Let us now explore different interesting techniques used to implement time lenses and compare their performances.

Time-Lens Systems Based on Electro-Optic Modulation

The most straightforward approach to creating a time lens involves using an electro-optic phase modulator (EOPM) driven by a quadratic voltage. The first experimental demonstrations of time-lens systems employed this technique. It is usually built using a nonlinear crystal having a high electro-optic coefficient such as Lithium Niobate LiNbO_3 . In practice, the RF signal driving the phase modulator is sinusoidal, which is locally quadratic near its extrema. The induced phase shift can be approximated as:

$$\varphi(t) = \pm \left(\frac{\pi V_{\text{RF}}}{V_\pi} \right) \cos(\omega_{\text{RF}} t) \approx \pm \left(\frac{\pi V_{\text{RF}}}{V_\pi} \right) \left(1 - \frac{\omega_{\text{RF}}^2 t^2}{2} \right) \quad (2.76)$$

where V_{RF} and ω_{RF} are the amplitude and frequency of the modulating voltage, respectively, and V_π is the voltage required for the modulator to produce a phase shift of π . For standard LiNbO_3 , it is possible to achieve typical values around $V_\pi = 5V$ [148]. Eq. (2.76) can be rewritten in terms of much-known quantities:

$$\varphi(t) = \delta \cos(2\pi f_{\text{RF}} t) \approx \delta \left(1 - \frac{(2\pi f_{\text{RF}} t)^2}{2} \right), \quad (2.77)$$

2.1. SPACE-TIME DUALITY AND TEMPORAL IMAGING

where $\delta = \pm \frac{\pi V_{\text{RF}}}{V_{\pi}}$, a real constant, is the modulation amplitude and f_{RF} is the modulation frequency. From Eq. (2.77), we can approximate the induced phase :

$$e^{i\varphi(t)} = e^{i\delta t} \exp\left(-i \frac{(2\pi f_{\text{RF}})^2 \delta t^2}{2}\right) = e^{i\delta t} e^{-i \frac{t^2}{2D_f}} \quad (2.78)$$

From Eq. (2.78), we can derive the value of the time-lens focal GDD:

$$D_f = \frac{1}{4\pi^2 f_{\text{RF}}^2 \delta} = \pm \frac{V_{\pi}}{\pi V_{\text{RF}} \omega_{\text{RF}}^2}. \quad (2.79)$$

It's worth noting that the focal GDD can be either positive or negative. Deviations from the approximation in Eq. (2.77) introduce aberrations, but these are tolerable over a time window that is a small fraction of the sinusoidal drive's period $\Delta T \approx \frac{1}{f_{\text{RF}}}$.

Proof. To calculate more rigorously the time aperture ΔT , let us expand the Taylor expansion in Eq (2.77) and find the condition on the input pulse duration σ_0 for which the quadratic approximation is valid. The Taylor expansion of the cosine term can be written as:

$$\cos(2\pi f_{\text{RF}} t) = 1 - \frac{(2\pi f_{\text{RF}} t)^2}{2!} + \frac{(2\pi f_{\text{RF}} t)^4}{4!} - \frac{(2\pi f_{\text{RF}} t)^6}{6!} + \dots$$

Substitute this expansion into the phase modulation

$$\begin{aligned} & \exp\left[i\delta\left(1 - \frac{(2\pi f_{\text{RF}} t)^2}{2!} + \frac{(2\pi f_{\text{RF}} t)^4}{4!} - \frac{(2\pi f_{\text{RF}} t)^6}{6!} + \dots\right)\right] \\ &= e^{i\delta} \exp\left[-i\delta\left(\frac{(2\pi f_{\text{RF}} t)^2}{2!} - \frac{(2\pi f_{\text{RF}} t)^4}{4!} + \frac{(2\pi f_{\text{RF}} t)^6}{6!} - \dots\right)\right]. \end{aligned} \quad (2.80)$$

For the quadratic approximation to be valid, we want the fourth-order term (at least) to be negligible compared to the second-order term, which means

$$\frac{(2\pi f_{\text{RF}} t)^4 / 4!}{(2\pi f_{\text{RF}} t)^2 / 2!} = \frac{(2\pi f_{\text{RF}} t)^2}{12} \ll 1. \quad (2.81)$$

Solving for t :

$$t^2 \ll \frac{3}{(\pi f_{\text{RF}})^2} \iff t \ll \frac{\sqrt{3}}{\pi f_{\text{RF}}}. \quad (2.82)$$

Now, if we consider σ_0 as a measure of the pulse duration (e.g., standard deviation for a Gaussian pulse), we can relate it to the maximum time t for which the approximation holds:

$$\sigma_0 \ll \frac{\sqrt{3}}{\pi f_{\text{RF}}}. \quad (2.83)$$

This proves the statement that

$$\Delta T = \frac{\sqrt{3}}{\pi f_{\text{RF}}} \approx \frac{1}{f_{\text{RF}}}. \quad (2.84)$$

Therefore the pulses over which the EOPM time lens operates must satisfy $\sigma_0 \ll \Delta T$ to ensure that the higher-order terms in the Taylor expansion of the cosine function are negligible compared to the quadratic term. When this condition is met, the phase modulation can be accurately approximated by a quadratic function, which is essential for the time lens to operate without significant aberrations. If this condition is not satisfied, the higher-order terms become significant, introducing non-quadratic phase components. These components lead to temporal aberrations, analogous to spatial aberrations in conventional lenses, which can distort the temporal focusing properties of the time lens. \square

Before we jump into the theory of temporal cavities, let's check another component that will be needed.

2.1.5 Diffraction gratings

A diffraction grating consists of a large number of equally spaced parallel grooves, which diffract incoming light into several beams travelling in different directions. The grating equation relates the angles at which these diffracted beams propagate to the wavelength of the incident light and the spacing between the grooves. We will also describe some parameters allowing to characterize diffraction gratings from the Grating Equation.

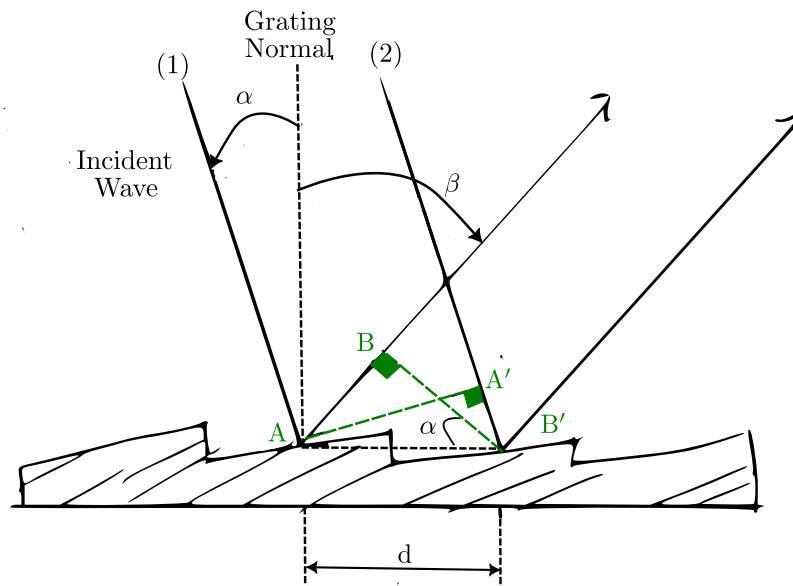


Figure 2.3: Diffraction gratings.

Grating Equation

Consider two rays diffracted by adjacent grooves of the grating in Fig. 2.3. Ray 1 propagates a distance AB while Ray 2 propagates a distance $A'B'$, where $A'B'$ exceeds AB by an additional distance due to the grating's geometry. The optical path difference δ between the two rays is given by:

$$\delta = AB - A'B' \quad (2.85)$$

Expressing AB and $A'B'$ in terms of the groove spacing d , incident angle α , and diffraction angle β gives:

$$AB = d \sin \alpha$$

$$A'B' = -d \sin \beta \quad (\text{since } \beta < 0)$$

$$\delta = d(\sin \alpha + \sin \beta) \quad (2.86)$$

Constructive interference occurs when the optical path difference is an integer multiple of

2.1. SPACE-TIME DUALITY AND TEMPORAL IMAGING

the wavelength λ :

$$\delta = m\lambda = d(\sin \alpha + \sin \beta) \quad (2.87)$$

This leads to the grating equation:

$$m\lambda = d[\sin \alpha + \sin \beta] \quad (2.88)$$

where m is the diffraction order, d is the groove spacing, α is the incident angle, β is the diffraction angle.

Alternatively, using groove density f (grooves per unit length in lines/mm), the equation can be rewritten as:

$$fm\lambda = \sin \alpha + \sin \beta \quad (2.89)$$

Littrow configuration

From Eq. (2.88), the diffraction angle β as a function of wavelength λ is given by:

$$\beta(\lambda) = \sin^{-1} \left(\frac{m\lambda}{d} - \sin \alpha \right). \quad (2.90)$$

In the Littrow configuration, the diffracted light is reflected back along the same path as the incident light, meaning $\alpha = \beta$. Substituting this condition into the grating equation yields:

$$m\lambda = 2d \sin \alpha. \quad (2.91)$$

Angular Dispersion

Angular dispersion quantifies how the diffraction angle β changes with wavelength λ . It is defined as the derivative of β with respect to λ :

$$D = \frac{d\beta}{d\lambda} \quad (2.92)$$

Starting from the grating equation:

$$\sin \beta = -\sin \alpha + m \frac{\lambda}{d} \quad (2.93)$$

Taking the derivative with respect to λ :

$$\begin{aligned} \frac{d \sin \beta}{d \lambda} &= m \frac{1}{d} \\ \cos \beta \frac{d \beta}{d \lambda} &= \frac{m}{d}, \end{aligned} \quad (2.94)$$

yielding the expression for the angular dispersion in grating parameters including the groove density f :

$$D = \frac{m}{d \cos \beta} = \frac{m f}{\sqrt{1 - \sin^2 \beta}} \quad (2.95)$$

The angular dispersion increases with higher diffraction orders m and higher groove densities f , leading to greater separation of wavelengths.

Temporal Dispersion with Pairs of Gratings (Treacy Grating)

Temporal dispersion arises when different wavelengths experience different path lengths, resulting in time delays between them. A pair of gratings, known as a Treacy grating, can introduce a frequency-dependent time delay in pulses, which is essential in applications like Chirped Pulse Amplification (CPA). This fundamental principle was instrumental in the groundbreaking work [161] that earned Gérard Mourou and Donna Strickland half of the 2018 Nobel Prize in Physics.

Consider a pair of gratings introducing an angle θ_m and a slight deviation $\delta\theta_m$ for longer wavelengths (λ) compared to shorter ones. The optical path difference δ between two paths is:

$$\delta = \widehat{ABC} - \widehat{AB'} \quad (2.96)$$

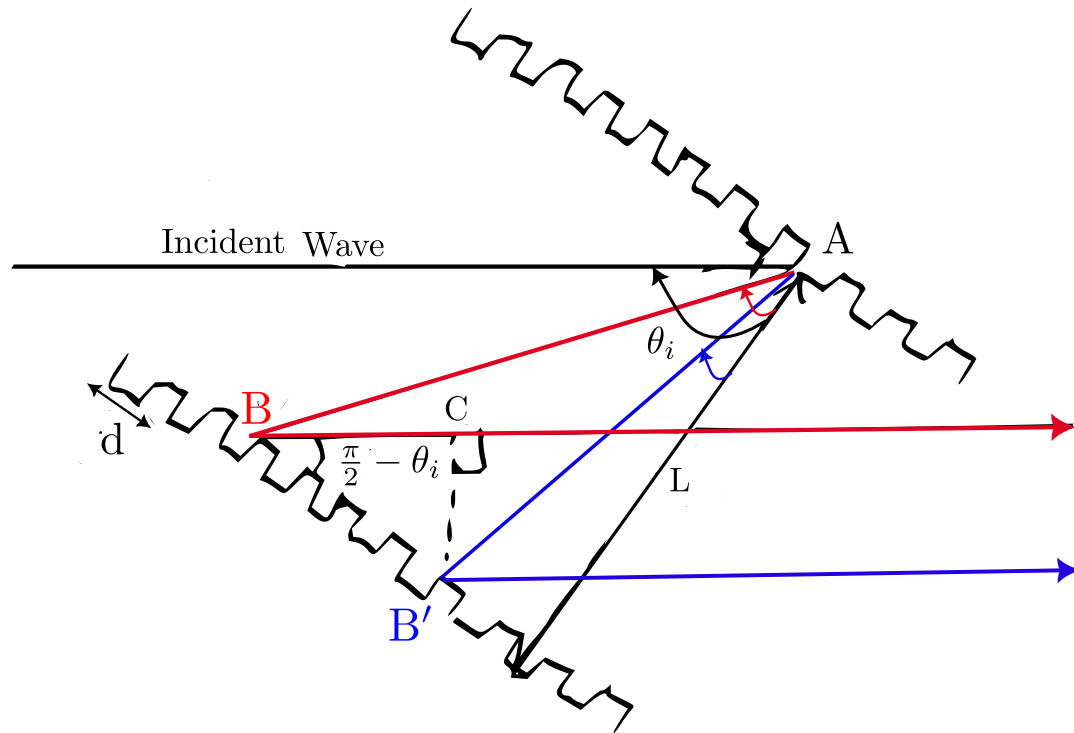


Figure 2.4: Grating pairs in Treacy configuration.

Where:

$$AB = \frac{L}{\cos(\theta_m + \delta\theta_m)} \quad \text{and} \quad AB' = \frac{L}{\cos(\theta_m)} \quad (2.97)$$

The additional path BB' caused by the angle deviation is:

$$BB' = -L [\tan(\theta_m + \delta\theta_m) - \tan(\theta_m)], \quad (2.98)$$

since both angles are negative.

Considering the inclination θ_i :

$$BC = BB' \cos\left(\frac{\pi}{2} - \theta_i\right) = -L [\tan(\theta_m + \delta\theta_m) - \tan(\theta_m)] \sin \theta_i \quad (2.99)$$

2.1. SPACE-TIME DUALITY AND TEMPORAL IMAGING

Thus, the total optical path difference becomes:

$$\delta = L \left[\frac{1}{\cos(\theta_m + \delta\theta_m)} - (\tan(\theta_m + \delta\theta_m) - \tan \theta_m) \sin \theta_i - \frac{1}{\cos(\theta_m)} \right] \quad (2.100)$$

The time delay $\delta\tau$ associated with the optical path difference is:

$$\delta\tau = \frac{\delta}{c} \quad (2.101)$$

where c is the speed of light. The rate of change of the time delay with the θ_m can be obtained by the following approximation:

$$\frac{d\tau}{d\theta_m} = \lim_{\delta\theta_m \rightarrow 0} \frac{\delta\tau}{\delta\theta_m} \quad (2.102)$$

By multiplying and dividing Eq. (2.102) by $\delta\theta_m$, the rate of change of the time delay with respect to the angle θ_m can be obtained as:

$$\frac{d\tau}{d\theta_m} = \frac{m\lambda f L}{c \cos^2 \theta_m} \quad (2.103)$$

The temporal dispersion parameter measured along the normal direction of the Grating Surface D_{\perp} measures the time delay per unit wavelength and is given by:

$$D_{\perp} = \frac{1}{L} \frac{d\tau}{d\lambda} = \frac{1}{L} \frac{d\tau}{d\theta_m} \frac{d\theta_m}{d\lambda}, \quad (2.104)$$

which when considering $\frac{d\theta_m}{d\lambda}$ is the angular dispersion (Eq. (2.92)) gives:

$$D_{\perp} = \frac{m^2 \lambda f^2}{c \cos^3 \theta_m} \quad \text{in ps/nm.} \quad (2.105)$$

This parameter indicates that longer wavelengths experience greater delays compared to shorter wavelengths, resulting in temporal separation of different spectral components.

The Group Delay Dispersion (GDD) quantifies the dispersion of different frequency components in a pulse. To quantify the GDD of the grating pairs, recall that the phase $\phi(\omega)$ can be approximated by its Taylor Expansion:

$$\phi(\omega) = \phi(\omega_0) + \left. \frac{d\phi}{d\omega} \right|_{\omega_0} (\omega - \omega_0) + \frac{1}{2} \left. \frac{d^2\phi}{d\omega^2} \right|_{\omega_0} (\omega - \omega_0)^2 + \dots \quad (2.106)$$

where $\tau = \left. \frac{d\phi}{d\omega} \right|_{\omega_0}$ is the Time Delay / Group Delay and $\left. \frac{d^2\phi}{d\omega^2} \right|_{\omega_0}$ is the GDD. We can write the Temporal dispersion as a function of the GDD:

$$\begin{aligned} D_{\perp} &= \frac{1}{L} \frac{d\tau}{d\lambda} = \frac{1}{L} \frac{d}{d\lambda} \left(\frac{d\phi}{d\omega} \right) = -\frac{2\pi c}{L\lambda^2} \frac{d}{d\omega} \left(\frac{d\phi}{d\omega} \right) \\ D_{\perp} &= -\frac{2\pi c}{L\lambda^2} \frac{d^2\phi}{d\omega^2} = -\frac{2\pi c}{L\lambda^2} \frac{d^2\phi}{d\omega^2} \text{GDD}. \end{aligned} \quad (2.107)$$

Therefore the GDD is expressed as:

$$\begin{aligned} \text{GDD} &= -\frac{L\lambda^2}{2\pi c} D_{\perp} = -\frac{m^2\lambda^3 f^2 L}{2\pi c^2 \cos^3 \theta_m} \\ \text{GDD} &= -\frac{m^2\lambda^3 f^2}{2\pi c^2} NL \left[1 - (m\lambda f - \sin \theta_i)^2 \right]^{-\frac{3}{2}}. \end{aligned} \quad (2.108)$$

When we consider multiple passes of the grating pairs (N passes), the total GDD becomes:

$$\text{GDD} = -\frac{m^2\lambda^3 f^2}{2\pi c^2} NL \left[1 - (-m\lambda f - \sin \theta_i)^2 \right]^{\frac{3}{2}}. \quad (2.109)$$

Treacy Configuration Limitations

Eq. (2.109) clearly demonstrates an already known limitation of the Grating pairs in Treacy configuration: it produces a GDD that is inherently negative. This explains that the Treacy configuration can only provide negative dispersion, indicating that longer wavelengths (red) travel a longer path than shorter wavelengths (blue), resulting in pulse compression. For the main application, this is not a limitation since EOPM and XPM-based time lenses can be made with negative GDD. However, using a different configuration of grating pairs known as Martinez con-

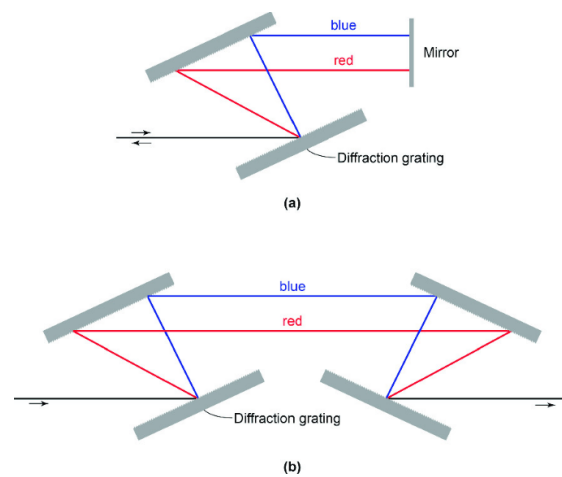


Figure 2.5: **Grating pairs in Treacy vs Martinez configuration.**

figuration [162] as in Fig 2.5b, one can produce both positive (for pulse stretcher) and negative (for pulse compressor) dispersion. This is achieved by incorporating additional optical elements (typically lenses or curved mirrors) between the gratings.

Feature	Treacy Configuration	Martinez Configuration
Dispersion Type	Negative only	Both positive and negative
Optical Elements	Gratings only	Gratings + focusing elements
Complexity	Simpler	More complex

Table 2.4: Comparison between Treacy and Martinez Configurations

2.2 Temporal cavity

In this subsection, we demonstrate the first implementation of a genuine temporal mode filter utilizing the first (to our knowledge) temporal cavity architecture [63]. A temporal cavity is obtained by using the time-frequency analogue of a spatial-mode cleaning cavity (Section 1.2.6, Fig. 2.1a), a cavity whose eigenvectors are Hermite-Gaussian transverse modes, with mode-dependent reflection and transmission coefficients (Eq. (3.2)). This effect is due to a mode-dependent spatial Gouy phase accumulated in a round trip.

Similarly, temporal cavities possess resonances generated by the combination of a cavity build-up effect and the temporal Gouy phase shift [65] and that are distinct with respect to the family of Hermite-Gaussian TMs (HGTM). Fundamentally different from other TM sorting approaches, we will show that temporal cavities not only behave as genuine filters but are also device-independent, in the sense that their operation is based only on the principles of temporal imaging and it does not depend on whether they are implemented by nonlinear processes or electro-optic phase modulators [148].

2.2.1 From mode cleaner cavity to temporal cavity

When a paraxial monochromatic beam impinges on a spatial-mode cleaner that is tuned on a particular transverse mode, its modal content at resonance with the cavity is transferred, while the not resonant modal content is reflected (Fig. 1.5). A typical design for a spatial-mode cleaner cavity consists of two flat partially reflecting mirrors (the input and output couplers) and one spherical perfectly reflecting mirror arranged in triangular geometry as in Fig. 2.1a. Since we have shown that the principle of space-time duality expresses a formal equivalence between the spatial and temporal degrees of freedom of optical beams and concluded that the dispersive propagation of a short pulse in the quasi-monochromatic approximation is the dual, in time domain, of the diffractive evolution of a paraxial monochromatic beam. As a consequence, the free space propagation in Fig. 2.1.a must be replaced by the propagation of a pulse in a dispersive medium. The flat mirrors do not have any special role apart from deflecting the trajectory of the optical beam without changing its shape.

These elements are kept in the time domain framework with no need for translation. On the contrary, the spherical mirror plays a major role in the emergence of mode-selective resonances.

Despite “time reflection” being a possible phenomenon [163], at the best of our knowledge there is no simple practical way of implementing a spherical mirror in the time domain. This issue can be resolved by observing that the ABCD matrix of a spherical mirror of radius of curvature R is formally similar to that of a thin lens of focal f whose dual, in time domain, is a

2.2. TEMPORAL CAVITY

time lens which, instead, can be easily implemented in experiments [148, 149, 164]:

$$M_{\text{mirror}} = \begin{pmatrix} 1 & 0 \\ -\frac{2}{R} & 1 \end{pmatrix}, \quad , M_{\text{thin lens}} = \begin{pmatrix} 1 & 0 \\ -\frac{1}{f} & 1 \end{pmatrix}. \quad (2.110)$$

The alternative scheme for a spatial-mode cleaner involves, thus, three flat mirrors (two partially reflecting, one perfectly reflecting) and one thin lens as represented in Fig. 2.1.b.

The temporal cavity is obtained as the equivalent of the alternative scheme and it is drawn in Fig. 2.1.c. The beam splitters, with real reflection and transmission coefficients r_1, t_1 and r_2, t_2 , implement the input and output couplers. The perfectly reflecting flat mirrors deflect the trajectory in order to create a loop. The dispersive elements are characterised by a total GDD D_1 and D_2 , respectively. Notice that, in principle, a scheme with only one dispersive element is also possible, but for reasons that will be clear later in this section, we consider two dispersive elements. The time lens is placed between the dispersive elements and it is characterised by a focal-GDD of D_f . The physical process used for its implementation is not important as far as it does not change the carrier of the pulse. Therefore, for this application, the best choice would be electro-optic modulators [65, 66, 67, 165, 69] or processes such as cross-phase modulation [166, 167].

The translation to the time domain is, finally, completed by considering the input beam. For mode-cleaners, this is a paraxial monochromatic beam while its dual, in time domain, is a quasi-monochromatic pulse. However, in order to get the typical build-up effect for resonant cavities, it is necessary that at the input coupler, the k -th pulse after one round-trip interferes with a new pulse, say the $(k + 1)$ -th, entering the cavity. As a consequence, a temporal cavity can be realized only when impinged by a train of pulses such that their repetition period T matches the round-trip time of the loop (or it is a sub-multiple of it):

$$T = \frac{L_{\text{loop}}}{c}, \quad (2.111)$$

where $L_{\text{loop}} = d_0 + d_1 + d_2$ is the cavity optical length, d_0 is the distance (in empty space) between the input and output couplers and d_i (for $i = 1, 2$) are the optical lengths of the two

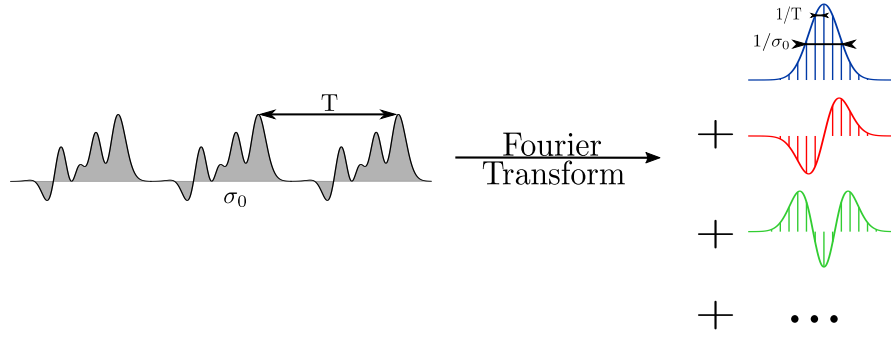


Figure 2.6: **Train of Pulse decomposition:** (left) A periodic train of pulses separated by period T with pulse duration σ_0 . (right) Its Fourier transform shows the frequency comb spectrum with spacing $1/T$ and spectral width $1/\sigma_0$. The spectrum can be decomposed into orthogonal Hermite-Gaussian (HG) frequency comb modes.

dispersive media. Such train of pulse is a frequency comb in the Fourier domain and can be decomposed into an orthogonal basis of HG frequency combs modes as in Fig. 2.6.

2.2.2 Eigenvalue and Eigenmode conditions

The cavity's behaviour is characterized by its ABCD matrix, as we did with the spatial mode cleaner. The ABCD matrix for a round trip is derived by sequentially multiplying the matrices of each component:

$$\begin{aligned}
 M_{\text{Loop}} &= \begin{pmatrix} 1 & D_2 \\ 0 & 1 \end{pmatrix} \begin{pmatrix} 1 & 0 \\ -\frac{1}{D_f} & 1 \end{pmatrix} \begin{pmatrix} 1 & D_1 \\ 0 & 1 \end{pmatrix} = \begin{pmatrix} 1 - \frac{D_2}{D_f} & D_1 \left(1 - \frac{D_2}{D_f}\right) + D_2 \\ -\frac{1}{D_f} & 1 - \frac{D_1}{D_f} \end{pmatrix} \\
 M_{\text{Loop}} &= \begin{pmatrix} A_{\text{Loop}} & B_{\text{Loop}} \\ C_{\text{Loop}} & D_{\text{Loop}} \end{pmatrix} = \begin{pmatrix} 1 - \frac{D_2}{D_f} & D_{\text{tot}} - \frac{D_1 D_2}{D_f} \\ -\frac{1}{D_f} & 1 - \frac{D_1}{D_f} \end{pmatrix}, \tag{2.112}
 \end{aligned}$$

where $D_{\text{loop}} = D_1 + D_2$ is the total GDD. For the cavity to be stable, using Eq. (1.109), the following conditions must be satisfied:

$$\begin{aligned}
 -2 &\leq 2 - \frac{(D_1 + D_2)}{D_f} \leq 2 \\
 0 &\leq |D_{\text{tot}}| \leq 4|D_f|, \tag{2.113}
 \end{aligned}$$

2.2. TEMPORAL CAVITY

where D_{tot} and D_f must have the same sign.

A second condition necessary for assuring an interference-based cavity build-up effect is that the duration and chirp of the circulating pulse at loop k matches that of the $(k + 1)$ -th incoming pulse at the input coupler. This is formally expressed by requiring that the temporal q -parameter remains unchanged after each round trip $q_{k+1} = q_k$ (say q). By using the ABCD formalism, this condition leads to the eigenvalue condition

$$q = \frac{A_{\text{loop}}q + B_{\text{loop}}}{C_{\text{loop}}q + D_{\text{loop}}} \quad (2.114)$$

We shown in Section 1.2.6 that solving Eq. (2.114) comes back to solving:

$$C_{\text{Loop}}q^2 + (D_{\text{Loop}} - A_{\text{Loop}})q - B_{\text{Loop}} = 0 \quad (2.115)$$

to get the eigenmodes of the temporal cavity. This leads to the quadratic equation:

$$\begin{aligned} -\frac{1}{D_f}q^2 + \left(\frac{D_2 - D_1}{D_f}\right)q - (D_1 + D_2) + \frac{D_1D_2}{D_f} &= 0 \\ q^2 - (D_2 - D_1)q + (D_1 + D_2)D_f - D_1D_2 &= 0 \end{aligned} \quad (2.116)$$

Calculating the discriminant:

$$\begin{aligned} \Delta &= (D_2 - D_1)^2 - 4D_f(D_1 + D_2) + 4D_1D_2 \\ \Delta &= (D_1 + D_2)^2 - 4D_f(D_1 + D_2) + 4D_1D_2 \\ \Delta &= D_{\text{tot}}^2 - 4D_fD_{\text{tot}} \leq 0. \end{aligned} \quad (2.117)$$

The roots of the quadratic equation expressed as:

$$q = \frac{D_2 - D_1}{2} \pm i\sqrt{D_{\text{tot}}\left(D_f - \frac{D_{\text{tot}}}{4}\right)} \quad (2.118)$$

defines the q -parameter that a train of pulses must have in order to be a cavity eigenvector or, conversely, it defines the parameters that the temporal cavity needs to have in order to sustain

the train of pulses with a given q -parameter. From Eq. (2.118), it is clear that with two dispersion elements it is possible to arrange the setup so that $\text{Re}[q] = 0$ when $D_1 = D_2$. This allows to consider the simpler situation of not chirped input pulses.

And using the definition of the temporal q parameters Eq. (2.17) and for a input pulse duration σ_0^2 , the input q parameter writes:

$$q_{\text{in}} = i\sigma_0^2, \quad (2.119)$$

yielding another condition from Eq. (2.118)

$$\sigma_0^4 = D_{\text{tot}} \left(D_f - \frac{D_{\text{tot}}}{4} \right). \quad (2.120)$$

This gives the constraints between the input pulse duration and GDD of the dispersive components and the time lens. In the case where we have only considered a single dispersive component D , the input pulse would have to always be chirped with a chirp value corresponding to D to be an eigenvector of the cavity.

2.2.3 Input-output relations

Equations (2.111) and (2.118) represent the two fundamental equations for the temporal cavity. When they are both satisfied, the input and output fields can thus be written as

$$\hat{A}_f(t, z) = \sum_{k=-\infty}^{+\infty} \sum_{m \in \mathbb{N}} \hat{a}_{f,m}^{(k)} u_m(t - kT, z), \quad (2.121)$$

where the indexes $f = \{\text{in1, r, in2, t}\}$ identify, respectively, the input and the reflected beams at the first coupler, the input and the transmitted beams at the second coupler (see Fig.2.7). The modal functions $u_m(t - kT, z)$ form a complete orthonormal set of Gauss-Hermite pulses that are non-zero in the interval $[(k - 1)T, kT]$. In the steady state regime, the quantum formalism simplifies significantly. Two doubts were raised when using this formalism

1. Do we lose the formalism by not sticking to the frequency comb formalism round trip by trip?

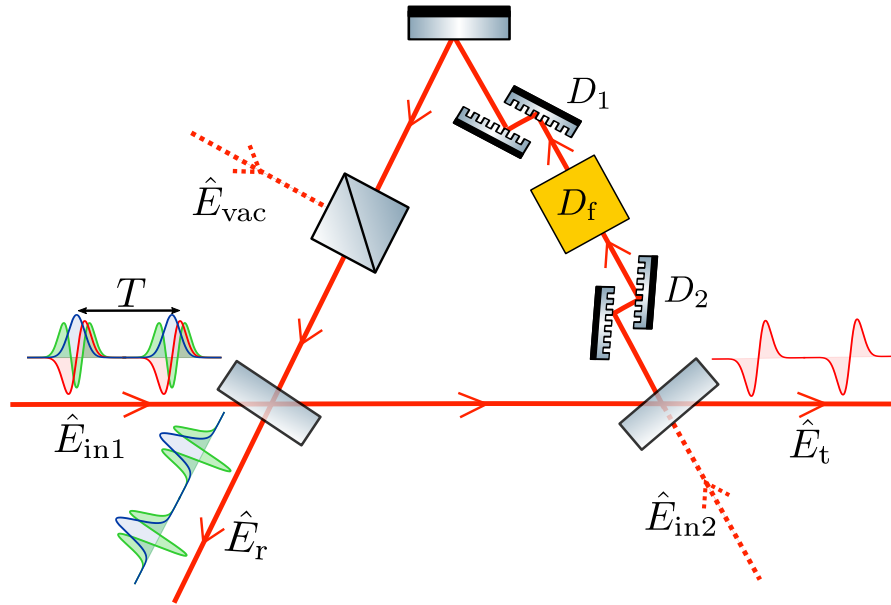


Figure 2.7: **Schematic of a temporal cavity** with two inputs \hat{E}_{in1} and \hat{E}_{in2} and two outputs \hat{E}_r and \hat{E}_t . The two couplers are characterized by real reflection and transmission coefficients r_1, r_2 and t_1, t_2 . A third coupler with reflection coefficient ρ models possible sources of losses during a round-trip. The two dispersive elements (two gratings in the picture) have equivalent GDD D_1 and D_2 . A time lens of focal GDD D_f is inserted between them. The multimode input, Eq. (2.121), is represented by the first three HGTM's (blue, red and green). Note that, the spatial mode of the beam remains the same through propagation in the temporal cavity.

2. The ABCD formalism being valid only in the delayed time reference frame, are we neglecting some phases during the propagation?

We deal with both concerns in Appendix A respectively and we show that, while more complex, they lead to the same conclusion. We consider a different rearrangement of the components of the temporal resonator in Fig. 2.9, that's formally equivalent to that of Fig. 2.7, with the advantage of allowing much easier tracking of the round-trip propagation.

In the steady state regime, for the k -round trip, the transformation between the annihilation operators is given by :

$$\begin{aligned}\hat{c}_m^{(k)} &= e^{i\delta_2} \hat{c}_m^{(k)}, \\ \hat{a}_m^{(k)} &= e^{i\delta_1} \hat{a}_m^{(k)}.\end{aligned}\tag{2.122}$$

with $e^{i\delta_1} \cdot e^{i\delta_2} = e^{i\delta_m}$, where the δ_2 correspond the propagation between the second coupler and

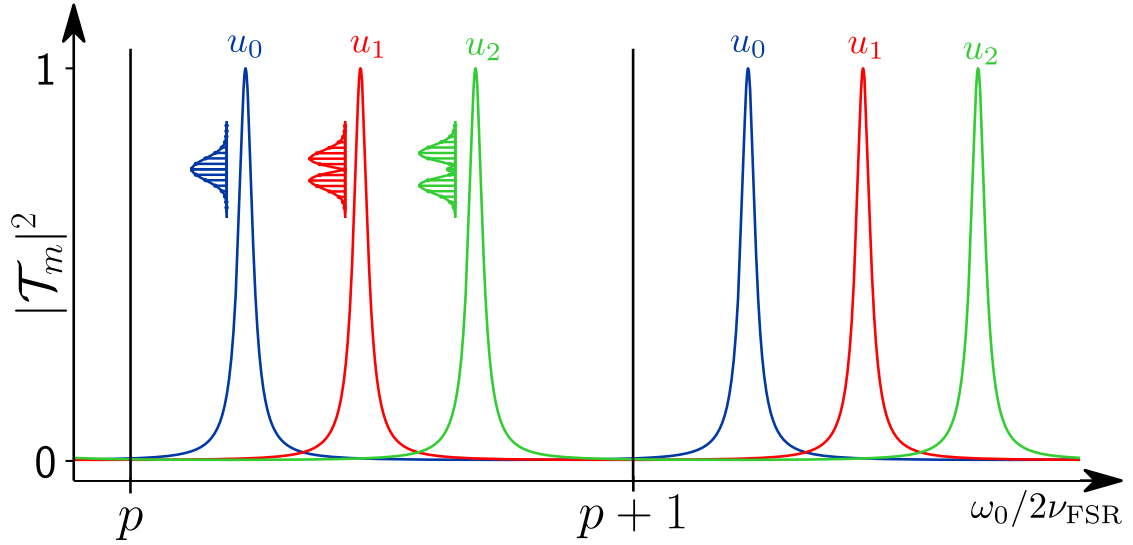


Figure 2.8: **Temporal cavity resonances:** Scheme of the resonances (2.137) of a temporal cavity. The integers p and m can be interpreted as the longitudinal and transverse orders of the resonance.

the fully reflective mirror (see Fig.2.7), while $\delta_1 = l_{\text{Loop}} - \delta_2$ and $\delta_m = k_0 L_{\text{loop}} - \psi_m$ is the phase accumulated during one loop.

In the steady state regime, the transformation of the annihilation operators through the couplers can be expressed as:

$$\begin{pmatrix} \hat{a}_{rm}^{(k)} \\ \hat{a}_m^{(k)} \end{pmatrix} = \begin{pmatrix} t_1 & r_1 \\ -r_1 & t_1 \end{pmatrix} \begin{pmatrix} \hat{c}_m^{\prime(k)} \\ \hat{a}_{in1}^{(k)} \end{pmatrix}$$

$$\begin{pmatrix} \hat{a}_{tm}^{(k)} \\ \hat{c}_m^{(k)} \end{pmatrix} = \begin{pmatrix} t_2 & r_2 \\ -r_2 & t_2 \end{pmatrix} \begin{pmatrix} \hat{a}_m^{\prime(k)} \\ \hat{a}_{in2}^{(k)} \end{pmatrix}. \quad (2.123)$$

Expanding these transformations and plugging Eqs. (2.122) lead to:

$$\hat{a}_m^{(k)} = t_1 \hat{a}_{in1}^{(k)} - r_1 \hat{c}_m^{\prime(k)} = t_1 \hat{a}_{in1}^{(k)} - r_1 \hat{c}_m^{(k)} e^{i\delta_2}$$

$$\hat{c}_m^{(k)} = -r_2 \hat{a}_m^{\prime(k)} + t_2 \hat{a}_{in2}^{(k)} = -r_2 \hat{a}_m^{(k)} e^{i\delta_1} + t_2 \hat{a}_{in2}^{(k)} \quad (2.124)$$

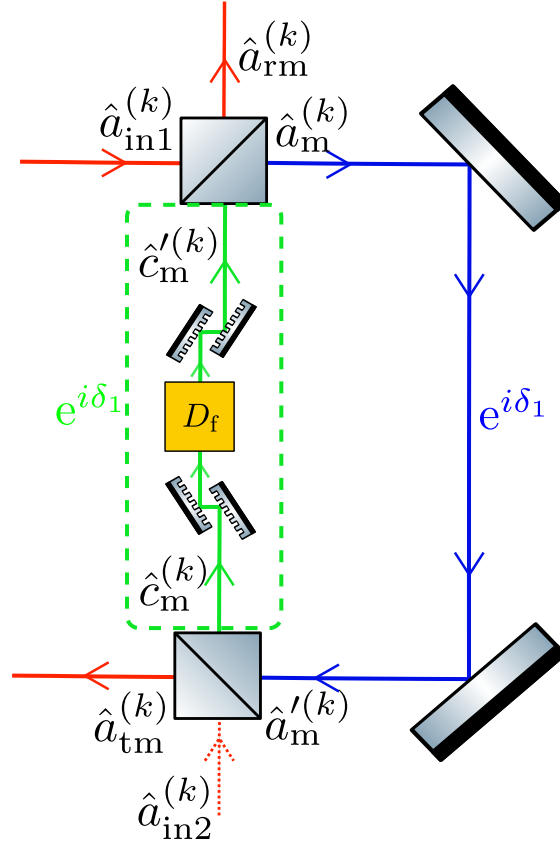


Figure 2.9: **Different schematic of a temporal cavity:** We use this configuration to calculate the input-output relations.

From Eqs. (2.124), we get the transformed operator $\hat{a}_m^{(k)}$ and $\hat{c}_m^{(k)}$:

$$\begin{aligned}\hat{a}_m^{(k)} &= t_1 \hat{a}_{in1}^{(k)} + r_1 r_2 \hat{a}_m^{(k)} e^{i\delta_m} - r_1 t_2 e^{i\delta_2} \hat{a}_{in2}^{(k)} \\ \hat{a}_m^{(k)} &= \frac{t_1}{1 - r_1 r_2 e^{i\delta_m}} \hat{a}_{in1}^{(k)} - \frac{r_1 t_2 e^{i\delta_2}}{1 - r_1 r_2 e^{i\delta_m}} \hat{a}_{in2}^{(k)}\end{aligned}\quad (2.125)$$

$$\begin{aligned}\hat{c}_m^{(k)} &= \frac{-r_2 t_1 e^{i\delta_1}}{1 - r_1 r_2 e^{i\delta_m}} \hat{a}_{in1}^{(k)} + \frac{r_1 r_2 t_2 e^{i\delta_m}}{1 - r_1 r_2 e^{i\delta_m}} \hat{a}_{in2}^{(k)} + t_2 \hat{a}_{in2}^{(k)} \\ \hat{c}_m^{(k)} &= \frac{-r_2 t_1 e^{i\delta_1}}{1 - r_1 r_2 e^{i\delta_m}} \hat{a}_{in1}^{(k)} + \frac{t_2}{1 - r_1 r_2 e^{i\delta_m}} a_{in2}^{(k)}\end{aligned}\quad (2.126)$$

2.2. TEMPORAL CAVITY

Further transformations yield expressions for transmitted and reflected operators \hat{a}_{rm} and \hat{a}_{tm} :

$$\begin{aligned}
 \hat{a}_{rm}^{(k)} &= r_1 \hat{a}_{in1}^{(k)} + t_1 c_m^{(k)} e^{i\delta_m} \\
 \hat{a}_{rm}^{(k)} &= \left(r_1 - \frac{r_2 t_1^2 e^{i\alpha}}{1 - r_1 r_2 e^{i\delta_m}} \right) \hat{a}_{in1}^{(k)} + \frac{t_1 t_2 e^{i\delta_m}}{1 - r_1 r_2 e^{i\delta_m}} \hat{a}_{in2}^{(k)} \\
 \hat{a}_{rm}^{(k)} &= \frac{r_1 - r_2 e^{i\delta_m}}{1 - r_1 r_2 e^{i\delta_m}} \hat{a}_{in1}^{(k)} + \frac{t_1 t_2 e^{i\delta_m}}{1 - r_1 r_2 e^{i\delta_m}} \hat{a}_{in2}^{(k)}
 \end{aligned} \tag{2.127}$$

$$\begin{aligned}
 \hat{a}_{tm}^{(k)} &= t_2 \hat{a}_m^{(k)} e^{i\delta_1} + r_2 \hat{a}_{in2}^{(k)} \\
 \hat{a}_{tm}^{(k)} &= \frac{t_1 t_2 e^{i\delta_1}}{1 - r_1 r_2 e^{i\delta_m}} \hat{a}_{in1}^{(k)} + \left(r_2 - \frac{r_1 t_2^2 e^{i\delta_m}}{1 - r_1 r_2 e^{i\delta_m}} \right) \hat{a}_{in2}^{(k)} \\
 \hat{a}_{tm}^{(k)} &= \frac{t_1 t_2 e^{i\delta_1}}{1 - r_1 r_2 e^{i\delta_m}} \hat{a}_{in1}^{(k)} + \frac{r_2 - r_1 e^{i\delta_m}}{1 - r_1 r_2 e^{i\delta_m}} \hat{a}_{in2}^{(k)}
 \end{aligned} \tag{2.128}$$

We finally obtain the mode-dependent input-output relation, which reads

$$\begin{pmatrix} \hat{a}_{t,m}^{(k)} \\ \hat{a}_{r,m}^{(k)} \end{pmatrix} = M \begin{pmatrix} \hat{a}_{in1,m}^{(k)} \\ \hat{a}_{in2,m}^{(k)} \end{pmatrix} \tag{2.129}$$

where

$$M = \begin{pmatrix} \mathcal{T}_m & -e^{i\delta_m} \mathcal{R}_m^* \\ \mathcal{R}_m & e^{i\delta_m} \mathcal{T}_m^* \end{pmatrix} \tag{2.130}$$

with $\mathcal{T}_m = \frac{t_1 t_2 e^{i\alpha}}{1 - r_1 r_2 e^{i\delta_m}}$ and $\mathcal{R}_m = \frac{r_1 - r_2 e^{i\delta_m}}{1 - r_1 r_2 e^{i\delta_m}}$. In these expressions, α is the phase accumulated by diffractive propagation from the input coupler to the output coupler. As a reminder, $\delta_m = k_0 L_{loop} - \psi_m$ is the phase accumulated during one loop, and it is the sum of two terms: the first is the phase of free space evolution along the full length of the loop L_{loop} and the second, $\psi_{Gouy} = -\text{Arg}[A_{loop} - iB_{loop}/\sigma_0^2]$, is the mode-dependent temporal Gouy phase accumulated during the propagation through the two dispersive media of total GDD $D_{tot} = D_1 + D_2$, with a time lens in between.

The Temporal Gouy phase can be more explicitly expressed in terms of the parameters of

2.2. TEMPORAL CAVITY

the cavity:

$$\begin{aligned} \frac{1}{A_{\text{Loop}} + \frac{B_{\text{Loop}}}{q_{\text{in}}}} &= \frac{1}{A_{\text{Loop}} + B_{\text{Loop}}C_{\text{in}} - \frac{B_{\text{Loop}}}{\sigma_{\text{in}}^2}} \\ &= \frac{A_{\text{Loop}} + B_{\text{Loop}}C_{\text{in}} + \frac{B_{\text{Loop}}}{\sigma_{\text{in}}^2}}{(A_{\text{Loop}} + B_{\text{Loop}}C_{\text{in}})^2 - \frac{B_{\text{Loop}}^2}{\sigma_{\text{in}}^4}} \end{aligned} \quad (2.131)$$

The Temporal Gouy phase corresponds to the argument of the complex expression (Eq. (1.106)):

$$\psi_{\text{out}} = \text{Arg} \left(\sqrt{\frac{1}{A_{\text{Loop}} + \frac{B_{\text{Loop}}}{q_{\text{in}}}}} \right) = \frac{1}{2} \arctan \left(\frac{B_{\text{Loop}}}{\sigma_{\text{in}}^2 (A_{\text{Loop}} + B_{\text{Loop}}C_{\text{in}})} \right) \quad (2.132)$$

For the temporal cavity, A_{Loop} and B_{Loop} are defined by Eq. (2.112) and considering an input pulse defined in Eq. (2.119), we can write:

$$\begin{aligned} \psi_{\text{Gouy}} &= \frac{1}{2} \arctan \left(\frac{D_{\text{f}}D_{\text{tot}} - D_1D_2}{\sigma_0^2(D_{\text{f}} - D_2)} \right) \\ \psi_{\text{Gouy}} &= \frac{1}{2} \arctan \left[\frac{D_{\text{tot}}}{2\sigma_0^2} \left(\frac{4D_{\text{f}} - D_{\text{tot}}}{2D_{\text{f}} - D_{\text{tot}}} \right) \right] \end{aligned} \quad (2.133)$$

The transformation in Eq. (2.130) is symplectic when M is unitary $M \cdot M^\dagger = I$. Since t_i and r_i are chosen real and $t_i^2 + r_i^2 = 1$ (for $i = 1, 2$), one can easily prove that M is a unitary matrix, so that the boson commutation relations for the output field operators are respected.

The temporal cavity effect becomes evident by considering the transmittance coefficient

$$|\mathcal{T}_m|^2 = \frac{\mathcal{T}_{\text{max}}}{1 + \left(\frac{2\mathcal{F}}{\pi}\right)^2 \sin^2 \left(\frac{\omega_0}{2\nu_{\text{FSR}}} - \frac{\psi_m}{2} \right)}, \quad (2.134)$$

where the maximum transmittance \mathcal{T}_{max} , the Finesse \mathcal{F} and the Free Spectral Range ν_{FSR} of the cavity are defined as:

$$\begin{aligned} \mathcal{T}_{\text{max}} &= \frac{t_1^2 t_2^2}{1 - r_1^2 r_2^2} \\ \mathcal{F} &= \frac{\pi \sqrt{r_1 r_2}}{1 - r_1 r_2} \\ \nu_{\text{FSR}} &= \frac{c}{L_{\text{Loop}}} \end{aligned} \quad (2.135)$$

2.2. TEMPORAL CAVITY

Let us finally find the resonant frequencies $\omega_{(p,m)}$:

$$|\mathcal{T}_m|^2 = \mathcal{T}_{\max} \iff \sin^2 \left(\frac{\omega_0}{2\nu_{\text{FSR}}} - \frac{\psi_m}{2} \right) = 0. \quad (2.136)$$

Therefore mode-dependent resonances are found at:

$$\omega_{(p,m)} = (2\pi p + \psi_m)\nu_{\text{FSR}}, \quad (2.137)$$

with $p \in \mathbb{Z}$. In close analogy with the spatial case, these resonances are characterized by the two integers p and m that can be interpreted as the temporal equivalent of the longitudinal and transverse order of a resonance. First considerations for the temporal cavity were initially for a full-fibered experimental design. In that case, $D_{\text{tot}} = \beta_2 L_{\text{Loop}}$ and Eq. (2.111) can be rewritten as:

$$T = \frac{\beta_1}{\beta_2} D_{\text{tot}} \quad (2.138)$$

where β_1 and β_2 represent the first and second-order dispersion parameters of the fiber, respectively.

This equation reveals a critical dependence between the choice of T and D_{tot} . As we will demonstrate later, D_{tot} is subject to additional constraints, which in turn put the burden on choosing an appropriate fiber, where the flexibility in the ratio between β_1 and β_2 is limited.

In order to decouple T from D_{tot} , a partially fibered design with fibers serving as local dispersive components can be considered. However, this approach suffers from high insertion losses at the free space-to-fiber interfaces. While these configurations are feasible regardless of constraints, we opt for a fully free-space design to maximize flexibility and potentially minimize insertion losses. Furthermore, dispersive components such as diffraction gratings for free-space applications are readily available in the market.

2.2.4 Application of temporal cavities in communication protocols

The mode-dependent resonances of a temporal cavity can be employed for filtering multimode frequency combs. Consider a configuration where a multimode input frequency comb is sent through the first coupler (port “in1”) while keeping the second input (port “in2”) in a vacuum state. Since M is unitary and $|\mathcal{T}_m|^2 + |\mathcal{R}_m|^2 = 1$, tuning the cavity on the suitable resonance (p, m) allows for complete transmission ($|\mathcal{T}_m|^2 = 1$ and $|\mathcal{R}_m|^2 = 0$) of the mode “ m ” in the output \hat{E}_t . As far as the other resonances do not overlap with the one corresponding to (p, m) , the modes $m' \neq m$ are reflected at the first coupler, in the mode \hat{E}_r , with $|\mathcal{T}_{m'}|^2 = 0$ and $|\mathcal{R}_{m'}|^2 = 1$. Therefore, this configuration enables the genuine filtering or demultiplexing of mode m without altering either the carrier frequency or the modal shape of the TM. For a partially transmitted mode, a non-zero coefficient \mathcal{R}_m mixes the mode’s quantum state with the vacuum entering through “in2.”

A different configuration can multiplex frequency combs of different orders. For simplicity, consider only two modes and suppose that the mode m is sent through the port “in1”, while the mode $m' \neq m$ enters the cavity through the port “in2”. When the cavity is tuned on the m -th resonance, the mode m is completely transmitted while the mode m' is reflected at the second coupler. They are now joined in the output mode \hat{E}_t .

A key application of temporal cavities lies in quantum communication, where quantum information must be encoded by a sender (Alice) and transmitted to a receiver (Bob) over distant locations. Frequency comb temporal modes provide an attractive avenue for encoding and transmitting such quantum information. By utilizing different temporal modes as distinct communication channels through temporal mode multiplexing, multiple channels can be combined onto a single transmission line. This multiplexing approach differs fundamentally from conventional time or frequency multiplexing schemes. Rather than separating channels by non-overlapping time windows or spectral slices, the intrinsically field-orthogonal nature of the temporal modes enables dense packing of channels in time-frequency space while maintaining negligible crosstalk between modes.

Figure 2.10 illustrates a possible application where four TMs are used for encoding in different communication channels. At the sender’s location, Alice can employ a series of temporal

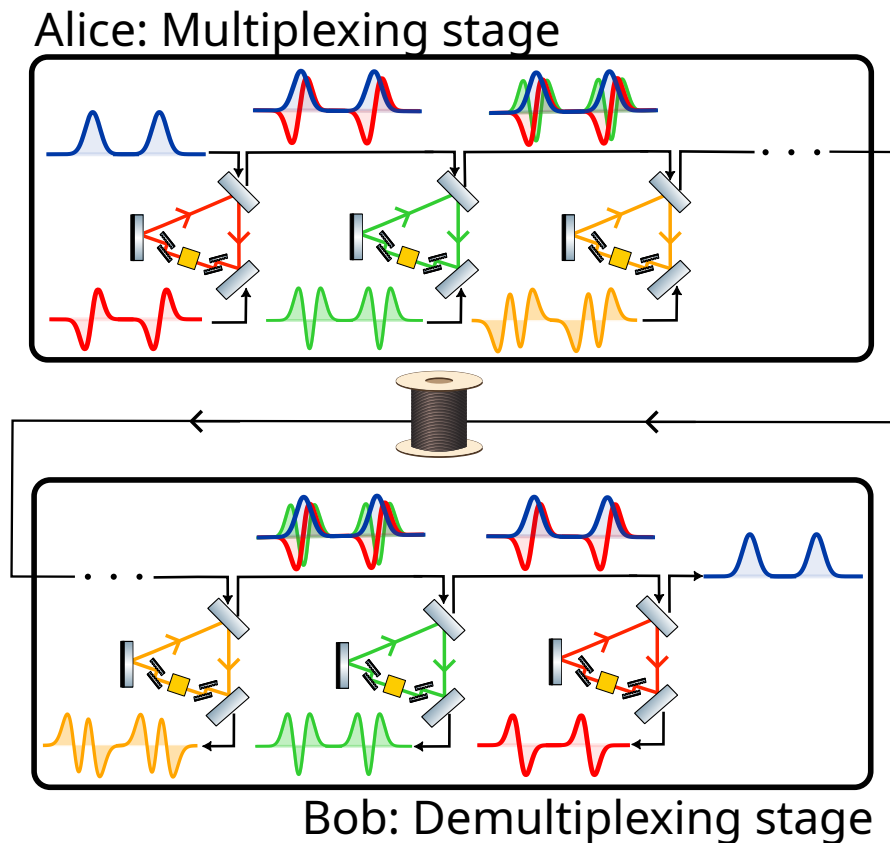


Figure 2.10: **Temporal cavities for quantum communication:** Multiplexing/demultiplexing scheme for communication between two parties, Alice and Bob, using orthogonal TMs as independent channels. Alice's multiplexing stage (*top*) utilizes a succession of temporal cavities to combine different TM channels into a single communication line, which is sent to Bob through one single physical fiber. Bob's demultiplexing stage (*bottom*) employs a series of temporal cavities to demultiplex the channels, allowing him to independently read out the information from each original TM channel.

cavities to multiplex different quantum channels, each encoded in a particular temporal mode, onto the communication line. After transmission, Bob can then implement a cascaded sequence of temporal cavities to demultiplex the received signal, separating the individual modal channels onto distinct output ports for subsequent readout of the encoded quantum information. Compared to alternative multiplexing techniques, this temporal mode approach leverages the mathematical orthogonality of the modes to maximize the channel density and transmission fidelity. Temporal cavities provide a powerful tool to robustly multiplex and demultiplex these modal channels, enabling high-dimensional quantum communication over optical networks while main-

taining the original modal shapes and carrier frequencies.

Before we examine the main application of the temporal cavity, one may wonder what the figures of merit of the cavity are. For that, we have to first account for the intrinsic losses of the cavity and settle on some characterization parameters.

2.2.5 Cavity Characterisation: Figures of merit

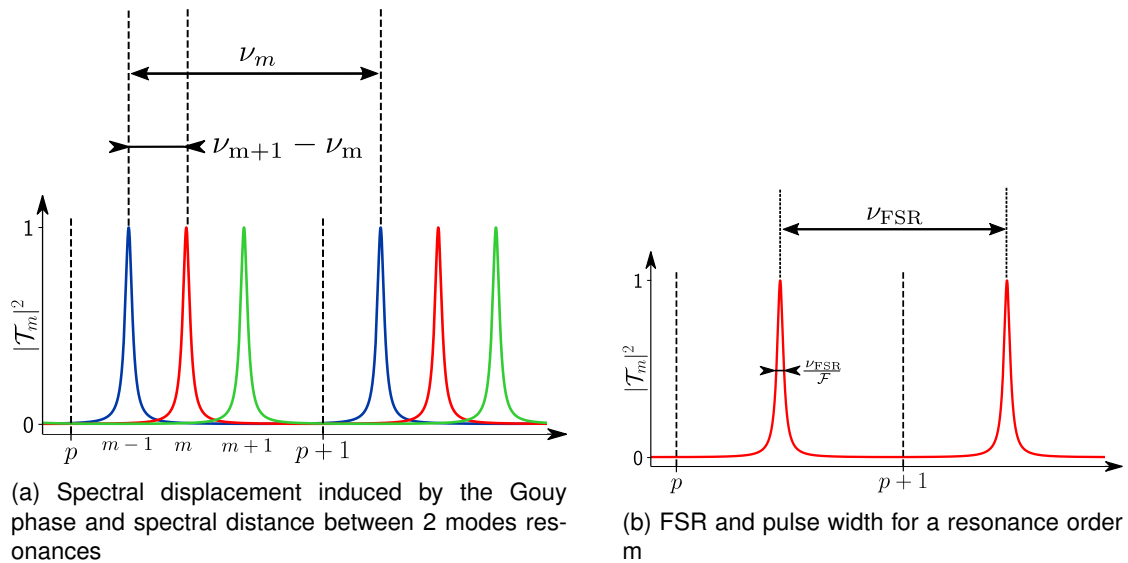


Figure 2.11: **Characterisation of the temporal cavity resonances**

One of the figures of merit of the cavity is N which accounts for the number of modes that can be discriminated. More explicitly, N accounts for the number of resonances that fit in one cavity FSR. For that, recall that the temporal cavity can discriminate between different HG modes because the cavity resonances present distinct temporal Gouy phase ψ_m shifts with respect to the family of HG TMs. Therefore to evaluate the spectral displacement of a resonance of order $m + 1$ with regard to the resonance of order m , we need to evaluate the spectral displacement induced by the ψ_m .

Because of the presence of the Gouy phase in the transmission coefficient, the spectral displacement for every mode will be a function of the mode order m . Considering that for a round trip (2π), the total spectral displacement phase is known as the FSR ν_{FSR} , the spectral

displacement ν_m (Fig. 2.11a) induced by the Gouy phase alone for one round trip is:

$$\nu_m = \frac{\psi_m}{2\pi} \nu_F = \frac{m + 1/2}{2\pi} \nu_F \psi_{\text{Gouy}}, \quad (2.139)$$

where ψ_{Gouy} is defined as in Eq. (2.133). ν_m basically quantifies the spectral distance between resonances of order 0 and m .

We introduced the spectral distance between 2 consecutive resonance orders $\Delta = |\nu_{m+1} - \nu_m|$ and using Eq. (2.139), we find

$$\Delta = \frac{\nu_F}{2\pi} |\psi_{\text{Gouy}}|, \quad (2.140)$$

which doesn't depend on the order m of the HG modes. We might think, looking at this parameter, that a bigger Δ means less overlap between the transmission coefficient of different modes. One could be tempted to attempt to increase ν_F to increase Δ . But two problems come to mind:

1. The FSR is fixed by the input train of pulses repetition rate Eq. (2.111).
2. Increase ν_F would also increase in a similar order of magnitude the width of each resonance $\frac{\nu_F}{\mathcal{F}}$ (Fig. 2.11b), therefore making such an increase almost irrelevant for mode separation. It will essentially just scale up the resonances. So increasing D requires increasing ψ_{Gouy} instead.

Using Eq. (2.139), we can rewrite the transmission coefficient as

$$T = \frac{T_{max}}{1 + \left(\frac{2\mathcal{F}}{\pi}\right)^2 \sin^2\left(\frac{\pi(\nu - \nu_m)}{\nu_F}\right)}. \quad (2.141)$$

As we can see, it is very similar to the transmission coefficient of a Fabry-Perot cavity, with the exception of the peaks happening at different frequencies $\nu - \nu_m$. That allows us to confirm, as predicted, that the value of the frequency spacing or FSR is ν_F and each peak width will be characterised by ν_f/\mathcal{F} (Fig. 2.11b). This confirms that a better separation between modes involves a higher finesse, which can be achieved according to Eq. (2.135) by having high reflection coefficients for the couplers.

2.2. TEMPORAL CAVITY

To evaluate the number of modes we can separate N , we can use the following expression:

$$N = \frac{\nu_F}{\Delta} = \frac{2\pi}{|\psi_{\text{Gouy}}|}. \quad (2.142)$$

Note that this definition is only fitting when the number of modes is approximately an integer. When N is not an integer, we can theoretically separate an extra mode depending on the values of its decimal part and the finesse.

Based on Eq. (2.133), the values of D_{tot} and D_f play crucial roles in determining ψ_{Gouy} . Considering that both parameters share the same sign and satisfy the stability condition $|D_{\text{tot}}| \leq 4|D_f|$, increasing $|D_{\text{tot}}|$ leads to a larger argument within the arctangent function, thereby increasing $|\psi_{\text{Gouy}}|$, so reducing N . On the other hand, if $|D_f|$ is increased while keeping D_{tot} constant, the ratio $\frac{4D_f - D_{\text{tot}}}{2D_f - D_{\text{tot}}}$ decreases, which reduces the overall argument of the arctangent function and consequently decreases $|\psi_{\text{Gouy}}|$ and increasing N . This inverse relationship ensures that within the specified magnitude constraints, D_{tot} serves to amplify ψ_{Gouy} , whereas D_f acts to diminish it. However, at fixed input pulse duration σ_0 , Eq. (2.120) defines the constraining relation between D_{tot} and D_f . So they can't be tuned independently. Say we consider D_{tot} as the free parameter for the choice of N ; it still requires a good balance between higher dispersion meaning better separation (high value of $|D_{\text{tot}}|$) and a high value of N (low value of $|D_{\text{tot}}|$ so lower dispersion).

In the worst-case scenario, it's easy to see that $N \rightarrow 2$, which means at worst we will be able to separate two modes with the appropriate choice parameters.

While N tells us the number of modes that can be discriminated, it does not tell us how well these modes are discriminated. And we introduced a distinguishability parameter δ , taking inspiration from the Rayleigh criteria for spatial or angular separation.

The metric represents a measure of distinguishability between resonant modes. The distinguishability parameter δ , defined as the ratio of peak separation Δ to their FWHM, directly indicates how well-resolved modes are in units of peak width. Using Eq. (2.139) and Fig. 2.11b, one can give a formula for this parameter:

$$\delta \propto \frac{|\psi_{\text{Gouy}}| \mathcal{F}}{2\pi}. \quad (2.143)$$

Through empirical analysis of simulation results, we arbitrarily chose $\delta = 1.5$ as a threshold, where values below this limit indicate insufficient separation for the effective implementation of temporal cavities. A larger δ value indicates better mode separation, which can be achieved either through Eq. (2.143) by increasing the Gouy phase shift (affecting mode spacing) and/or by improving the cavity finesse (reducing peak width) Fig. 2.11b. We showed previously that increasing the temporal Gouy requires careful consideration as it reduces N (Eq. (2.142)). When it comes to the Finesse, theoretically, we could increase it to very high values by increasing the reflectivity of the beam splitters. However, we show in the next subsection that this increase comes at the cost of efficiency. Both approaches, as discussed, require careful optimization, as they can impact other cavity parameters - the Gouy phase affects mode degeneracy and stability while increasing finesse typically involves trade-offs with cavity losses and throughput.

2.2.6 Intrinsic Losses and Compromises

The development we have done in this section until now didn't account for the unavoidable round-trip losses. These losses account for propagation losses, coupling losses, insertion losses, and inefficient components like beamsplitters and time lenses. These losses can be modelled as a non-zero reflectance \mathcal{P} of an additional beam splitter, as depicted in Fig. (2.7).

The goal is to do the transmission of the cavity similarly to the lengthy development we did in Subsection 2.2.3. To get to the result faster, we will, without loss of generality, instead take here a classical approach.

Before propagating the chirpless input complex amplitude of an HG pulse $A_{m,\text{in}}(t, z)$, the complex amplitude through the first amplitude

$$t_1 A_{m,\text{in}}(t, 0) = t_1 A_{m,\text{in}} G_m \left(\frac{t}{\tau_0} \right) \quad (2.144)$$

Assuming the conditions outlined in Eq. (2.111) are satisfied for the cavity, the pulse retains the

2.2. TEMPORAL CAVITY

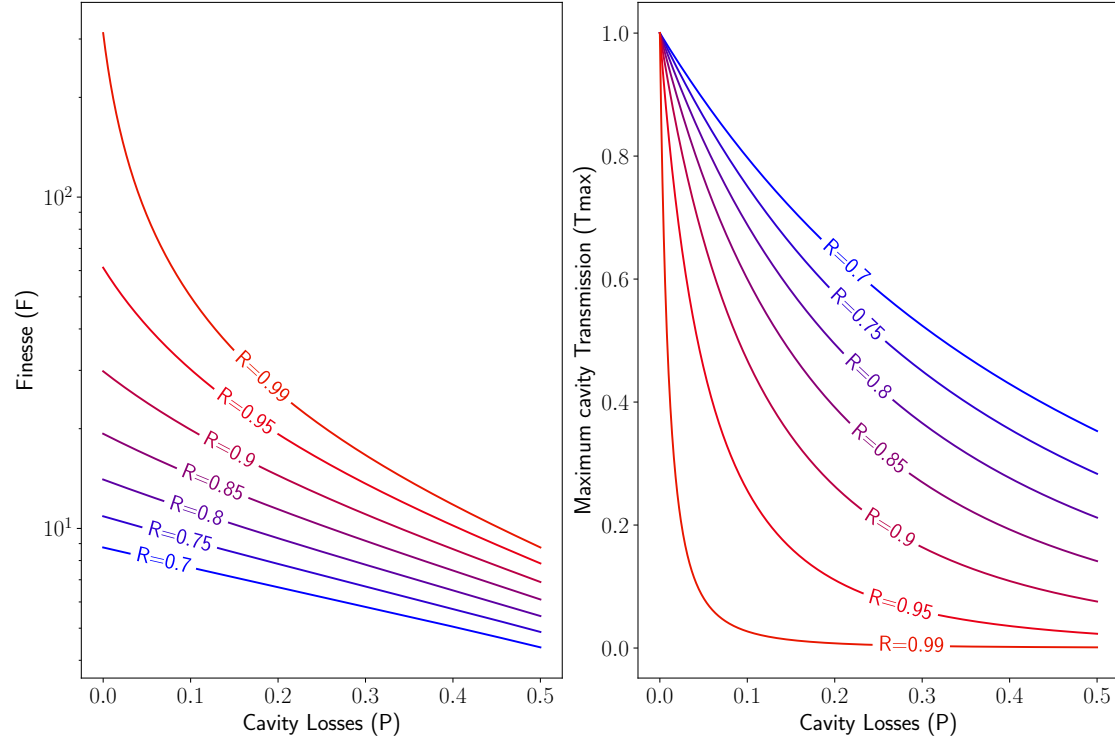


Figure 2.12: **Temporal cavities with losses:** (Left) Evolution of the maximal transmittance T_{\max} Eq. (2.148) and (right) the finesse \mathcal{F} (Eq. (2.149)) for different values of the reflectance of the beamsplitters R .

form of Eq. (2.144) after each round trip. During each round trip, the pulse acquires additional transmission and reflection factors from the beam splitters and a phase shift induced by propagation in free space and within the grating pairs and the time lens. Specifically, in a single round trip, we are reminded that the temporal Gouy phase accumulates to $\psi_m = (\frac{1}{2} + m)\psi_{\text{Gouy}}$. - The total phase accumulated is $\delta_m = k_0 L_{\text{loop}} - \psi_m$.

After n round trips, the complex amplitude of a pulse evolution can be simply written as:

$$A_m(t, z) = t_1(\rho r_1 r_2)^n A_{m,\text{in}} G_m \left(\frac{t}{\tau_0} \right) e^{i\delta_m} \quad (2.145)$$

Due to the pulse train structure, each round trip causes the pulse to interfere with all previously propagating pulses. Summing over all round trips, the total amplitude of the pulse inside the

cavity is given by the geometric series:

$$A_{\text{out}}(t, z) = \sum_{n=0}^{\infty} A_n(t, z) = \frac{t_1}{1 - \rho r_1 r_2 e^{\delta_m}} A_{m, \text{in}}(t, 0). \quad (2.146)$$

To obtain the complex amplitude of the output pulse, it propagates to the second beam splitter. The transmission through this beam splitter introduces an additional transmission coefficient t_2 and a phase factor. However, since we evaluate the transmission coefficient in terms of intensity rather than complex amplitude, the phase factor does not affect the final expression.

The transmission of the cavity, therefore, has the same form as in Eq. (2.134), but the finesse and the maximal transmittance are now

$$\begin{aligned} \mathcal{F} &= \frac{\pi \sqrt{\rho r_1 r_2}}{1 - \rho r_1 r_2} \\ \mathcal{T}_{\text{max}} &= \frac{(t_1 t_2)^2}{1 - \rho r_1 r_2} \end{aligned} \quad (2.147)$$

respectively, with $\rho^2 = 1 - \mathcal{P}$.

Considering $\mathcal{R} = r_1^2 = r_2^2$ the reflectivity of the input and output couplers, which can be adjusted to achieve the desired level of finesse and maximal transmittance, we can rewrite Eq. (2.147) as:

$$\mathcal{T}_{\text{max}} = \frac{(1 - \mathcal{R})^2}{(1 - \mathcal{R} \sqrt{1 - \mathcal{P}})^2}, \quad (2.148)$$

$$\mathcal{F} = \frac{\pi \sqrt{\mathcal{R} \sqrt{1 - \mathcal{P}}}}{1 - \mathcal{R} \sqrt{1 - \mathcal{P}}}. \quad (2.149)$$

For better mode selectivity for temporal mode filters, a higher value of the finesse is desirable for achieving better separation between the mode-dependent resonances. However, a high finesse leads to a longer photon lifetime in the cavity that induces an increased sensitivity of the maximal transmittance to the cavity losses.

This trade-off is illustrated in Fig. 2.12. In the left panel, for a given value of losses \mathcal{P} , the finesse can be increased (reduced) by increasing (reducing) the reflectivity \mathcal{R} of the input-output couplers. On the contrary, on the right, an increase of the reflectivity \mathcal{R} leads to a decrease of \mathcal{T}_{max} . As losses increase, the value of \mathcal{T}_{max} decreases accordingly, and this effect is more

pronounced for higher values of \mathcal{R} , as seen from the steeper drop in \mathcal{T}_{\max} observed at these higher reflectivities.

As a result, the choice of reflectivity for the beamsplitters must balance out the desire for a high finesse and therefore longer photon lifetime with the need for a high maximal transmittance and therefore greater efficiency. This results in a trade-off between the two quantities that must be carefully considered when designing temporal mode filters through temporal cavities.

For classical applications, where pulse amplification is possible, the value of \mathcal{T}_{\max} is generally not critical. In such cases, the choice of \mathcal{R} should prioritize a high degree of finesse, as it corresponds to better separation between cavity modes. However, in quantum applications, the sensitivity of \mathcal{T}_{\max} to losses becomes a much more important consideration since it determines the efficiency of the filtered mode. Thus, the choice of \mathcal{R} for such applications needs to ensure maximizing the efficiency of the cavity while maintaining a sufficient level of finesse. That will depend on the overall losses in the cavity.

2.2.7 Parameter choice

Eqs. (2.111), (2.118), (2.137) are the three fundamental equations of the temporal cavity from which the choice of the parameters L_{loop} , D_{tot} and D_{f} must be done.

As an example, let us consider an input multimode frequency comb described by Eqs (2.1) and (2.4) with carrier ω_0 , repetition rate T , and a given q -parameter. Injecting these values in Eqs. (2.111), (2.118) and (2.137) produces three constraints on the cavity parameters L_{loop} , D_{f} , and D_{tot} . As a result, for a given input, there is no free parameter for the cavity. For all examples, we will present, we choose to input a train of $\sigma_0 = 5$ ps pulses of carrier $\lambda_0 = 800$ nm and repetition rate 80 Mhz (Fig. 2.6). Since the repetition rate must match the FSR of the cavity, from Eq. (2.111) we get $L_{\text{loop}} = 3.74$ m.

Since L_{loop} and the cavity free spectral range ν_{FSR} are blocked, via Eq. (2.111), by the train repetition rate, the remaining parameters can be controlled to induce the resonance condition for the m -th TM and at the same time to match the input q -parameter. This is an important difference with respect to the spatial-mode cleaner where there is one free parameter, for example, its length, that can be used to tune the cavity on a particular resonance. This circumstance does

not prevent selecting specific TMs by tuning the temporal cavity to a particular resonance, but it certainly makes the operation more challenging. We finally point out that it is possible to free one additional parameter by allowing control of the carrier frequency ω_0 , the period T , or the temporal q -parameter of the input. As for how we choose parameters in this thesis, we always assume the input parameter is fixed and given as a constraint similar to a realistic experimental setup.

2.2.8 Experimental feasibility

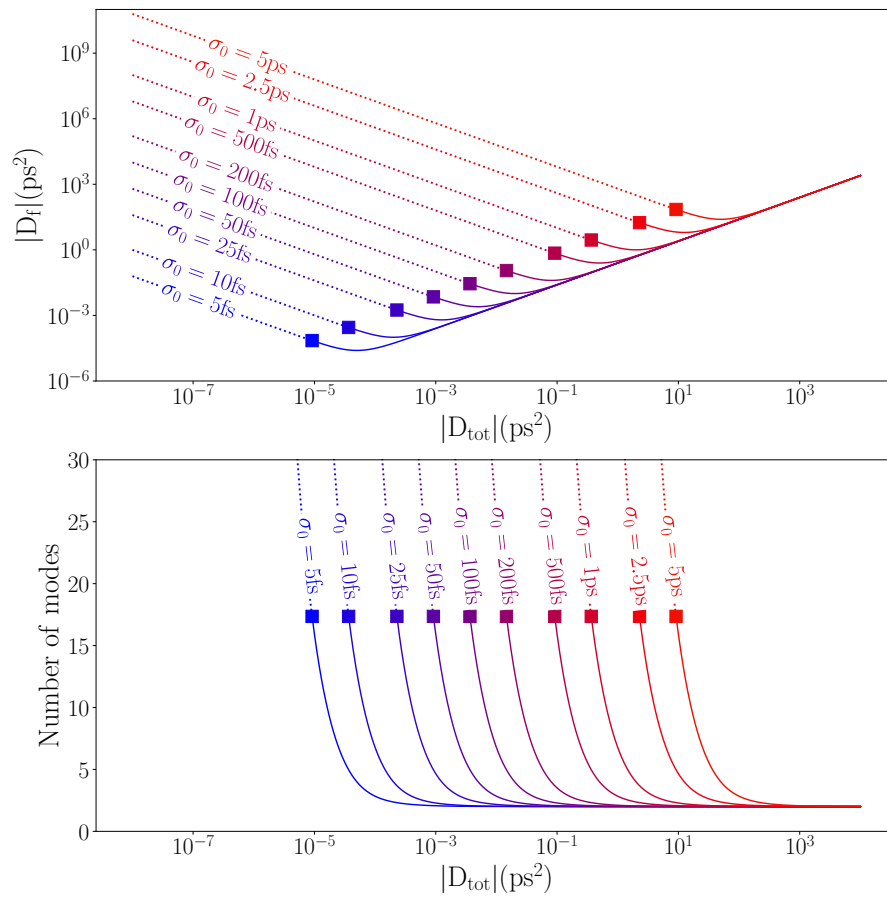


Figure 2.13: **Constraints on low loss:** (*Top*) diagram of the relation Eq. (2.118). (*Bottom*) number of modes fitting one cavity FSR. Full squares correspond to $\mathcal{T}_{\max} = 0.77$, $\mathcal{F} = 26$, $\mathcal{P} = 3\%$. At these points, the distance between neighbour resonances is about 1.5 times their linewidth. On the left (dotted line) the distance is smaller and the two resonances are not resolved.

2.2. TEMPORAL CAVITY

The shortest focal lengths experimentally available to date for efficient electro-optic time lenses we have seen in Subsection 2.1.5 are about 10 ps^2 [148, 164]. Figs. 2.13-top and 2.17-top depicts the relation Eq. (2.118) constraining the values of D_f and D_{tot} for a wide range (from 5 fs to 1 ps) of the pulse duration σ_0 of the input train. Because of the “V” shape of these curves, it would always be possible to find a suitable D_{tot} for the experimentally available D_f . We note that these values of dispersion are easily achievable [164, 148] through for example grating pairs described in Subsection 2.1.5. However, as previously discussed, some compromise needs to be made and three factors limit the choice of D_{tot} : the number $N = 2\pi/\psi_{\text{Gouy}}$ of resonances that fit in one cavity FSR, the cavity finesse \mathcal{F} and the round-trip losses \mathcal{P} . Indeed, two different modes $0 \leq m \leq N$ and $m' > N$ cannot be discriminated when a resonance of order (p', m') overlaps with the resonance (p, m) (see Fig. 2.8). As in Figs. 2.13-bottom and 2.17-bottom, shows, N rapidly increases when D_{tot} decreases. In this case, the separation ψ_{Gouy} between consecutive resonances of the same longitudinal order p might become smaller than their line-width $\nu_{\text{FSR}}/\mathcal{F}$. Therefore one should seek high values of finesse. On the other side, competing behaviour appears when the unavoidable round-trip losses are kept into account. As we have shown previously, the higher the \mathcal{F} , the higher the photon lifetime in the cavity and the sensitivity of \mathcal{T}_{max} to losses. This can rapidly become much smaller than 1 with \mathcal{P} increasing. Therefore a compromise should be sought between N and \mathcal{F} for a given value of losses. In Figs. 2.13, we show an example with low losses. In particular, full squares mark the optimal configurations when $\mathcal{P} = 3\%$ and $\mathcal{F} = 26$ with $R = 0.9$. Here $\delta = 1.5$, meaning the resonances are resolved with a relative distance of 1.5 times their linewidth. It corresponds GDD values of $D_f = 28.22\text{ps}^2$ and $D_{\text{tot}} = 30.26\text{ps}^2$ $\mathcal{T}_{\text{max}} = 0.77$ is high enough to guarantee a good efficiency in sorting multimode quantum frequency combs. We show the transmittivity of the cavity configuration (Eq; (2.134) in Figs. 2.14, showing we can separate $N = 17$ modes with decent resolution. On the left of these squares (dotted line), while the N is increasing because $|D_{\text{tot}}|$ is decreasing while D_f is increasing, δ is decreasing, therefore the resonances are not sufficiently resolved because ψ_{Gouy} is decreasing. Overlaps between the resonances are getting worse than in Figs. 2.14. As we move to the right side, δ is increasing, resonances are better and better separated than what's observed in Figs. 2.14. However, the value of N decreases and approaches the limit value of 2 (Fig. 2.13-bottom).

2.2. TEMPORAL CAVITY

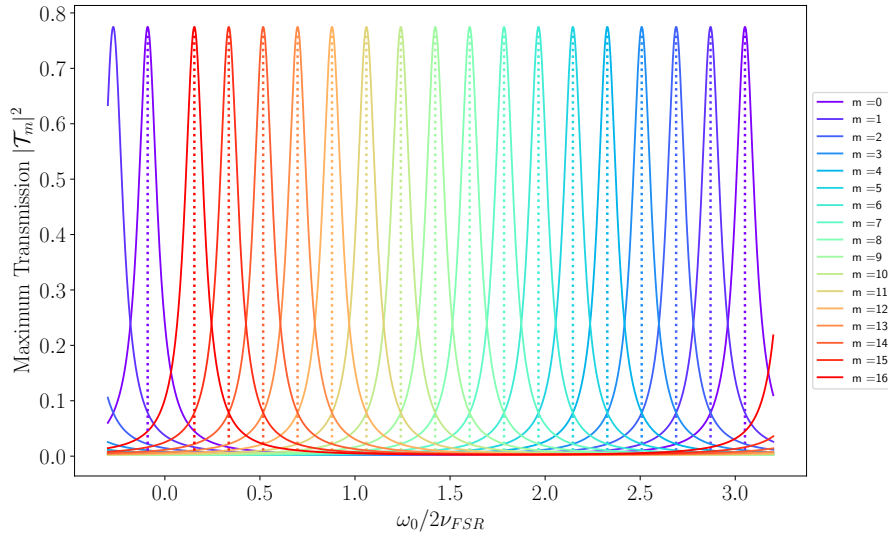


Figure 2.14: **Resonances at square:** Resonances of a temporal cavity with parameters corresponding to the point in square in Fig 2.13 for an input pulse duration of $\sigma_0 = 5$ ps

Cascaded Mode Selection in Temporal Cavities

For temporal cavities, the value of N limits the number of modes that can be handled by the cavity. When more modes are sent, the periodicity of the cavity will make k group of modes where each group with the following pattern $k + Nm$ where $m = 0, 1, 2, \dots$ will overlap. This overlap is always detrimental for mode selection and the degree of overlap entirely depends on the decimal part of N . The smaller this decimal part, the smaller this overlap, until resonances of modes inside these groups are completely undistinguishable where N is an integer. With a finite mode handling capability N , selective mode filtering remains still possible even when the total number of input modes exceeds N , provided N is an integer. This can be achieved through a cascaded arrangement of temporal cavities. The first stage groups the input modes into N distinct sets, where each group k ($k = 0, 1, \dots, N - 1$) contains modes following the pattern $k + N \times m$ (where $m = 0, 1, 2, \dots$). For instance, in Fig 2.15, we show a temporal cavity configuration where $R = 0.85$, $P = 5\%$, $D_f = 32$ ps² and $D_{tot} = 24$ ps². While for this cavity, $N = 7$, we input a train of pulses where each pulse can be decomposed into a basis of 21 HG modes. In this group, each peak of transmission in Fig 2.15 corresponds to a group of 3 modes whose transmissions are indistinguishable. The grouping is :

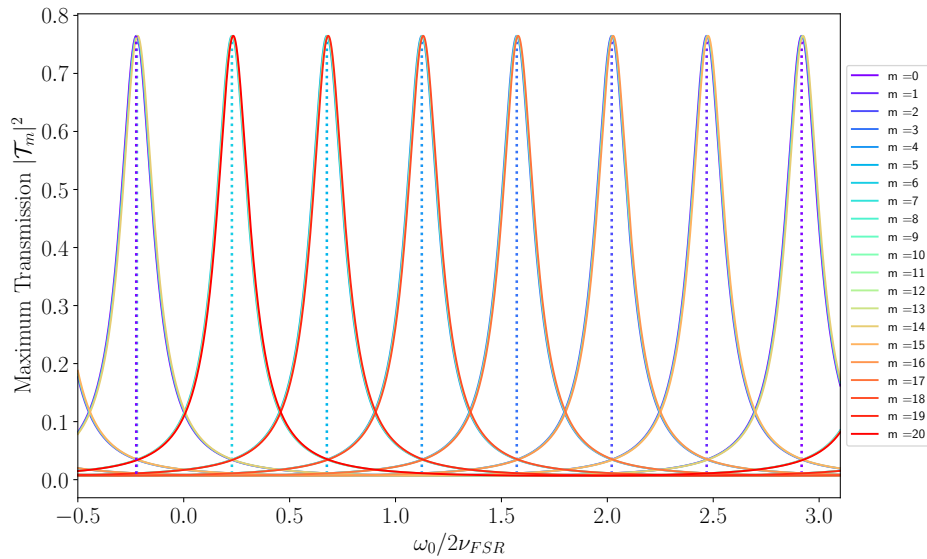


Figure 2.15: **Resonances at the first stage for cascaded temporal cavities.**

- Group 0: modes $\{0, 7, 14\}$
- Group 1: modes $\{1, 8, 15\}$
- Group 2: modes $\{2, 9, 16\}$
- ...
- Group 6: modes $\{6, 13, 20\}$.

With the first stage of the temporal cavity, $\mathcal{T}_{\max} = 0.764$, $\mathcal{F} = 16.67$, and $\delta = 2.38$. To select mode 9 for example, the first cavity stage would isolate Group 2, containing modes $\{2, 9, 16\}$. A subsequent stage can then specifically select mode 9 from this reduced set, as shown in Fig 2.16. While this cascaded approach enables the selection of more modes, it's important to note that the overall system losses increase with the amount of losses. In FIGURE for example, because of the addition of a second stage, the maximal transmittance drops to $\mathcal{T}_{\max} = 0.6$.

Current time lens limitations

As a final consideration, as discussed in Subsection 2.1.4, one should ensure that the duration of the pulse at the time lens is shorter than its aperture in order to minimize aberrations. While

2.2. TEMPORAL CAVITY

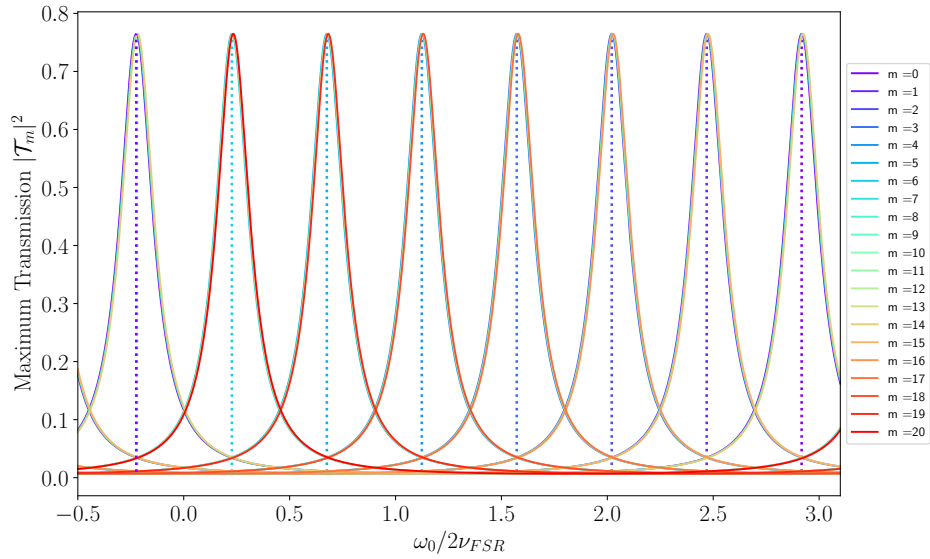


Figure 2.16: **Resonances at the second stage for cascaded temporal cavities.**

a time lens based on cross-phase modulation provides large enough apertures (10 – 20 ps), in the specific case of electro-optic time lenses, the aperture and focal length are not independent Eq. (2.84).

We verified that this condition can be satisfied for ps-long input pulses. We considered the condition as met when double FWHM of the pulse was smaller than the aperture. In Figure 2.18, we compare the pulse duration at the time lens (in terms of FWHM) with respect to the time lens aperture. We have discussed in Subsection 2.1.4 that the time lens aperture determines the maximum pulse durations that can be supported before distortions and aberrations take place. For an electro-optic (EO) implementation, the time lens aperture depends on the modulation frequency f_{RF} of the EO modulator and we showed in Eq. (2.76) that it is $\Delta_T = \frac{\sqrt{3}}{\pi f_{RF}}$. The pulse duration and the FWHM at the time lens, after propagation through the first dispersive element are respectively:

$$\sigma_{TL} = \sigma_0 \left[\sqrt{1 + \left(\frac{D_{tot}}{\sigma_0^2} \right)^2} \right], \quad (2.150)$$

$$FWHM_{TL} = 2\sqrt{2 \ln 2} \sigma_{TL}, \quad (2.151)$$

2.2. TEMPORAL CAVITY

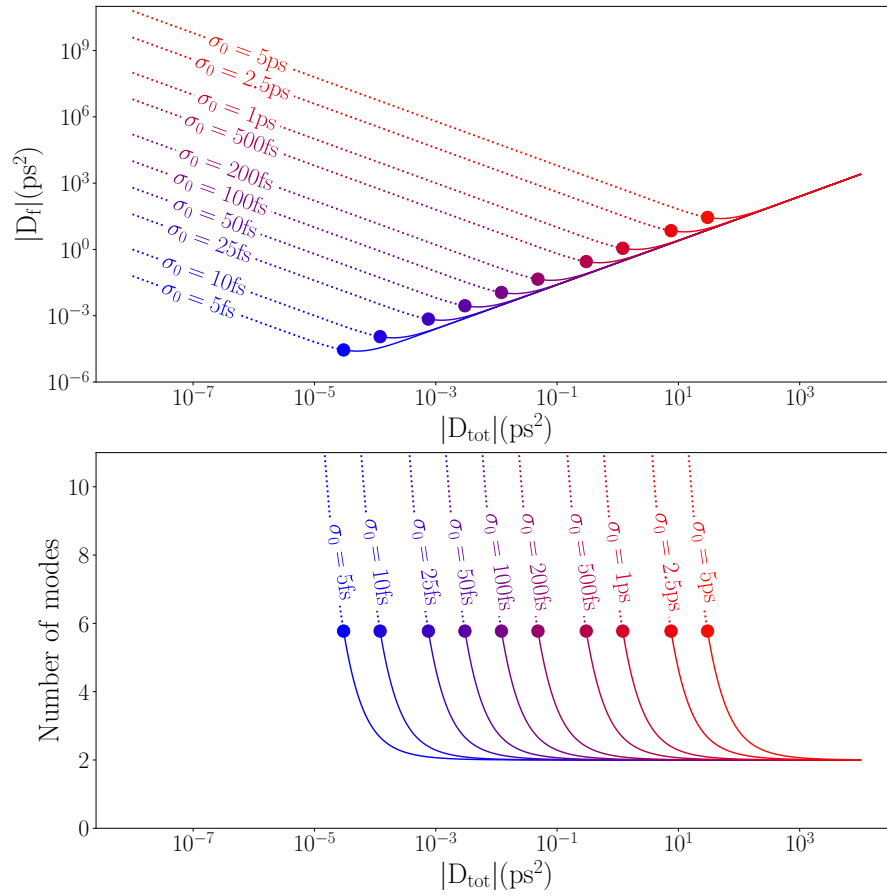


Figure 2.17: **Constraints on high loss:** (Top) diagram of the relation Eq. (2.118). (Bottom) number of modes fitting one cavity FSR. Full circles correspond to $\mathcal{T}_{\text{max}} = 0.11$, $\mathcal{F} = 8.7$, $\mathcal{P} = 40\%$, respectively. At these points, the distance between neighbour resonances is about 1.5 times their linewidth. On the left (dotted line), the distance is smaller and the two resonances are not resolved.

where we have chosen the FWHM as a better metric for pulse duration. In Figure 2.18, the pulse FWHM is plotted for different input durations over a range of RF modulation frequencies f_{RF} . The FWHM, represented by the V-shaped curves, is compared against the temporal aperture of the time lens, represented by the solid black line. For proper operation, the double of the FWHM should be shorter than the temporal aperture.

There are two values of FWHM for each f_{RF} because while the RF modulation frequency determines time lens GDD $D_f = 1/4\pi^2\delta f_{\text{RF}}^2$ (Eq. (2.79)), for a given value of D_f , there are two possible values of D_{tot} (Fig. 2.17) and therefore two possible values of pulse durations

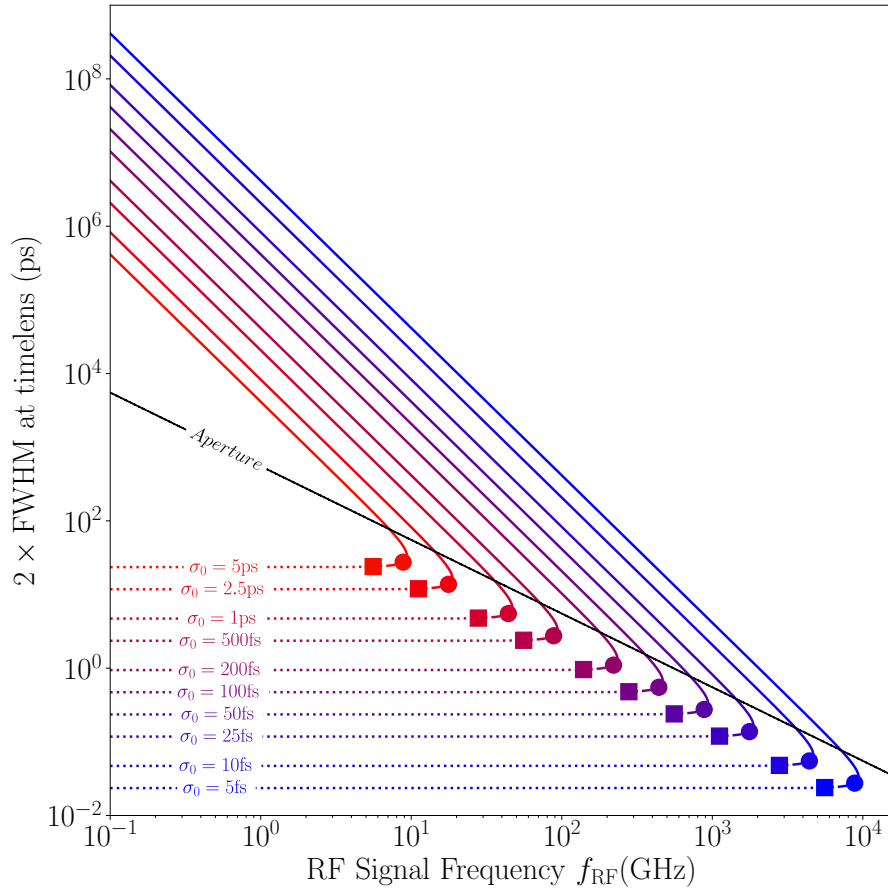


Figure 2.18: **EOPM time lens aperture:** Analysis of electro-optic time lens temporal aperture for different pulse durations

(Eq. (2.120)). This analysis shows that with a realistic modulation amplitude of $\delta = 11$ rad, RF frequencies above 10 GHz are necessary in order to provide sufficient temporal aperture to support input pulses shorter than ps. A 10 GHz modulation can manage ps long input pulses and verify the experimental feasibility using commercial electro-optic time lens capabilities. As electro-optic modulation technologies progress, larger temporal apertures are expected at given RF frequencies. For example, more favourable aperture scaling can be achieved with more complex RF driving that involves higher harmonics and implements the temporal equivalent of a Fresnel lens [168]. For a free-space coupled configuration with commercial electro-optic and dispersive elements, we expect around 40% losses, mainly due to insertion losses. For this level of losses, the parameter region for which resonances are resolved on the right side of

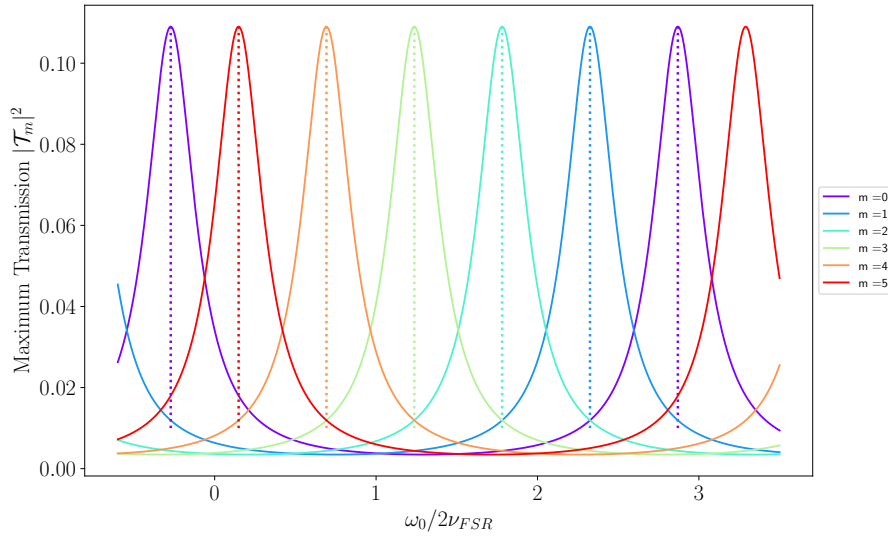


Figure 2.19: **Resonances at circle:** Resonances of a temporal cavity with parameters corresponding to the point in circle in Fig 2.17

the full circles in Figs. 2.17. The corresponding transmittance $\mathcal{T}_{\max} = 0.11$ is high enough to be detected in an experimental test. We show the transmission for $N = 6$ modes in Fig 2.19, corresponding to the parameters at the circle points in Fig. 2.17. The development of integrated thin-film lithium niobate technologies, where dispersive elements and phase modulators can be combined [169, 170], has the potential of significantly reducing losses for a better robustness in the quantum regime. For classical applications where pulse re-amplification is feasible, it is possible to make \mathcal{T}_{\max} arbitrarily close to 1. This allows the flexibility to choose higher values for the finesse, similar to what we observe in Fig. 2.8.

Chapter 3

Generalized quantum mode-matching through interferometry with memory

Contents

3.1	Quadratic Hamiltonian in cavity quantum optics	159
3.1.1	Quadratic Hamiltonian evolution in cavity	159
3.1.2	Resolution of the Hamiltonian Problem	162
3.1.3	Analytic Bloch-Messiah Decomposition	167
3.1.4	Spectral covariance matrix of the multimode state	172
3.1.5	Hidden squeezing	174
3.2	Conditions for a spectral covariance matrix	180
3.2.1	Framework	181
3.2.2	Boundaries to complex spectral covariance matrices	183
3.2.3	Case studies	187
3.3	Achieving generalized quantum mode-matching	192

3.3.1	Implementing the interferometer with memory effect	199
3.3.2	Smooth two-mode decomposition	200
3.3.3	Smooth single-mode decomposition	206
3.4	Measuring morphing supermodes	211
3.4.1	Optimization strategy	211
3.4.2	Single-mode OPO	218
3.4.3	Two-mode OPO	225
3.4.4	Four-mode OPO	237
3.4.5	Scaling and losses	241

In Section 1.1.4, we described CV quantum states of light which are crucial for various quantum information processing protocols such as quantum computation via cluster states [8, 9], quantum metrology [10] and quantum communication [11, 12]. Among these, Gaussian states are widely used due to their mathematical simplicity [12, 7] and their ability to be generated and manipulated experimentally [13, 6]. However, fully characterizing and exploiting these states requires a thorough understanding of measurement schemes (Section 1.5) and their limitations. Their characterization is commonly achieved through the use of homodyne detection (HD). A crucial aspect in HD is the matching of the local oscillator (LO) to the mode of the targeted beam. The resulting mode-matching guarantees an efficient utilization of the carried quantum resource. However, when the LO is not matched to the desired mode of this beam, it behaves as a filter, leading to quadrature measurement involving all the modal content that overlaps with the LO.

On one side, in a series of papers [55, 56], Barbosa and colleagues showed the possibility of quantum states presenting an unbalance between symmetric spectral components. For these states, they showed that a full characterization of its quantum properties cannot be performed through homodyne detection, a phenomenon recently coined as hidden [54] or complex [139] squeezing. On the other side, integrated photonics has developed recently with the generation of quantum light being proven on chip-scale devices [171, 172, 173, 174]. The integration in silicon substrates comes with $\chi^{(3)}$ nonlinearities [50, 52] and this increases the complexity of the quantum light that is produced. Indeed in these materials, the four-wave mixing gives origin to processes of cross- and self-phase modulation and parametric amplification. In the pioneering

works of [57, 54], the characterization of the quantum properties of their outputs in terms of morphing supermodes. These are normal modes, exhibiting frequency-dependent coefficients, that decouple the system dissipative dynamics by mapping the output multimode CV entangled state into a collection of independent squeezed states.

In [54, 86], it was demonstrated that both aspects can be reduced to a mode-matching problem and that achieving perfect matching through HD is not possible. The main goal of this chapter is to introduce and develop the theory and the possible implementation for a more general mode-matching strategy that is based on “interferometers with memory effect” (IME). They operate as an interface bridging the generation stage and the HD and provide the required mode-matching by exploiting the characteristics of both interferometers and cavities.

3.1 Quadratic Hamiltonian in cavity quantum optics

The nonlinear dynamics of a N boson modes optical system in a cavity can be linearized around a stable classical steady-state solution and can be associated in the most general case with an effective quadratic Hamiltonian. In Subsection 1.4.1, we show that these Hamiltonians in cavities lead to a set of linear quantum Langevin equations that govern the evolution of the system’s quadratures, in the presence of coupling to the external fields.

First, we explore the different methods of resolution of these evolution equations developed in [175] and their limitations. We, then, introduce their resolution in the most general case using Analytic Bloch Messiah decomposition, first introduced in [57].

3.1.1 Quadratic Hamiltonian evolution in cavity

As discussed in Section 1.2, any multimode optical field can be decomposed over an orthonormal family of modes $\{\vec{u}_n(\vec{r}, t)\}$, involving different degrees of freedom (spatial, time, frequency, polarization), each associated to boson operators $\hat{a}_m, \hat{a}_m^\dagger$ satisfying the commutation relations $[\hat{a}_m, \hat{a}_n^\dagger] = \delta_{m,n}$ and $[\hat{a}_m, \hat{a}_n] = 0$. With this notation, the positive frequency part of the electric

field reads as:

$$\hat{\vec{E}}^{(+)}(\vec{r}, t) = \sum_m \mathcal{E}_m \hat{a}_m \vec{u}_m(\vec{r}, t), \quad (3.1)$$

where \mathcal{E}_m is the single photon electric field.

Here, we will focus on the case of longitudinal modes of an optical cavity, all sharing the same spatial transverse mode and linear polarization:

$$\vec{u}_m(\vec{r}, t) \rightarrow \vec{e} \exp i(k_m z - \Omega_m t). \quad (3.2)$$

This covers the very broad category of multi-colour quantum states and quantum frequency combs out of optical cavities or single-mode waveguides. Nevertheless, the strategies we are discussing here could be easily extended to other kinds of modes. In this subsection, we do not take into account the intrinsic losses in the cavity, we will discuss those in the next subsections.

In the Heisenberg picture, we show in Subsection 1.4.2 the nonlinear dissipative evolution of a system of N bosonic modes is described by a system of coupled quantum Langevin equations. A standard linearization procedure around a stable stationary solution allows reducing such evolution to the effective Hamiltonian

$$\hat{H} = \hbar \sum_{m,n} G_{m,n} \hat{a}_m^\dagger \hat{a}_n + \frac{\hbar}{2} \sum_{m,n} [F_{m,n} \hat{a}_m^\dagger \hat{a}_n^\dagger + hc] \quad (3.3)$$

which represents the most general time-independent quadratic Hamiltonian, we first introduced in Eq. (1.217). The $N \times N$ matrices G and F incorporate the details of the linearized dynamics of the considered physical system and verify, respectively, $F = F^\top$, and $G = G^\dagger$. The latter ensures that \hat{H} is a hermitian operator. In practical situations, the matrix F has the nature of pairs production, as those arising from spontaneous parametric down-conversion in $\chi^{(2)}$ or $\chi^{(3)}$ interactions with undepleted pumps [176, 50]. The very general shape of the matrix G takes into account various mode-hopping processes whose details depend on the nature of the boson modes considered. In the case of cavity longitudinal modes, G includes frequency conversion processes [177], $\chi^{(3)}$ -induced self- and cross-phase modulation [50], mode detunings

from perfect resonance and linear dispersion effects.

We showed in Subsection 1.4.2 that using the Heisenberg representation, Eq. (3.3) generates the set of linear quantum Langevin equations

$$\frac{d\hat{R}(t)}{dt} = (-\Gamma + \mathcal{M})\hat{R}(t) + \sqrt{2\Gamma}\hat{R}_{\text{in}}(t), \quad (3.4)$$

where $\hat{R}(t) = (\hat{x}(t)|\hat{y}(t))^\top$, $\hat{x}(t) = (\hat{x}_1, \dots, \hat{x}_N)^\top$ and $\hat{y}(t) = (\hat{y}_1, \dots, \hat{y}_N)^\top$ are the column vectors of the amplitude and phase quadratures of the intracavity modes: $\hat{x}_m = \frac{1}{\sqrt{2}}(\hat{a}_m^\dagger + \hat{a}_m)$ and $\hat{y}_m = \frac{i}{\sqrt{2}}(\hat{a}_m^\dagger - \hat{a}_m)$. These equations describe the system's dynamics below the oscillation threshold. $\vec{R}_{\text{in}}(t)$ represents the quadrature vector of input modes entering the system via losses. The diagonal matrix Γ describes mode-dependent cavity losses and the mode coupling matrix \mathcal{M} is expressed as :

$$\mathcal{M} = \left(\begin{array}{c|c} \text{Im}[G + F] & \text{Re}[G - F] \\ \hline -\text{Re}[G + F] & -\text{Im}[G + F]^\top \end{array} \right). \quad (3.5)$$

Because of the properties of G and F ($G = G^\dagger$ and $F = F^\top$), both $\text{Re}[G - F]$ and $\text{Re}[G + F]$ are symmetric matrices. The system threshold is determined by the eigenvalue λ_0 of $\mathcal{M} - \Gamma$ with the highest real part, where $\text{Re}[\lambda_0] = 0$:

$$\text{Re}[\lambda_0] = 0, \quad \text{where } \lambda_0 = \max_{\lambda \in \text{eig}(\mathcal{M} - \Gamma)} \text{Re}[\lambda]. \quad (3.6)$$

This will be later used on examples to define how close/far we are from the threshold of the system considered.

All of the mathematical tools necessary for describing this physical problem have been introduced in Sections 1.2 and 1.4. First, we want to think about the different resolution techniques and their limits before we look into the resolution of Eq. (3.4) in the most general case.

3.1.2 Resolution of the Hamiltonian Problem

To solve the quadratic Hamiltonian described in Eq. (3.3), we must address the dynamics governed by the quantum Langevin equation presented in Eq. (3.4). The primary objective is to diagonalize the coupling matrix \mathcal{M} to decouple the equations of motion for the quadrature operators (Eq. (3.4)). This section outlines the methods and conditions necessary for achieving such a diagonalization, leveraging the mathematical framework of symplectic matrices. For the full resolution of the Langevin equations, one must find common transformation matrices for both \mathcal{M} and Γ . One can consider the case where \mathcal{M} and Γ commutent, with a particular case being equal dissipation coefficients: $\Gamma = \gamma I_{2N}$. Therefore, a matrix diagonalizing \mathcal{M} will also always diagonalize Γ . A deeper dive into these diagonalization techniques and their limitations can be found in [175].

Direct Diagonalization of \mathcal{M}

The most straightforward approach to solving the quantum Langevin equation involves the direct diagonalization of the coupling matrix \mathcal{M} . While this mathematically solves the problem, it does it without considering the physical properties of the bosonic operators involved, which means through eigenmodes which by default can have any commutation relations. The procedure involves finding a matrix U such that:

$$\mathcal{M} = UDU^T \tag{3.7}$$

where D is a diagonal matrix containing the eigenvalues of \mathcal{M} and U comprises the corresponding eigenvectors. A necessary condition for \mathcal{M} to be diagonalizable can be taken from the well-known spectral theorem, which for a real-valued matrix such as \mathcal{M} implies it has to be symmetric: $\mathcal{M} = \mathcal{M}^T$.

To account for the properties of the bosonic operators involved, one can attempt instead symplectic diagonalization of \mathcal{M} . Symplectic diagonalization leverages symplectic transition matrices to diagonalize the coupling matrix \mathcal{M} , ensuring the preservation of the canonical commutation relations inherent to the bosonic quadrature operators (\hat{x}_m, \hat{y}_m) and therefore provides

a clear physical interpretation of the system's dynamics. The procedure is a particular case of Eq. (3.7) where U belong to the real symplectic group $\text{Sp}(2N, \mathbb{R})$: $U\Omega U^\top = \Omega$, where we have already introduced the symplectic form Ω . Besides, whenever \mathcal{M} is diagonalizable, it can be proven [175] that \mathcal{M} is automatically symplectically diagonalizable.

Therefore, for \mathcal{M} to be symplectically diagonalizable, it must be symmetric: $\mathcal{M} = \mathcal{M}^\top$ to ensures that U in Eq. (3.7) is real, orthogonal, and symplectic. D is a real diagonal matrix that has two opposite blocks:

$$\mathcal{M} = U \begin{pmatrix} d & 0 \\ 0 & -d \end{pmatrix} U^\top. \quad (3.8)$$

Exploring the expression in Eq. (3.5) and remembering that G and F must verify $G = G^\dagger$ and $F = F^\top$, one can see that in order for \mathcal{M} to be symmetric, the following conditions must be verified:

$$\begin{cases} \text{Im}(G) = \text{Im}(G^\top) = \text{Im}(G^*), \\ \text{Re}(G) = -\text{Re}(G^\top) = -\text{Re}(G^*). \end{cases} \quad (3.9)$$

These conditions correspond to the case where $G = 0$ in the original interaction Hamiltonian (Eq. (3.3)).

One can see this more clearly when moving in the bosonic operators' basis for $U \rightarrow \tilde{U}$ and $\mathcal{M} \rightarrow M$. Any $2N \times 2N$ real unitary symplectic matrix U can be expressed with real U_1 and U_2 in the form:

$$U = \begin{pmatrix} U_1 & -U_2 \\ U_2 & U_1 \end{pmatrix} \text{ with } \begin{cases} U_1^\top U_1 + U_2^\top U_2 = I_N \\ U_1 U_1^\top + U_2 U_2^\top = I_N \\ U_1^\top U_2 = U_2^\top U_1 \\ U_1 U_2^\top = U_2 U_1^\top. \end{cases} \quad (3.10)$$

The conversion to notations adapted to bosonic operators was already detailed in Section 1.3. We denote \tilde{U} the matrix associated with the transformation for bosonic operators, $\tilde{U} = L^\dagger U L$

with always:

$$L = \frac{1}{\sqrt{2}} \begin{pmatrix} I_N & I_N \\ -iI_N & iI_N \end{pmatrix} \text{ and } L^\dagger = \frac{1}{\sqrt{2}} \begin{pmatrix} I_N & iI_N \\ I_N & -iI_N \end{pmatrix}. \quad (3.11)$$

By performing the block calculation, we obtain:

$$\tilde{U} = \begin{pmatrix} U_1 + iU_2 & 0 \\ 0 & U_1 - iU_2 \end{pmatrix} = \begin{pmatrix} U_a & 0 \\ 0 & U_a^* \end{pmatrix}, \quad (3.12)$$

with $U_a = U_1 + iU_2$ unitary $U_a U_a^\dagger = U_a^\dagger U_a = I_N$. This form corresponds to passive interferometers: the \hat{a}_i and \hat{a}_j^\dagger are not mixed, we will come back to this in later sections when discussing a new class of interferometers. Additionally, if we now consider a general real symplectic matrix S , the application of the Bloch-Messiah theorem (Subsection 1.3.5) allows us to write it as the product of an orthogonal symplectic matrix U , a real diagonal matrix D divided into two blocks inverse to each other, and a second orthogonal symplectic matrix V :

$$S = U \begin{pmatrix} d & 0 \\ 0 & -d \end{pmatrix} V^\top. \quad (3.13)$$

The associated transformation is therefore interpreted as the succession of a passive interferometer, single-mode squeezers, and then another passive interferometer, as we described in Subsection 1.3.5 and illustrated in Fig. 1.6. Furthermore, it's easy to see from Eq. (3.13) that S

is unitary if and only if the diagonal matrix of the Bloch-Messiah decomposition is the identity.

$$\begin{aligned}
 M &= iL^\dagger \mathcal{M} L \\
 &= i(L^\dagger U L) L^\dagger \begin{pmatrix} d & 0 \\ 0 & -d \end{pmatrix} L (L^\dagger U^\top L) \\
 &= i\tilde{U} L^\dagger \begin{pmatrix} d & 0 \\ 0 & -d \end{pmatrix} L \tilde{U}^\dagger \\
 &= i \begin{pmatrix} U_a & 0 \\ 0 & U_a^* \end{pmatrix} \begin{pmatrix} 0 & d \\ d & 0 \end{pmatrix} \begin{pmatrix} U_a & 0 \\ 0 & U_a^* \end{pmatrix}^\dagger \\
 M &= i \begin{pmatrix} 0 & U_a d U_a^\top \\ U_a^* d U_a^\dagger & 0 \end{pmatrix}, \tag{3.14}
 \end{aligned}$$

confirming from Eq. (3.14), the case where $G = 0$ and $F = iU_a d U_a^\top$. This occurs in systems with second-order nonlinearities ($\chi^{(2)}$) without detuning, which is common in many multimode squeezing systems [178, 179, 144, 180]. Additionally, when all dissipation coefficients are equal, the matrix U that diagonalizes \mathcal{M} also diagonalizes the loss matrix Γ . This reduces the problem to a set of single-mode quantum Langevin equations, which can be solved independently. However, in the cases where $G \neq 0$, the interpretation of symplectic diagonalization becomes more complex, and alternative approaches may be necessary.

Block Diagonalization

While a method consisting of symplectic diagonalization of \mathcal{M} is not always possible, another possibility, more general, is to try to put the evolution matrix in the form of diagonal blocks. Such a strategy does not allow direct resolution of the evolution equation or the Langevin equation, but it has the merit of reducing the problem to that of single-mode squeezing in the presence of frequency detuning, which is a known situation.

Let us suppose that such a decomposition is possible and let us deduce the necessary conditions from it. We will work in the boson operators basis since it gives a better insight. Suppose that M ($M = iL^\dagger \mathcal{M} L$) decomposes into a block diagonal matrix \tilde{D} via a real, symplectic, and

unitary passage matrix representing a linear interferometer. This is expressed as :

$$M = \begin{pmatrix} U_a & 0 \\ 0 & U_a^* \end{pmatrix} \tilde{D} \begin{pmatrix} U_a^\dagger & 0 \\ 0 & U_a^\top \end{pmatrix}, \quad (3.15)$$

This implies a specific expression for \tilde{D}

$$\begin{aligned} \tilde{D} &= \begin{pmatrix} U_a^\dagger & 0 \\ 0 & U_a^\top \end{pmatrix} \begin{pmatrix} G & F \\ -F^* & -G^* \end{pmatrix} \begin{pmatrix} U_a & 0 \\ 0 & U_a^* \end{pmatrix}, \\ \tilde{D} &= \begin{pmatrix} U_a^\dagger G U_a & U_a^\dagger F U_a^* \\ -(U_a^\dagger F U_a^*)^* & -(U_a^\dagger G U_a)^* \end{pmatrix} = \begin{pmatrix} d_1 & d_2 \\ -d_2^* & -d_1^* \end{pmatrix}. \end{aligned} \quad (3.16)$$

Eq. (3.16) shows that for the block diagonalization to be possible, there needs to exist diagonal d_1 and d_2 , and unitary U_a such that:

$$\begin{cases} G &= U_a d_1 U_a^\dagger \\ F &= U_a d_2 U_a^\top. \end{cases} \quad (3.17)$$

Note that the decomposition of G is a diagonalization, while that of F is a symmetric singular value decomposition. Since F is complex, there are no other constraints on d_2 than being diagonal, in particular, d_2 can have complex coefficients. On the contrary, since the decomposition on G is a diagonalization and G is Hermitian, necessarily d_1 is a real matrix.

It is straightforward from this analysis and Eqs. (3.17) to verify that, only when the simultaneous decompositions of F and G are possible, M is block diagonalizable via a passage matrix corresponding to a passive interferometer. Note that each of these decompositions is always individually possible because $G = G^\dagger$ and $F = F^\top$. However, it is not obvious that they are simultaneously possible. When F admits a symmetric singular value decomposition $F = U_a d_2 U_a^\top$, $F F^\dagger = U_a |d_2|^2 U_a^\dagger$. So such simultaneous decomposition is possible when G and $F F^\dagger$ are co-diagonalizable or equivalently that they commute. This is for example possible in the context of $\chi^{(2)}$ type non-linearities, in with mode-independent detuning Δ : $G = \Delta I_N$. In that case, choosing a symmetric singular value decomposition on F that ensures that d_2 is real will

automatically realize the diagonalization of G with the same U_a .

The physical interpretation of such a decomposition is that we reduce the problem to a set of independent modes, recoverable via a passive interferometer, each governed by a squeezing equation.

3.1.3 Analytic Bloch-Messiah Decomposition

We have seen in Subsection 3.1.2 that standard methods for analyzing multimode quantum optical systems face significant limitations. Direct diagonalization fails to preserve bosonic commutation relations, while symplectic approaches like Bloch-Messiah decomposition (BMD) require constraining assumptions for the interaction \mathcal{M} (Eq. (3.5)) in the systems. These limitations become particularly relevant when dealing with resonant systems exploiting third-order non-linear interactions, such as those in silicon and silicon nitride platforms [54].

To overcome these constraints, we present the Analytic Bloch-Messiah Decomposition (ABMD) [57], a generalized strategy to solve Eq. (3.4) that extends traditional symplectic approaches like BMD, which are restricted to problems where dynamic evolution can be ignored. By analyzing the transfer function $S(\omega)$ in the frequency domain, ABMD provides a complete description of the system's evolution through frequency-dependent passive interferometers and squeezers. This method enables the identification of supermodes - coherent superpositions of original modes that decouple the system dynamics - without requiring prior assumptions about linear dispersion or non-linear interactions. However, this decomposition comes with a cost: the passive interferometers required by ABMD must be frequency-dependent, matching the cavity's response characteristics: a term coined as morphing supermodes [57].

The versatility of ABMD makes it applicable to various scenarios, from low-dimensional systems with single- or double-mode squeezing [57, 85, 86] to highly multimode states produced via four-wave mixing in integrated systems [54].

To use ABMD, we look at the steady-state solutions in the frequency domain by using the Fourier transform of the quadrature vector introduced earlier:

$$\hat{R}(\omega) = \int \frac{dt}{\sqrt{2\pi}} e^{-i\omega t} \hat{R}(t). \quad (3.18)$$

3.1. QUADRATIC HAMILTONIAN IN CAVITY QUANTUM OPTICS

It is important to note here since we work in the interaction picture with fields in the slowly varying amplitude approximation, ω can be taken to rigorously coincide with the sideband frequency offset from the optical carriers at Ω_m . Eq. (3.4) becomes in the Fourier basis:

$$i\omega\hat{R}(\omega) = (-\Gamma + \mathcal{M})\hat{R}(\omega) + \sqrt{2\Gamma}\hat{R}_{in}(\omega) \quad (3.19)$$

The quadratures \hat{R}_{out} of the multimode state at the device output can be conveniently obtained as functions of input modes' quadratures, thanks to standard input-output relations $\hat{R}_{in} + \hat{R}_{out} = \sqrt{2\Gamma}\hat{R}$ we demonstrated in Section 1.4, Eq. (1.228). These output quadratures are then given by:

$$\hat{R}_{out}(\omega) = S(\omega)\hat{R}_{in}(\omega), \quad (3.20)$$

where $S(\omega)$ is the system's transfer function. $S(\omega)$ is a complex matrix-valued function of the continuous parameter ω given by the expression

$$S(\omega) = \sqrt{2\Gamma}(i\omega\mathbb{I} + \Gamma - \mathcal{M})^{-1}\sqrt{2\Gamma} - \mathbb{I} \quad (3.21)$$

with \mathbb{I} the $2N \times 2N$ identity matrix. The input spectral quadrature operators satisfy the commutation rule $[\hat{R}_{in}(\omega), \hat{R}_{in}^\dagger(\omega')] = i\Omega\delta(\omega + \omega')$, where we remind $\Omega = \begin{pmatrix} 0 & I_N \\ -I_N & 0 \end{pmatrix}$ is the N -mode symplectic form and I_N is the $N \times N$ identity matrix. The output quadratures $\hat{R}_{out}(\omega)$ are the Fourier transform of *bona fide* boson quadrature operators in time domain, since $S(\omega)$ has the two following properties [57]:

Property 3.1.1. *S is conjugate symmetric: $S(-\omega) = S^*(\omega)$. This assures the reality of S in time domain.*

Proof. *Let us define the inverse Fourier Transform of the transfer function:*

$$S(t) = \frac{1}{\sqrt{2\pi}} \int_{-\infty}^{+\infty} d\omega S(\omega)e^{i\omega t}. \quad (3.22)$$

Assuming $S(\omega)$ verify the conjugate symmetry property : $S^(\omega) = S(-\omega)$, we can substitute it*

into Eq. (3.22), giving

$$S(t) = \frac{1}{\sqrt{2\pi}} \left(\int_{-\infty}^0 d\omega S(\omega) e^{i\omega t} + \int_0^{+\infty} d\omega S^*(\omega) e^{-i\omega t} \right). \quad (3.23)$$

By changing variables in the first integral and combining them with the second:

$$S(t) = \frac{1}{\sqrt{2\pi}} \left(\int_0^{+\infty} d\omega S(-\omega) e^{-i\omega t} + \int_0^{+\infty} d\omega S^*(\omega) e^{-i\omega t} \right), \quad (3.24)$$

we use the conjugate symmetry property to conclude that

$$\begin{aligned} S(t) &= \frac{1}{\sqrt{2\pi}} \left(\int_0^{+\infty} d\omega S^*(\omega) e^{-i\omega t} d\omega + \int_0^{+\infty} d\omega S^*(\omega) e^{-i\omega t} d\omega \right) \\ S(t) &= \frac{1}{\sqrt{2\pi}} \int_{-\infty}^{+\infty} d\omega S^*(\omega) e^{-i\omega t} = S^*(t). \end{aligned} \quad (3.25)$$

This conjugate property in frequency of S ensures the reality of the temporal counterpart. \square

We define a set of transformations dependent on a continuous real parameter ω (frequency) such that:

$$\mathbb{S}_\omega = \{S \in \mathcal{C}_\omega \mid \forall \omega \in \mathbb{R}, S(\omega) \in \text{Sp}^*(2N, \mathbb{C})\}. \quad (3.26)$$

We call this the ω -Symplectic group. Here, \mathcal{C}_ω represents the set of smooth matrix-valued functions in $\mathbb{C}^{2N \times 2N}$ with respect to ω . We refer to elements of \mathbb{S}_ω as " ω -symplectic" transformations. The conjugate-symplectic group $\text{Sp}^*(2N, \mathbb{C})$ is defined as the set of $2N \times 2N$ complex matrices such that $S(\omega)\Omega S^\top(-\omega) = \Omega$, with Ω the symplectic form. The temporal equivalent of such conjugate-symplectic property is :

$$\int_{-\infty}^{+\infty} d\tau S(t-\tau)\Omega S^\top(t'-\tau) = \Omega\delta(t-t') \quad (3.27)$$

Property 3.1.2. S is always " ω -symplectic" which means $S \in \mathbb{S}_\omega$

Proof. We begin with the definition of $S(\omega)$ in Eq. (3.21). To prove the ω -symplectic nature, we need to show that: $S(\omega)\Omega S^\top(-\omega) = \Omega$ where Ω is the symplectic form.

3.1. QUADRATIC HAMILTONIAN IN CAVITY QUANTUM OPTICS

Let us expand the left-hand side:

$$S(\omega)\Omega S^T(-\omega) = [\sqrt{2\Gamma}(i\omega\mathbb{I} + \Gamma - \mathcal{M})^{-1}\sqrt{2\Gamma} - \mathbb{I}] \Omega [\sqrt{2\Gamma}(-i\omega\mathbb{I} + \Gamma - \mathcal{M})^{-1}\sqrt{2\Gamma} - \mathbb{I}]^T \quad (3.28)$$

We can simplify this expression using the properties of \mathcal{M} and Γ :

$$1. \mathcal{M} \text{ is Hamiltonian: } (\Omega\mathcal{M})^T = \Omega\mathcal{M}$$

$$2. \Gamma \text{ is skew-Hamiltonian: } (\Omega\Gamma)^T = -\Omega\Gamma$$

These properties allow us to write: $\mathcal{M}^T = \Omega^{-1}\mathcal{M}\Omega^{-1}$ and $\Gamma^T = -\Omega^{-1}\Gamma\Omega^{-1}$. Using these relations and the fact that $\mathbb{I} = \Omega\mathbb{I}\Omega^{-1} = -\Omega^{-1}\mathbb{I}\Omega^{-1}$, we can rewrite the transpose term as:

$$[\sqrt{2\Gamma}(-i\omega\mathbb{I} + \Gamma - \mathcal{M})^{-1}\sqrt{2\Gamma} - \mathbb{I}]^T = \sqrt{2\Gamma}\Omega(i\omega\mathbb{I} - \Gamma - \mathcal{M})^{-1}\Omega\sqrt{2\Gamma} - \mathbb{I} \quad (3.29)$$

Substituting this back into our original equation and using the properties $\Gamma\Omega = \Omega\Gamma$ and $\Omega\Omega = -\mathbb{I}$, we get:

$$\begin{aligned} S(\omega)\Omega S^T(-\omega) &= -\sqrt{2\Gamma}(i\omega\mathbb{I} + \Gamma - \mathcal{M})^{-1}(2\Gamma)(i\omega\mathbb{I} - \Gamma - \mathcal{M})^{-1}\sqrt{2\Gamma}\Omega \\ &\quad - \sqrt{2\Gamma}(i\omega\mathbb{I} + \Gamma - \mathcal{M})^{-1}\sqrt{2\Gamma}\Omega \\ &\quad + \sqrt{2\Gamma}(i\omega\mathbb{I} - \Gamma - \mathcal{M})^{-1}\sqrt{2\Gamma}\Omega + \Omega \end{aligned} \quad (3.30)$$

The key step is to recognize that the terms in square brackets cancel out:

$$[-(2\Gamma) - (i\omega\mathbb{I} - \Gamma - \mathcal{M}) + (i\omega\mathbb{I} + \Gamma - \mathcal{M})] = 0 \quad (3.31)$$

This leaves us with:

$$S(\omega)\Omega S^T(-\omega) = \Omega. \quad (3.32)$$

Thus, we have proven that $S(\omega)$ is indeed an ω -symplectic matrix for all ω . \square

Since the transformation connecting input and output modes, associated with Eq. (3.21), is

symplectic in a generalized sense, for any element of \mathbb{S}_ω , there exists an ABMD:

$$S(\omega) = U(\omega)D(\omega)V^\dagger(\omega) \quad (3.33)$$

where $U(\omega)$, $D(\omega)$, and $V(\omega)$ are smooth matrix-valued functions. For any given ω , $U(\omega)$ and $V(\omega)$ belong to $Sp^*(2N, \mathbb{C}) \cap \mathcal{U}(2N)$, with $\mathcal{U}(2N)$ being the unitary group and they characterize the structure of what is coined "morphing supermodes". The matrix

$$D(\omega) = \text{diag}\{d_1(\omega), \dots, d_N(\omega) | d_1^{-1}(\omega), \dots, d_N^{-1}(\omega)\}$$

(with $d_i(\omega) \geq 1$ for $i = \{1, \dots, N\}$, for all ω) contains their (optimal) anti-squeezing $d_i(\omega)$ and squeezing $d_i^{-1}(\omega)$ levels. All of these functions inherit Property 1 of the transfer matrix, making them conjugate symmetric. In general, ABMD differs from a simple point-by-point Bloch-Messiah decomposition for each ω , as it ensures the smoothness of supermodes that allows to define the continuously evolving physical observables.

Morphing supermodes

In experiments, the characterization of the covariance matrix (Eq. (1.138)) of a multimode state requires the simultaneous measure of the noise features of the different optical modes and then retrieving their correlations. This strategy, although quite current in two mode scenarios [48], is not viable when the number of correlated modes scales up. In many practical situations, a preferred way to proceed is to introduce a set of normal modes (a.k.a. supermodes) that decouple the system dissipative dynamics and map the CV multimode entangled state into a collection of (anti-)squeezed states that, since they are statistically uncorrelated, can be measured independently of each other [176, 181]. Identifying supermodes therefore involves finding linear combinations of a_n and a_n^\dagger that diagonalize \mathcal{M} while preserving the symplectic structure. However, as seen in 3.1.2, \mathcal{M} generally cannot be diagonalized by symplectic unitary transformations, except when G is null. Consequently, the system typically lacks a set of traditional supermodes with unchanging shapes during evolution. To characterize the system's quantum properties, one requires statistically independent physical observables. As demonstrated in Ref. [57], in

the general case of a quadratic Hamiltonian, the modes containing the optimal (anti-)squeezing are “morphing”. Morphing supermodes are a generalization of standard (static) supermodes and are expressed as linear combinations of the initial system optical modes with *frequency-dependent* coefficients that vary with ω . A morphing behavior is quite common in nonlinear optical cavities. It appears, for instance, in single-mode degenerate optical parametric oscillators with signal or pump detuning [58, 59] and in optomechanical cavities [60, 61, 182]. At their output, optimal squeezing is found in a frequency-dependent quadrature that varies at scales of the cavity bandwidth. Surprisingly, it was only recently that it has been unveiled in highly multi-mode systems such as silicon-based microresonators [54]. It also appears in the description of non-Gaussian states generated in ultra-fast second-order nonlinear photonics beyond the pump depletion approximation [183, 184].

Remarkably, a smooth dependence on spatial and temporal coordinates, rather than frequency, has also been observed in the symplectic eigenvalues when characterizing the spatiotemporal properties of entanglement [47].

The ABMD in Eq. (3.33) allows us to obtain the quadrature of supermodes:

$$\hat{R}'_{\text{out}}(\omega) = U^\dagger(\omega)\hat{R}_{\text{out}}(\omega) \quad (3.34)$$

assuming an input vacuum state. Notably, the shape of the supermodes depends on the frequency ω , indicating that optimal detection modes vary with the analysis frequency in practical scenarios. These quadratures therefore represent the optimally (anti-)squeezed quadrature operators. Their noise level is given by $d_i(\omega)$ for the anti-squeezed supermode i and by $d_i^{-1}(\omega)$ for squeezed supermode $N + i$. Since $U(\omega)$ is ω -symplectic and conjugate symmetric, the new quadratures have a symmetric real part and anti-symmetric imaginary part so to correspond to Hermitian quadratures in time domain.

3.1.4 Spectral covariance matrix of the multimode state

The transfer function $S(\omega)$ is in general non-diagonal, leading to a coupling between the quadratures of different output modes. This reflects the presence, at the output of the device, of continuous variable entanglement among field optical modes at frequencies Ω_m . In other words,

when measuring the quadrature \hat{R}_{out} , a correlation appears among noise fluctuations of the different optical modes. The noise fluctuations can be collected in a global covariance matrix (Eq. (1.138)) that, for Gaussian states, up a displacement leading to zero mean values, offer a full characterization of these quantum states [124, 185, 186]. However, in cavity-based optical systems, boson field operators are slowly-varying with time in the interaction picture. To therefore capture the temporal properties of these fields, second-order momenta are instead collected in a correlation matrix [47] that is a function of two different times t and t' , introduced in Eq. (1.230). When considering stationary-in-time systems where the correlation matrix depends only on the time difference $t - t'$, such matrix for the resonator output quadrature vector writes:

$$\sigma_{\text{out}}(t) = \frac{1}{2} \langle \hat{R}_{\text{out}}(0) \hat{R}_{\text{out}}^{\text{T}}(t) + (\hat{R}_{\text{out}}(t) \hat{R}_{\text{out}}^{\text{T}}(0))^{\text{T}} \rangle \quad (3.35)$$

where we have assumed input vacuum states \hat{R}_{in} . Because of this stationarity property, for such systems, one can introduce the Fourier transform of the correlation matrix that depends only on one frequency ω [47]: the spectral covariance matrix $\sigma_{\text{out}}(\omega)$, which we can directly express in terms of the transfer function $S(\omega)$:

$$\sigma_{\text{out}}(\omega) = \frac{1}{2\sqrt{2\pi}} S(\omega) S^{\text{T}}(-\omega). \quad (3.36)$$

The passage from the correlation matrix to the spectral covariance matrix and their correlated properties have been extensively detailed in Subsection 1.4.4, where we have also expressed in Eq. (1.249) the correlation matrix of an input vacuum field, that we have used for Eq. (3.36).

Using ABMD of $S(\omega)$ in Eq. (3.33), we obtain the output spectral covariance matrix in terms of the morphing supermodes $U(\omega)$.

$$\sigma_{\text{out}}(\omega) = \frac{1}{2\sqrt{2\pi}} U(\omega) D^2(\omega) U^{\dagger}(\omega). \quad (3.37)$$

We proved in Section 1.4.4 that $\sigma_{\text{out}}(\omega)$, in general, is a non-real Hermitian matrix and, is from Property 3.1.1, conjugate symmetric, *i.e.* $\sigma(-\omega) = \sigma^*(\omega)$; as a consequence, the real

part of the spectral covariance matrix is symmetric with respect to the exchange $\omega \leftrightarrow -\omega$, $\text{Re}[\sigma(-\omega)] = \text{Re}[\sigma(\omega)]$, and its imaginary part is anti-symmetric, $\text{Im}[\sigma(-\omega)] = -\text{Im}[\sigma(\omega)]$. This, as we will discuss in the next subsection, has profound implications on the full characterization of the output quantum state.

3.1.5 Hidden squeezing

The complex nature of the spectral covariance matrix is generally ignored in the literature [48, 49, 50, 187] and only the real part of Eq. (3.36) is typically considered. This assumption leads, however, to disregard the presence of correlations among noise components that emerge from the properties of complex covariance matrices $\sigma_{\text{out}}(\omega)$. From a physical point of view, the full characterization of the quantum state should involve measurement of both quantum noise components at frequencies ω and $-\omega$. However, in some situations [58] the qumodes at ω and $-\omega$ are essentially in the same quantum state and only the subspace ω (or the subspace $-\omega$) can be considered: such a state symmetry with respect to $\omega \leftrightarrow -\omega$ makes the assumption of a real $\sigma_{\text{out}}(\omega)$ correct and justifies the use of standard homodyne detector to fully retrieve the state quantum properties.

A complex $\sigma_{\text{out}}(\omega)$ implies, instead, a state that is not symmetric with respect to qumodes at ω and $-\omega$. For those states, considering only qumodes at ω means neglecting quantum correlations between them and those at $-\omega$, that are encoded in the imaginary part of the spectral covariance matrix. As it will be detailed in the following, their measurement is not accessible to a standard HD, a phenomenon that has been named “hidden” [54] or “complex squeezing” [139] and requires more sophisticated strategies. These extra correlations are essential for fully characterizing the corresponding quantum state and could also be exploited for enhancing the performances of QIP and MBQC protocols.

The concept of hidden squeezing was first explored and explained by Barbosa *et al.* (see for example [55, 56]). In their works, the authors pointed out that the squeezing of a single beam of light actually involves two-mode squeezing correlations between symmetric noise sidebands at ω and $-\omega$. An effective single-mode description can be applied when the noise spectral power of these symmetrical components are identical, while in general, a two-mode description

becomes necessary: in such cases, homodyne detection lacks the necessary degrees of freedom to detect correlations between the symmetrical components and, as a consequence, to reconstruct the complete information [55, 56]. The solution proposed by Barbosa and coworkers showed that a "resonator detection" (RD) successfully detects correlations between noise spectral components at ω and $-\omega$ [55, 56]. However, such architecture does not easily scale with the number of entangled modes nor can cope with the frequency-dependent behaviour of the morphing supermodes.

Theoretically, the characterization of the covariance matrix, either in the original basis of the longitudinal modes or in the supermodes basis, requires the detection of mode quadratures, *i.e.* of the field continuous variables [48, 49, 181]. In experiments, quadratures are typically accessed via HD by making the fields under scrutiny beat with a bright reference beam called "local oscillator" (LO) [188]. The optical beat signal, after photodetection, gives a photocurrent that encodes the quadrature mean value and quantum noise [188]. For quantum states generated in the longitudinal modes of a cavity, the LO takes the following form

$$E_{\text{LO}}(t) = i \sum_m \alpha_m e^{-i\Omega_m t} + \text{H.c.} \quad (3.38)$$

where each α_m is the complex amplitude of the LO components in the optical mode at frequency Ω_m . We show in subsection 1.5.3, HD as an example of mode quadrature detection scheme, showing that the corresponding photocurrent operator can be written as

$$\begin{aligned} \hat{i}(t) &\propto \sum_m \left(\text{Re}[\alpha_m] \hat{x}_{\text{out},m}(t) + \text{Im}[\alpha_m] \hat{y}_{\text{out},m}(t) \right) = \\ &= \vec{Q}^T \hat{R}_{\text{out}}(t). \end{aligned} \quad (3.39)$$

By defining $\vec{\alpha} = (\alpha_1, \dots, \alpha_N)^T$, in this expression, $\vec{Q} = (\text{Re}[\vec{\alpha}] | \text{Im}[\vec{\alpha}])^T$ is the normalized column vector of LO coefficients in the quadrature representation. We concluded in that section that although LOs with arbitrary spectral amplitudes $\vec{\alpha}$ are accessible to experiments [181], for the case of HD, the amplitudes and phases of their spectral components always combine to give real quadratures, *i.e.* a real \vec{Q} : this guarantees that, in the time domain, the photocurrent operator Eq. (3.39) is Hermitian. The projective measurement described by Eq. (3.39) gives

3.1. QUADRATIC HAMILTONIAN IN CAVITY QUANTUM OPTICS

a combination of the quadratures of optical fields at frequencies Ω_m with coefficients given by \vec{Q} : by shaping the LO it is thus possible to measure the quadratures of individual longitudinal modes or of their linear combinations (for example in the basis of the supermodes). For frequency homodyning [188], the Fourier transform of the photocurrent (Eq. (3.39)) returns the noise spectrum of the chosen quadrature:

$$\Sigma_{\vec{Q}}(\omega) = \Sigma_{\text{HD}}(\omega) = \vec{Q}^T \sigma_{\text{out}}(\omega) \vec{Q}. \quad (3.40)$$

As it should be for any measurable quantity, this expression always returns a real noise spectrum $\Sigma_{\vec{Q}}(\omega)$ (we prove just after in Proof 3.1.5), even when the covariance matrix $\sigma_{\text{out}}(\omega)$ exhibits an imaginary part.

When dealing with quantum states that have a complex spectral covariance matrix, the limitations of standard HD can be illustrated with the very simple case of a single-mode state described by its amplitude and phase quadratures $(\hat{x}, \hat{y})^T$,

$$\sigma_{\text{out}}(\omega) = \begin{pmatrix} \alpha(\omega) & \gamma(\omega) + i\delta(\omega) \\ \gamma(\omega) - i\delta(\omega) & \beta(\omega) \end{pmatrix} = \begin{pmatrix} \alpha(\omega) & \gamma(\omega) \\ \gamma(\omega) & \beta(\omega) \end{pmatrix} + i \begin{pmatrix} 0 & \delta(\omega) \\ \delta(\omega) & 0 \end{pmatrix} \quad (3.41)$$

where $\alpha(\omega)$, $\beta(\omega)$, $\gamma(\omega)$ and $\delta(\omega)$ are real functions of ω defined as:

$$\alpha(\omega) = \frac{1}{2} \langle \hat{x}(\omega) \hat{x}(-\omega) + \hat{x}(-\omega) \hat{x}(\omega) \rangle, \quad (3.42)$$

$$\beta(\omega) = \frac{1}{2} \langle \hat{y}(\omega) \hat{y}(-\omega) + \hat{y}(-\omega) \hat{y}(\omega) \rangle, \quad (3.43)$$

$$\gamma(\omega) + i\delta(\omega) = \frac{1}{2} \langle \hat{x}(\omega) \hat{y}(-\omega) + \hat{y}(-\omega) \hat{x}(\omega) \rangle, \quad (3.44)$$

and as required to guarantee the Hermiticity of $\sigma_{\text{out}}(\omega)$. The corresponding noise spectral power Eq. (3.40), as detected from HD, for a given LO $\vec{Q} = (\cos \theta | \sin \theta)^T$, corresponds to

$$\Sigma_{\vec{Q}}(\omega) = \cos^2 \theta \alpha(\omega) + \sin^2 \theta \beta(\omega) + 2 \cos \theta \sin \theta \gamma(\omega). \quad (3.45)$$

Whatever the choice of θ (*i.e.* of the selected quadrature), $\Sigma_{\vec{Q}}(\omega)$ clearly does not encode

any information about the imaginary part of the spectral covariance matrix $\delta(\omega)$ that, therefore, carries quantum correlations that are hidden to HD.

Intuitively, in the case of an arbitrarily large number of modes, the spectral covariance matrix is easier to characterize in terms of the optimal (anti-)squeezing levels associated with individual supermodes: Eq. (3.37). In this basis, the limitations of the HD in dealing with Gaussian states with complex $\sigma(\omega)$ and with morphing behaviour can be formalized as a problem of mode-matching: the occurrence of sub-optimal detection of squeezing originates from a LO not perfectly projecting on the targeted supermode.

By replacing Eq. (3.37) in Eq. (3.40), the detected noise spectral power takes the following form

$$\Sigma_{\vec{Q}}(\omega) = \frac{1}{2\sqrt{2\pi}} [\vec{Q}^T U(\omega)] D^2(\omega) [U^\dagger(\omega) \vec{Q}]. \quad (3.46)$$

This expression shows that to measure the optimal degree of squeezing, *i.e.* $\Sigma_{\vec{Q}}(\omega) \sim d_i^{-2}(\omega)$, the LO should perfectly match the $(N + i)$ -th supermode. This corresponds to achieving a perfect projection on the supermode identified by the $(N + i)$ -th column of $U(\omega)$, $\vec{U}_{N+i}(\omega)$. Such a projection formally corresponds to shaping the LO column vector \vec{Q} so that the scalar product $\vec{Q}^T \vec{U}_{N+i}(\omega) = 1$. We show in the next lines a much more rigorous proof that this mode-matching condition cannot be satisfied as the LO \vec{Q} is constant and real while, in general, U depends on the frequency ω and is complex. Even in the special case of a real $U(\omega)$, an LO with a non-morphing profile (corresponding to a frequency-independent \vec{Q}), can retrieve the optimal squeezing only at the frequency $\bar{\omega}$ for which \vec{Q} and $\vec{U}_{N+i}(\bar{\omega})$ are matched. In the general case of a complex $U(\omega)$, no mode-matching is possible and the HD measure is suboptimal, as we will show for any nonzero values of ω [54], thus leaving a part of the quantum correlations hidden.

Proof. To prove that HD with a real \vec{Q} cannot recover optimal squeezing in the most general case. For that, we want to rewrite the output spectral covariance matrix in a much more convenient form by noticing Eq. (3.37) corresponds to a symplectic diagonalization where the complex eigenvectors correspond to the orthonormal basis of the morphing supermodes ($\hat{U}_j(\omega)$, column of $U(\omega)$) and the real eigenvalues (since σ_{out} is hermitian) the squeezing and antisqueezing spectrums. In this new form, using the spectral theorem, we write the spectral covariance ma-

trix as :

$$\sigma_{out}(\omega) = \frac{1}{2\sqrt{2\pi}} \sum_{i=1}^{2N} \lambda_i^2(\omega) \vec{U}_i(\omega) \vec{U}_i^\dagger(\omega) \quad (3.47)$$

where:

$$\lambda_i^2(\omega) = \begin{cases} d_i^{-2}(\omega) & \text{for } i \in [1, N] \\ d_{i-N}^2(\omega) & \text{for } i \in [N+1, 2N] \end{cases} \quad (3.48)$$

Here, $d_i^2(\omega)$ represents the anti-squeezing spectrum and $d_i^{-2}(\omega)$ represents the squeezing spectrum. Thus, the extended expression of the spectral covariance matrix becomes:

$$\sigma_{out}(\omega) = \frac{1}{2\sqrt{2\pi}} \left(\sum_{i=1}^N d_i^2(\omega) \vec{U}_i(\omega) \vec{U}_i^\dagger(\omega) + \sum_{i=1}^N d_i^{-2}(\omega) \vec{U}_{N+i}(\omega) \vec{U}_{N+i}^\dagger(\omega) \right) \quad (3.49)$$

For the sake of subsequent proofs, we want to express the noise spectral power in terms of the most general quadratic measurement first before we look at the specific case of HD. Consider the most general unitary complex vector $\vec{Q}(\omega)$. We can decompose $\vec{Q}(\omega)$ in the basis of the morphing supermodes:

$$\vec{Q}(\omega) = \sum_{i=1}^{2N} \beta_i(\omega) \vec{U}_i(\omega) \quad \text{with} \quad \beta_i(\omega) = \langle \vec{Q}(\omega), \vec{U}_i(\omega) \rangle \quad (3.50)$$

The noise spectral power is then given by:

$$\begin{aligned}
 \Sigma_{\vec{Q}}(\omega) &= \vec{Q}^\dagger(\omega) \sigma_{out}(\omega) \vec{Q}(\omega) \\
 &= \frac{1}{2\sqrt{2\pi}} \left(\sum_{i=1}^{2N} \beta_i^*(\omega) \vec{U}_i^\dagger(\omega) \right) \left(\frac{1}{2\sqrt{2\pi}} \sum_{j=1}^{2N} \lambda_j^2(\omega) \vec{U}_j(\omega) \vec{U}_j^\dagger(\omega) \right) \left(\sum_{k=1}^{2N} \beta_k(\omega) \vec{U}_k(\omega) \right) \\
 &= \frac{1}{2\sqrt{2\pi}} \sum_{i,j,k=1}^{2N} \beta_i^*(\omega) \lambda_j^2(\omega) \beta_k(\omega) \vec{U}_i^\dagger(\omega) \vec{U}_j(\omega) \vec{U}_j^\dagger(\omega) \vec{U}_k(\omega) \\
 &= \frac{1}{2\sqrt{2\pi}} \sum_{i,j,k=1}^{2N} \beta_i^*(\omega) \lambda_j^2(\omega) \beta_k(\omega) \langle \vec{U}_i(\omega), \vec{U}_j(\omega) \rangle \langle \vec{U}_j(\omega), \vec{U}_k(\omega) \rangle \\
 &= \frac{1}{2\sqrt{2\pi}} \sum_{i,j,k=1}^{2N} \beta_i^*(\omega) \lambda_j^2(\omega) \beta_k(\omega) \delta_{ij} \delta_{jk} \\
 &= \frac{1}{2\sqrt{2\pi}} \sum_{i=1}^{2N} \beta_i^*(\omega) \lambda_i^2(\omega) \beta_i(\omega) \\
 \Sigma_{\vec{Q}}(\omega) &= \frac{1}{2\sqrt{2\pi}} \sum_{i=1}^{2N} \lambda_i^2(\omega) |\beta_i(\omega)|^2 > 0, \tag{3.51}
 \end{aligned}$$

which we can expand to:

$$\Sigma_{\vec{Q}}(\omega) = \frac{1}{2\sqrt{2\pi}} \left(\sum_{i=1}^N d_i^2(\omega) |\beta_i(\omega)|^2 + \sum_{i=1}^N d_i^{-2}(\omega) |\beta_{N+i}(\omega)|^2 \right) > 0. \tag{3.52}$$

First, from here we already show two intrinsic properties of the noise spectral power: it is always real and positive, regardless of whether $\vec{Q}(\omega)$ is real or complex. Then, to recover for example the squeezing spectrum of mode j ($d_j^2(\omega)$), the measurement technique must ensure that:

$$|\beta_{N+j}(\omega)|^2 = 1 \quad \text{and} \quad \beta_i(\omega) = 0 \quad \text{for } i \neq N+j, \tag{3.53}$$

which equivalently means that $\vec{Q}(\omega)$ must project perfectly into the corresponding morphing supermodes \vec{U}_{N+j} . Any non-perfect projection will induce unwanted projections to the other measuring supermodes. It is obvious from here for HD, since \vec{Q} is real, this is only possible when $\vec{U}_i(\omega)$ is real $\forall \omega$, i.e. when the spectral covariance is real. In this case and in this case only can, HD access the optimal squeezing for a given morphing supermodes and at a given frequency $\bar{\omega}$: $\vec{Q} = \vec{U}_j(\bar{\omega})$. \square

In this proof, we also showed a crucial property of the noise spectral power:

Property 3.1.3. *Regardless of whether the $\vec{Q}(\omega)$ is real or complex, the noise spectral power is always real and positive.*

Limited access to squeezing as well as the impossibility of following the morphing behaviour are extremely detrimental in practical situations. Many quantum optical protocols require homodyne to be performed in the time domain: in these cases, the detection signal is acquired as a function of the time over a certain time slot. In the Fourier domain, such a signal simultaneously carries contributions from spectral components at different ω s [189]. Working with a non-morphing LO means projecting the detected field onto the *same* linear combination of longitudinal modes whatever ω . Even if such a linear combination would match a squeezed supermode at $\bar{\omega}$, this is a priori not the case for all other frequency components. As a consequence, time-homodyne signal mixes noise levels associated to the optimal squeezing at $\bar{\omega}$, with the sub-optimal or even anti-squeezed noise contributions associated to all other Fourier components. As understandable, the presence of hidden squeezing further worsens the situation. The inability to work with standard homodyne detection affects a wide range of situations where time-domain homodyning is essential, including heralded state preparations [189, 190, 191] or MBCQ [192], making it urgent to identify a different, better-adapted detection strategy.

Intuitively, we could detect the optimal degree of squeezing (anti-squeezing) only by replacing the real and constant LO coefficients \vec{Q} by a complex and ω -depending vector $\vec{Q}(\omega)$ so that:

$$\Sigma_{\vec{Q}}(\omega) = \vec{Q}^\dagger(\omega) \sigma_{\text{out}}(\omega) \vec{Q}(\omega) \quad (13)$$

which requires a different detection scheme that cannot be homodyne detection, A novel type of detection that we will elucidate in the next subsection.

3.2 Conditions for a spectral covariance matrix

While in previous subsections, we have effectively linked the presence of hidden squeezing to the complex nature of the spectral covariance matrix, it's essential to remind that in the literature

this matrix is generally assumed to be real [50, 49, 48, 187, 51, 53], indicates that a substantial portion quantum correlations might remains elusive to Traditional measurement approaches, such as homodyne detection (HD). Current literature already points to the existence of these hidden correlations [55, 56, 54], the focus has always been on more advanced detection methods such as “resonator detection” [55, 56], “synodine detection” [139] or our novel “interferometers with memory effect” [85]. However, a systematic framework for precisely identifying the underlying interactions responsible for this behaviour is missing.

In this section, we provide precise criteria on cavity-based optical system’ physical parameters (i.e. damping rates, mode hopping and pair production terms) to determine whether a spectral covariance matrix is real or complex. These criteria allow predicting the nature of the Gaussian state solely from the system’s interaction parameters without the necessity of fully characterizing the spectral covariance matrix or the complete quantum state reconstruction. As a consequence, our results allow the appropriate choice of measurement strategies for a better characterization and exploitation of these quantum states. In a complementary way, these criteria also provide a guideline for the design of optical devices to tailor or avoid hidden squeezing.

The goal of the subsections can be summarized as elucidating the relation between \mathcal{M} (Eq. (3.5)) and spectral covariance matrix (Eq. (3.37)) and establishing conditions for distinguishing classes of quantum states with detectable or hidden correlations to HD-like schemes.

3.2.1 Framework

To establish these criteria, we want to gain insights into relating the transfer function $S(\omega)$ (Eq. (3.21)) to the output spectral covariance matrix (Eq. (3.36)) and for that it is useful to explicitly decompose it into the real and imaginary parts $S(\omega) = S_{\text{R}}(\omega) + iS_{\text{I}}(\omega)$ (due to its hermitian

3.2. CONDITIONS FOR A SPECTRAL COVARIANCE MATRIX

nature) using $S_R(\omega) = \frac{1}{2} [S(\omega) + S(-\omega)]$ and $S_I(\omega) = \frac{1}{2i} [S(\omega) - S(-\omega)]$. More explicitly,

$$\begin{aligned}
 S_R(\omega) &= \frac{1}{2} \left(S(\omega) + S^*(\omega) \right) \\
 &= \frac{1}{2} \left(S(\omega) + S(-\omega) \right) \\
 &= \frac{\sqrt{2\Gamma}}{2} \left[(i\omega\mathbb{I} + \Gamma - \mathcal{M})^{-1} + (-i\omega\mathbb{I} + \Gamma - \mathcal{M})^{-1} \right] \sqrt{2\Gamma} - \mathbb{I} \\
 &= \frac{\sqrt{2\Gamma}}{2} \left[(-i\omega\mathbb{I} + \Gamma - \mathcal{M})\text{Inv}(\omega) + (i\omega\mathbb{I} + \Gamma - \mathcal{M})\text{Inv}(\omega) \right] \sqrt{2\Gamma} - \mathbb{I} \\
 S_R(\omega) &= \sqrt{2\Gamma} \left[(\Gamma - \mathcal{M})\text{Inv}(\omega) \right] \sqrt{2\Gamma} - \mathbb{I}
 \end{aligned} \tag{3.54}$$

where we have considered that the product:

$$\begin{aligned}
 \text{Inv}(\omega) &= (-i\omega\mathbb{I} + \Gamma - \mathcal{M})^{-1} (i\omega\mathbb{I} + \Gamma - \mathcal{M})^{-1} \\
 &= (i\omega\mathbb{I} + \Gamma - \mathcal{M})^{-1} (-i\omega\mathbb{I} + \Gamma - \mathcal{M})^{-1} \\
 &= \left((i\omega\mathbb{I} + \Gamma - \mathcal{M})(-i\omega\mathbb{I} + \Gamma - \mathcal{M}) \right)^{-1} \\
 \text{Inv}(\omega) &= \left(\omega^2\mathbb{I} + (\Gamma - \mathcal{M})^2 \right)^{-1}.
 \end{aligned} \tag{3.55}$$

We can further simplify Eq. (3.54) by absorbing the \mathbb{I} in the expression:

$$\begin{aligned}
 S_R(\omega) &= \sqrt{2\Gamma} \left[(\Gamma - \mathcal{M})\text{Inv}(\omega) \right] \sqrt{2\Gamma} - \frac{1}{\sqrt{2\Gamma}} \text{Inv}^{-1}(\omega) \text{Inv}(\omega) \sqrt{2\Gamma} \\
 &= \frac{1}{\sqrt{2\Gamma}} \left[2\Gamma(\Gamma - \mathcal{M}) - \text{Inv}^{-1}(\omega) \right] \text{Inv}(\omega) \sqrt{2\Gamma} \\
 &= \frac{1}{\sqrt{2\Gamma}} \left[2\Gamma(\Gamma - \mathcal{M}) - [\omega^2\mathbb{I} + (\Gamma - \mathcal{M})^2] \right] \text{Inv}(\omega) \sqrt{2\Gamma} \\
 &= \frac{1}{\sqrt{2\Gamma}} \left[(\Gamma + \mathcal{M})(\Gamma - \mathcal{M}) - \omega^2\mathbb{I} \right] \text{Inv}(\omega) \sqrt{2\Gamma} \\
 S_R(\omega) &= \frac{1}{\sqrt{2\Gamma}} \left(\Gamma^2 + [\mathcal{M}, \Gamma] - \mathcal{M}^2 - \omega^2\mathbb{I} \right) \text{Inv}(\omega) \sqrt{2\Gamma},
 \end{aligned} \tag{3.56}$$

where $[\mathcal{M}, \Gamma] = \mathcal{M}\Gamma - \Gamma\mathcal{M}$ represents the commutator between the two matrices.

And similarly

$$\begin{aligned}
 S_I(\omega) &= \frac{1}{2i} (S(\omega) + S^*(\omega)) \\
 &= \frac{1}{2i} (S(\omega) + S(-\omega)) \\
 &= \frac{\sqrt{2\Gamma}}{i} [-i\omega \text{Inv}(\omega)] \sqrt{2\Gamma} \\
 S_I(\omega) &= \sqrt{2\Gamma} [-\omega \text{Inv}(\omega)] \sqrt{2\Gamma}.
 \end{aligned} \tag{3.57}$$

Using Eq. (3.36), we can now decompose the spectral covariance matrix into its real and imaginary parts: $\sigma(\omega) = \sigma_R(\omega) + i\sigma_I(\omega)$ where we have expressed $\sigma_R(\omega)$ and $\sigma_I(\omega)$ in terms of $S_R(\omega)$ and $S_I(\omega)$:

$$\sigma_R(\omega) = \frac{1}{2\sqrt{2\pi}} (S_R(\omega)S_R^T(\omega) + S_I(\omega)S_I^T(\omega)), \tag{3.58}$$

$$\sigma_I(\omega) = \frac{1}{2\sqrt{2\pi}} (S_R(\omega)S_I^T(\omega) - S_I(\omega)S_R^T(\omega)). \tag{3.59}$$

3.2.2 Boundaries to complex spectral covariance matrices

We now seek conditions on the damping matrix Γ and the mode interaction matrix \mathcal{M} that lead to a complex-valued or real-valued spectral covariance matrix $\sigma_{\text{out}}(\omega)$. From Eq. (3.57), it is evident that $S(\omega)$ and consequently $\sigma_{\text{out}}(\omega)$ are always real at $\omega = 0$.

A trivial case, where a complex $S_{\text{out}}(\omega)$ leads to a real $\sigma_{\text{out}}(\omega)$, occurs in the absence of pair-production processes, i.e. $F = 0$. For example, these processes are responsible for the generation of multimode entanglement and squeezing in optical parametric oscillators [96, 144, 193]. Without pair-production processes, the transfer function in Eq. (3.21) becomes unitary, yielding a $\sigma_{\text{out}}(\omega)$ proportional to the identity matrix and therefore real, as illustrated in the grey region of Fig. 3.1. However, this case is not particularly interesting when the primary objective of quantum optical systems is the generation of non-classical quantum states.

When $F \neq 0$, the structure of Eq. (3.59) suggests that a necessary and sufficient condition for the output spectral covariance to be real is that the product $S_R(\omega)S_I^T(\omega)$ must be symmetric.

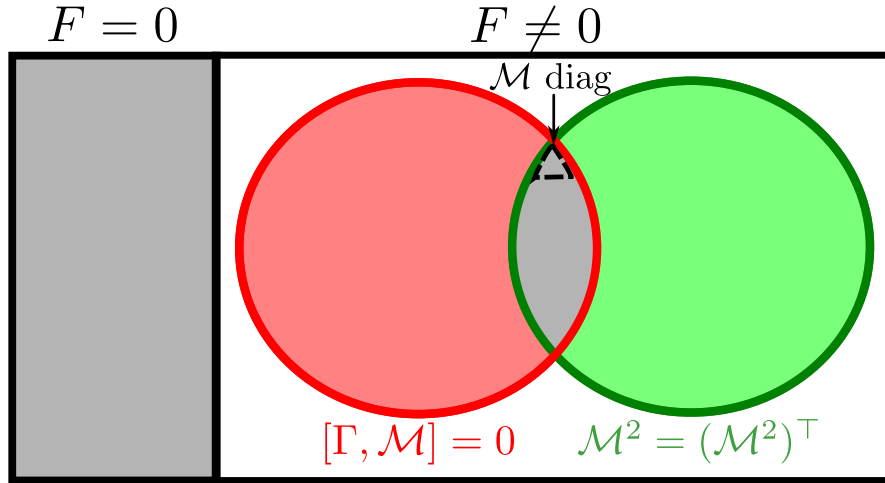


Figure 3.1: **Conditions for a real-valued spectral covariance matrix** $\sigma_{\text{out}}(\omega)$ are represented by the grey areas. The left region represents the trivial case where pair-production processes are absent ($F = 0$), which always leads to a real $\sigma_{\text{out}}(\omega)$. The right region depicts the scenario where pair-production processes are present ($F \neq 0$). In this case, the conditions for achieving a real-valued $\sigma_{\text{out}}(\omega)$ are represented by the overlap of the red circle, corresponding to the commutation between the damping and mode interaction matrices $[\Gamma, \mathcal{M}] = 0$, and the green circle, corresponding to the symmetry of the mode interaction matrix squared $\mathcal{M}^2 = (\mathcal{M}^2)^\top$. This overlap region (grey) delineates the boundaries between real and complex $\sigma_{\text{out}}(\omega)$. Within this region, we represented a subset “ \mathcal{M} diag” corresponding to the case where \mathcal{M} is diagonal. Here, both conditions necessary for a real spectral covariance matrix, are verified.

By substituting Eq. (3.54) and (3.57) into this product, we obtain:

$$\begin{aligned} S_{\text{R}}(\omega)S_{\text{I}}^\top(\omega) &= \frac{-2\omega}{\sqrt{2\Gamma}} \left(\Gamma^2 + [\mathcal{M}, \Gamma] - \mathcal{M}^2 - \omega^2 \mathbb{I} \right) \left[\text{Inv}(\omega)\Gamma\text{Inv}^\top(\omega) \right] \sqrt{2\Gamma} \\ S_{\text{R}}(\omega)S_{\text{I}}^\top(\omega) &= \frac{-2\omega}{\sqrt{2\Gamma}} A(\omega)B(\omega)\sqrt{2\Gamma}, \end{aligned} \quad (3.60)$$

where $A(\omega) = \Gamma^2 + [\mathcal{M}, \Gamma] - \mathcal{M}^2 - \omega^2 \mathbb{I}$ and $B(\omega) = \text{Inv}(\omega)\Gamma\text{Inv}^\top(\omega)$ a symmetric matrix. One can also write the transpose of this Eq. (3.60), $S_{\text{I}}(\omega)S_{\text{R}}^\top(\omega)$ which writes:

$$S_{\text{I}}(\omega)S_{\text{R}}^\top(\omega) = -2\omega\sqrt{2\Gamma}B(\omega)A(\omega)^\top \frac{1}{\sqrt{2\Gamma}}. \quad (3.61)$$

To find out when the product is $S_{\text{R}}(\omega)S_{\text{I}}^\top(\omega)$ is symmetric, we write the difference between

Eq. (3.60) and Eq. (3.61):

$$\begin{aligned} S_R(\omega)S_I^T(\omega) - S_I(\omega)S_R^T(\omega) &= \frac{-2\omega}{\sqrt{2\Gamma}}A(\omega)B(\omega)\frac{2\Gamma}{\sqrt{2\Gamma}} + 2\omega\frac{2\Gamma}{\sqrt{2\Gamma}}B(\omega)A^T(\omega)\frac{1}{\sqrt{2\Gamma}}, \\ S_R(\omega)S_I^T(\omega) - S_I(\omega)S_R^T(\omega) &= \frac{-4\omega}{\sqrt{2\Gamma}}\left(A(\omega)B(\omega)\Gamma - \Gamma B(\omega)A^T(\omega)\right)\frac{1}{\sqrt{2\Gamma}}. \end{aligned} \quad (3.62)$$

By examining the difference $S_R(\omega)S_I^T(\omega) - S_I(\omega)S_R^T(\omega)$ (Eq. (3.62)), it becomes evident that the product $S_R(\omega)S_I^T(\omega)$ is symmetric when $A(\omega)B(\omega)\Gamma = \Gamma B(\omega)A^T(\omega)$. This condition holds only when these 2 following conditions are met at the same time:

- Γ , $A(\omega)$ and $B(\omega)$ commute pair-wise,
- $A(\omega)$ is symmetric : $A^T(\omega) = A(\omega)$.

We prove that the first condition is equivalent to Γ and \mathcal{M} commuting $[\Gamma, \mathcal{M}] = 0$.

Proof. We want to show that for Γ , $A(\omega)$ and $B(\omega)$ to commute pair-wise, one must ensure $[\Gamma, \mathcal{M}] = 0$.

First, for Γ to commute with $A(\omega)$, it must commute with $\Gamma\mathcal{M}$, $\mathcal{M}\Gamma$ and \mathcal{M}^2 . One can easily show that $[\Gamma, \mathcal{M}\Gamma] = 0$ and $[\Gamma, \Gamma\mathcal{M}] = 0$ are both equivalent to $[\Gamma, \mathcal{M}] = 0$, which also ensures that $[\Gamma, \mathcal{M}^2] = 0$. Therefore for Γ to commute with $A(\omega)$, it must commute with \mathcal{M} .

It is also easy to show that since Γ commutes with \mathcal{M} and therefore with \mathcal{M}^2 and $\mathcal{M}\Gamma$, it consequently also commutes with $(\Gamma - \mathcal{M})^2$ and therefore with both $\text{Inv}(\omega)$ and $\text{Inv}^T(\omega)$. This ensures that for Γ to commute with both $A(\omega)$ and $B(\omega)$, it must commute with \mathcal{M} .

To ensure pair-wise commutation between Γ , $A(\omega)$ and $B(\omega)$, it is left to show when $[A(\omega), B(\omega)] = 0$. We can also notice that when Γ commutes with \mathcal{M} , all the previous commutations we mentioned earlier hold true also for Γ^2 and \mathcal{M}^2 . In particular, they both commute with $\text{Inv}(\omega)$ and therefore with $\text{Inv}^T(\omega)$. □

For the second condition, $A(\omega)$ is symmetric if and only if the following two requirements are met:

- (i) $[\Gamma, \mathcal{M}] = [\Gamma, \mathcal{M}^T]$ and
- (ii) $\mathcal{M}^2 = (\mathcal{M}^2)^T$.

3.2. CONDITIONS FOR A SPECTRAL COVARIANCE MATRIX

When Γ and \mathcal{M} commute, condition (i) is automatically satisfied, leaving only condition (ii). This leads us to the following proposition:

Proposition 3.2.1. *For $F \neq 0$, necessary and sufficient conditions for the spectral covariance to be real are $[\Gamma, \mathcal{M}] = 0$ and \mathcal{M}^2 symmetric.*

This proposition is visually represented in the right side of Fig. 3.1, where the grey overlap region of the Venn diagram depicts the intersection of these two conditions: the red subset corresponds to the commutation between the damping and mode interaction matrices, $[\Gamma, \mathcal{M}] = 0$, while the green subset corresponds to the symmetry of the mode interaction matrix squared, $\mathcal{M}^2 = (\mathcal{M}^2)^\top$. Failing to satisfy either of these conditions necessarily leads to an asymmetry of the product $S_R(\omega)S_I^\top(\omega)$, consequently giving rise to a complex spectral covariance matrix.

On one hand, since Γ is diagonal, the commutator $[\Gamma, \mathcal{M}]$ can be zero only if either (i) Γ is proportional to the identity matrix, corresponding to mode-independent damping rates, or (ii) \mathcal{M} is diagonal, or both. It is straightforward to see that scenario (ii) leads to a configuration where $G = 0$ and $F = iD$, with D a real diagonal matrix corresponding to the case of N decoupled squeezed modes. Since a diagonal \mathcal{M} also implies \mathcal{M}^2 symmetric, this situation directly leads to a real spectral covariance matrix. This is represented in Fig. 3.1 by a dashed circle in the intersection between the red and green subsets.

On the other hand, to see how the symmetry of \mathcal{M}^2 reflects on the structure of G and F , it is better to move to the representation of complex amplitudes, where \mathcal{M} transforms into the $2N \times 2N$ matrix $M = iL^\dagger \mathcal{M}L$ (Eq. (1.218)). Specifically, the symmetry of \mathcal{M}^2 is equivalent to the hermiticity of M^2 . In particular, writing out M^2 explicitly

$$M^2 = \begin{pmatrix} G^2 - FF^* & GF - FG^* \\ G^*F^* - F^*G & G^{*2} - F^*F \end{pmatrix}$$

$$M^2 = \begin{pmatrix} G^2 - FF^* & GF - FG^* \\ -(GF - FG^*)^\dagger & (G^2 - FF^*)^\top \end{pmatrix}. \quad (3.63)$$

and examining its block structure, the hermiticity of M^2 implies the hermiticity of its block elements. Since $G = G^\dagger$ and $F = F^\top$, the diagonal blocks are always hermitian. However, the

3.2. CONDITIONS FOR A SPECTRAL COVARIANCE MATRIX

off-diagonal blocks are hermitian only when $GF - FG^* = 0$, or equivalently $GF = (GF)^\top$. One can easily verify that this condition is satisfied, for example, and potentially not limited to, the case where a real-valued G commutes with F . This condition leads us to the following proposition, equivalent to proposition 3.2.1:

Proposition 3.2.2. *For $F \neq 0$, necessary and sufficient conditions for the spectral covariance to be real are $[\Gamma, \mathcal{M}] = 0$ and that the product GF is symmetric $GF = (GF)^\top$.*

Propositions 3.2.1 and 3.2.2 elucidate the transitional boundary between standard and hidden squeezing. Notice that, beyond the trivial cases $F = 0$ and \mathcal{M} diagonal, a generic M , for which $GF = (GF)^\top$, leads to a real spectral covariance matrix only in the case of mode-independent losses, i.e. when Γ is proportional to the identity matrix. These conditions provide insights into the underlying interactions that govern the system's dynamics and can also guide the engineering of complex multimode correlations.

In summary, we have derived key conditions under which the output spectral covariance matrix $\sigma_{\text{out}}(\omega)$ of a cavity-based optical quantum system, characterized by the most general quadratic Hamiltonian, is constrained to be either real- or complex-valued. Specifically, we showed that beyond the trivial cases, $F = 0$ and \mathcal{M} diagonal, the spectral covariance matrix is real for systems with mode-independent damping rates and when the product of the interaction matrices GF is symmetric. Failing to satisfy either of these conditions necessarily results in a complex spectral covariance matrix, indicating the presence of hidden correlations. This connects the structure of the fundamental mode interaction matrices F and G to the real or complex nature of the spectral covariance matrix.

3.2.3 Case studies

To illustrate these conditions, we will present some case studies of cavity-based optical quantum systems which focus on low-dimensional examples, ranging from single- to four-mode systems in Section 3.4.

But already a straightforward prediction from these criteria is that single-mode detuned OPO cannot exhibit complex spectral covariance. First, without multiple modes, there cannot be any relative asymmetry between dissipation rates contained in Γ . Then, since there is only one

3.2. CONDITIONS FOR A SPECTRAL COVARIANCE MATRIX

mode, the matrices F and G are simply reduced to scalars, which guarantees their product GF is always symmetric, satisfying both conditions for a real covariance matrix in Proposition 3.2.2. Intuitively, there are no possibilities to break these symmetries within a single-mode system. Consequently, the spectral covariance matrix $\sigma_{\text{out}}(\omega)$ of the single-mode optical cavity must be real-valued.

Here we particularly want to focus on two specific examples in the literature where the predictive nature of these criteria can lead to interesting conclusions. For example, in their study of broadband squeezing generation in microresonators, Vaidya et al. [194] relied on HD for the full characterization of the generated broadband squeezing. To access a configuration of parameters similar to their experimental setup, we focus on a two-mode detuned $\chi^{(3)}$ -based OPO system described by identical mode decay rates γ . Below the oscillation threshold, the system can be described by a set of linear quantum Langevin equations in the form of Eq. (3.4) where we have the 4×4 damping matrix $\Gamma = \gamma I_{4 \times 4}$ and the mode interaction matrix (Eq. (3.5)) with:

$$G = \begin{pmatrix} g_{11} & 0 \\ 0 & g_{22} \end{pmatrix}, F = \begin{pmatrix} 0 & f_{12} \\ f_{12} & 0 \end{pmatrix}. \quad (3.64)$$

When $g_{11} = g_{22}$, the product GF is symmetric, resulting from Proposition 3.2.2 in a real spectral covariance matrix. This scenario corresponds, exactly, to the parameter configuration in [194]. Notably, in their work, Vaidya et al. relied on HD to access the maximum optimal squeezing levels. Since our criteria predict the absence of hidden squeezing, they also validate the approach taken by Vaidya et al., showing that they indeed could access the maximum optimal squeezing through HD in their experimental configuration. On the other side, in the case of the generation of broadband squeezing in dual-pumped microresonators [195], the authors relying solely on HD schemes, attributed the lower detected squeezing levels entirely to “parasitic” effects from additional interactions. In this work, the authors analyze the generation of squeezed light through SFWM in a dual-pumped microring resonator, focusing on the detection of squeezing in the signal mode s . Their work highlights how squeezing is reduced primarily by unwanted parasitic processes.

Considering their three-mode system m , s and n with two strong classical pumps, the Hamil-

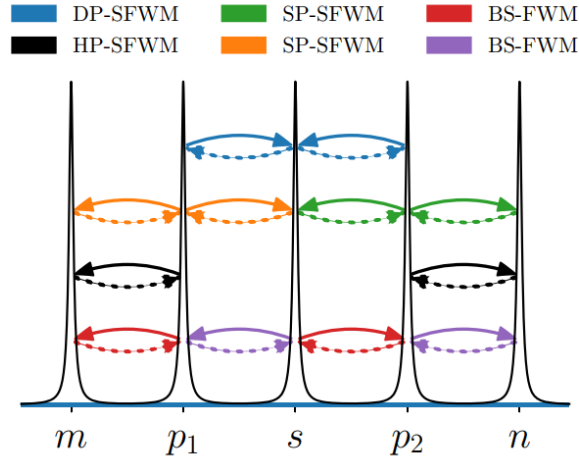


Figure 3.2: **SFWM main and parasitic processes:** figure taken from Seifoory et al. [195] showing four-wave mixing processes in a dual-pumped microring resonator. The diagram illustrates the various nonlinear processes occurring when two resonances p_1 and p_2 are pumped. DP-SFWM (dual-pump spontaneous four-wave mixing) generates squeezing in the s mode, while SP-SFWM (single-pump spontaneous four-wave mixing) and BS-FWM (Bragg-scattering four-wave mixing) are parasitic processes that can degrade squeezing quality. Solid arrows indicate the primary transitions, while dotted arrows of the same colour show the corresponding conjugate processes. The processes are presented at different levels for clarity: BS-FWM (lowest), HP-SFWM (hyperparametric spontaneous four-wave mixing, second level), SP-SFWM (third level), and DP-SFWM (top-level).

tonian for the nonlinear processes includes interactions such self-phase modulation (SPM), cross-phase modulation (XPM), dual-pump spontaneous four-wave mixing (DP-SFWM), single-pump spontaneous four-wave mixing (SP-SFWM), Bragg-scattering four-wave mixing (BS-FWM), and hyperparametric spontaneous four-wave mixing (HP-SFWM), each contributing to the overall dynamics of the system:

$$H = \hbar \sum_J \omega_J b_J^\dagger b_J + H_{\text{SPM}} + H_{\text{XPM}} + H_{\text{DP-SFWM}} \quad (3.65)$$

$$+ H_{\text{SP-SFWM}} + H_{\text{BS-FWM}} + H_{\text{HP-SFWM}} \quad (3.66)$$

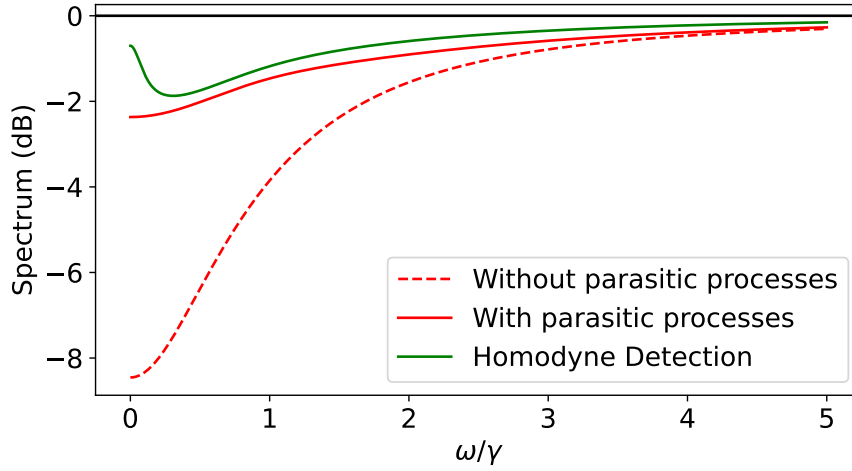


Figure 3.3: Squeezing spectrum of the signal mode (s) with (solid red) and without (dashed red) parasitic processes compared to the squeezing obtained through standard HD (green) optimized at a chosen frequency $\omega = 0.5\gamma$. We considered a dual pumped microresonator system for broadband squeezing generation where G and F are characterized by Eq. (3.73) with $\beta_{p1}\beta_{p2} = 0.46\gamma$ and $|\beta_{p1}|^2 + |\beta_{p2}|^2 - \Delta = 0.15\gamma$. We see that a large portion of the signal squeezing is reduced due to the presence of parasitic processes. However, the squeezing measured via HD (green) still does not match the optimized frequency, the maximum remaining squeezing. In particular, at this frequency, 13% of the squeezing remaining after reduction from the parasitic processes is inaccessible to HD schemes.

where $J \in \{m, s, n\}$, and:

$$H_{\text{SPM}} = -\hbar \frac{\Lambda}{2} (b_{p1}^\dagger b_{p1}^\dagger b_{p1} b_{p1} + b_{p2}^\dagger b_{p2}^\dagger b_{p2} b_{p2}) \quad (3.67)$$

$$H_{\text{XPM}} = -2\hbar\Lambda (b_s^\dagger b_{p1}^\dagger b_s b_{p1} + b_s^\dagger b_{p2}^\dagger b_s b_{p2} + b_{p1}^\dagger b_{p2}^\dagger b_{p1} b_{p2}) \quad (3.68)$$

$$H_{\text{DP-SFWM}} = -\hbar\Lambda b_s^\dagger b_s^\dagger b_{p1} b_{p2} + \text{H.c.} \quad (3.69)$$

$$H_{\text{SP-SFWM}} = -\hbar\Lambda (b_s^\dagger b_s^\dagger b_{p1} b_{p1} + b_s^\dagger b_s^\dagger b_{p2} b_{p2}) + \text{H.c.} \quad (3.70)$$

$$H_{\text{BS-FWM}} = -2\hbar\Lambda (b_{p2}^\dagger b_s^\dagger b_{p1} b_s + b_{p1}^\dagger b_s^\dagger b_{p2} b_s) + \text{H.c.} \quad (3.71)$$

$$H_{\text{HP-SFWM}} = -2\hbar\Lambda b_s^\dagger b_s^\dagger b_{p1} b_{p2} + \text{H.c.} \quad (3.72)$$

The main process for producing degenerate squeezed vacuum state DP-SFWM and the main process responsible for squeezing reduction is SP-SFWM, which injects uncorrelated photons into the signal resonance. BS-FWM and HP-SFWM also contribute to squeezing degradation but to a lesser extent than SP-SFWM.

3.2. CONDITIONS FOR A SPECTRAL COVARIANCE MATRIX

In the classical pumps approximation and moving to the interaction picture, the dynamics of the system can be described by the quantum Langevin equations in Eq. (3.4) where $\Gamma = \gamma I_{6 \times 6}$ and the matrices G and F are :

$$G = - \begin{pmatrix} |\beta_{p1}|^2 + |\beta_{p2}|^2 - \Delta & \beta_{p1}\beta_{p2}^* & 0 \\ \beta_{p1}^*\beta_{p2} & |\beta_{p1}|^2 + |\beta_{p2}|^2 - \Delta & \beta_{p1}\beta_{p2}^* \\ 0 & \beta_{p1}^*\beta_{p2} & |\beta_{p1}|^2 + |\beta_{p2}|^2 - \Delta \end{pmatrix},$$

$$F = - \begin{pmatrix} 0 & \beta_{p1}^2 & 2\beta_{p1}\beta_{p2} \\ \beta_{p1}^2 & \beta_{p1}\beta_{p2} & \beta_{p2}^2 \\ 2\beta_{p1}\beta_{p2} & \beta_{p2}^2 & 0 \end{pmatrix}. \quad (3.73)$$

Here, β_{p1} and β_{p2} are proportional to the complex classical pump amplitudes β'_j with $\beta_j = \sqrt{2\Lambda}\beta'_j$, j in $\{p_1, p_2\}$ and Λ represents the nonlinear coefficient quantifying the strength of the nonlinear optical processes. We have considered without loss of generality the same detuning Δ to the microring resonances for both pumps.

To verify Proposition 3.2.2, we observe that the product GF is not symmetric:

$$GF - (GF)^\top = \begin{pmatrix} 0 & -\beta_{p1}^2|\beta_{p2}|^2 & \beta_{p1}\beta_{p2}(|\beta_{p2}|^2 - |\beta_{p1}|^2) \\ \beta_{p1}^2|\beta_{p2}|^2 & 0 & \beta_{p2}^2|\beta_{p1}|^2 \\ \beta_{p1}\beta_{p2}(|\beta_{p1}|^2 - |\beta_{p2}|^2) & -\beta_{p2}^2|\beta_{p1}|^2 & 0 \end{pmatrix} \neq 0, \quad (3.74)$$

leading a complex spectral covariance matrix for the three-mode system. This complexity persists even when we trace down the system to a single mode, focusing only on the signal mode. The corresponding spectral covariance therefore remains complex. As discussed previously and shown in [86], this complexity has a significant implication: even after the reduction of squeezing due to parasitic processes, HD still cannot fully access all the remaining squeezing still available in the s mode. This is illustrated in Fig. 3.3 where we show the squeezing spectrum of the signal mode (s) under various conditions for the dual-pumped microresonator system described by Seifoory et al. [195] with chosen parameters $\beta_{p1}\beta_{p2} = 0.46\gamma$ and $|\beta_{p1}|^2 + |\beta_{p2}|^2 - \Delta = 0.15\gamma$. The solid (dashed) red line represents the spectrum without (with) parasitic processes and the green line indicates the squeezing obtained through standard HD,

optimized at $\omega = 0.5\gamma$. As shown by the difference between the solid and dashed red lines, it's evident that a significant portion of the signal squeezing is reduced when parasitic processes are present. Furthermore, the squeezing measured via HD (green line) accounts only for 83% of the maximum available remaining squeezing, in the presence of parasitic processes at the optimized frequency $\omega = 0.5\gamma$. Suboptimal squeezing measurements are therefore not solely due to parasitic processes, as suggested by Seifoory et al. Rather, our criteria predict 13% of the detectable squeezing is hidden from HD and can be revealed by the use of novel detection schemes [55, 139, 85].

The squeezing spectrum without parasitic processes shown in dashed-red in Fig. 3.3 was obtained using the strategy described by Zhang et al. [196]. Their approach employs a photonic molecule consisting of two coupled microring resonators on an integrated nanophotonic chip. This design selectively hybridizes only the modes involved in unwanted processes, effectively suppressing parasitic processes such as DP-SFWM, BS-FWM, and HP-SFWM.

In particular, beyond the effectiveness of this method in suppressing parasitic processes, our criteria show that this method also addresses the issue of hidden squeezing. This can be demonstrated by examining the new interaction matrices of the new system when parasitic processes are suppressed: $G = (|\beta_{p1}|^2 + |\beta_{p2}|^2 - \Delta)I_{3 \times 3}$ and $F = -\text{diag}\{0, \beta_{p1}\beta_{p2}, 0\}$. The symmetry of the product GF implies that homodyne detection can access the optimal squeezing in cases where these parasitic processes are suppressed.

Our analysis predicts, however, that even when accounting for these parasitic processes, there exists additional hidden and detectable squeezing that remains inaccessible to conventional HD techniques.

3.3 Achieving generalized quantum mode-matching

Now we cleared out criteria that allow to predict whether or not the spectral covariance matrix is complex, we discuss our strategy for a new type of interferometer that allows us to deal with not only the complexity of the spectral covariance matrix but also the morphing behaviour required to recover optimal squeezing in a the bandwidth.

In order to project onto the i -th morphing supermode, not only one should be able to produce

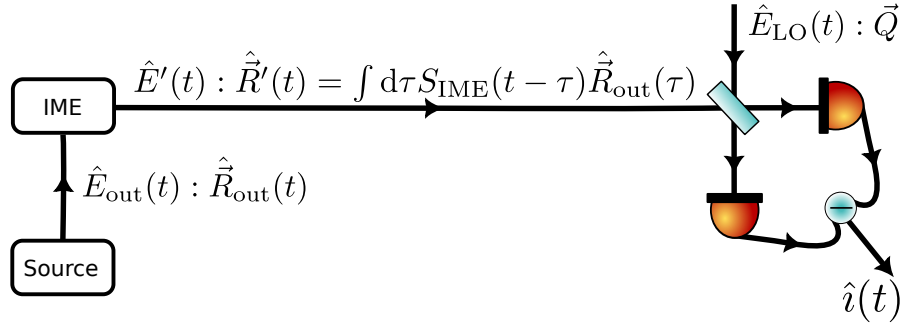


Figure 3.4: This scheme outlines the generalized mode-matching through an interferometer with memory. In the first stage, the physical system generates the CV quantum resource, with its output denoted as $\hat{E}_{\text{out}}(t)$ and associated with the vector of quadratures $\hat{\vec{R}}_{\text{out}}(t)$. This output then undergoes the second stage, which is an IME characterized by a transfer function $S_{\text{IME}}(\omega)$. Subsequently, the IME output, characterized by the vector of quadratures $\hat{\vec{R}}'(t)$, is directed into a traditional HD scheme with a LO described by the vector \vec{Q} .

a LO associated with a complex and frequency-dependent $\vec{Q}(\omega)$

$$\vec{Q} \rightarrow \vec{Q}(\omega), \quad (3.75)$$

but also to implement, in the frequency domain, the multiplication between this LO and the targeted field, so as to induce a linear combination giving the quadrature, $\hat{R}_{\text{out},i}^{(s)}(\omega)$, of the i -th morphing supermode

$$\hat{R}_{\text{out},i}^{(s)}(\omega) = \vec{Q}^\dagger(\omega) \hat{\vec{R}}_{\text{out}}(\omega) \quad (3.76)$$

when $\vec{Q}(\omega)$ is shaped as $\vec{U}_i(\omega)$. A simple shaping of the LO in order to produce a time-dependent profile with Fourier transform $\vec{Q}(\omega)$ would not be sufficient. Indeed, in a standard HD, the mixing of the LO and the signal field at a beamsplitter rather leads to a multiplication in time domain. Therefore this approach, known as "synodyne detection" and proposed by Buchmann *et al.* in [139] for the HD of singlemode ponderomotive squeezing and then we expanded to its multimode scenario in Subection 1.5.5 is able to mode-match complex supermodes but not their morphing behaviour.

To obtain, in the frequency domain, a transformation such as Eq. (3.76), we must look for a

3.3. ACHIEVING GENERALIZED QUANTUM MODE-MATCHING

physical system that implements, in time domain, the following transformation of the signal field

$$\hat{R}_{\text{out},i}^{(s)}(t) = \int d\tau \vec{Q}^T(t - \tau) \hat{\vec{R}}_{\text{out}}(\tau). \quad (3.77)$$

In other words, we need a physical system that is linear and possesses both memory, as optical cavities, and the capability to mix the input quadratures, as interferometers. These two characteristics define a device we refer to as an "interferometer with a memory effect"(IME). The transformation Eq. (3.76) or, equivalently, Eq. (3.77) can be physically implemented by cascading, at the output of the source of quantum light, an IME and a standard HD, as depicted in (3.4).

The IME transforms the quadratures, $\hat{\vec{R}}_{\text{out}}(\omega)$, of the output of the multimode source according to the relation:

$$\hat{\vec{R}}'(\omega) = S_{\text{IME}}(\omega) \hat{\vec{R}}_{\text{out}}(\omega), \quad (3.78)$$

where $S_{\text{IME}}(\omega)$ is the IME transfer function. The HD photocurrent operator, thus, becomes:

$$\hat{i}(\omega) \propto \vec{Q}^T \hat{\vec{R}}'(\omega) \propto \vec{Q}^{\dagger}(\omega) \hat{\vec{R}}_{\text{out}}(\omega), \quad (3.79)$$

with a generalized LO given by $\vec{Q}^{\dagger}(\omega)$

$$\vec{Q}^{\dagger}(\omega) = \vec{Q}^T S_{\text{IME}}(\omega). \quad (3.80)$$

The combination of a tailored LO, with real and non-morphing \vec{Q} , and of a suitably engineered $S_{\text{IME}}(\omega)$ allows $\vec{Q}^{\dagger}(\omega)$ to match $\vec{U}_{N+i}(\omega)$ as required to fully detect the squeezing of the $(N+i)$ -th morphing supermode.

Proof. Leveraging the Eqs. (3.50) and (3.52) we got in Proof 3.1.5 where we decompose the generalized LO obtained with an IME $\vec{Q}^{\dagger}(\omega)$ and decomposed in the basis of the morphing su-

3.3. ACHIEVING GENERALIZED QUANTUM MODE-MATCHING

permodes

$$\vec{Q}(\omega) = \sum_{i=1}^{2N} \beta_i(\omega) \vec{U}_i(\omega) \quad \text{with} \quad \beta_i(\omega) = \langle \vec{Q}(\omega), \vec{U}_i(\omega) \rangle \quad (3.81)$$

and recovered the general expression of the noise spectral power in terms of the projection of the generalized noise spectral power in terms of morphing supermodes :

$$\Sigma_{\vec{Q}}(\omega) = \frac{1}{2\sqrt{2\pi}} \left(\sum_{i=1}^N d_i^2(\omega) |\beta_i(\omega)|^2 + \sum_{i=1}^N d_i^{-2}(\omega) |\beta_{N+i}(\omega)|^2 \right) > 0. \quad (3.82)$$

Because the generalized LO $\vec{Q}(\omega)$ is always complex and frequency-dependent $\vec{u}_i(\omega)$ as are the morphing supermodes, it is always possible to engineer the IME such that the condition in Eq. (3.53) holds. This means to recover for example the squeezing spectrum of mode j ($d_j^2(\omega)$)

$$|\beta_{N+j}(\omega)|^2 = 1 \quad \text{and} \quad \beta_i(\omega) = 0 \quad \text{for} \quad i \neq N + j. \quad (3.83)$$

□

It is also natural to wonder after such assessment, how this type of interferometer deals with real spectral covariance matrices, since the new local oscillator is always complex for nonzero frequencies as shown by Eq. (3.80). We show that projecting $|\vec{Q}(\omega)|$ in the real desired morphing supermodes will be enough for spectral covariance matrices.

Proof. In scenarios where the spectral covariance matrix $\sigma_{out}(\omega)$ is real, the IME can still achieve optimal squeezing despite using a complex local oscillator (LO) vector $\vec{Q}(\omega)$. When $\sigma_{out}(\omega)$ is real, the morphing supermodes $\vec{U}_j(\omega)$ are also real. From Proof 3.1.5, the noise spectral power in the IME is given by:

$$\Sigma_{\text{IME}}(\omega) = \frac{1}{2\sqrt{2\pi}} \sum_{i=1}^{2N} \lambda_i^2(\omega) |\beta_i(\omega)|^2 \quad (3.84)$$

3.3. ACHIEVING GENERALIZED QUANTUM MODE-MATCHING

where

$$\lambda_i^2(\omega) = \begin{cases} d_i^{-2}(\omega) & \text{for } i \in [1, N] \\ d_{i-N}^2(\omega) & \text{for } i \in [N + 1, 2N] \end{cases} \quad (3.85)$$

and $\beta_i(\omega) = \vec{Q}^\top(\omega)\vec{U}_i(\omega)$. To recover the squeezing or antisqueezing spectrum $\lambda_j^2(\omega)$ for a specific supermode $\vec{U}_j(\omega)$, it is necessary to ensure that $|\beta_j(\omega)|^2 = 1$ while $\beta_i(\omega) = 0$ for all $i \neq j$. For real valued $\vec{U}_j(\omega)$, this condition is satisfied when choosing the LO vector $\vec{Q}(\omega)$ to align with the desired supermode $\vec{U}_j(\omega)$ up to local frequency dependent phase factor:

$$\vec{Q}(\omega) = \varphi(\omega)\vec{U}_j(\omega) \quad (3.86)$$

where $\varphi(\omega)$ is a diagonal phase matrix defined as $\phi(\omega) = \text{diag}(e^{i\phi_1(\omega)}, \dots, e^{i\phi_{2N}(\omega)})$. Evaluating $|\beta_j(\omega)|^2$ under this choice yields:

$$|\beta_j(\omega)|^2 = |\vec{Q}^\top(\omega)\vec{U}_j(\omega)|^2 = |\phi(\omega)\vec{U}_j^\top(\omega)\vec{U}_j(\omega)|^2 = |\vec{U}_j^\top(\omega)\vec{U}_j(\omega)|^2 = 1 \quad (3.87)$$

This equality holds because $\vec{U}_j(\omega)$ is real and normalized, satisfying $\vec{U}_j^\top(\omega)\vec{U}_j(\omega) = 1$. Additionally, for $i \neq j$, the orthonormality of the supermodes ensures that $\beta_i(\omega) = 0$. Consequently, the noise spectral power simplifies to:

$$\Sigma_{\text{IME}}(\omega) = \frac{1}{2\sqrt{2\pi}}\lambda_j^2(\omega) \quad (3.88)$$

This result demonstrates that, when the spectral covariance matrix is real, the IME can achieve the desired squeezing spectrum $\lambda_j^2(\omega)$ by appropriately choosing the complex LO vector $\vec{Q}(\omega)$. Therefore, even though the LO in the IME is inherently complex, it can fully recover the optimal squeezing performance when operating with a real covariance matrix. \square

Since the IME stage must not change the amount of squeezing (anti-squeezing), this system should implement a passive transformation ($F = 0$ in Eqs. (3.3) and (3.5)). Thus, the corresponding transfer function that solves the quantum Langevin equations Eq. (3.21), in Fourier

3.3. ACHIEVING GENERALIZED QUANTUM MODE-MATCHING

domain, reads as:

$$S_{\text{IME}}(\omega) = \sqrt{2\Gamma_{\text{IME}}} (i\omega\mathbb{I} + \Gamma_{\text{IME}} - \mathcal{M}_{\text{IME}})^{-1} \sqrt{2\Gamma_{\text{IME}}} - \mathbb{I} \quad (3.89)$$

with mode-dependent losses matrix Γ_{IME} and the coupling matrix given by

$$\mathcal{M}_{\text{IME}} = \left(\begin{array}{c|c} \text{Im}[G_{\text{IME}}] & \text{Re}[G_{\text{IME}}] \\ \hline -\text{Re}[G_{\text{IME}}] & -\text{Im}[G_{\text{IME}}]^{\text{T}} \end{array} \right), \quad (3.90)$$

where G_{IME} is the most general hermitian matrix. At the output of the IME the state is characterized by the spectral covariance matrix

$$\sigma'(\omega) = \hat{R}'(\omega) \hat{R}'^{\text{T}}(-\omega) \quad (3.91)$$

$$= S_{\text{IME}}(\omega) \sigma_{\text{out}}(\omega) S_{\text{IME}}^{\text{T}}(-\omega), \quad (3.92)$$

and the noise spectral power obtained by the HD after the IME (considering again input vacuum for the input source) is

$$\Sigma_{\vec{Q}}(\omega) = \Sigma_{\text{IME}}(\omega) = \frac{1}{2\sqrt{2\pi}} [\vec{Q}^{\dagger}(\omega) U(\omega)] D^2(\omega) [U^{\dagger}(\omega) \vec{Q}(\omega)] \quad (3.93)$$

where $\vec{Q}(\omega)$ is given by expression Eq. (3.80).

The IME can be realized to ensure mode-matching in different ways:

- The most obvious one is to consider realizing the mode-matching simultaneously for all the frequency-dependent supermodes through a unique IME configuration by requiring the product $S_{\text{IME}}(\omega)U(\omega)$ to not only be real but also verify

$$\frac{d}{d\omega} [S_{\text{IME}}(\omega)U(\omega)] = 0. \quad (3.94)$$

This condition only leverages the degree of freedom of the IME and says $S_{\text{IME}}(\omega)U(\omega) = C$ where C is a constant matrix, the noise spectral power in Eq. (3.93) can now be written

3.3. ACHIEVING GENERALIZED QUANTUM MODE-MATCHING

as

$$\Sigma_{\tilde{Q}}(\omega) = \frac{1}{2\sqrt{2\pi}} Q^T C D^2(\omega) C^T Q. \quad (3.95)$$

In this case to access $d_i(\omega)$, we just have to choose the phase of the LO such that QC is a vector where only the i -th element value is 1 while others are 0. For example, for $QC = (1, 0, \dots, 0)^T$,

$$\Sigma_{\text{IME}}(\omega) = \frac{1}{2\sqrt{2\pi}} d_1^2(\omega), \quad (3.96)$$

For example, for $QC = (0, 0, \dots, 1)^T$,

$$\Sigma_{\text{IME}}(\omega) = \frac{1}{2\sqrt{2\pi}} d_1^{-2}(\omega), \quad (3.97)$$

As a special case, the condition for full mode-matching is verified by C matrices such that $|C| = I_{2N}$. This involves matrices like I_{2N} and S such that

$$S = \begin{pmatrix} I_N & 0 \\ 0 & -I_N \end{pmatrix} \quad (3.98)$$

Other solutions are also possible since any passive transformation that allows us to turn the noise spectral power into any form similar to Eq. (3.149) but with any permutation of the eigenvalues in $D^2(\omega)$, for example with elements such as:

$$\Omega = \begin{pmatrix} 0 & I_N \\ I_N & 0 \end{pmatrix}, K = \begin{pmatrix} 0 & I_N \\ -I_N & 0 \end{pmatrix}, \quad (3.99)$$

Focusing on a specific case where we required for example $S_{\text{IME}}(\omega)U(\omega) = I_{2N}$ implies a transformation $S_{\text{IME}}(\omega)$ that matches U^\dagger . This is a very important comment to have in mind in later sections when thinking of decomposing the IME in terms of elementary photonic components. Such decomposition is equivalent in a way to the decomposition of the morphing supermodes.

However, it is clear that trying to find an IME that satisfies this condition represents in Eq. (3.94) requires a much harder optimization problem since it involves an optimization on matrices whose elements are functions of a continuous variable ω . More advanced tools for continuous variable optimizations would be required, which are not the focus of this thesis. Additionally, this method requires the full knowledge of the morphing supermodes matrix with extreme precisions, something that is not always possible in experimental situations.

- The second option is the one we consider mostly in this thesis and involves as we discussed earlier, focusing on a configuration of the IME allowing $\vec{Q}(\omega)$ to match $\vec{U}_{N+i}(\omega)$ (respectively $\vec{U}_i(\omega)$) to detect the squeezing (respectively) antisqueezing of the $(N+i)$ -th (respectively i -th) morphing supermode. We later practically show that this option does not require a knowledge of the morphing supermodes but only access to the noise spectral power of the considered detection, a situation that's more realistic when accounting for experimental constraints. In the same spirit of thinking about experimental setup, in this thesis, our focus also is on the detection of squeezing spectrum mostly since the noise levels of the antisqueezing in an experimental setup are amplified.

3.3.1 Implementing the interferometer with memory effect

The IME is a passive, linear system that is able to implement an arbitrary transformation described by a frequency-dependent unitary $S_{\text{IME}}(\omega)$ or equivalently $U(\omega)$ for some the more general case. To identify the optical system implementing the IME, we introduce an original technique to decompose any $S_{\text{IME}}(\omega)$ (or equivalently $U(\omega)$) in terms of networks of basic photonic components arranged in specific architectures: changing the components' parameters allows realizing different $S_{\text{IME}}(\omega)$. To detect a target squeezed morphing supermode, such parameters are numerically optimized to make $\vec{Q}^\dagger(\omega)$ match $\vec{U}_{N+i}(\omega)$ in Eq. (3.80) or in a much more optimistic scenario to $S_{\text{IME}}(\omega)$ match $U(\omega)$. Our method extends ideas introduced in the context of discrete spatial modes [197] in order to find decompositions that are smooth with respect to ω .

For practical purposes, we approach this problem in the representation $\hat{\xi} = (\hat{a}|\hat{a}^\dagger)^T$ of the

3.3. ACHIEVING GENERALIZED QUANTUM MODE-MATCHING

complex field amplitudes, where $\hat{a} = (\hat{a}_1, \dots, \hat{a}_N)$. In this case, the transfer function of the IME is given by $\mathbb{U}_{\text{IME}}(\omega) = L^\dagger S_{\text{IME}}(\omega) L$, with $L = \frac{1}{\sqrt{2}} \begin{pmatrix} I & I \\ -iI & iI \end{pmatrix}$, I being the identity matrix, and it assumes the form

$$\mathbb{U}_{\text{IME}}(\omega) = \left(\begin{array}{c|c} U_{\text{IME}}(\omega) & 0 \\ \hline 0 & U_{\text{IME}}^*(-\omega) \end{array} \right), \quad (3.100)$$

where $U_{\text{IME}}(\omega)$ is a $N \times N$ smooth unitary matrix-valued function of ω .

In the following subsections we will introduce two novel frequency-dependent decomposition into elementary components, each with their own advantages.

3.3.2 Smooth two-mode decomposition

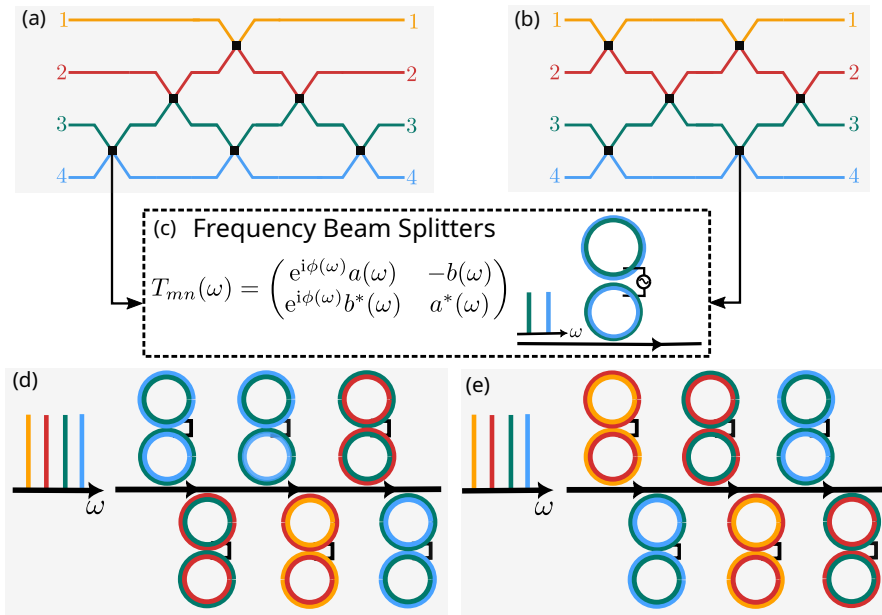


Figure 3.5: Smooth two-mode decomposition of a 4-mode passive transformation with (a) triangular mesh and (b) rectangular mesh. Two-mode unitary (c) and its physical implementation via a two-mode coupled cavity. Implementation in an integrated platform of microresonators of respectively the (d) triangular and (e) rectangular decomposition.

A first possible decomposition of the matrix $U_{\text{IME}}(\omega)$ can be done in terms of elementary bricks that correspond to 2-mode passive transformations. Specifically, we show that frequency-

3.3. ACHIEVING GENERALIZED QUANTUM MODE-MATCHING

dependent unitary transformations can be systematically synthesized from basic components through the following proposition:

Proposition 3.3.1. *Any $N \times N$ frequency-dependent unitary can be decomposed into a mesh of at most $N(N - 1)/2$ two-mode frequency-dependent unitaries $T_{mn}(\omega)$, Fig. 3.5c.*

Therefore,

$$U_{\text{IME}}(\omega) = \prod_{(m,n)} T_{mn}(\omega), \quad (3.101)$$

where the $T_{mn}(\omega)$ are the most general $N \times N$ unitary transformations that leave uncoupled all the modes with the exception of the two modes labelled with indices $m, n \in \{1, 2, \dots, N\}$.

The explicit and full expression of these matrices, known in the literature as “two-level unitaries”, in a practical situation where the decomposition involves only neighbouring modes m and $n = m \pm 1$, is given by

$$T_{mn}(\omega) = \begin{pmatrix} 1 & 0 & \cdots & \cdots & \cdots & \cdots & \cdots & 0 \\ 0 & 1 & & & & & & \vdots \\ \vdots & & \ddots & & & & & \vdots \\ \vdots & & & e^{i\phi(\omega)}a(\omega) & -b(\omega) & & & \vdots \\ \vdots & & & e^{i\phi(\omega)}b^*(\omega) & a^*(\omega) & & & \vdots \\ \vdots & & & & & \ddots & & \vdots \\ \vdots & & & & & & 1 & 0 \\ 0 & \cdots & \cdots & \cdots & \cdots & \cdots & 0 & 1 \end{pmatrix}, \quad (3.102)$$

where $a(\omega)$ and $b(\omega)$ are frequency dependant complex coefficients satisfying $|a(\omega)|^2 + |b(\omega)|^2 = 1$ and $e^{i\phi(\omega)}$ the determinant of the two level unitary. For the sake of brevity and with a (minor) abuse of notation, we have assimilated the $T_{mn}(\omega)$ to their 2×2 form in their most interesting two-dimension subspace:

$$T_{mn}(\omega) = \begin{pmatrix} e^{i\phi(\omega)}a(\omega) & -b(\omega) \\ e^{i\phi(\omega)}b^*(\omega) & a^*(\omega) \end{pmatrix}, \quad (3.103)$$

3.3. ACHIEVING GENERALIZED QUANTUM MODE-MATCHING

and our discussion will involve mostly that two-dimensional subspace. From this point, we would like to look at ways to implement these two-level unitaries.

Initially, we could consider the most general passive transformation given by Eqs. (3.89) and (3.90) with the most general 2×2 complex hermitian matrix

$$G_{\text{IME}}^{(2)} = \begin{pmatrix} \Delta_m & \theta_d e^{-i\phi_d} \\ \theta_d e^{i\phi_d} & \Delta_n \end{pmatrix}. \quad (3.104)$$

While $T_{mn}(\omega)$ can have arbitrary frequency-dependent profiles subject only to the unitarity constraint $|a(\omega)|^2 + |b(\omega)|^2 = 1$, the general passive transformation obtained from Eqs. (3.89) provides a specific functional form, but by combining these passive transformations, we can approximate more general frequency-dependent profiles required by the two-level unitaries.

Note that, while coupled two-mode cavities serve as useful building blocks, their frequency-dependent coupling profiles may become insufficient to match the required $T_{mn}(\omega)$ over large optical bandwidths. In particular, as the bandwidth increases, a single two-mode cavity may not have the spectral flexibility needed to implement, even in an approximated way, any arbitrary $T_{mn}(\omega)$ in the whole spectrum. In this condition, the degrees of freedom can be increased by using a linear cascade of two-mode cavities for each $T_{mn}(\omega)$ or handling each subset of the overall bandwidth with different cavities.

Implementing a desired IME thus relies on the capability to engineer $G_{\text{IME}}^{(2)}$. Its elements represent couplings between two frequency modes. This can be physically implemented by means of systems of coupled cavities, that act as a frequency beam splitter, and that are accessible to experimental realizations in integrated optics as already demonstrated in the literature [198, 199].

The approach presented in [198], for example, employs an integrated photonic platform involving two coupled microresonators, as illustrated in Eq. (3.5)c. Through evanescent coupling, the resonances of a pair of hybridized modes can be precisely tuned close to the targeted optical modes Ω_m and Ω_n , achieving the desired elements Δ_m and Δ_n . Additionally, the microwave driving (or electro-optic modulation) applied to the resonators allows to engineering the coupling $\theta_d e^{-i\phi_d}$ between the hybrid modes. In particular, θ_d and ϕ_d can be controlled through the

3.3. ACHIEVING GENERALIZED QUANTUM MODE-MATCHING

driving modulation strength and the phase of the microwave field, respectively, with an effective Hamiltonian in the form:

$$\hat{H} = \theta \left(e^{-i\phi_p} \hat{a}_1^\dagger \hat{a}_2 + e^{i\phi_p} \hat{a}_2^\dagger \hat{a}_1 \right). \quad (3.105)$$

The $T_{m,n}(\omega)$ can therefore be implemented through this coupled cavity involving the modes m and n , leaving the remaining $N - 2$ modes unchanged. The complete N -mode transformation $U_{\text{IME}}(\omega)$ can be systematically constructed by choosing a specific order in which to perform the multiplication in Eq. (3.101) of the appropriate two-mode mode coupled cavity $T_{mn}(\omega)$. The frequency-dependent unitary $T_{mn}(\omega)$ is chosen in order to null the element $[U_{\text{IME}}(\omega)]_{mn}$ using the following proposition :

Proposition 3.3.2. *By using matrix elements in the same row or column, any element $u_{mn}(\omega)$ of a unitary matrix $U_{\text{IME}}(\omega)$ can be nulled through the multiplication by the appropriate two-level unitaries $T_{m,n}(\omega)$.*

The allowed structure of the unitaries is provided by a relation on the relation on the product of the determinant:

$$\prod_{(mn)} \det [T_{m,n}(\omega)] = \det [U(\omega)]. \quad (3.106)$$

We illustrate this Proposition in the case of a 4×4 smooth unitary matrix

$$U_{\text{IME}}(\omega) = \begin{bmatrix} u_{11}(\omega) & u_{12}(\omega) & u_{13}(\omega) & u_{14}(\omega) \\ u_{21}(\omega) & u_{22}(\omega) & u_{23}(\omega) & u_{24}(\omega) \\ u_{31}(\omega) & u_{32}(\omega) & u_{33}(\omega) & u_{34}(\omega) \\ u_{41}(\omega) & u_{42}(\omega) & u_{43}(\omega) & u_{44}(\omega) \end{bmatrix}, \quad (3.107)$$

however, the general case to N dimensions can be proved by recursion.

To null for example the element $u_{21}(\omega)$ using an element of the same column (say $u_{31}(\omega)$),

3.3. ACHIEVING GENERALIZED QUANTUM MODE-MATCHING

we can use the following frequency-dependant transformation between modes 2 and 3:

$$T_{23}(\omega) = \frac{1}{\sqrt{|u_{21}(\omega)|^2 + |u_{31}(\omega)|^2}} \begin{bmatrix} 1 & 0 & 0 & 0 \\ 0 & e^{i\phi_{23}(\omega)}u_{31}(\omega) & -e^{i\phi_{23}(\omega)}u_{21}(\omega) & 0 \\ 0 & u_{21}^*(\omega) & u_{31}^*(\omega) & 0 \\ 0 & 0 & 0 & 1 \end{bmatrix} \quad (3.108)$$

$$\Rightarrow T_{23}(\omega)U(\omega) = \begin{bmatrix} * & * & * & * \\ 0 & * & * & * \\ * & * & * & * \\ * & * & * & * \end{bmatrix}. \quad (3.109)$$

Similarly, one can choose to null the element $u_{21}(\omega)$ using instead an element of the same line (say $u_{22}(\omega)$) with the following frequency-dependent transformation between modes 1 and 2:

$$T_{12}(\omega) = \frac{1}{\sqrt{|u_{21}(\omega)|^2 + |u_{22}(\omega)|^2}} \begin{bmatrix} 1 & 0 & 0 & 0 \\ 0 & e^{i\phi_{12}(\omega)}u_{22}(\omega) & -e^{i\phi_{12}(\omega)}u_{21}(\omega) & 0 \\ 0 & u_{21}^*(\omega) & u_{22}^*(\omega) & 0 \\ 0 & 0 & 0 & 1 \end{bmatrix} \quad (3.110)$$

$$\Rightarrow U(\omega)T_{12}^\dagger(\omega) = \begin{bmatrix} * & * & * & * \\ 0 & * & * & * \\ * & * & * & * \\ * & * & * & * \end{bmatrix}. \quad (3.111)$$

Each nulling operation corresponds to a two-mode coupled cavity between adjacent modes. The geometry of the full mesh is defined by the nulling sequence. For example, nulling elements using only other elements of their same column, column-by-column from the bottom left, going up, as shown in Fig. 3.6 for 4 modes generate a triangular mesh (Fig. 3.5a), reminiscing of Reck's arrangement [200] for spatial modes. This is because once all the lower diagonal elements have been nulled, the final product of smooth matrices is an upper triangular matrix. Due to the unitary nature of $U_{\text{IME}}(\omega)$, such an upper triangular matrix is necessarily diagonal. And by respecting the determinant structure from (3.106), such diagonal matrix is necessarily

3.3. ACHIEVING GENERALIZED QUANTUM MODE-MATCHING

$$\begin{aligned}
 U(\omega) &= \begin{bmatrix} * & * & * & * \\ * & * & * & * \\ * & * & * & * \\ \oplus & * & * & * \end{bmatrix} \xrightarrow{T_{34}(\omega)} T_{34}(\omega)U(\omega) = \begin{bmatrix} * & * & * & * \\ * & * & * & * \\ \oplus & * & * & * \\ 0 & * & * & * \end{bmatrix} \xrightarrow{T_{23}(\omega)} T_{23}(\omega)T_{34}(\omega)U(\omega) = \begin{bmatrix} * & * & * & * \\ \oplus & * & * & * \\ 0 & * & * & * \\ 0 & * & * & * \end{bmatrix} \xrightarrow{T_{12}(\omega)} \\
 T_{12}(\omega)T_{23}(\omega)T_{34}(\omega)U(\omega) &= \begin{bmatrix} * & * & * & * \\ 0 & * & * & * \\ 0 & * & * & * \\ 0 & \oplus & * & * \end{bmatrix} \xrightarrow{T'_{34}(\omega)} T'_{34}(\omega)T_{12}(\omega)T_{23}(\omega)T_{34}(\omega)U(\omega) = \begin{bmatrix} * & * & * & * \\ 0 & * & * & * \\ 0 & \oplus & * & * \\ 0 & 0 & * & * \end{bmatrix} \xrightarrow{T'_{23}(\omega)} \\
 T'_{23}(\omega)T'_{34}(\omega)T_{12}(\omega)T_{23}(\omega)T_{34}(\omega)U(\omega) &= \begin{bmatrix} * & * & * & * \\ 0 & * & * & * \\ 0 & 0 & * & * \\ 0 & 0 & \oplus & * \end{bmatrix} \xrightarrow{T'_{34}(\omega)} T''_{34}(\omega)T'_{23}(\omega)T'_{34}(\omega)T_{12}(\omega)T_{23}(\omega)T_{34}(\omega)U(\omega) = \begin{bmatrix} * & * & * & * \\ 0 & * & * & * \\ 0 & 0 & * & * \\ 0 & 0 & 0 & * \end{bmatrix}
 \end{aligned}$$

Figure 3.6: Smooth decomposition method for triangular decomposition: nulling order

$$\begin{aligned}
 U(\omega) &= \begin{bmatrix} * & * & * & * \\ * & * & * & * \\ * & * & * & * \\ \oplus & * & * & * \end{bmatrix} \xrightarrow{T_{12}^\dagger(\omega)} U(\omega)T_{12}^\dagger(\omega) = \begin{bmatrix} * & * & * & * \\ * & * & * & * \\ \oplus & * & * & * \\ 0 & * & * & * \end{bmatrix} \xrightarrow{T_{23}(\omega)} T_{23}(\omega)U(\omega)T_{12}^\dagger(\omega) = \begin{bmatrix} * & * & * & * \\ * & * & * & * \\ 0 & * & * & * \\ 0 & \oplus & * & * \end{bmatrix} \xrightarrow{T_{34}(\omega)} \\
 T_{34}(\omega)T_{23}(\omega)U(\omega)T_{12}^\dagger(\omega) &= \begin{bmatrix} * & * & * & * \\ * & * & * & * \\ 0 & * & * & * \\ 0 & 0 & \oplus & * \end{bmatrix} \xrightarrow{T'_{34}(\omega)} T_{34}(\omega)T_{23}(\omega)U(\omega)T_{12}^\dagger(\omega)T'_{34}(\omega) = \begin{bmatrix} * & * & * & * \\ * & * & * & * \\ 0 & \oplus & * & * \\ 0 & 0 & * & * \end{bmatrix} \xrightarrow{T'_{23}(\omega)} \\
 T_{34}(\omega)T_{23}(\omega)U(\omega)T_{12}^\dagger(\omega)T'_{34}(\omega)T'_{23}(\omega) &= \begin{bmatrix} * & * & * & * \\ \oplus & * & * & * \\ 0 & 0 & * & * \\ 0 & 0 & * & * \end{bmatrix} \xrightarrow{T'_{12}(\omega)} T_{34}(\omega)T_{23}(\omega)U(\omega)T_{12}^\dagger(\omega)T'_{34}(\omega)T'_{23}(\omega)T'_{12}(\omega) = \begin{bmatrix} * & * & * & * \\ 0 & * & * & * \\ 0 & 0 & * & * \\ 0 & 0 & 0 & * \end{bmatrix}
 \end{aligned}$$

Figure 3.7: Smooth decomposition method for rectangular decomposition: nulling order

the identity matrix. The final decomposition, therefore, still in the example in the case of four modes :

$$U_{\text{IME}}(\omega) = T_{34}^\dagger(\omega)T_{23}^\dagger(\omega)T_{12}^\dagger(\omega)T'_{34}(\omega)T'_{23}(\omega)T''_{34}(\omega), \quad (3.112)$$

maps onto a triangular mesh connectivity between the frequency modes (Fig. 3.5a) and the implementation in terms of coupled-cavity arrays is described in Fig. 3.5d.

However such configuration leads to unequal optical path lengths and unbalanced loss due to differing numbers of $T_{mn}(\omega)$ operations applied to each mode. So alternatively, one can null elements in an order that alternates in a symmetric way between column and row elements as in, to get a much more regular meshing of rectangular shape (Fig.3.5b), akin to the Clements' scheme [201].

Alternatively, one can null elements in an order that alternates between column and row elements Fig. 3.7, akin to the Clements scheme [201]. For example, for 4 modes, the process is

shown in Fig. 3.5b, the decomposition in terms of coupled-cavity arrays is described in Fig. 3.5e and the final decomposition writes:

$$U_{\text{IME}}(\omega) = T_{23}^\dagger(\omega)T_{34}^\dagger(\omega)T_{12}'(\omega)T_{23}'(\omega)T_{34}'(\omega)T_{12}(\omega). \quad (3.113)$$

This gives a highly regular tiling of two-mode frequency coupling, with average equal path lengths between modes (Fig. 3.5b). This leads to a final proposition for this subsection:

Proposition 3.3.3. *Any frequency-dependent unitarie $U(\omega)$ can be decomposed into a mesh of at least $N(N - 1)/2$ coupled two-mode cavities, with frequency couplings.*

Note that, while coupled two-mode cavities serve as useful building blocks, their frequency-dependent coupling profiles may become insufficient to match the required $T_{mn}(\omega)$ over large optical bandwidths. In particular, as the bandwidth increases, a single two-mode cavity may not have the spectral flexibility needed to implement, even in an approximated way, any arbitrary $T_{mn}(\omega)$ in the whole spectrum. In this condition, the degrees of freedom can be increased by using a linear cascade of two-mode cavities for each $T_{mn}(\omega)$ [202, 203] or handling each subset of the overall bandwidth with different cavities. Such a strategy enables in principle the synthesis of arbitrary $S_{\text{IME}}(\omega)$ over wider bandwidths, although, of course, at the price of increasing the complexity of the implemented architectures. Integrated photonic platforms like lithium niobate (LN) microring resonators are promising choices for implementing the full-frequency transformation capabilities required by the IME. We show in (Fig. 3.5d) and (Fig. 3.5e) a possible implementation in the case of 4 modes, for a triangular and rectangular configuration respectively, in such integrated platforms.

3.3.3 Smooth single-mode decomposition

An alternative approach relies on performing the smooth decomposition of $U_{\text{IME}}(\omega)$ in terms of more elementary optical components, involving only 50:50 frequency beam-splitters and single-mode optical cavities. The advantage is that the only two-mode unitaries are fixed and do not require a specific optimization such as in the approach described in the previous subsection. Although this modular architecture has increased circuit depth, it reduces complex intermodal

3.3. ACHIEVING GENERALIZED QUANTUM MODE-MATCHING

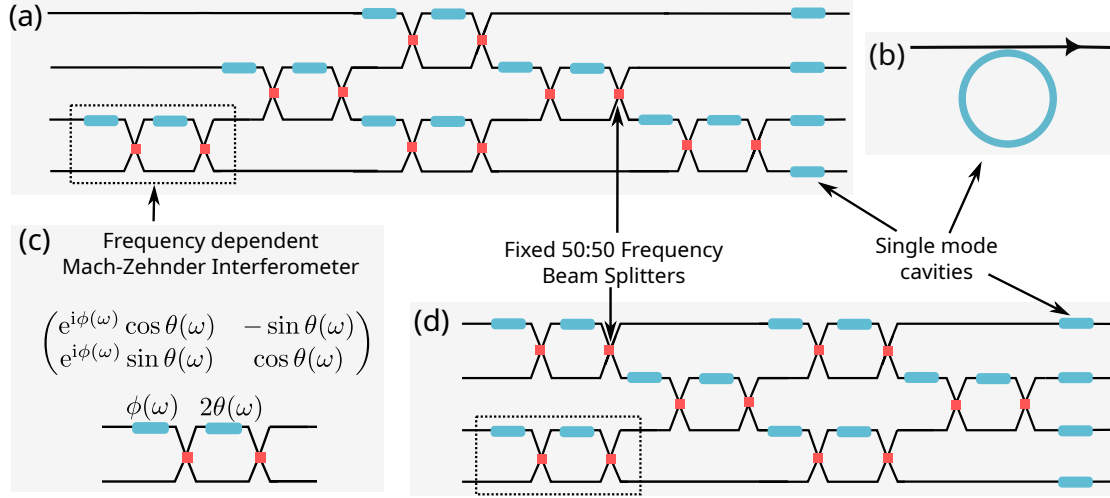


Figure 3.8: (a) **Smooth single-mode decomposition** of a 4-modes passive transformation with triangular mesh. (b) Single mode cavity. (c) Frequency-dependent Mach-Zehnder interferometer. (d) Smooth single-mode decomposition with rectangular mesh.

interactions in our IME to much simpler, well-understood fundamental photonic components building blocks.

By emulating the Reck's and Clements' implementations for spatial modes [200, 201], we can rewrite the unitary Eq. (3.103) as

$$T_{mn}(\omega) = \begin{pmatrix} e^{i\alpha_m(\omega)} & 0 \\ 0 & e^{i\alpha_n(\omega)} \end{pmatrix} T_{mn}^{\text{MZI}}(\omega) \quad (3.114)$$

where the first matrix corresponds to single-mode frequency-dependent phase shifters (corresponding to frequency-dependent output phases) that allow to access the full 4 degrees of freedom needed to represent the most general two-mode coupling $T_{mn}(\omega)$. On the other side, the unitaries $T_{mn}^{\text{MZI}}(\omega)$ correspond, in the relevant subspace, to frequency-dependent Mach-Zehnder interferometers (MZI) between modes m and n , as depicted in Fig. 3.8c, and are given by

$$T_{mn}^{\text{MZI}}(\omega) = \begin{pmatrix} e^{i\phi(\omega)} \cos \theta(\omega) & -\sin \theta(\omega) \\ e^{i\phi(\omega)} \sin \theta(\omega) & \cos \theta(\omega) \end{pmatrix}, \quad (3.115)$$

where $\theta(\omega)$ and $\phi(\omega)$ are frequency-dependent coupling parameters. In the relevant subspace,

3.3. ACHIEVING GENERALIZED QUANTUM MODE-MATCHING

this realizes a frequency-dependent Mach-Zehnder interferometer (MZI) between modes m and n . Again, we have simplified Eq. (3.115) (and we will do so going forward) by taking the expression in the most interesting two-mode subspace and the full matrix instead writes :

$$T_{mn}^{\text{MZI}}(\omega) = \begin{pmatrix} 1 & 0 & \cdots & \cdots & \cdots & \cdots & \cdots & \cdots & 0 \\ 0 & 1 & & & & & & & \vdots \\ \vdots & & \ddots & & & & & & \vdots \\ \vdots & & & e^{i\phi(\omega)} \cos \theta(\omega) & -\sin \theta(\omega) & & & & \vdots \\ \vdots & & & e^{i\phi(\omega)} \sin \theta(\omega) & \cos \theta(\omega) & & & & \vdots \\ \vdots & & & & & \ddots & & & \vdots \\ \vdots & & & & & & & 1 & 0 \\ 0 & \cdots & \cdots & \cdots & \cdots & \cdots & \cdots & 0 & 1 \end{pmatrix}, \quad (3.116)$$

The final decomposition therefore writes:

$$U_{\text{IME}}(\omega) = \Phi(\omega) \left(\prod_{(m,n)} T_{mn}^{\text{MZI}}(\omega) \right), \quad (3.117)$$

where

$$\Phi(\omega) = \begin{pmatrix} e^{i\alpha_1(\omega)} & 0 & \cdots & 0 \\ 0 & e^{i\alpha_2(\omega)} & & \vdots \\ \vdots & & \ddots & \vdots \\ 0 & \cdots & \cdots & e^{i\alpha_N(\omega)} \end{pmatrix}, \quad (3.118)$$

collects the single-mode frequency-dependent phase shifters. The difference with the equivalent stationary decomposition [200, 201] is that the matrix elements are smooth functions of the parameter ω , especially with the $T_{m,n}^{\text{MZI}}(\omega)$ where the dependency in ω comes from the parameters $\theta(\omega)$ and $\phi(\omega)$, whose choice depends of the decomposition method. It is important to note that θ and ϕ can formally have any dependency in ω . Similarly to proposition 3.3.1, this decomposition is based on the fact that for any arbitrary unitary matrix $U(\omega)$, there always exist specific functions θ and ϕ smooth in ω that make sure any target element in row m or n of matrix $U(\omega)$ or $T_{m,n}U(\omega)$ or $T_{m,n}^{\text{MZI}}(\omega)$. This generates one complex equation to get the specific unitary

complex combination of the rows or columns involved. Therefore, these MZI unitaries being described by the two real parameters smooth in ω : $\theta(\omega)$ and $\phi(\omega)$ ensures that the choice of the couple $(\theta(\omega), \phi(\omega))$ is unique, hence the equivalent MZI transformation. This suggests that the decomposition in Eq. (3.117), once the method is chosen, is unique. The decomposition will be fixed as in the two-mode decomposition cases by the choice in which we choose to null the elements of U_{IME} . For example, using a nulling order as described in Fig. 3.6 will give the triangular meshing of MZIs as described in Fig. 3.8a in the case for 4 modes and reminiscent of Reck's decomposition [200] in the case of spatial modes. After nulling all the elements, the decomposition in this case writes :

$$\left(\prod_{(m,n)} T_{mn}^{\text{MZI}'\dagger}(\omega) \right) U_{\text{IME}}(\omega) = \Phi'(\omega) \implies U_{\text{IME}}(\omega) = \left(\prod_{(m,n)} T_{mn}^{\text{MZI}'\dagger}(\omega) \right) \Phi'(\omega). \quad (3.119)$$

Considering that it always exists another single-mode frequency-dependent phase shifter matrix $\Phi(\omega)$ such that :

$$\left(\prod_{(m,n)} T_{m,n}^{\text{MZI}'\dagger}(\omega) \right) \Phi'(\omega) = \Phi(\omega) \left(\prod_{(m,n)} T_{m,n}^{\text{MZI}}(\omega) \right), \quad (3.120)$$

which when combined with Eq. (3.119) gives us the smooth decomposition in Eq. (3.117).

Using instead the nulling order as described in Fig. 3.7, we get

$$\begin{aligned} U_{\text{IME}}(\omega) &= \left(\prod_{(m,n)} T_{m,n}^{\text{MZI}'\dagger}(\omega) \right) \Phi'(\omega) \left(\prod_{(m',n')} T_{m',n'}^{\text{MZI}}(\omega) \right), \\ &= \Phi(\omega) \left(\prod_{(m,n)} \prod_{(m',n')} T_{m,n}^{\text{MZI}}(\omega) T_{m',n'}^{\text{MZI}}(\omega) \right), \\ U_{\text{IME}}(\omega) &= \Phi(\omega) \left(\prod_{(m,n)} T_{m,n}^{\text{MZI}}(\omega) \right). \end{aligned} \quad (3.121)$$

This case gives a rectangular meshing of MZIs as described in Fig. 3.8d in the case for 4 modes and reminiscent of Clements' decomposition [201] in the case of spatial modes.

These meshes of MZIs can be further decomposed into a series of fixed 50:50 frequency beamsplitters interspersed with frequency-dependent single-mode phase shifters (Fig. 3.8c). On the other side, we proved that arbitrary frequency-dependent phase shifter can be imple-

mented by chains of single-mode cavities as in Fig. 3.8b).

Proof. The quantum Langevin equation of a single-mode single-sided cavity in the interaction picture using Eq. (1.213) in Subsection 1.4.2 :

$$\frac{d}{dt}\hat{a}(t) = (-\gamma + i\Delta)\hat{a}(t) + \sqrt{2\gamma}\hat{a}_{in}(t), \quad (3.122)$$

with \hat{a} the boson annihilation operator, γ the cavity damping, Δ the detuning from cavity resonance and \hat{a}_{in} the input mode entering the cavity via losses. In the Fourier space, we get:

$$\hat{a}(\omega) = \frac{\sqrt{2\gamma}}{\gamma - i(\omega + \Delta)} \hat{a}_{in}(\omega), \quad (3.123)$$

and using the input-output relations $\hat{a}_{out}(t) + \hat{a}_{in}(t) = \sqrt{2\gamma}$, we get the output mode:

$$\hat{a}_{out}(\omega) = \frac{\gamma + i(\omega + \Delta)}{\gamma - i(\omega + \Delta)} \hat{a}_{in}(\omega), \quad (3.124)$$

which is an ω -dependant unitary transformation equivalent to a ω dependant phase shift:

$$\hat{a}_{out}(\omega) = e^{i\theta(\omega)} \hat{a}_{in}(\omega). \quad (3.125)$$

□

In the case of 4 modes, we show in Fig. 3.8a and Fig. 3.8d two possible implementations of the IME in integrated photonic platforms for triangular and rectangular meshes, respectively.

It's opportune to mention again that, as the bandwidth grows, a single cavity becomes insufficient for shaping an arbitrary spectral phase such as those that can be encountered in integrated CV quantum photonics [54]. However, it can always be approximated to any desired accuracy by using a linear chain of single-mode cavities, to either increase the degrees of freedom [202, 203] or to let each cavity handle a subset of the overall bandwidth. Therefore, all these arguments allow to formulate the following

Proposition 3.3.4. Any passive linear transformation $U_{\text{IME}}(\omega)$ between frequency modes can be constructed from fixed 50:50 frequency beamsplitters and chains of single-mode cavities

approximating frequency phase shifters.

This decomposition is well implemented in the case of the stationary case in *strawberryfields* from Xanadu. Our algorithm for the single-mode case is just a frequency-dependent version of such code.

3.4 Measuring morphing supermodes

In this section we illustrate an application of IMEs to the field measurement of the non-classical properties of the light generated by single-mode, two-mode and four-mode OPOs. The detection scheme employs an IME before the HD. The analysis of these simple few-mode scenarios elucidates the core capabilities of IMEs and concretely demonstrates its advantages over standard HD. As per

3.4.1 Optimization strategy

Since we're going to compare the performance of the interferometer with memory effect with homodyne detection in recovering the squeezing spectrum, for simulated cavity-based quantum systems of different sizes, we will first be clear about the different strategies used for our simulations.

Optimal squeezing spectrums are always obtained via analytic Bloch-Messiah decomposition (ABMD) [57] and implemented in Python as an adaptation to conjugate symplectic matrices of the smooth singular value decomposition [204]. ABMD allow us also to access the morphing supermode matrix $U(\omega)$. With full knowledge of the morphing supermodes, the optimization would entail for example finding the $S_{\text{IME}}(\omega)$ configuration that allows matching $U^\dagger(\omega)$, which equivalently means using the smooth decompositions we introduced in Subsections 3.3.2 and 3.3.3 to decompose the morphing supermodes matrices.

Equivalently, a much simpler and more accessible optimization would involve finding the IME configuration that allows projecting only in a desired morphing supermode to recover the desired squeezing spectrum. This can be done in any order since the morphing supermodes are supposedly known. These algorithms depend on the full knowledge of the morphing supermodes

3.4. MEASURING MORPHING SUPERMODES

which is far from trivial.

The optimization process can be significantly simplified by configuring the IME to project specifically onto a target morphing supermode, thereby extracting its corresponding squeezing spectrum. Since morphing supermodes a set of independent observables, this projection can be performed in any sequential order. However, this algorithmic approach relies heavily on having complete knowledge of the morphing supermodes' structure, which is not trivial.

In designing our optimization routine, we therefore deliberately exclude prior knowledge of morphing supermodes to simulate real experimental conditions. We demonstrate that even with this limitation, we can develop a straightforward optimization procedure that can recursively access all the squeezing/antisqueezing spectrum. This approach relies on two crucial properties that we have previously alluded to but not formally stated or proven. Here are the two properties:

Property 3.4.1. *For any quadrature-based measurement scheme (HD or using IME), the noise spectral power is bounded below by the squeezing spectrum of the maximally squeezed supermode, denoted by $d_1^{-2}(\omega)$.*

Proof. *Considering the most general unitary LO $\vec{Q}(\omega)$ decomposed into the orthonormal basis of morphing supermodes as in Eq. (3.50), the noise spectral power will write as in Eq. (3.51) :*

$$\Sigma_{\vec{Q}}(\omega) = \frac{1}{2\sqrt{2\pi}} \sum_{i=1}^{2N} \lambda_i^2(\omega) |\beta_i(\omega)|^2, \quad (3.126)$$

where the $\lambda_i^2(\omega)$ correspond to the squeezing/antisqueezing spectrum as in Eq. (3.48). Let $\lambda_{min}(\omega)$ denote the minimum eigenvalue among all $\lambda_i(\omega)$, we then have $\lambda_i(\omega) \geq \lambda_{min}(\omega)$ for all i , and consequently $\lambda_i^2(\omega) \geq \lambda_{min}^2(\omega)$ for all i . Therefore:

$$\sum_{i=1}^{2N} \lambda_i^2(\omega) |\beta_i(\omega)|^2 \geq \lambda_{min}^2 \sum_{i=1}^{2N} |\beta_i(\omega)|^2 \quad (3.127)$$

Moreover, since the $\beta_i(\omega)$ coefficients come from a decomposition in an orthonormal basis, we know that:

$$\sum_{i=1}^{2N} |\beta_i(\omega)|^2 = 1 \quad (3.128)$$

3.4. MEASURING MORPHING SUPERMODES

Thus, we can conclude:

$$\sum_{i=1}^{2N} \lambda_i^2(\omega) |\beta_i(\omega)|^2 \geq \lambda_{min}^2 \quad (3.129)$$

Throughout this thesis, we have used a notation where the squeezing of the most squeezed supermode is $d_1^{-2}(\omega)$, so this equation finally writes :

$$\sum_{i=1}^{2N} \lambda_i^2(\omega) |\beta_i(\omega)|^2 \geq d_1^{-2}(\omega), \quad (3.130)$$

proving our first property. □

Property 3.4.2. For any quadrature-based measurement scheme restricted to the subspace orthogonal to the maximally squeezed supermode, the noise spectral power is bounded below by the squeezing spectrum of the second-most squeezed supermode $d_2^{-2}(\omega)$. More generally, when restricted to the subspace orthogonal to the k most squeezed supermodes, the noise spectral power is bounded below by $d_{k+1}^{-2}(\omega)$.

Proof. When we restrict ourselves to the orthonormal basis excluding the eigenvector corresponding to $d_1^{-2}(\omega)$, any vector in this subspace can be written as a linear combination of the remaining eigenvector. In particular, the generalized LO can be written as:

$$\vec{Q}(\omega) = \sum_{i=1}^{2N-1} \beta'_i(\omega) \vec{U}_i(\omega) \quad \text{with} \quad \beta'_i(\omega) = \langle \vec{Q}(\omega), \vec{U}_i(\omega) \rangle. \quad (3.131)$$

And for any of this decomposition in this restricted basis, the equation

$$\sum_{i=2}^{2N-1} |\beta'_i(\omega)|^2 = 1 \quad (3.132)$$

In this restricted space, $d_2^{-2}(\omega)$ becomes the new minimum eigenvalue., following the same reasoning as in Prop 3.4.1:

$$\sum_{i=1}^{2N-1} \lambda_i^2(\omega) |\beta'_i(\omega)|^2 \geq d_2^{-2}(\omega) \sum_{i=1}^{2N-1} |\beta'_i(\omega)|^2 \quad (3.133)$$

$$\geq d_2^{-2}(\omega). \quad (3.134)$$

3.4. MEASURING MORPHING SUPERMODES

This process can be continued iteratively: when restricting to the orthonormal basis excluding the eigenvectors corresponding to the k smallest eigenvalues, the $(k + 1)$ -th smallest eigenvalue becomes the minimum value achievable by noise spectral power. \square

These two properties provide a powerful method to experimentally reconstruct the complete squeezing and antisqueezing spectrum of the morphing supermodes without requiring prior knowledge of their structure. This comes at the cost of a recursive reconstruction in the specific order described by Property 3.4.2. This reconstruction method is applicable to both HD and IME. However, IME offers a significant advantage: it can always achieve the minimum noise power across an entire spectral bandwidth simultaneously. Because of that, IME allows also reconstruct the morphing supermode structure $U(\omega)$ as whenever the associated noise power recovers a given squeezing or antisqueezing profile, the corresponding generalized LO is always matched and therefore gives full information on the corresponding morphing supermode. In contrast, HD can only reach this minimal value under two restrictive conditions: the absence of hidden squeezing and measurement at a single frequency at a time.

As discussed previously, we are essentially only interested in recovering squeezing spectrums and in some cases, only the squeezing associated with the most squeezed supermode. But the routine we're going to describe works beyond these situations.

The optimization procedure was implemented using the SciPy library's optimization module (*scipy.optimize*), primarily employing two methods: the Limited-memory Broyden-Fletcher-Goldfarb-Shanno (*L-BFGS*) algorithm, a quasi-Newton method efficient for large-scale unconstrained optimization problems, and the trust-region constrained (*trust-constr*) algorithm, which is well-suited for constrained nonlinear optimization tasks.

For the optimization routine HD, the goal is to recover the squeezing spectrum recursively starting from $d_1^{-2}(\omega)$. Let us remember that HD can recover the desired squeezing only at a given frequency and only when the spectral covariance is real.

- We start by recovering $d_1^{-2}(\omega)$ (lowest eigenvalue) by finding the $2N - 1$ parameters $\vec{\theta}_1$ of the real local oscillator $\vec{Q}(\vec{\theta}_1)$ that minimize the noise spectral power (in at a given

3.4. MEASURING MORPHING SUPERMODES

frequency ω_c). The problem statement is as follows:

$$\text{Minimize } \Sigma_{HD}(\vec{\theta}_1, \omega_c) \quad (3.135)$$

- Then we recover $d_2^{-2}(\omega_c)$ by finding the parameters $\vec{\theta}_2$ of the real local oscillator $\vec{Q}(\vec{\theta}_2)$ that minimizes the noise spectral power a constraint of being in the orthogonal space of the previous optimal LO $\vec{Q}(\vec{\theta}_1)$. By moving into the orthogonal space to $\vec{Q}(\vec{\theta}_1)$, we ensure that the optimal squeezing is $d_2^{-2}(\omega)$. The problem statement is :

$$\text{Minimize } \Sigma_{HD}(\vec{\theta}_2, \omega_c) \quad (3.136)$$

$$\text{Subject to } \vec{Q}(\vec{\theta}_2) \cdot \vec{Q}(\vec{\theta}_1) = 0.$$

- The last step is done recursively and for to recover $d_j^{-2}(\omega_c)$

$$\text{For } j = 2, \dots, N, \text{ Minimize } \Sigma_{HD}(\vec{\theta}_j, \omega_c) \quad (3.137)$$

$$\text{Subject to } \vec{Q}(\vec{\theta}_j) \cdot \vec{Q}(\vec{\theta}_k) = 0, \quad \text{for } k = 1, 2, \dots, j - 1.$$

Such routine can be done to multiple values of frequency for an attempt to recover squeezing in the whole spectrum. Especially for HD, we will not use this routine since we want to ensure we're taking into account the best that HD can achieve without optimization uncertainties. We instead use the following property, introduced in [175]:

Property 3.4.3. *For HD, the noise spectral power for the spectral covariance matrix $\sigma_{\text{out}}(\omega_c)$ is equivalent to the noise spectral power accounting only for the real part $[\sigma_{\text{out}}(\omega_c)]$.*

Proof. *Let's break down $\sigma_{\text{out}}(\omega)$ into its real and imaginary parts: $\sigma_{\text{out}}(\omega) = \text{Re}[\sigma_{\text{out}}(\omega)] + i\text{Im}[\sigma_{\text{out}}(\omega)]$. The noise spectral power for HD in Eq. (3.40) expands to:*

$$\Sigma_{HD}(\omega) = \vec{Q}^T \text{Re}[\sigma_{\text{out}}(\omega)] \vec{Q} + i \vec{Q}^T \text{Im}[\sigma_{\text{out}}(\omega)] \vec{Q}. \quad (3.138)$$

In the case of HD where \vec{Q} is real, both $\vec{Q}^T \text{Re}[\sigma_{\text{out}}(\omega)] \vec{Q}$ and $\vec{Q}^T \text{Im}[\sigma_{\text{out}}(\omega)] \vec{Q}$ are real and correspond respectively to the real and imaginary part of the noise spectral power. Therefore

3.4. MEASURING MORPHING SUPERMODES

using the property of the reality of the noise spectral power (Prop. 3.1.3), the imaginary part $\vec{Q}^T \text{Im}[\sigma_{\text{out}}(\omega)] \vec{Q}$ must be zero and the noise power finally writes :

$$\Sigma_{\text{HD}}(\omega) = \vec{Q}^T \text{Re}[\sigma_{\text{out}}(\omega)] \vec{Q}. \quad (3.139)$$

This is also valid also valid at a single frequency ω_c . □

For the optimization routine of the IME, the optimization is done recursively in a similar fashion to that for HD. It involves the parameters of the IME in addition to the parameters of the real local oscillator. Both combined, give the parameters of the complex local oscillator.

As for HD, we will try to recover the squeezing spectrum one by one. We find the parameters from the real local oscillator θ_1 and the IME θ_1^{IME} that minimize the noise spectral power, giving us the lowest squeezing spectrum $d_1^{-2}(\omega)$. Then we will recover $d_2^{-2}(\omega)$ by minimizing the noise spectral power while putting a constraint of being in the space orthogonal to the already recovered squeezing spectrum. And so on. The problem statement is as follows:

$$\text{Minimize } \Sigma_{\text{IME}}(\vec{\theta}_1, \vec{\theta}_1^{\text{IME}}, \omega) \quad (3.140)$$

$$\text{For } j = 2, \dots, N, \text{ Minimize } \Sigma_{\text{IME}}(\vec{\theta}_j, \vec{\theta}_j^{\text{IME}}, \omega)$$

$$\text{Subject to } \vec{Q}(\vec{\theta}_j, \vec{\theta}_j^{\text{IME}}, \omega) \cdot \vec{Q}(\vec{\theta}_k, \vec{\theta}_k^{\text{IME}}, \omega) = 0, \quad \text{for } k = 1, 2, \dots, j-1.$$

It is very straightforward in the case where the recovery of the squeezing spectrum is successful to recover also the corresponding morphing supermodes $\vec{Q}(\vec{\theta}_j, \vec{\theta}_j^{\text{IME}}, \omega) = \vec{u}_{N+j}$. The difference in indexing comes from the arrangement chosen for both $U(\omega)$ and $D(\omega)$. We remind that the morphing supermodes correspond to :

$$U(\omega) = (\vec{u}_1(\omega), \vec{u}_2(\omega), \dots, \vec{u}_N(\omega) | \vec{u}_{N+1}(\omega), \dots, \vec{u}_{2N}(\omega)) \quad (3.141)$$

and the (anti)-squeezing spectrum :

$$D(\omega) = \text{diag}\{d_1(\omega), \dots, d_N(\omega) | d_1^{-1}(\omega), \dots, d_N^{-1}(\omega)\}. \quad (3.142)$$

3.4. MEASURING MORPHING SUPERMODES

We therefore recover recursively all the squeezing spectrum without knowledge of the morphing supermodes, just by minimizing the noise spectral power with constraints. Furthermore, the optimal parameters will give you the corresponding morphing supermodes.

Each squeezing spectrum requires a different cavity configuration (different parameters $\vec{\theta}_j^{IME}$). This means the amount of N -modes IME configuration required to recover all squeezing spectrums is at minimum N . To reduce this number, the option of recycling a previous cavity configuration during the recursion while modifying only the real local oscillator parameters was considered highlighting the flexibility of the IME.

When a single IME configuration is not enough to recover a specific $d_j^{-2}(\omega)$ as we mentioned previously, a couple of options are available to us :

- Cascading IMEs to increase the degree of freedom available to us to recover the desired squeezing spectrum in a larger/whole bandwidth,
- Using different configurations of the IME to handle different subsets of the full spectrum.

For this option, we consider also recycling the IME configuration for a subset of the spectrum to another part of the spectrum, varying only the real local oscillator parameters.

We explore always the first options and we show examples of recycling IMEs in Appendix C for some particular cases of the examples we will present on later sections. Regardless of these, the number of IME configurations required scales linearly $\sim N$ with the number of modes when the goal is to recover all the noise spectrums.

Finally, we cannot end without discussing the scaling behavior of the IME optimization procedure. For an N -mode system, the IME is characterized by the hermitian matrix G_{IME} (Eq. (3.90)) that accounts for N^2 real parameters (N diagonal elements and $2 \times \frac{N(N-1)}{2}$ upper diagonal elements). When considering frequency-independent external coupling rates γ , the total number of parameters to optimize scales quadratically as $(N^2 + 1) \sim N^2$. Adding the parameters for the HD LO ($2N - 1$), the overall scaling remains quadratic $\sim N^2$. While this is more complex than standard homodyne detection, which scales linearly with the number of modes ($2N - 1 \sim N$), the IME's capability to simultaneously handle both hidden squeezing and morphing supermodes justifies this trade-off.

Identifying the most effective strategies for the optimization of large parameter problems is

beyond the scope of this thesis. However, the quadratic scaling ($\sim N^2$) of optimization parameters, rather than exponential, suggests that efficient, tailored algorithms could be developed to handle these optimization challenges effectively.

3.4.2 Single-mode OPO

The single-mode degenerate optical parametric oscillator (OPO) [59, 58] represents one of the simplest systems exhibiting squeezing. Here, it will serve as an introductory example to illustrate the limitations of standard HD as well as the advantages of generalized mode-matching through an IME. The system consists of a single-mode nonlinear cavity driven by a continuous wave pump at frequency ω_p and working in frequency and polarization degeneracy, below the OPO oscillation threshold. The pump generates, by parametric down-conversion [205] of coupling strength g , pairs of degenerate signal photons, whose frequency ω_s is taken to be close to a given resonance ω_0 of the cavity. We will indicate the detuning from perfect resonance as $\Delta = \omega_s - \omega_0$ and the signal damping rate as γ . The dynamics of the signal field can be linearized around stationary values leading to quantum Langevin equations of the form of Eq. (3.4) in the quadrature basis. One can use the same procedure that in Subsection 1.4.2 or directly Eq. (1.212) with an interaction Hamiltonian in the form: $\hat{H}_I(t) = ig\hat{a}^\dagger\hat{a}$ before absorption of the detuning terms. As we are dealing with a single-mode system, the quadrature vector is $\hat{R} = (\hat{x}|\hat{y})^\top$, $G = \Delta$ and $F = ig$.

The corresponding mode coupling matrix \mathcal{M} is, then, given by

$$\mathcal{M} = \begin{pmatrix} g & \Delta \\ -\Delta & -g \end{pmatrix}. \quad (3.143)$$

We will consider particular values of g and Δ normalized to the damping rate γ for single-mode OPO of different percentages below the threshold, as per Eq. (3.6). In particular, we consider three cases:

- $\Delta = \gamma$ and $g = 1.38\gamma$ for an a single mode OPO 5% below threshold,
- $\Delta = \gamma$ and $g = 1.12\gamma$ for an a single mode OPO 50% below threshold,

3.4. MEASURING MORPHING SUPERMODES

- $\Delta = 2\gamma$ and $g = \gamma$ for an a single mode OPO 100% below threshold.

For all these cases and in particular, for any purely single-mode cavity-based open system, we predicted in Section 3.2.3 from our criteria in Proposition 3.2.2 that the spectral covariance matrix is always real because the For all three configurations of OPOs, we show in Fig. 3.9 the four elements of the 2×2 output transfer function and spectral covariance matrix at two representative frequencies ($\omega = 0$ and $\omega \neq 0$). We see that, while the output transfer function is always complex except at $\omega = 0$, the spectral covariance matrix presents no imaginary elements as predicted by our criteria.

This prediction allows us to confirm directly from the OPOs parameters the absence of hidden squeezing. This ensures that optimal squeezing produced by these single-mode OPOs should theoretically be accessible through standard HD. The next paragraph will confirm this prediction. The ABMD of the transfer function Eq. (3.21) of these OPO configurations returns two frequency-dependent singular values $d(\omega)$ and $d^{-1}(\omega)$ (see Fig. 3.10, representing respectively the optimal levels of anti-squeezing (red-dashed) and squeezing (red-solid). They are associated with two morphing supermodes whose structure is given by the columns of the matrix $U(\omega)$

$$U(\omega) = \begin{pmatrix} u_{1,1}(\omega) & u_{1,2}(\omega) \\ -u_{2,1}(\omega) & u_{2,2}(\omega) \end{pmatrix} = \begin{pmatrix} \cos [\theta(\omega)] & \sin [\theta(\omega)] \\ -\sin [\theta(\omega)] & \cos [\theta(\omega)] \end{pmatrix}. \quad (3.144)$$

Because the spectral covariance matrices for all configurations of the single mode OPO are real, so are $U(\omega)$, and so are the coefficients of the linear combinations leading to the supermodes, as shown in Fig 3.10(*middle*) and (*right*). Therefore these examples represent situations where hidden squeezing is not present but a morphing behaviour is present. In what follows, we will focus on the detection of the optimal squeezing spectrum $d^{-1}(\omega)$ in Fig 3.10(*left*) of the quadrature $\hat{y}_{\text{out}}^{(s)}(\omega) = \sin [\theta(\omega)] \hat{x}_{\text{out}}(\omega) + \cos [\theta(\omega)] \hat{y}_{\text{out}}(\omega)$. The coefficients of this linear combination are given by $\vec{U}_2(\omega)$, *i.e.* the second column of $U(\omega)$. Here again (a), (b) and (c) correspond to cases where we're respectively 5%, 50% and 100% below threshold.

We start by considering the measurement of squeezing through a standard HD, as depicted in Fig. 3.11a, corresponding to a LO with a real and non-morphing profile $\vec{Q} = (\cos \theta_{\text{LO}} | \sin \theta_{\text{LO}})^{\text{T}}$.

3.4. MEASURING MORPHING SUPERMODES

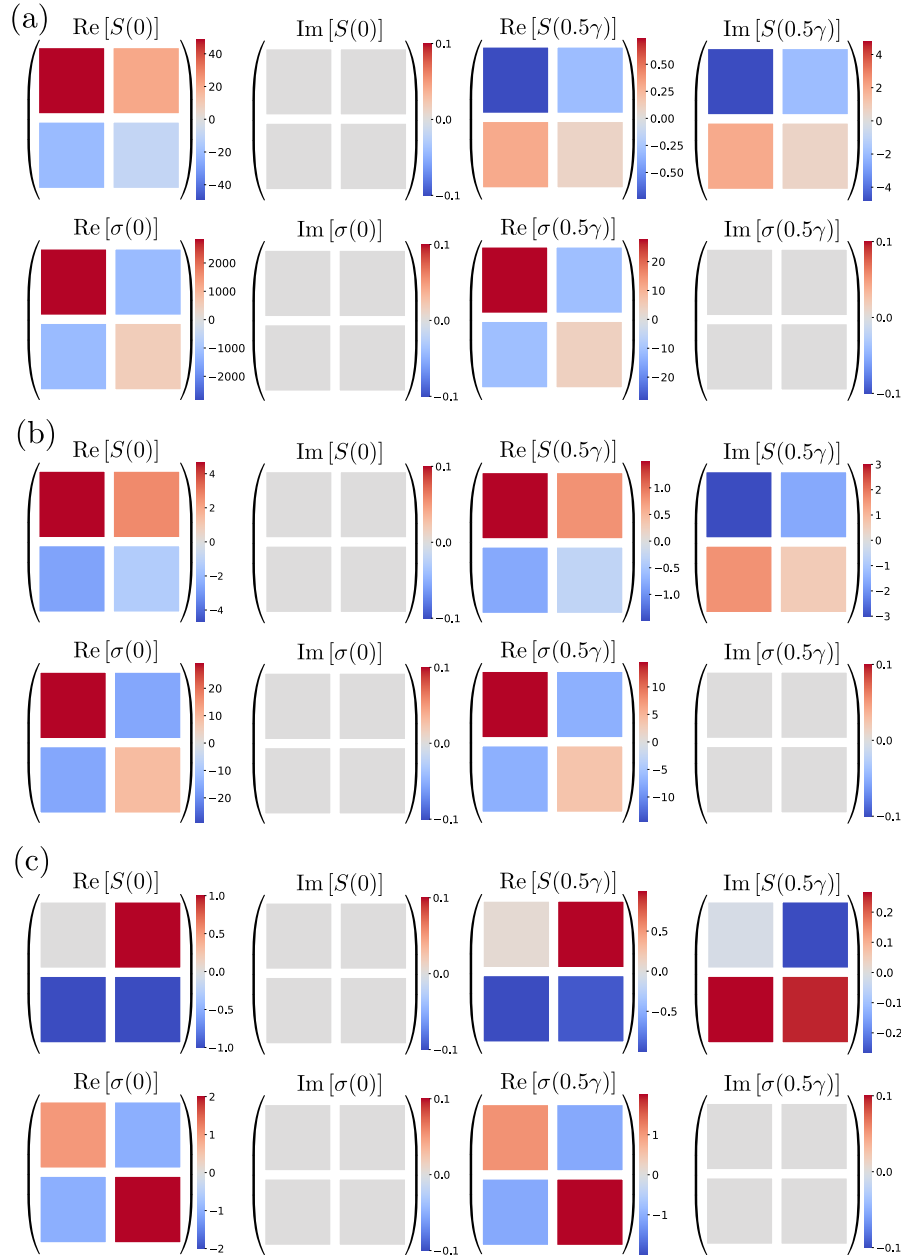


Figure 3.9: Output transfer function and spectral covariance of single mode OPOs: We show the real and imaginary part of the elements of the 2×2 output transfer function $S_{\text{out}}(\omega)$ and spectral covariance matrix $\sigma_{\text{out}}(\omega)$. They are shown for detuned degenerate single mode OPOs (a) 5%, (b) 50% and (c) 100% below the threshold for 3 values of two values of frequencies $\omega = 0$ and $\omega \neq 0$. We see that the output transfer function is always complex at nonzero frequencies. However, because of the nature of single mode OPO, $(GF)^{\text{T}} = GF$ and that translates to as we see always real-valued spectral covariance matrices.

3.4. MEASURING MORPHING SUPERMODES

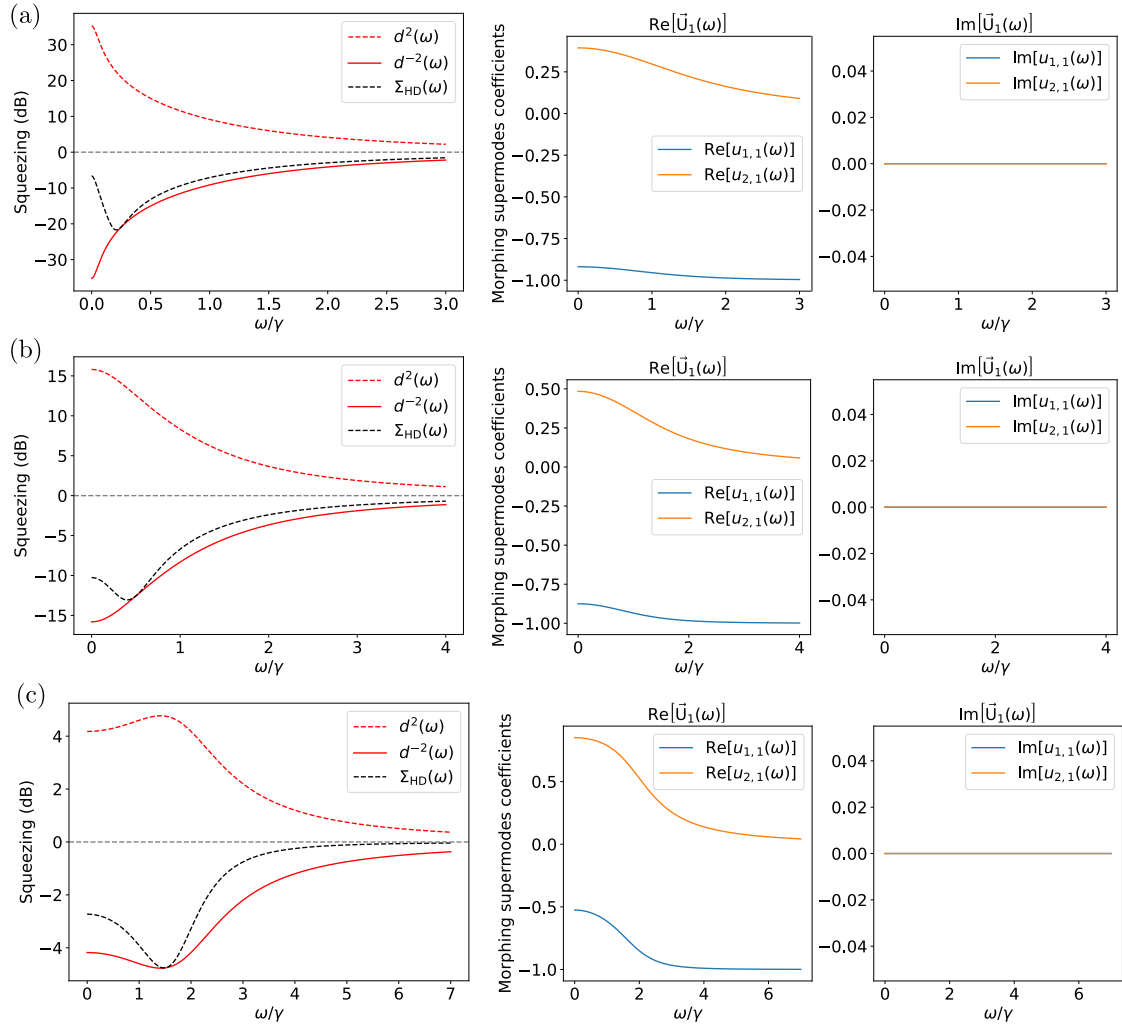


Figure 3.10: **Antisqueezing and squeezing levels and morphing supermodes of single mode OPOs:** (left) Antisqueezing and squeezing spectrum of the three configuration single mode OPOs : (a) 5%, (b) 50% and (c) 100% below threshold. (middle) Real and (right) imaginary parts.

The measured noise spectral power $\Sigma_{\text{HD}}(\omega)$ is traced for all three configurations of OPO in Figs. 3.12, 3.13, 3.14(top-left) (see black-dashed lines). In these figures, four different choices of θ_{LO} , thus of \vec{Q} , are considered. As it can be seen, for each choice of \vec{Q} , optimal squeezing is detected only at a given frequency $\bar{\omega}$ and not through the whole bandwidth: the value of $\bar{\omega}$ corresponds to the frequency at which the LO profile \vec{Q} matches the supermode $\vec{U}_2(\omega)$ and it is obtained by setting $\theta_{\text{LO}} = \pi/2 - \theta(\bar{\omega})$.

In Figs. 3.12, 3.13, 3.14(bottom-left), the sub-optimal mode-matching (black-dashed) be-

3.4. MEASURING MORPHING SUPERMODES

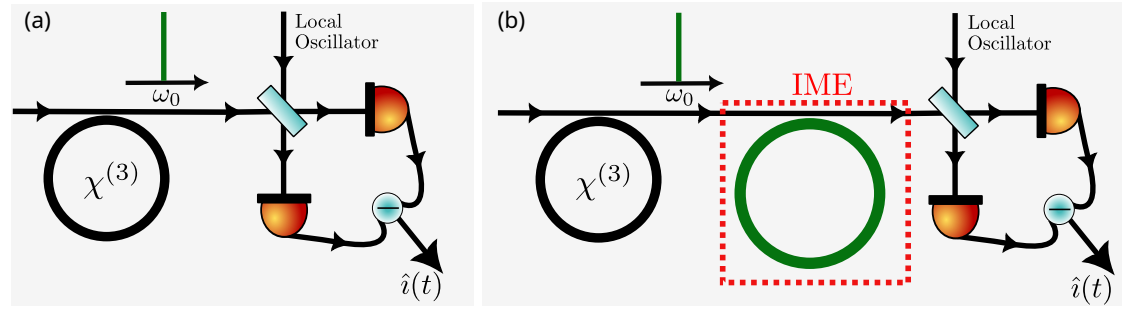


Figure 3.11: Measurement of squeezing level of a single mode OPO using (a) HD and (b) an IME stage.

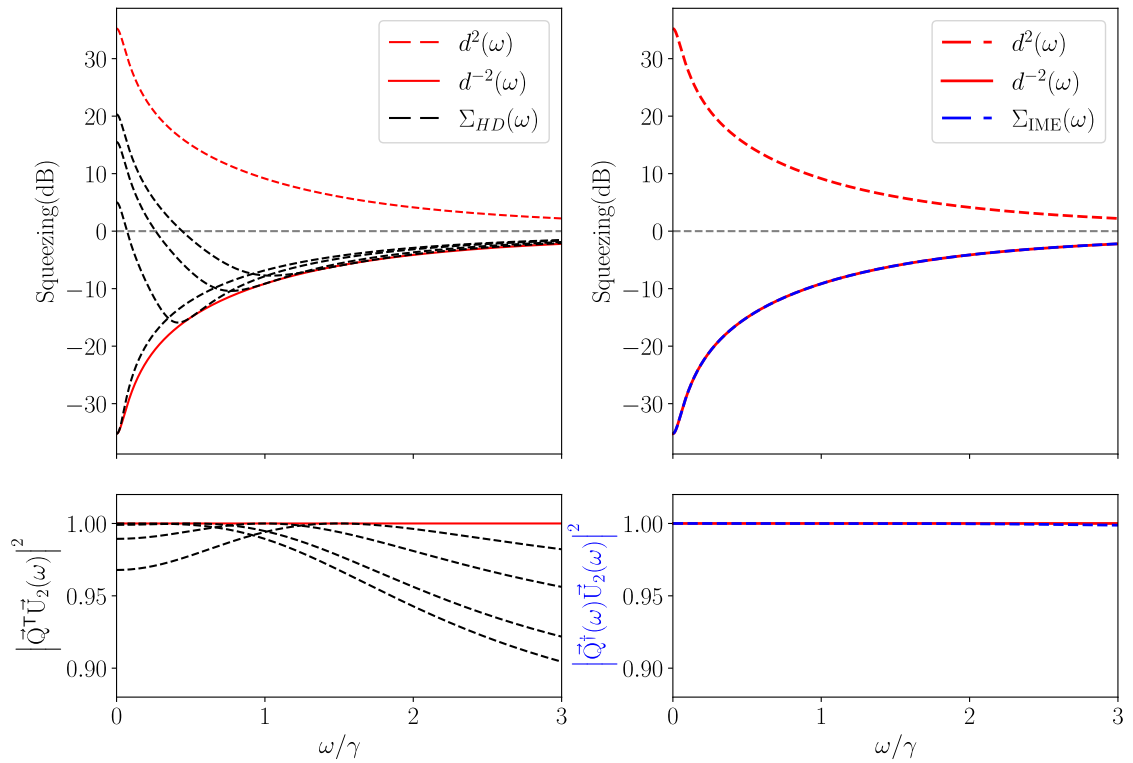


Figure 3.12: (Top-left) Optimal squeezed/anti-squeezed noise spectral power from singular values $d^{\pm 2}(\omega)$ (red solid/dashed lines) vs. standard HD measurements $\Sigma_{HD}(\omega)$ for four different \vec{Q} that optimize the detected squeezed signal at a particular ω (dashed-black lines), and (Bottom-left) standard LO-squeezed supermode overlap for four different angles θ_{LO} (dashed-black lines) vs. perfect overlap (solid-red). (Top-right): Same comparison with IME measurements $\Sigma_{IME}(\omega)$ (dashed-blue line) and (bottom-right) generalized LO-supermode overlap (dashed-blue line). This is for the OPO configuration 5% below threshold.

tween the LO and the morphing supermode $\vec{U}_2(\omega)$ is traced: perfect projection is reached only at a fixed frequency. In experiments, this means that the only way to perform a complete recon-

3.4. MEASURING MORPHING SUPERMODES

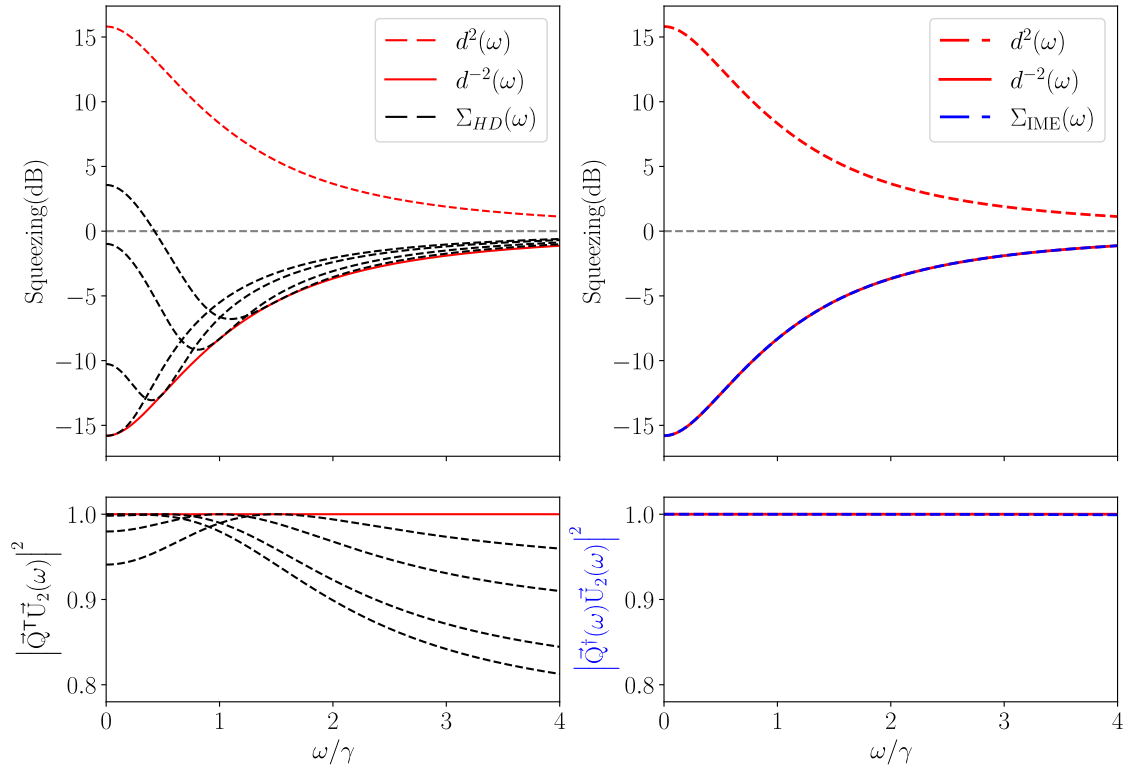


Figure 3.13: (*Top-left*) Optimal squeezed/anti-squeezed noise spectral power from singular values $d^{\pm 2}(\omega)$ (red solid/dashed lines) vs. standard HD measurements $\Sigma_{HD}(\omega)$ for four different \vec{Q} that optimize the detected squeezed signal at a particular ω (dashed-black lines), and (*Bottom-left*) standard LO-squeezed supermode overlap for four different angles θ_{LO} (dashed-black lines) vs. perfect overlap (solid-red). (*Top-right*): Same comparison with IME measurements $\Sigma_{IME}(\omega)$ (dashed-blue line) and (*bottom-right*) generalized LO-supermode overlap (dashed-blue line). This is for the OPO configuration 50% below threshold.

struction of squeezing spectrum would be to adjust for any value of ω , the LO phase so as to minimize the noise spectral power: a procedure highly impractical from the experimental point of view and not at all applicable to time homodyne schemes for example.

This aspect of the HD does not represent, at least in this situation, a limit for the complete reconstruction of the squeezing spectrum that can, indeed, be obtained by sweeping the LO angle. However, this is a clear limitation of the HD in those situations where the exploitation of the full squeezing spectrum is required simultaneously.

The use of IME as an interface between the state generation stage and the HD allows to overcome this limitation. In order to implement the generalized mode-matching, the cavity output is now made to pass through an IME before the HD stage as shown in Fig 3.11b.

3.4. MEASURING MORPHING SUPERMODES

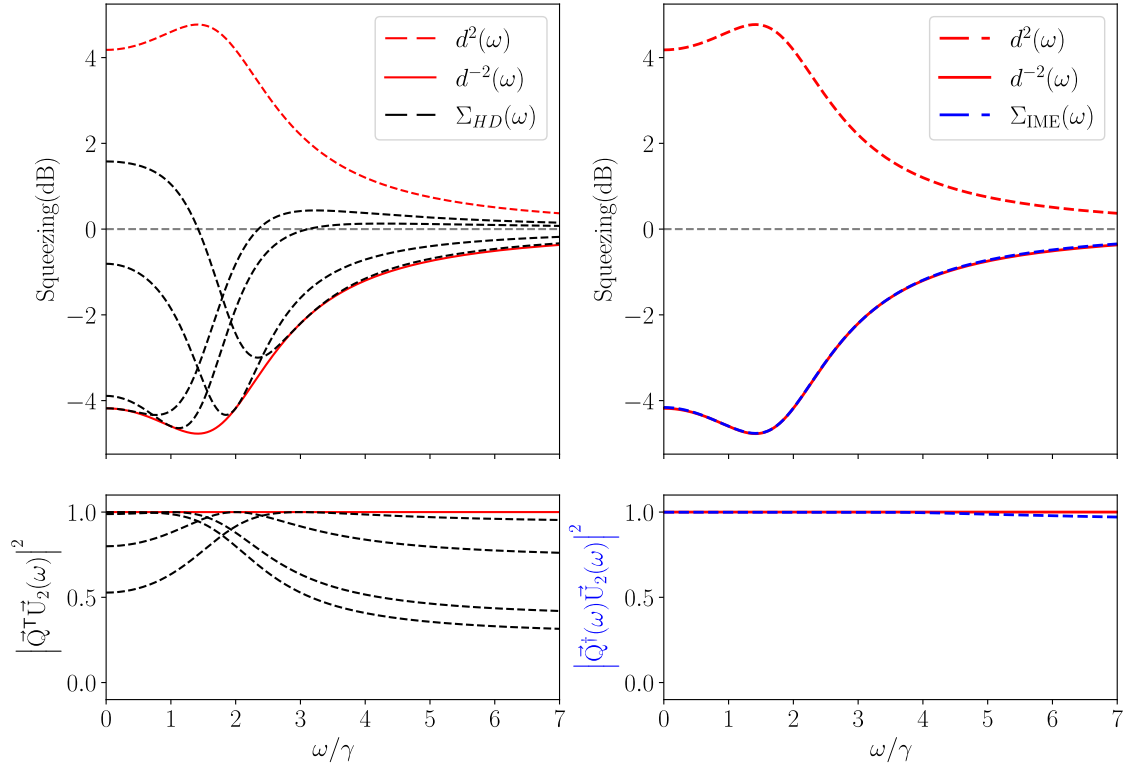


Figure 3.14: (*Top-left*) Optimal squeezed/anti-squeezed noise spectral power from singular values $d^{\pm 2}(\omega)$ (red solid/dashed lines) vs. standard HD measurements $\Sigma_{HD}(\omega)$ for four different \vec{Q} that optimize the detected squeezed signal at a particular ω (dashed-black lines), and (*Bottom-left*) standard LO-squeezed supermode overlap for four different angles θ_{LO} (dashed-black lines) vs. perfect overlap (solid-red). (*Top-right*): Same comparison with IME measurements $\Sigma_{IME}(\omega)$ (dashed-blue line) and (*bottom-right*) generalized LO-supermode overlap (dashed-blue line). This is for the OPO configuration 100% below threshold.

For single-mode systems, the most general passive transformation $S_{IME}(\omega)$ (see Eq. (3.89)) is characterized by a 2×2 damping matrix $\Gamma_{IME} = \text{diag}\{\gamma_{IME}|\gamma_{IME}\}$ and 2×2 mode coupling matrix (see Eq. (3.90)):

$$\mathcal{M}_{IME}^{(1)} = \begin{pmatrix} 0 & \Delta_{IME} \\ -\Delta_{IME} & 0 \end{pmatrix}. \quad (3.145)$$

The corresponding transfer function is, therefore, the transformation induced by a single-mode empty cavity with damping γ_{IME} and detuned with respect to the input beam of a quantity Δ_{IME} . As already discussed, such a type of "resonator detection" was proposed by Barbosa *et al.* [55,

3.4. MEASURING MORPHING SUPERMODES

56] as a solution to overcome the HD limits in detecting hidden squeezing but never thought as a solution to mode-match a morphing behaviour.

For given values of the parameters of the different OPO configurations, we can numerically optimize the IME parameters in order to achieve optimal mode-matching over the largest bandwidth:

- $\gamma_{\text{IME}} = 1.85\gamma$, $\Delta_{\text{IME}} = -0.46\gamma$ and $\theta_{\text{LO}} = 1.65$ rad for the single mode OPO 5% below threshold.
- $\gamma_{\text{IME}} = 1.62\gamma$, $\Delta_{\text{IME}} = -0.46\gamma$ and $\theta_{\text{LO}} = 1.62$ rad for the single mode OPO 50% below threshold.
- $\gamma_{\text{IME}} = 2\gamma$, $\Delta_{\text{IME}} = -1.51\gamma$ and $\theta_{\text{LO}} = 4.96$ rad for the single mode OPO 100% below threshold.

These results are shown in Figs. 3.12, 3.13, 3.14(*top-right*), where the dashed-blue curves represent the noise spectral power detected by a standard HD after a passage of the signal through the IME. In Figs. 3.12, 3.13, 3.14(*bottom-right*), we show that the projection between the generalized LO, $\vec{Q}(\omega)$, and the squeezed supermode is optimal (close to one) through the whole bandwidth. As we will see next, this advantage becomes even stronger in multimode scenarios.

As a last comment for the single-mode OPO configurations, operation closer to threshold yields higher maximum optimal squeezing levels. However, this enhancement comes with a narrower spectral bandwidth, as the squeezing rapidly approaches the shot noise level. This spectral compression effectively reduces the frequency range where squeezing recovery is significant, thus diminishing the relevance of the generalized LO's frequency dependence. This is seen when comparing the Figs. 3.12, 3.13 and 3.14.

3.4.3 Two-mode OPO

The case of two-mode detuned $\chi^{(3)}$ -based OPO will clearly show the limitations of HD to fully characterize the quantum dynamics, even in simple bimodal scenarios. We consider a non-degenerate OPO, pumped in continuous-wave regime below the oscillation threshold. This case

3.4. MEASURING MORPHING SUPERMODES

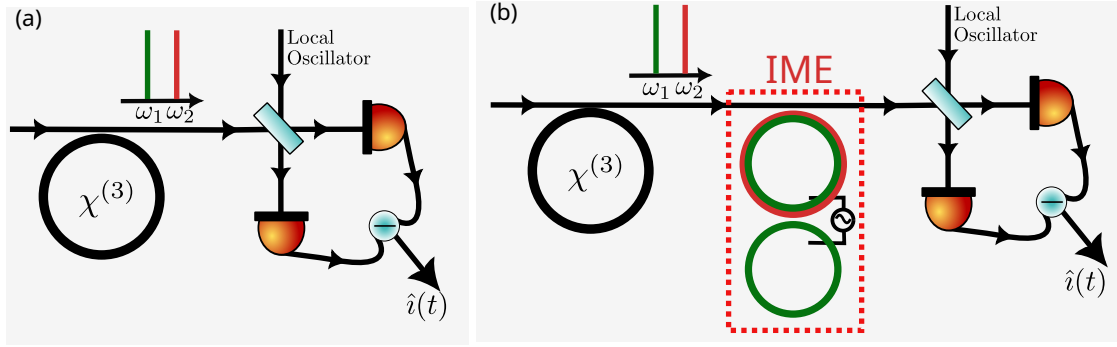


Figure 3.15: **HD vs IME scheme for two-mode OPO:** (left) Scheme of a standard HD for the characterization of bi-colour fields with carriers ω_1 and ω_2 . (Right) Schematic of a generalized mode matching between a bi-colour quantum field from a $\chi^{(3)}$ OPO source and the standard HD, using a coupled cavity system as an IME.

is described by a system of linear quantum Langevin equations Eq. (3.4) with a 4×4 damping matrix $\Gamma = \text{diag}\{\gamma_1, \gamma_2 | \gamma_1, \gamma_2\}$ and 4×4 mode-coupling matrices Eq. (3.5) corresponding to

$$G = \begin{pmatrix} g_{11} & g_{12} \\ g_{12}^* & g_{22} \end{pmatrix}, F = \begin{pmatrix} 0 & f_{12} \\ f_{12} & 0 \end{pmatrix}. \quad (3.146)$$

This scenario occurs, for example, in microring resonators driven by one pump [194], or in the linearized dynamics driven slightly above threshold. We consider for these systems three configurations based on their proximity to the threshold value:

- $\gamma_2 = 1.5\gamma_1$, $g_{11} = g_{22} = 0.8\gamma_1$ and $f_{12} = 1.42i\gamma_1$ for a two-mode OPO 7% below threshold,
- $\gamma_1 = \gamma_2$, $g_{11} = g_{22} = \gamma_1$ and $f_{12} = 1.38i\gamma_1$ for a two-mode OPO 5% below threshold,
- $\gamma_1 = \gamma_2$, $g_{11} = 0.8\gamma_1$, $g_{22} = \gamma_1$ and $f_{12} = i\gamma_1$ for a two-mode OPO 43% below threshold.

For these parameters only, beyond a spectral covariance matrix always real at $\omega = 0$, for nonzero frequencies, we can already make some predictions about these configurations. First, for the OPO 7% below threshold, because $\gamma_1 \neq \gamma_2$, Γ does not commute with \mathcal{M} , which implies based on Prop. 3.2.2 that the spectral covariance matrix and the morphing supermodes are always complex for nonzero frequencies, hinting at the presence of hidden squeezing. This is shown in Fig. 3.16a where we display the real and imaginary parts of the 16 elements contained in the 4×4 spectral covariance $\sigma_{\text{out}}(\omega)$.

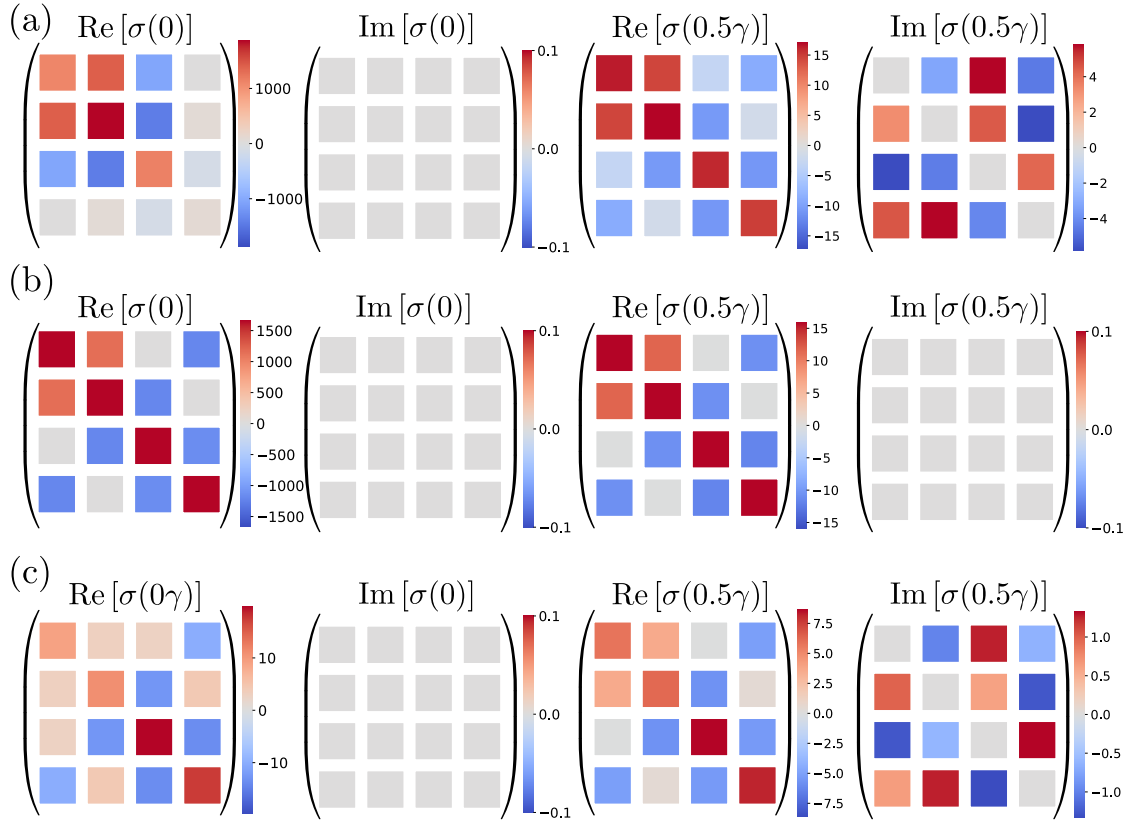


Figure 3.16: **Output spectral covariance of two-mode OPOs:** We show the real and imaginary part of the elements of the 4×4 spectral covariance matrix $\sigma_{\text{out}}(\omega)$. They are shown for two-mode detuned $\chi^{(3)}$ -based OPO (a) 7%, (b) 5% and (c) 43% below threshold for 2 values of two representative values of frequencies $\omega = 0$ and $\omega \neq 0$. As predicted in Subection 3.2.2, the spectral covariance matrix is always real at $\omega = 0$. For $\omega \neq 0$, however, the OPO configuration in (a) and (c) give rise to complex spectral covariances because of respectively mode-dependant damping rates and asymmetry of the product GF : $(GF)^{\text{T}} \neq GF$. On the contrary, the configuration of parameters in (b) shows always a real spectral covariance matrix since it verifies both conditions in Prop. 3.2.2: $[\Gamma, \mathcal{M}] = 0$ and $(GF)^{\text{T}} = GF$.

When you move to the scenario of mode-independent damping rates ($\gamma_1 = \gamma_2$) for the commutation between Γ and \mathcal{M} to be 0, two possibilities are open to us:

- When $g_{11} = g_{22}$, the product GF is symmetric, resulting from Proposition 3.2.2 in a real spectral covariance matrix. This scenario corresponds the two-mode OPO configuration 5% below threshold and we show in Fig. 3.16b the real and imaginary (always 0) parts of the 16 elements contained in the 4×4 spectral covariance $\sigma_{\text{out}}(\omega)$. The consequence is that optimal levels of squeezing can be fully accessed through standard HD. And since

3.4. MEASURING MORPHING SUPERMODES

this configuration corresponds to degenerate squeezing levels: $d_1^{-2} = d_2^{-2}$ and $d_1^2 = d_2^2$, this configuration is similar to what we observe in the case of the single-mode detuned OPO in Subsection 3.4.2, so we put more focus in the other configurations.

- However, slight asymmetries between modes can often be present such that $g_{11} \neq g_{22}$. This induces a breaking of the symmetry of the product GF and could be generated in this type of system by, but not limited to, something as simple as dispersion-induced mode-dependent detuning. Therefore, even with equal damping rates, the asymmetry introduced in the interaction matrices is sufficient to generate complex spectral covariance. This is shown in Fig. 3.16c where we display the real and imaginary parts of the 16 elements contained in the 4×4 spectral covariance $\sigma_{\text{out}}(\omega)$ and where we see nonzero imaginary components at a representative nonzero frequency. As a consequence, we predict the presence of hidden squeezing. The consequence is that optimal levels of squeezing cannot be fully accessed through standard HD.

So despite the apparent simplicity of this two-mode system, the interplay between parametric amplification and dispersion leads to hidden squeezing and complex morphing supermodes structure [86] for both configurations at 7% and 43% below threshold as shown respectively in Fig 3.17b and 3.18b. The noise spectral power measured by a traditional HD detection scheme with a two-color LO, as depicted in Fig. 3.15b, is not even able to reach the optimal squeezing value of the first supermode as like in the example with a single-mode OPO. This is due to a sub-optimal mode-matching problem between the LO, associated with a real \vec{Q} , and a complex supermode structure $U(\omega)$. We can see that, respectively for configuration 7% and 43% below threshold, in Figs. 3.17(a-left) and 3.18(a-left) for a single frequency and in Figs. 3.19(a-top-left) and 3.20(top-left). In these figures, HD noise power is plotted in dashed-black and the optimal squeezing value is in solid-red. One additional observation is that the presence of hidden squeezing is even more pronounced as we get closer to the OPO threshold. To see that, notice the amount of undetection squeezing in Fig. 3.20(top-left) when we're 7% below threshold, is much higher than in Fig. 3.19a(top-left), 43% below threshold.

In Figs. 3.19a(bottom-left) and 3.20(top-left), the sub-optimal mode-matching (black-dashed) between the LO and the morphing supermode $U_2(\omega)$ is traced for both configuration: the ob-

3.4. MEASURING MORPHING SUPERMODES

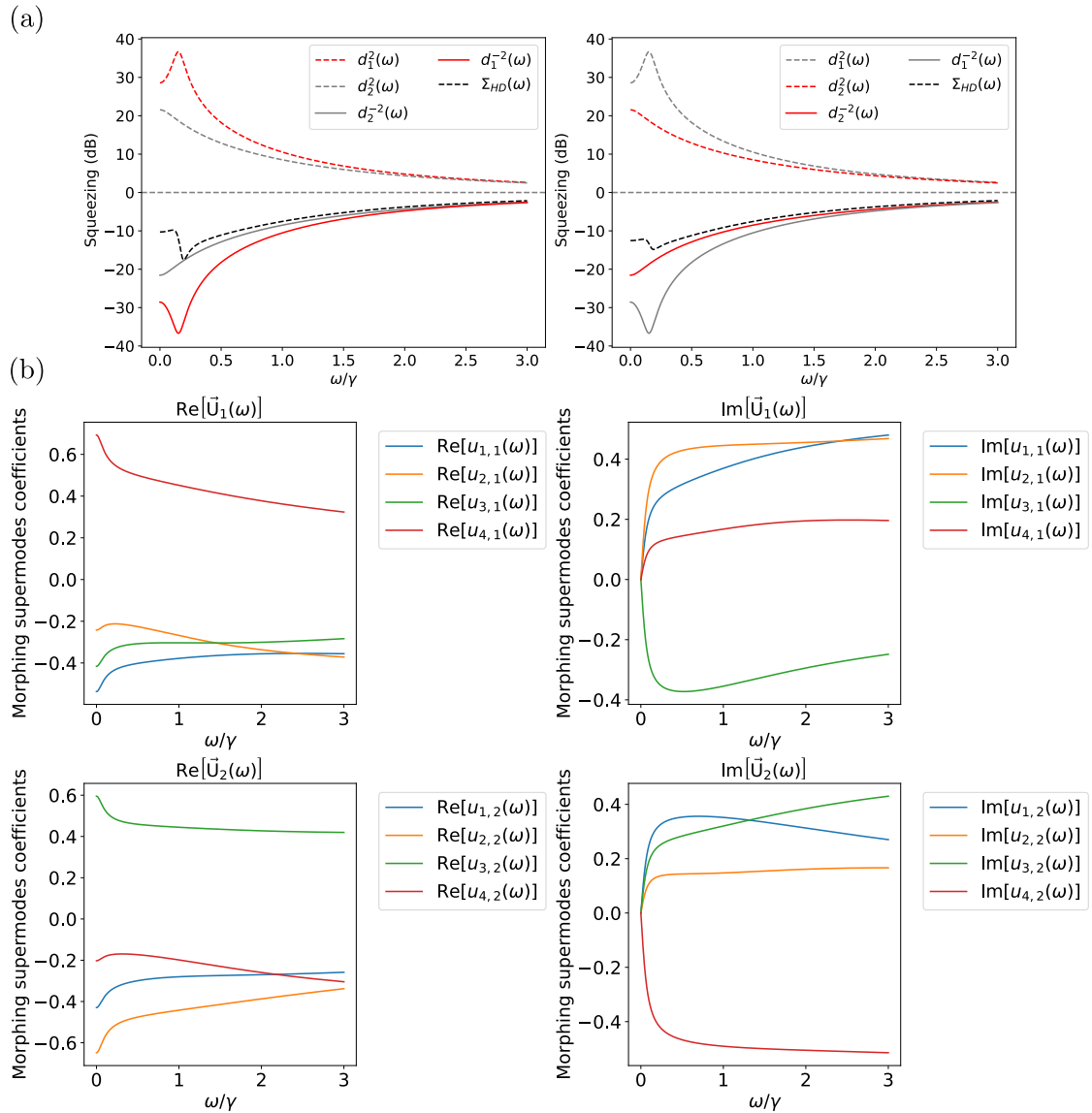


Figure 3.17: **Antisqueezing and squeezing levels and morphing supermodes of two-mode detuned $\chi^{(3)}$ -based OPO** : (a) Antisqueezing and squeezing spectrum of the two-mode OPO configuration 7% below threshold and HD noise spectral power optimal at a single frequency (black-dotted). HD LO is always optimized for the squeezing level in solid red. (b) Real and imaginary parts of the coefficients of the two-first supermodes.

servations are even more striking as in the first mode-OPO case. Perfect projection is reached only at a zero frequency corresponding to the only frequency where the spectral covariance, hence the morphing supermodes are real. This means experimentally, the advantage of using IME with two-mode fields is even more striking than the single-mode case since it allows the

3.4. MEASURING MORPHING SUPERMODES

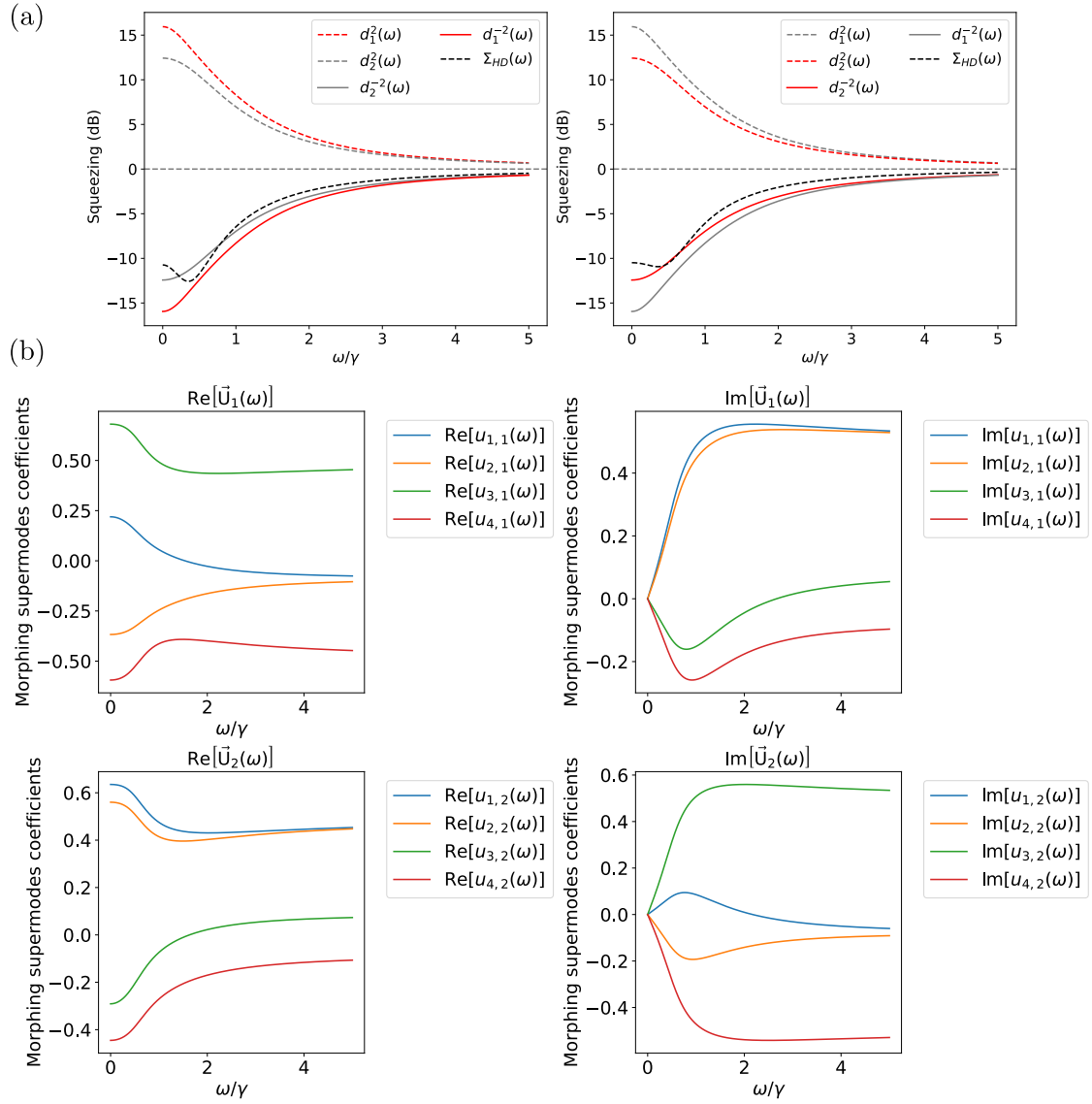


Figure 3.18: **Antisqueezing and squeezing levels and morphing supermodes of two-mode detuned $\chi^{(3)}$ -based OPO** : (a) Antisqueezing and squeezing spectrum of the two-mode OPO configuration 43% below threshold and HD noise spectral optimal at a single frequency (black-dotted). HD LO is always optimized for the squeezing level in solid red. (b) Real and imaginary parts of the coefficients of the two-first supermodes.

characterization of quantum correlations that are inaccessible with conventional HD. Instead, a generalized mode-matching that produces a complex frequency-dependent LO is necessary (see Section 3.3). The most general passive transformation $S_{\text{IME}}(\omega)$ [see Eq. (3.89)] is characterized by a 4×4 damping matrix $\Gamma_{\text{IME}} = \text{diag}\{\gamma_{\text{IME},1}, \gamma_{\text{IME},2} | \gamma_{\text{IME},1}, \gamma_{\text{IME},2}\}$ and 4×4 mode

3.4. MEASURING MORPHING SUPERMODES

coupling matrix Eq. (3.90) with a G_{IME} given by the most general Hermitian matrix Eq. (3.104). Therefore, as explained in Section 3.3, Subsection 3.3.2, this two-mode IME can be implemented by the coupled cavity system depicted in figure Fig. 3.5c, that is the main building block of our smooth two-mode decompositions. The full measurement scheme with IME is shown in Fig. 3.15.

For values of the two-mode OPO corresponding the configuration at 7% below threshold and 43% below threshold, the goal is to optimize the IME parameters so to shape the generalized LO, $\vec{Q}(\omega)$, as the most squeezed morphing supermode, the structure of which is given by the $(N + 1)$ -th column of $U(\omega)$. We want to remind that while this is formally what is happening, the optimization process did not require any knowledge of the morphing supermodes, as stressed in Subsection 3.4.1, we only require the noise spectral power.

For the configuration at 43%, we found that the use of just one IME allows implementing a generalized LO allowing mode-matching in the first half of the spectrum, as seen Fig 3.19a(*top-right*) in dashed-blue. For that, the optimization found the following optimal parameters for the IME: $\gamma_{\text{IME},1} = \gamma_{\text{IME},2} = 1.01\gamma_1$, $\Delta_1 = -1.51\gamma_1$, $\Delta_2 = -1.2\gamma_1$, $\theta_d = 1.21\gamma_1$ and $\phi_d = 4.32$. The optimization involved also the three angles of the two-colour LO, characterized by

$$\vec{Q} = (\vec{x}_{\text{LO}} | \vec{y}_{\text{LO}})^{\text{T}}, \quad (3.147)$$

where

$$\vec{x}_{\text{LO}} = \left(\cos \theta_{\text{LO},1} \cos \theta_{\text{LO},2}, \cos \theta_{\text{LO},3} \sin \theta_{\text{LO},2} \right)^{\text{T}} \quad (3.148)$$

and

$$\vec{y}_{\text{LO}} = \left(\sin \theta_{\text{LO},1} \cos \theta_{\text{LO},2}, \sin \theta_{\text{LO},3} \sin \theta_{\text{LO},2} \right)^{\text{T}}. \quad (3.149)$$

and it returns $\theta_{\text{LO},1} = 4.46$ rad, $\theta_{\text{LO},2} = 1.01$ rad and $\theta_{\text{LO},3} = 0.6$ rad.

A single cavity did not unfortunately yield any good result in the case at 7%. This hints at more difficulties for the generalised LO to match the morphing supermode profiles as we get closer to the OPE threshold.

3.4. MEASURING MORPHING SUPERMODES

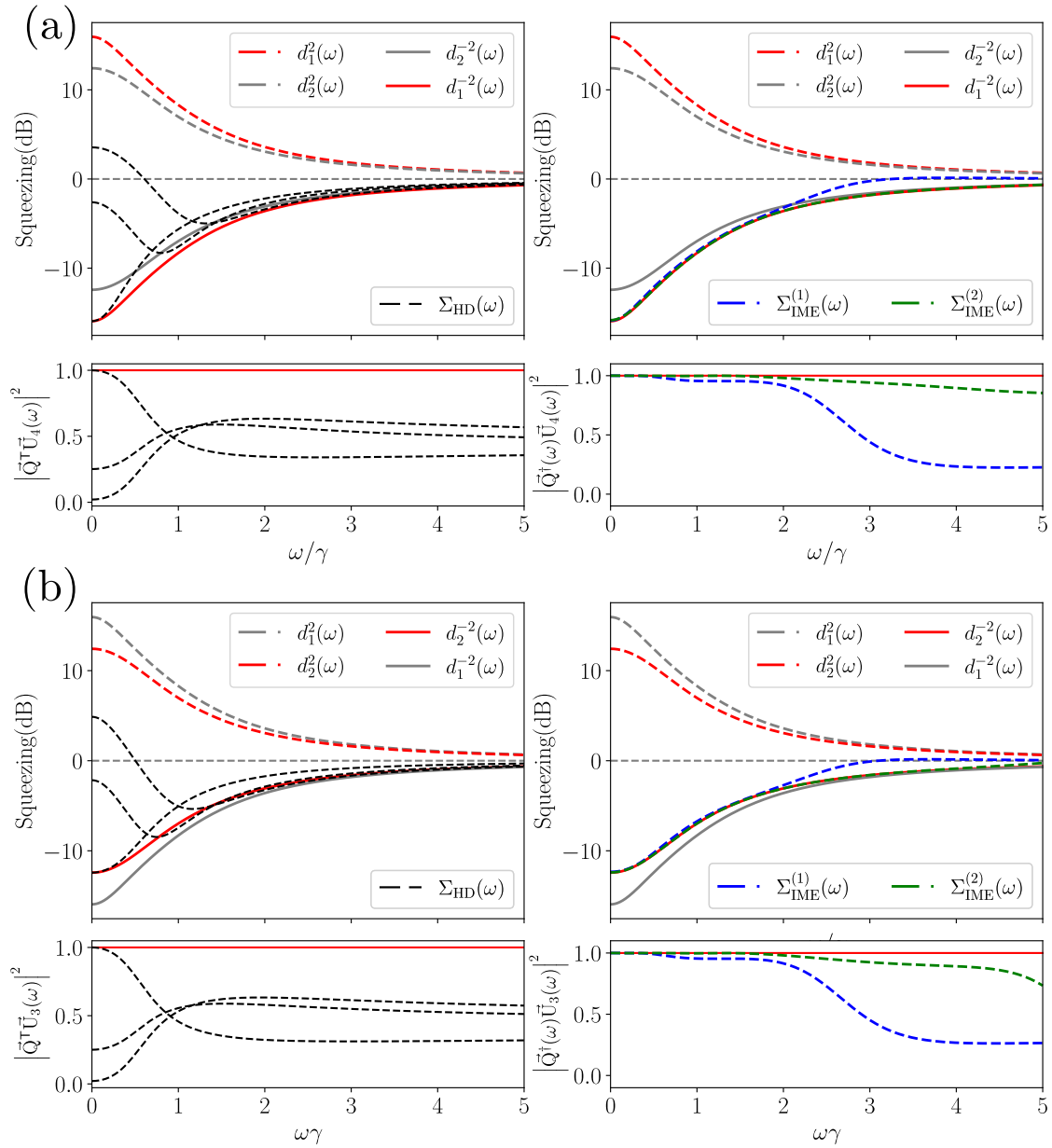


Figure 3.19: (*Top-left*) Optimal squeezed noise spectral power from singular value $d_1^{-2}(\omega)$ (solid red) vs. standard HD measurements $\Sigma_{HD}(\omega)$ for five different \vec{Q} that optimize the detected squeezed signal at a particular ω (dashed-black lines), and (*Bottom-left*) standard LO-squeezed supermode overlap for five different angles θ_{LO} (dashed-black lines) vs. perfect overlap (solid-red). (*Top-right*): Same comparison with measurements using two-chained IMEs $\Sigma_{IME}(\omega)$ (dashed-green line) and (*bottom-right*) generalized LO-supermode overlap (dashed-green line). This is for the OPO configuration 43% below threshold.

3.4. MEASURING MORPHING SUPERMODES

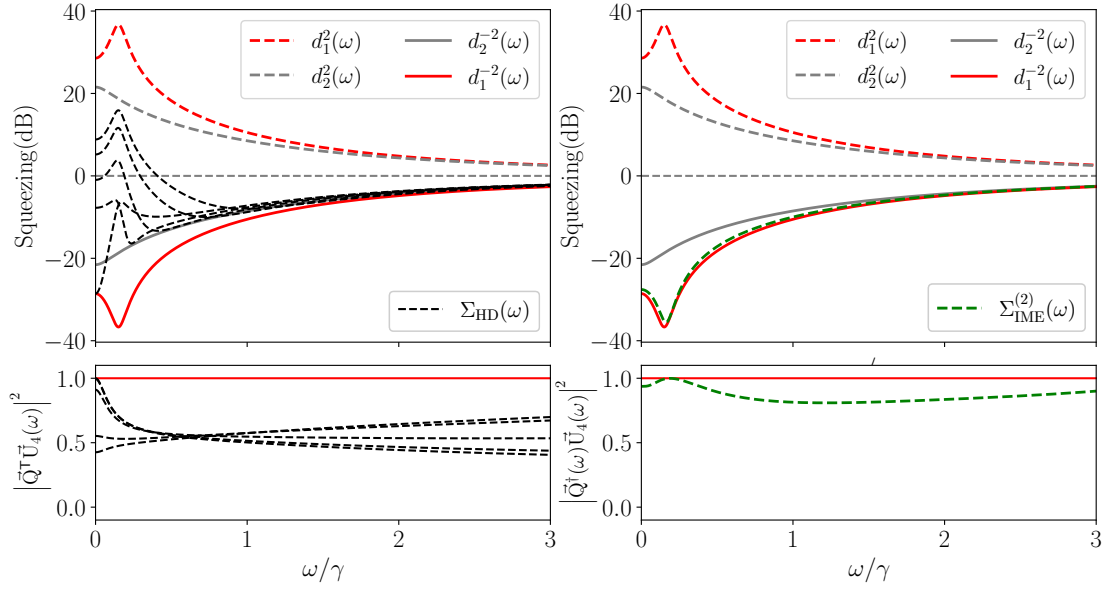


Figure 3.20: (*Top-left*) Optimal squeezed noise spectral power from singular value $d_2^{-2}(\omega)$ (solid red) vs. standard HD measurements $\Sigma_{\text{HD}}(\omega)$ for five different \vec{Q} that optimize the detected squeezed signal at a particular ω (dashed-black lines), and (*Bottom-left*) standard LO-squeezed supermode overlap for five different angles θ_{LO} (dashed-black lines) vs. perfect overlap (solid-red). (*Top-right*): Same comparison with measurements using two-chained IMEs $\Sigma_{\text{IME}}^{(2)}(\omega)$ (dashed-green line) and (*bottom-right*) generalized LO-supermode overlap (dashed-green line). This is for the OPO configuration 43% below threshold.

We, however, managed to achieve optimal matching over the full spectrum using two chained IME systems for both configurations, in Figs. 3.20(*top-right*) and 3.19b(*top-right*) for the cases at 7 and 43% below threshold respectively. In these plots, the noise power with two-chained IME is plotted in dashed-green and we show that the noise spectrum $d_1^{-2}(\omega)$ of the most squeezed morphing supermode can be completely recovered by setting specific parameters of the IMEs:

- For the configuration 7% below threshold $\gamma_{\text{IME},1} = \gamma_{\text{IME},2} = 0.23\gamma_1$, $\Delta_1 = 1.78\gamma_1$, $\Delta_2 = 1.99\gamma_1$, $\theta_d = -1.88\gamma_1$ and $\phi_d = 1.99$ for the first IME, $\gamma_{\text{IME},1} = \gamma_{\text{IME},2} = 2.17\gamma_1$, $\Delta_1 = 1.43\gamma_1$, $\Delta_2 = 0.46\gamma_1$, $\theta_d = 1.42\gamma_1$ and $\phi_d = 3.09$ for the second IME and $\theta_{\text{LO},1} = -1.08$ rad, $\theta_{\text{LO},2} = -1.33$ rad and $\theta_{\text{LO},3} = 1.86$ for the two-color LO.
- For the configuration 43% below threshold : $\gamma_{\text{IME},1} = \gamma_{\text{IME},2} = 0.94\gamma_1$, $\Delta_1 = -4.60\gamma_1$, $\Delta_2 = -2.86\gamma_1$, $\theta_d = 3.66\gamma_1$ and $\phi_d = 10.77$ for the first IME, $\gamma_{\text{IME},1} = \gamma_{\text{IME},2} = 1.45\gamma_1$, $\Delta_1 = -2.42\gamma_1$, $\Delta_2 = -1.61\gamma_1$, $\theta_d = 1.43\gamma_1$ and $\phi_d = 12.6$ for the second IME and $\theta_{\text{LO},1} =$

3.4. MEASURING MORPHING SUPERMODES

10.44 rad, $\theta_{LO,2} = 1.47$ rad and $\theta_{LO,3} = 7.68$ for the two-color LO.

While the algorithm doesn't require the knowledge of the morphing, we show in Fig. 3.19a(*bottom-right*) the almost optimal (close to one in the concerned bandwidth) overlapping between the generalized LO and the squeezed morphing supermode for single (dashed-blue line) and two (dashed-green) IMEs as a function of ω for the configuration at 43% below threshold. The solid-red line represents perfect overlapping at all frequencies. We show the same projection also Figs. 3.20(*bottom-right*) for the configuration at 7% below threshold. The analysis of

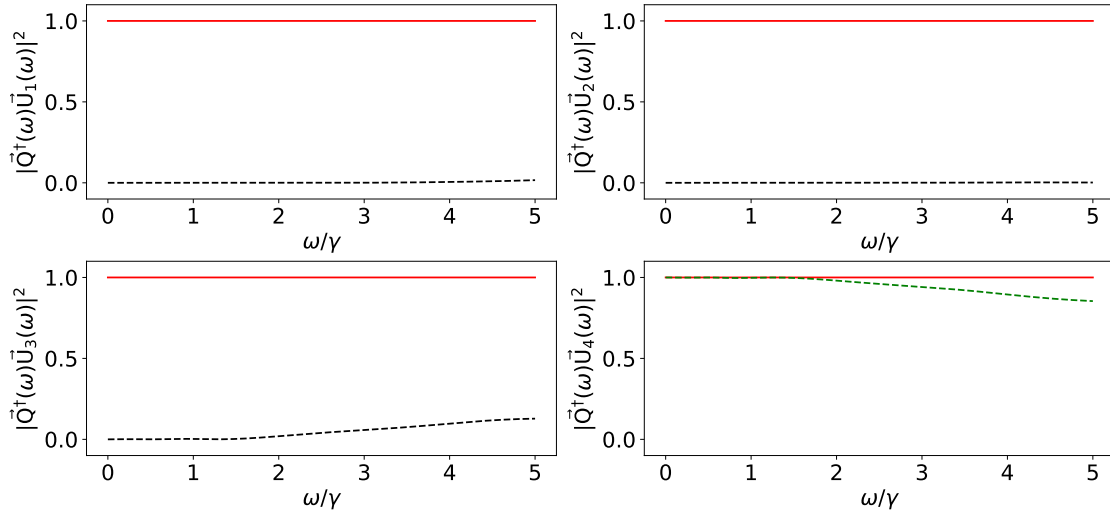


Figure 3.21: Frequency-dependent overlap between the optimal generalized LO and the four morphing supermodes in the case of a two-mode OPO 43% below threshold. The solid red line represents the dominant projections, while the dashed black lines show secondary contributions. The top panels demonstrate negligible overlap with the first two anti-squeezed supermodes, while the bottom panels reveal the primary overlap with the squeezed supermodes. Notably, we see the gradual decrease in $\vec{U}_4(\omega)$ overlap (bottom right) at higher frequencies, compensated by an increase in $\vec{U}_3(\omega)$ overlap (bottom left), caused by the degeneracy of the eigenvalues at frequencies approaching the shot noise limit.

these figures in both configurations reveals an interesting phenomenon: even when we achieve nearly perfect recovery using a two-IME chain, the overlap between the generalized LO and the squeezed morphing supermode deteriorates at higher frequencies approaching the shot noise limit (Figs. 3.20(*bottom-right*) and 3.19b(*bottom-right*)). This behavior stems from the degeneracy of $d_1^{(-2)}(\omega)$ and $d_2^{(-2)}(\omega)$ at these frequencies. When minimizing the noise spectral power, the algorithm begins to project onto a different morphing supermode, as the degeneracy

3.4. MEASURING MORPHING SUPERMODES

ate squeezing spectra result in equivalent cost function values regardless of which morphing supermode the generalized LO is projected onto.

We show this effect in Fig. 3.21 corresponding to our measurements at 43% below threshold. Our analysis of the overlap between the optimal generalized LO (using 2 IMEs) and the four morphing supermodes in $U(\omega)$ shows that while the projection onto the most squeezed morphing supermode $\vec{U}_4(\omega)$ maintains a value close to unity across most of the spectrum, it diminishes as we near the shot noise limit. At these frequencies, where $d_1^{(-2)}(\omega)$ and $d_2^{(-2)}(\omega)$ become degenerate, we observe a corresponding increase in projection onto the less squeezed morphing supermode $\vec{U}_3(\omega)$.

This projection issue represents a slight limitation of the optimization algorithm. However, it's worth noting that this wouldn't pose a problem if we assume complete knowledge of the morphing supermodes, and it typically occurs in spectral regions of lesser interest for our analysis (close to the shot noise).

In this thesis, while we primarily focus on recovering the squeezing spectrum for the most squeezed supermode, our optimization strategy described in Subsection 3.4.1 enables the recovery of other squeezing spectra and even anti-squeezing spectra, though the latter holds limited interest. With complete knowledge of the morphing supermodes, the optimization process becomes straightforward: it simply requires finding the cavity parameters that allow the generalized LO (Eq. (3.80)) to optimally match the morphing supermode corresponding to the desired squeezing spectrum.

We demonstrate the recursive process detailed in Subsection 3.4.1 for recovering the squeezing spectrum $d_2^{-2}d(\omega)$ of the lesser squeezed morphing supermode in a two-mode OPO. Fig 3.19b illustrates this for the two-mode OPO configuration at 43% below threshold. The dashed-blue line in Fig 3.19b(*top-right*) shows how a single IME configuration recovers $d_2^{-2}d(\omega)$ across most of the spectrum with IME parameters $\gamma_{\text{IME},1} = \gamma_{\text{IME},2} = 1.01\gamma_1$, $\Delta_1 = -1.51\gamma_1$, $\Delta_2 = -1.2\gamma_1$, $\theta_d = -1.21\gamma_1$, $\phi_d = 4.32$, and a two-color LO configuration where $\theta_{\text{LO},1} = 3.40$ rad, $\theta_{\text{LO},2} = -0.49$ rad, and $\theta_{\text{LO},3} = 2.25$. The targetted squeezing spectrum $d_2^{-2}d(\omega)$ is shown in solid-red. The dashed-green line demonstrates complete spectrum recovery using two chained IMEs. The first IME uses parameters $\gamma_{\text{IME},1} = \gamma_{\text{IME},2} = 0.88\gamma_1$, $\Delta_1 = -3.42\gamma_1$, $\Delta_2 = -2.15\gamma_1$, $\theta_d = 2.67\gamma_1$, and $\phi_d = 10.92$. The second IME employs $\gamma_{\text{IME},1} = \gamma_{\text{IME},2} = 1.73\gamma_1$, $\Delta_1 = -1.1\gamma_1$,

3.4. MEASURING MORPHING SUPERMODES

$\Delta_2 = -1.4\gamma_1$, $\theta_d = 0.97\gamma_1$, and $\phi_d = 15.64$. And finally the two-color LO parameters used are $\theta_{LO,1} = 11.98$ rad, $\theta_{LO,2} = -0.01$ rad, and $\theta_{LO,3} = 6.02$.

The recovery process was done by minimizing the noise spectral power in the subspace orthogonal to the optimal generalized LO $\vec{Q}(\omega)$ associated with $d_1^{-2}d(\omega)$ recovery. The IME cavity and HD LO configuration recovering $d_1^{-2}d(\omega)$ results in the optimal generalized LO equivalent to $\vec{U}_4(\omega)$, the most squeezed morphing supermode. This utilizes Property 3.4.2 to access $d_2^{-2}d(\omega)$.

While HD appears unaffected when recovering $d_2(\omega)$ even with the presence of hidden squeezing as we see its noise spectral power plotted in dashed-black in Fig 3.19b(*top-left*) for a LO optimized at 4 different angles, this is because suboptimal projection to morphing supermodes results in non-zero projections to other morphing supermodes, as shown in Eq. (3.52). The HD measurement in Fig 3.19b(*top-left*) does not represent a pure $d_2^{-2}(\omega)$ measurement but a linear combination of all squeezing/antisqueezing spectra approximating $d_2^{-2}(\omega)$. The comparison of HD and IME optimal LO projections to $\vec{U}_3(\omega)$ reveals that HD optimization at four different angles in dashed-black (Fig 3.19b(*bottom-left*)) approaches the optimal value of 1 (solid-red) only at $\omega = 0$. At $\omega \neq 0$, the overlaps are far from the optimal value at 1. IME projections, on the contrary, confirm the recovered squeezing associated with $\vec{U}_3(\omega)$, with single IME (dashed-blue) showing near-unity projection in the first part of the spectrum, and dual IME (dashed-green) achieving near-unity projection across almost the entire spectrum, with slight degradation approaching shot noise where squeezing spectra become degenerate. These two-mode OPO examples showcase the substantial enhancement provided by the IME approach that allows to mode-match complex morphing supermodes thus allowing to access to correlations that are hidden to standard HD.

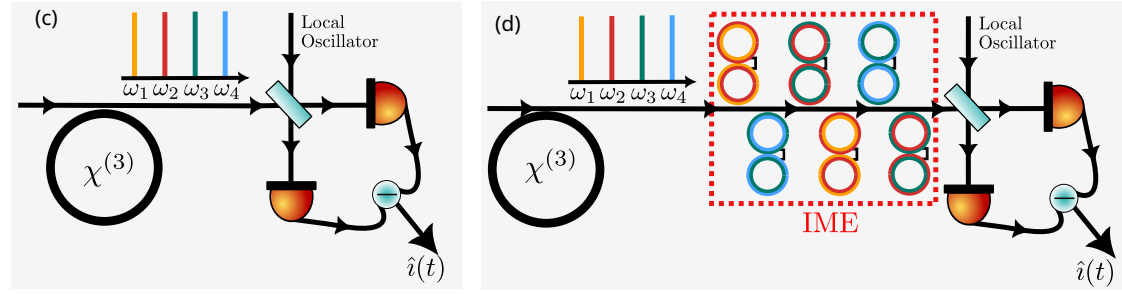


Figure 3.22: **HD vs IME scheme for four-mode OPO:** (left) Scheme of a standard HD for the characterization of four-mode fields with carriers ω_1 , ω_2 , ω_3 and ω_4 . (Right) Our generalized mode-matching by an IME for the four-mode case is implemented through a coupled-cavity systems whose decomposition details are given in Section 1.1.3.

3.4.4 Four-mode OPO

In order to demonstrate the scalability of the IME, we consider a four-mode quadratic open quantum system with dampings $\{\gamma_1, \gamma_2, \gamma_3, \gamma_4\}$ described by the following interaction matrices:

$$G = \begin{pmatrix} 2a & 0 & a & 0 \\ 0 & 2a & 0 & a \\ a & 0 & 2a & 0 \\ 0 & a & 0 & 2a \end{pmatrix}, \quad F = \begin{pmatrix} 0 & b & 0 & 2b \\ b & 0 & 2b & 0 \\ 0 & 2b & 0 & b \\ 2b & 0 & b & 0 \end{pmatrix} \quad (3.150)$$

and as in the single and two-mode case, we consider configurations at different proximity to the OPO threshold. We set the following for two configurations as follows:

- $\gamma_2 = 1.5\gamma_1$, $\gamma_3 = \gamma_1$, $\gamma_4 = 1.5\gamma_1$, $a = 0.6\gamma_1$ and $b = 0.3\gamma_1$, a configuration 100% away from threshold,
- $\gamma_2 = 1.5\gamma_1$, $\gamma_3 = \gamma_1$, $\gamma_4 = 1.5\gamma_1$, $a = 1.37\gamma_1$ and $b = 1.1\gamma_1$, a configuration closer to threshold at 7%.

This four-mode system could describe, for example, a $\chi^{(3)}$ nonlinear cavity driven by strong pumps that lead to parametric amplification and cross-phase modulation couplings between the modes [206]. From the structure of G and F , the product GF is symmetric but since we have mode-dependent damping rates, we can predict from Prop 3.2.2 that the spectral covariance matrix is complex. This is confirmed in Fig 3.23. While At zero frequency ($\omega = 0$), the $16 \times$

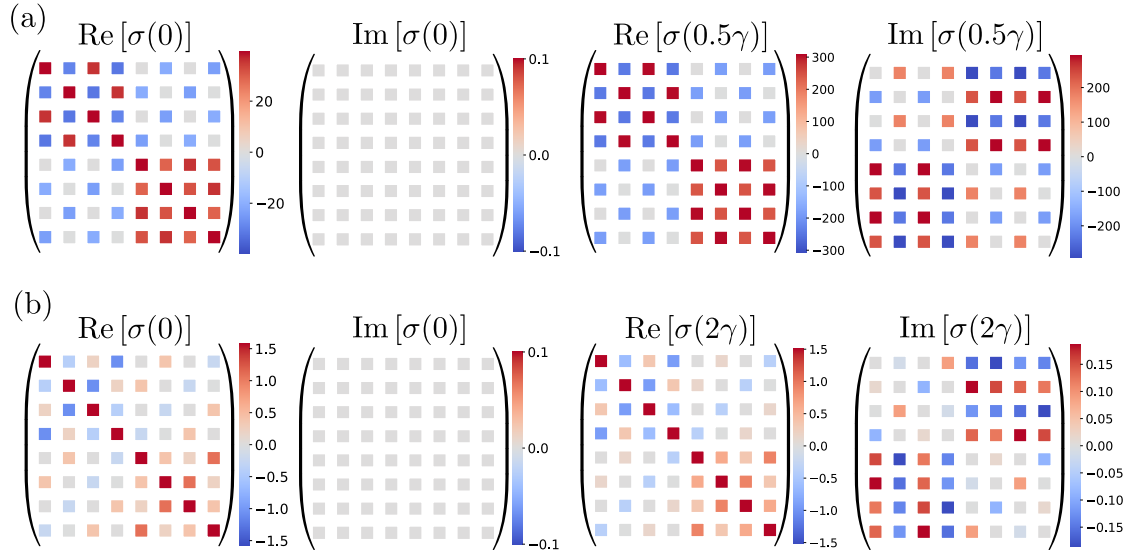


Figure 3.23: **Output spectral covariance of four-mode OPOs:** We show the real and imaginary part of the elements of the 16×16 spectral covariance matrix $\sigma_{\text{out}}(\omega)$. They are shown for four-mode $\chi^{(3)}$ -based OPO (a) 7%, and (b) 100% below threshold for two representative values of frequencies $\omega = 0$ and $\omega \neq 0$. As predicted in Subection 3.2.2, the spectral covariance matrix is always real at $\omega = 0$. For $\omega \neq 0$, however, both configurations in (a) and (b) give rise to complex spectral covariances because of mode-dependant damping rates even though the product GF is symmetric $(GF)^{\text{T}} = GF$.

16 spectral covariance matrix remains purely real, confirming our theoretical predictions from Subsection 3.2.2, a behaviour true regardless of whether we are 7% (a) or 100% (b) below threshold. However, when examining non-zero frequencies ($\omega \neq 0$), the spectral covariances show complex components. This complexity emerges, as predicted, due to the mode-dependent damping rates, even though the product GF remain symmetric: $(GF)^{\text{T}} = GF$. The presence of these imaginary components in the spectral covariance matrix at non-zero frequencies for both configurations shows the powerful prediction tools we pioneered in Fig 3.23. From this complexity, we predict the presence of hidden squeezing.

The ABMD allows to obtain the morphing supermodes which as the spectral covariance, are complex at nonzero frequencies and their corresponding level of squeezing or anti-squeezing. In particular, four supermodes present squeezed spectra $d_i^{-1}(\omega)$ (for $i = 1, \dots, 4$) and the others present anti-squeezed spectra $d_i(\omega)$). We show in Appendix C the real and imaginary parts of the frequency-dependent first four morphing supermodes revealing their complex nature at nonzero frequencies.

3.4. MEASURING MORPHING SUPERMODES

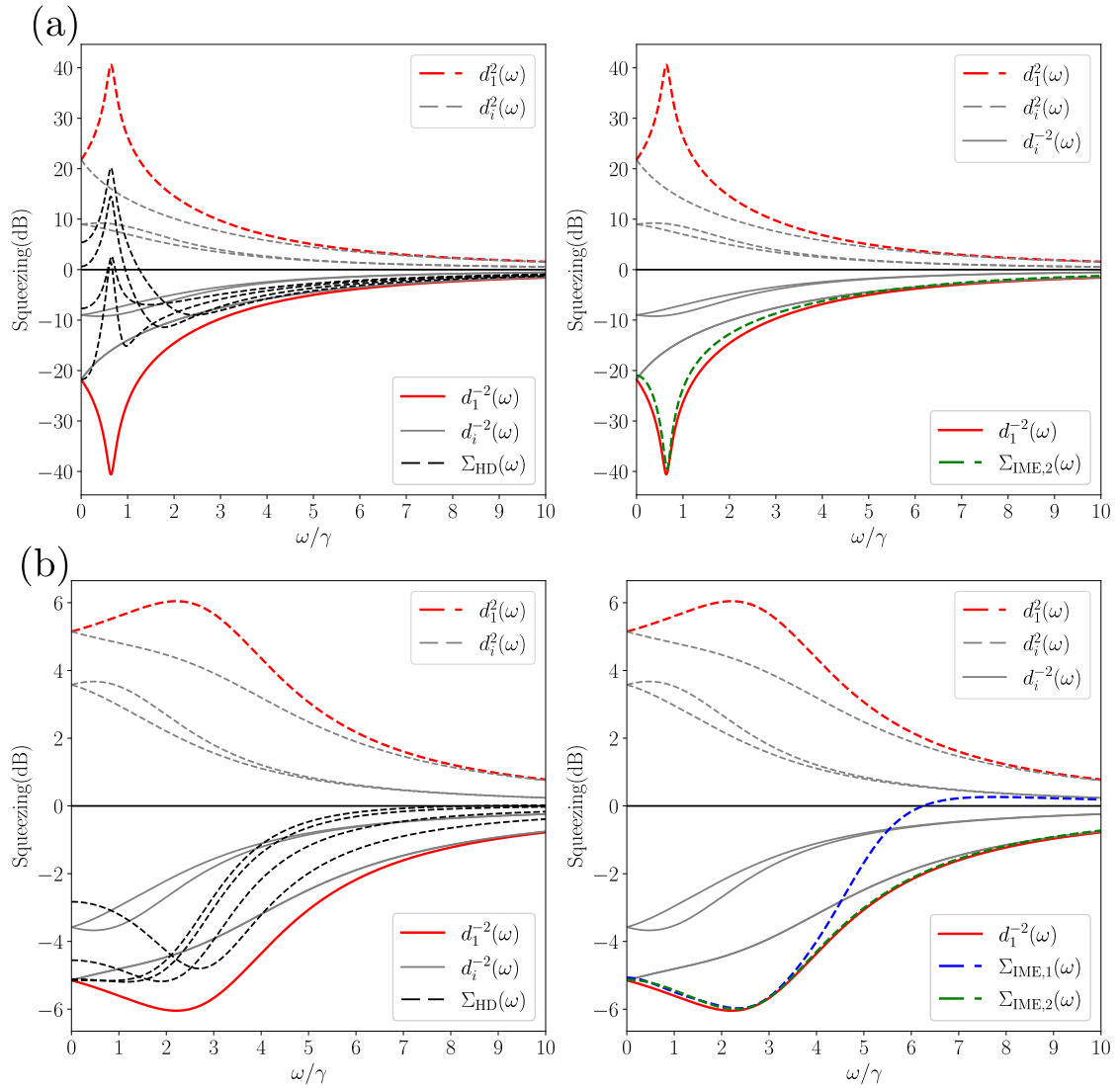


Figure 3.24: Four-mode OPO: for both configuration : (a) 7% and (b) 100% below threshold, (*left*) comparison between noise spectral power of the most squeezed and anti-squeezed morphing supermodes as predicted by the singular values $d_1^{-2}(\omega)$ (solid-red line) and $d_1^2(\omega)$ (dashed-red line) and the noise spectral power $\Sigma_{\text{HD}}(\omega)$ as measured through a standard HD for four different θ_{LO} that optimize the detected squeezed signal at a particular ω (dashed-black lines). The solid and dashed gray lines represent the noise $d_i^{-2}(\omega)$ of the least squeezed and $d_i^2(\omega)$ of the least anti-squeezed morphing supermodes (for $i = \{2, 3, 4\}$). The standard quantum limit is the zero dB level. (*Right*) The noise spectral power $d_1^{-2}(\omega)$ of the most squeezed morphing supermodes is partially recovered (dashed-blue) or fully recovered (dashed-green) by inserting one IME or a chain of two IME before the HD.

In Figs. 3.24a and 3.24b, the red-solid curve represents the squeezing spectrum of the most squeezed morphing supermode, the red-dashed is the noise spectrum of the most anti-

3.4. MEASURING MORPHING SUPERMODES

squeezed morphing supermode, while the grey-solid and grey-dashed curves represent the noise spectra of the other supermodes. In Figs. 3.24a(*left*) and 3.24b(*left*), the black-dashed curves represent the noise spectral power detectable by a standard HD (with a four-color LO), with a scheme showed at Fig 3.22a. Each spectrum is obtained for a specific LO optimized in order to measure the maximal squeezing possible at a given frequency. Because of the impossibility of reaching perfect mode-matching, HD fails to recover the noise spectrum $d_1^{-1}(\omega)$ of the most squeezed morphing supermode (red-solid curve) at all frequencies but $\omega = 0$. At $\omega = 0$, the spectral covariance matrix and the morphing supermodes are always real as we established in Section 3.2.

In contrast, optimal mode-matching can be achieved by introducing a four-mode IME between the source and the HD as depicted, for example, in the case of a rectangular mesh in Fig. 3.22b. Its transfer function $S_{\text{IME}}(\omega)$ (Eq. (3.89)) is now described by a 8×8 matrix with 17 free parameters if we choose equal damping rates for all the modes. We use the smooth decompositions developed in Subsection 3.3.1 in order to find a physical implementation for this system. As commented above, one can choose either a smooth-triangular or a smooth-rectangular decomposition for the two-mode decompositions (Subsection 3.3.2) or single-mode decomposition (Subsection 3.3.3). The result of this algorithm gives a structure represented in Figs. 3.5a and 3.5b. Each frequency mode, labelled with the numbers $i = 1, \dots, 4$ and different colours (yellow, red, green and blue) interact with the other modes through two-mode frequency beam-splitters (Fig. 3.5c). These pairwise interactions, represented by black solid squares, are implemented one by one, in the order specified by the figure. The physical implementation corresponding to these meshes is, instead, depicted in Fig. 3.5d for the case of a smooth-triangular decomposition and in Fig. 3.5d for the case of a smooth-rectangular decomposition. In these figures, the two colours of the frequency beam-splitters have been chosen in order to specify which frequency modes they couple. We can also adopt smooth single-mode decompositions (triangular or rectangular), as described in Section 3.3, Subsection 3.3.3 in terms of single-mode cavities and 50:50 frequency beam splitters. The result of this decomposition for the example considered is represented in Fig. 3.8a for the triangular and in Fig. 3.8d for the rectangular mesh. The optimization of the 17 free parameters of the IME transformation allows to mode-match the generalized LO to the targeted supermode in both configurations: here we consider

3.4. MEASURING MORPHING SUPERMODES

the most squeezed one. We show in Figs. 3.24a(right) and 3.24b(right) respectively for configurations at 7 and 100% that the detected noise spectral power (blue-dashed curve) overlaps with the desired squeezing spectrum $d_1^{-1}(\omega)$ in the most significant part of the total bandwidth. We can chain as many IMEs as necessary to increase the bandwidth where mode-matching is optimal, as we have shown the two-mode OPO in Section 3.4, Subsection 3.4.3. Two chained IME, for example, already allow to recover the full squeezing spectrum of the targeted morphing supermode as illustrated by the dashed-green curve in Figs. 3.24a(right) and 3.24b(right), for configurations at 7 and 100% below threshold. We show in Appendix C the optimized parameters of the single and double IME recovery and the shape of the 4 color-mode LO.

As a final remark, note that these results have been obtained with a basic optimization algorithm described in Subsection 3.4.1. In the perspective of increasing the number of modes, more efficient algorithms could be employed. But as we mentioned at the end of Subsection 3.4.1, identifying the most effective strategies for the optimization of large parameter problems is beyond the scope of this, however, the absence of exponential scaling indicates that efficient optimizations should allow parameters to remain computationally tractable even as system size increases

3.4.5 Scaling and losses

Intrinsic losses in the elemental components of an IME play a crucial role in any realistic implementation, particularly concerning its scalability. While fabrication technology is advancing rapidly and many current limitations affecting device performance may be alleviated in the near future [207], we can theoretically address this issue based on current technological capabilities.

Let's first address how the IME process is modified when accounting for intrinsic losses. We need to modify the set of coupled quantum Langevin equations 3.4 while considering the system's intrinsic losses:

$$\frac{d\hat{R}_{\text{IME}}(t)}{dt} = (-\Gamma - \mathcal{K} + \mathcal{M})\hat{R}(t) + \sqrt{2\Gamma}\hat{R}_{\text{out}}(t) + \sqrt{2\mathcal{K}}\hat{R}_{\text{in}}^{(\kappa)}(t), \quad (3.151)$$

where we remind that where $\hat{R}_{\text{in}}^{(\gamma)}(t) = \hat{R}_{\text{out}}(t)$ is the quadrature input vector from the external

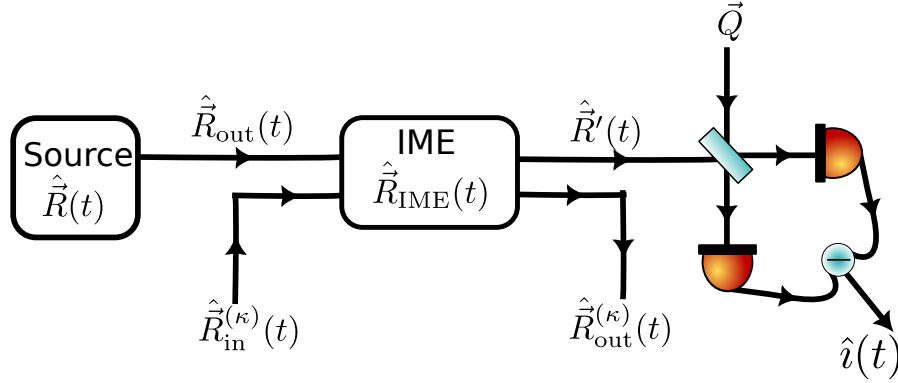


Figure 3.25: **Conventions for the input-output quadrature vector for the lossy IME treatment.**

coupling to the IME (therefore the input of the IME from the source) while $\hat{R}_{in}^{(\kappa)}$ is the quadrature input vector of the intrinsic loss modes (Fig. 3.25). In microresonators, Γ corresponds to mode-dependent damping rates accounting for extrinsic losses arising from interactions between the microresonator and external components (coupling losses to external modes, insertion losses). Meanwhile, \mathcal{K} corresponds to mode-dependent damping rates accounting for intrinsic losses inherent to the resonator's structure and materials (material absorption, propagation losses, scattering losses, bending losses) [208, 209]. To simplify our analysis, we can combine the losses into a single bus [54] as in Eq. (3.4) where the input quadrature vectors verify:

$$\sqrt{2(\Gamma + \mathcal{K})}\hat{R}_{in,tot}(t) = \sqrt{2\Gamma}\hat{R}_{out}(t) + \sqrt{2\mathcal{K}}\hat{R}_{in}^{(\kappa)}(t) \quad (3.152)$$

where $\Gamma_{tot} = \Gamma + \mathcal{K}$ representing the total mode-dependent loss rate. Now our equation has the familiar form of Eq. (3.4) which we already know the solution corresponding to the transfer function between the total input and output spectral quadratures as defined in Eq. (3.21): $\hat{R}_{out,tot}(\omega) = S_{IME,tot}(\omega)\hat{R}_{in,tot}(\omega)$ with

$$S_{IME,tot}(\omega) = \sqrt{2\Gamma_{tot}}(i\omega\Gamma_{tot} + \Gamma_{tot} - \mathcal{M}_{IME})^{-1}\sqrt{2\Gamma} - I. \quad (3.153)$$

To access the output spectral quadratures at the output of the IME $\hat{R}'(\omega)$, we use its associated

3.4. MEASURING MORPHING SUPERMODES

input-output relations:

$$\hat{R}'(\omega) = \sqrt{2\Gamma} \hat{R}_{\text{IME}}(\omega) - \hat{R}_{\text{in}}^{(\gamma)}(\omega). \quad (3.154)$$

To find the internal field quadratures $\hat{R}_{\text{IME}}(\omega)$, we write:

$$\hat{R}_{\text{IME}}(\omega) = \frac{1}{\sqrt{2\Gamma}} [\hat{R}_{\text{out,tot}}(\omega) + \hat{R}_{\text{in,tot}}(\omega)] = \frac{1}{\sqrt{2\Gamma}} [I + S_{\text{IME,tot}}(\omega)] \hat{R}_{\text{in,tot}}(\omega). \quad (3.155)$$

Now, we can express the internal field in terms of the individual input fields:

$$\hat{R}_{\text{IME}}(\omega) = \frac{1}{\sqrt{2\Gamma}} [I + S_{\text{IME,tot}}(\omega)] \left[\sqrt{\frac{\Gamma'}{\Gamma}} \hat{R}_{\text{out}}(\omega) + \sqrt{\frac{\mathcal{K}}{\Gamma}} \hat{R}_{\text{in}}^{(\kappa)}(\omega) \right]. \quad (3.156)$$

Substituting this into the input-output relation in Eq. 3.154, we obtain:

$$\hat{R}'(\omega) = \sqrt{\frac{\Gamma}{\Gamma_{\text{tot}}}} [I + S_{\text{IME,tot}}(\omega)] \left[\sqrt{\frac{\Gamma}{\Gamma_{\text{tot}}}} \hat{R}_{\text{out}}(\omega) + \sqrt{\frac{\mathcal{K}}{\Gamma_{\text{out}}}} \hat{R}_{\text{in}}^{(\kappa)}(\omega) \right] - \hat{R}_{\text{out}}(\omega). \quad (3.157)$$

This can be written in a more compact form:

$$\hat{R}'(\omega) = S_{\text{IME}}^{(\gamma)}(\omega) \hat{R}_{\text{out}}(\omega) + S_{\text{IME}}^{(\kappa)}(\omega) \hat{R}_{\text{in}}^{(\kappa)}(\omega). \quad (3.158)$$

where $S_{\text{IME}}^{(\gamma)}(\omega)$ is the transmission coefficient and $S_{\text{IME}}^{(\kappa)}(\omega)$ is the reflection coefficient, given by:

$$S_{\text{IME}}^{(\gamma)}(\omega) = \sqrt{\frac{\Gamma}{\Gamma_{\text{tot}}}} [I + S_{\text{IME,tot}}(\omega)] \sqrt{\frac{\Gamma}{\Gamma_{\text{tot}}}} - I, \quad (3.159)$$

$$S_{\text{IME}}^{(\kappa)}(\omega) = \sqrt{\frac{\Gamma}{\Gamma_{\text{tot}}}} [I + S_{\text{IME,tot}}(\omega)] \sqrt{\frac{\mathcal{K}}{\Gamma_{\text{tot}}}}. \quad (3.160)$$

These coefficients describe how the input fields from both the external coupling and internal losses contribute to the output field.

The coefficients describe how input fields from both external coupling and internal losses contribute to the output field. In the special case where there are no intrinsic losses ($\mathcal{K} = 0$), we have $\Gamma_{\text{tot}} = \Gamma$, which simplifies our equations to the expected $S_{\text{IME}}^{(\gamma)}(\omega) = S(\omega)$ in Eq. (3.21) and $S_{\text{IME}}^{(\kappa)}(\omega) = 0$.

The spectral covariance matrix at the output of the IME of the matrix in Eq. (3.91) changes

3.4. MEASURING MORPHING SUPERMODES

to :

$$\sigma'(\omega) = \hat{R}'(\omega)\hat{R}'^{\top}(-\omega) \quad (3.161)$$

$$\sigma'(\omega) = S_{\text{IME}}^{(\gamma)\dagger}(\omega)\sigma_{\text{out}}(\omega)S_{\text{IME}}^{(\gamma)}(\omega) + S_{\text{IME}}^{(\kappa)\dagger}(\omega)\sigma_{\text{in}}^{(\kappa)}(\omega)S_{\text{IME}}^{(\kappa)}(\omega). \quad (3.162)$$

, where again $\sigma_{\text{out}}(t)$ is the output spectral covariance matrix of the source. We see the covariance matrix of the output source is contaminated by the mode of the intrinsic losses (in general vacuum modes). We can further see this by looking at the noise spectral power after HD at the output of the IME when we have assumed vacuum modes for the input source and the intrinsic loss modes of the cavity and using ABMD Eq. (3.33):

$$\Sigma_{\text{IME}}(\omega) = \vec{Q}^{\top}\sigma'(\omega)\vec{Q} \quad (3.163)$$

$$= \frac{1}{2\sqrt{2\pi}} \left[\vec{Q}^{\top} S_{\text{IME}}^{(\gamma)\dagger}(\omega)U(\omega)D^2(\omega)U^{\dagger}(\omega)S_{\text{IME}}(\omega)\vec{Q} + \vec{Q}^{\top} S^{(\kappa)\dagger}(\omega)S^{(\kappa)}(\omega)\vec{Q} \right] \quad (3.164)$$

$$\Sigma_{\text{IME}}(\omega) = \frac{1}{2\sqrt{2\pi}} \left[[\vec{Q}^{(\gamma)\dagger}(\omega)U(\omega)]D^2(\omega)[U^{\dagger}(\omega)\vec{Q}^{(\gamma)}(\omega)] + \vec{Q}^{(\kappa)\dagger}(\omega)\vec{Q}^{(\kappa)}(\omega) \right], \quad (3.165)$$

where $\vec{Q}^{(\gamma)\dagger}(\omega) = \vec{Q}^{\top}S_{\text{IME}}^{(\gamma)}(\omega)$ and $\vec{Q}^{(\kappa)\dagger}(\omega) = \vec{Q}^{\top}S_{\text{IME}}^{(\kappa)}(\omega)$.

For an interpretation of what's happening let's project these complex vectors into the orthonormal basis of morphing supermodes:

$$\vec{Q}^{(\gamma)}(\omega) = \sum_{i=1}^{2N} \beta_i^{(\gamma)}(\omega)\vec{U}_i(\omega) \quad \text{with} \quad \beta_i^{(\gamma)}(\omega) = \langle \vec{Q}^{(\gamma)}(\omega), \vec{U}_i(\omega) \rangle \quad (3.166)$$

$$\vec{Q}^{(\kappa)}(\omega) = \sum_{i=1}^{2N} \beta_i^{(\kappa)}(\omega)\vec{U}_i(\omega) \quad \text{with} \quad \beta_i^{(\kappa)}(\omega) = \langle \vec{Q}^{(\kappa)}(\omega), \vec{U}_i(\omega) \rangle. \quad (3.167)$$

With the help of the decomposition of the spectral covariance matrix in Eq. (3.47), we can write the noise spectral power as:

$$\Sigma_{\text{IME}}(\omega) = \frac{1}{2\sqrt{2\pi}} \sum_{i=1}^{2N} \left(\lambda_i^2(\omega) |\beta_i^{(\gamma)}(\omega)|^2 + |\beta_i^{(\kappa)}(\omega)|^2 \right), \quad (3.168)$$

where again $\lambda_i^2(\omega)$ correspond to the squeezing/antisqueezing spectrum Eq. (3.48) and $|\beta_i^{(\gamma)}(\omega)|^2 + |\beta_i^{(\kappa)}(\omega)|^2 = 1$ for $i = \{1, \dots, 2N\}$. With Eq. (3.168), one can see that while our the projection of

3.4. MEASURING MORPHING SUPERMODES

our generalized LO $\vec{Q}^{(\gamma)}(\omega)$ in a desired morphing supermodes to recover the desired squeezing spectrum will be contaminated by the projection of $\vec{Q}^{(\kappa)}(\omega)$ in the vacuum.

We put in place a test procedure to see this in effect considering the two-mode decomposition of our IMEs in terms of coupled cavity arrays in Subection 3.3.2, implemented using coupled cavity arrays as in Fig 3.5. Considering the on-chip propagation losses we can expect from each coupled cavity on average, this value will be scaled accordingly to the number of modes to account for the losses induced by the whole IME. This is also relevant when cascading multiple IMEs. Regarding practical implementations, the intrinsic losses reported in the original frequency beam splitter [198] are approximately 1 dB per element, with potential improvement to 0.04 dB per element in the overcoupled regime.

To convert on-chip loss α in dB: $\alpha = -10 \log_{10} \left(\frac{P_{out}}{P_{in}} \right)$, we consider for simplicity, the case where we consider cavities with mode independent losses $\Gamma = \gamma \cdot I_{2N}$ and $\mathcal{K} = \kappa \cdot I_{2N}$ and we want to relate α to κ the amplitude decay rate from intrinsic losses. The relationship between output and input power from intrinsic losses decay can be expressed as: $\frac{P_{out}}{P_{in}} = e^{-2\kappa\tau_p}$ where τ_p is a photon mean lifetime inside the cavity. τ_p is related to the total quality factor and the resonance frequency of the cavity. It corresponds to the inverse of the total loss rate: $\tau_p = \frac{1}{\gamma + \kappa}$. The on-chip loss in decibels therefore writes

$$\alpha_{dB} = -10 \log \left(e^{-\frac{2\kappa}{\gamma + \kappa}} \right) = \frac{20\kappa}{(\gamma + \kappa) \ln(10)}. \quad (3.169)$$

Solving for κ , we get:

$$\kappa = \frac{\gamma \alpha_{dB} \ln(10)}{20 - \alpha_{dB} \ln(10)}. \quad (3.170)$$

α_{dB} corresponds to a single coupled cavity loss, to scale this it the whole IME, we need to account for the number of times each mode interacts with a coupled cavity. We start by reminding, for N modes, the number of two-mode coupled cavities required for both rectangular and triangular decomposition for the IME are $\frac{N(N-1)}{2}$, so it scales as $\sim N^2$. So in total, since each two-mode coupled cavity interacts with two modes, the total number the total number of mode-cavity interactions in the IME is $2 \times \frac{N(N-1)}{2} = N(N-1)$. So on average, each individual

3.4. MEASURING MORPHING SUPERMODES

mode interacts with $(N - 1)$ coupled cavities. This means each mode, on average experiences, the individual element losses $(N - 1)$ times. This implies a linear scaling of the mode losses with respect to the number of modes.

Particularly, for the triangular configuration described by the meshing in Fig 3.5a and implemented in Fig 3.5d, the exact distribution of the number of coupled cavity interactions for each mode, for a total number of mode $N > 2$ increases with N . The first mode interacts with only one cavity, while subsequent modes interact with an increasing odd number of cavities (3, 5, 7, ...). The last mode is a special case that interacts with $N - 1$ cavities. With 5 modes, the pattern would be [1, 3, 5, 3], indicating that the first mode interacts with 1 coupled cavity, the second with 3 cavities, and so on. This can be verified in Fig 3.5a and for the example of 11 modes, we get the pattern [1, 3, 5, 7, 9, 11, 13, 15, 17, 19, 10]. While not mentioned, this triangular configuration of the IME be reversed so that higher-numbered modes have fewer interactions. In this case, we get for example, the patterns [3, 5, 3, 1] and [10, 19, 17, 15, 13, 11, 9, 7, 5, 3, 1] respectively for $N = 4$ and $N = 11$.

For the rectangular configuration described by the meshing in Fig 3.5b and implemented in Fig 3.5e, the pattern creates a much more regular distribution where most modes interact with the maximum number of cavities, except for the first and last modes. This creates a much more regular tiling where the number of interactions to coupled cavities of each mode is balanced. The exact distribution from top to bottom mode is as follows:

- For even number of total modes N : first and last modes both interact with $\frac{N}{2}$ cavities and all intermediate modes interact with N cavities. Example with 4 modes: [2, 4, 4, 2] and example with 10 modes: [5, 10, 10, 10, 10, 10, 10, 10, 10, 5].
- For odd number of total modes N : first and last modes interact respectively with $\frac{N+1}{2}$ and $\frac{N-1}{2}$ cavities and all intermediate modes interact with N cavities. Example with 3 modes: [3, 4, 4, 3] and example with 10 modes: [6, 11, 11, 11, 11, 11, 11, 11, 11, 5].

Now we know the number of interactions to coupled cavities for each mode, we simulated its performance in both rectangular and triangular configurations. We added a hypothetical configuration where the number of coupled cavity interactions for each mode is constant regardless of the number of modes. This would produce a perfectly balanced mesh and could be obtained

3.4. MEASURING MORPHING SUPERMODES

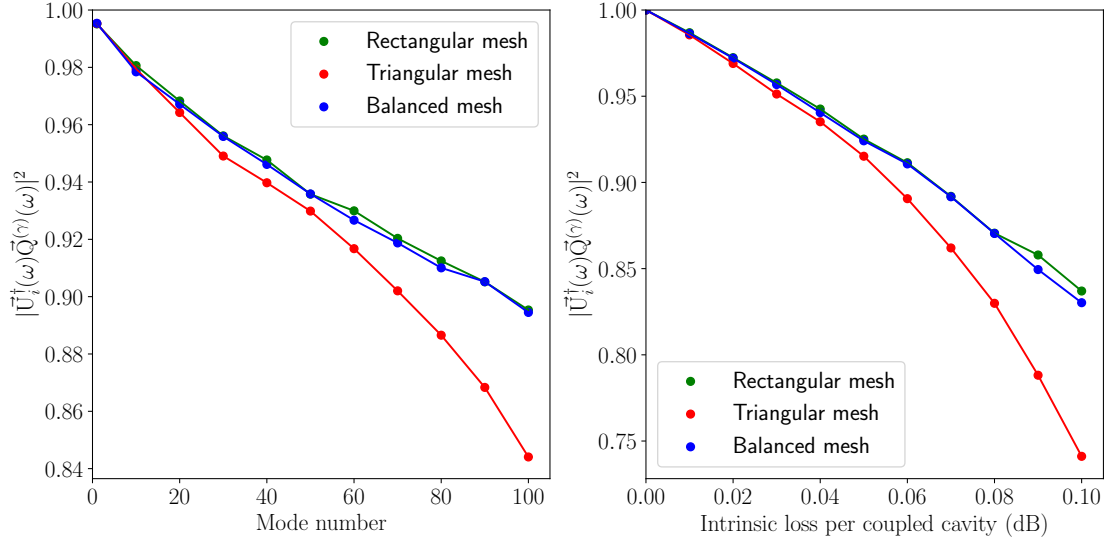


Figure 3.26: **Loss scaling:**(Left) average overlap between 500 random targeted supermode profiles $\vec{U}_i(\omega)$ and generalized LOs $\vec{Q}^{(\gamma)}(\omega)$ obtained from lossy IME, as a function of the number of modes. The plot is generated for an arbitrary frequency and with a fixed intrinsic loss of 0.04 dB per elemental component organized in a rectangular mesh (see Fig 3.5b and Fig 3.5b), a triangular mesh (see Fig 3.5a and Fig 3.5d) and in a hypothetical perfectly balanced mesh. (Right) average overlap versus intrinsic loss per elemental component (dB) for a 45-mode IME.

by adding dummy coupled cavities to a given rectangular configuration. We keep it hypothetical since our goal is to verify if such a configuration has a better loss scaling. For a given number of modes, we generated 500 random complex local oscillators (LO) $\vec{Q}(\omega)$ (Eq. (3.80)) implemented using our IME and incorporated a fixed intrinsic loss α for each two-mode coupled cavity. We quantify the mode matching between the ideal $\vec{Q}(\omega)$ corresponding to a random supermode profile $\vec{U}_i(\omega)$ and its lossy version $\vec{Q}^{(\gamma)}(\omega)$ obtained from the theory with intrinsic losses (Eq. (3.167)). We used the metric $|\vec{U}_i^\dagger(\omega)\vec{Q}^{(\gamma)}(\omega)|^2$, allowing us to assess how closely the lossy implementation matches the intended transformation. Figure 3.26 presents our simulation results for all three configurations. The left panel shows the average fidelity over the 500 complex LOs as a function of the number of modes, with a fixed intrinsic loss of 0.04 dB per coupled cavity. The right panel illustrates how the average fidelity changes with increasing intrinsic loss for a 45-mode IME. As we can see from these figures, for $N=100$, one still gets a mode-matching of 90% for the rectangular and balanced configuration and 84% for the triangular configuration. This corresponds to the overall loss effect for an IME containing about 5000

3.4. MEASURING MORPHING SUPERMODES

elements. This demonstrates that the IME design maintains high fidelity in mode-matching of the targeted supermodes as the number of modes increases. The rectangular configuration not only demonstrates superior performance to a perfectly balanced configuration, confirming that it's the most robust configuration against losses. Both configurations still prove these results that the IME implementation is robust against losses. While this is true, we still want to explore in future work a more compact implementation of the IME.

Two issues to discuss for this interpretation - while this interpretation shows the effect of intrinsic losses in the mode matching capabilities of the complex generalized LO with HD, We should have instead directly looked at the effect in the squeezing detection by minimizing the noise spectral power. Since our algorithm is quite basic and not at all optimized for a high number of modes, this task was impossible as we're writing this. - This same point works against our favour since instead of finding the perfect non-lossy generalized LO and applying the losses to it, it instead finds the closest lossy generalized LO to the targeted supermodes by essentially minimizing the lossy noise spectral power in Eq. (3.168). - While the rectangular decomposition shows a superior resilience to losses compared to the triangular configuration, we expected even better resilience from the rectangular decomposition when borrowing from interpretation to decomposition of spatial modes as in [201]. We didn't observe such behaviour in our case, revealing perhaps a better way to quantify the effect of the losses.

Conclusion and Perspectives

The work presented in this thesis advances multimode quantum optics through two major theoretical and practical contributions that address fundamental challenges: temporal cavities for genuine temporal mode filtering and interferometers with memory effect (IME).

Temporal cavities for temporal mode filtering

In Chapter 2, we propose a method to realize a genuine temporal mode filter for frequency combs, which transmits a single temporal mode while blocking other temporal modes. This novel concept, which we call "temporal cavity," leverages space-time duality principles to translate spatial mode-cleaning cavity principles to the temporal domain. The filter operation is based on the temporal mode dependence of the temporal Gouy phase combined with a cavity build-up effect.

Our theoretical framework demonstrates how temporal cavities can achieve mode-selective filtering while preserving the carrier frequency and original pulse shape. Unlike existing approaches like Quantum Pulse gates (QPGs), this filter operation does not rely on complex non-linear interactions or phase matching, is frequency independent, and maintains the temporal mode structure intact.

We show that temporal cavities can be practically implemented using a combination of electro-optic time lenses and diffraction gratings. This work includes comprehensive parameter optimization strategies accounting for intrinsic losses and technical constraints for classical and quantum applications, demonstrating feasibility with current technology components. These novel devices will facilitate new applications in multidimensional quantum information pro-

cessing and time-frequency metrology by enabling multiplexing and demultiplexing of temporal modes, including temporal mode-dependent detection. In particular, it will enable the synthesis of multimode quantum frequency combs as resources for quantum networks [145] as well as for quantum metrology [37].

The chapter concludes by addressing current limitations and technical challenges in time lens implementations with available components. Future investigations will focus on advancing temporal cavity implementations and capabilities in multiple directions. In the near term, developments in electro-optic phase modulation (EOPM) based time lenses [168] offer promising pathways for practical realizations with improved performance. Beyond the current Hermite-Gaussian-shaped frequency comb modes, exploration of different dispersion profiles could enable manipulation of modes with diverse shapes, significantly expanding the applicability of temporal cavities to advanced quantum communication protocols that require multiple dictionaries.

More fundamental studies will investigate temporal cavities' behaviour under more realistic conditions, including the effects of dispersion aberrations (higher-order dispersion) and time-lens imperfections (finite time-lens). These studies will be crucial for optimizing performance in practical implementations. Looking further ahead, the integration of temporal cavities into photonic integrated circuits presents an exciting opportunity for creating more compact and scalable implementations, potentially enabling new applications in quantum information processing and communication.

This progression from theoretical foundations to practical implementations, while addressing both immediate technical challenges and long-term integration goals, establishes a comprehensive roadmap for advancing temporal cavity technology.

Interferometer with memory effect (IME)

In the framework of CV quantum optics, the second major contribution of this work addresses fundamental limitations in quantum state detection through the introduction of Interferometers with memory effect (IME). Our analysis reveals that states exhibiting morphing behaviour and hidden squeezing, produced by the interplay of quadratic Hamiltonians and cavity-based dissi-

pative dynamics, are much more common than previously recognized. These features appear in various physical platforms, including $\chi^{(3)}$ -based microresonators, optomechanical systems, four-wave mixing in atomic ensembles, polaritons in semiconductor microcavities, and quantum cascade lasers. Homodyne detection, the most widely used measurement technique, is insufficient to deal with states presenting these features, hence hindering the efficiency of CV protocols for QIP.

We showed in Chapter 3 that this is due to the impossibility of HD of realizing perfect mode-match even in the best scenario. We present for the first time a universal approach to achieving perfect mode-matching through a novel detection scheme based on interferometers with memory effect. We provide a complete physical implementation design for these devices, establishing both theoretical frameworks and practical implementation strategies. The successful demonstration of IME advantages in systems with a small number of modes (1-4) suggests promising prospects for early proof-of-concept implementations using current photonic integrated platforms.

Looking ahead, several exciting research directions emerge. A primary focus will be developing more compact IME implementations through for example engineered frequency conversion interactions, particularly using multimode sum frequency generation, to improve implementation scaling. Another crucial direction involves investigating IME effects in systems where certain modes are traced out, particularly relevant for systems where a given subset of modes is inaccessible. These advances will be essential for extending IME capabilities to more complex quantum systems while maintaining practical feasibility.

Additionally, through the design of IMEs, we introduce several innovative theoretical tools and concepts.

Smooth Decomposition Methods

This work introduces two novel decomposition techniques that advance the implementation of frequency-dependent unitaries. In Subsection 3.3.2, the smooth two-mode decomposition provides a novel approach to breaking down arbitrary frequency-dependent unitaries into basic photonic components with different meshing configurations corresponding chosen from spe-

cific nulling orders. Property 3.3.1 states that any arbitrary frequency-dependent unitary can be decomposed into meshes of two-mod frequency-dependent unitaries, corresponding to tunable frequency-beam splitters. While such frequency beam splitters can have any complex profile, coupled-cavity, through cascading to increase the complexity of their frequency profile, can allow implementation of these two-level unitaries enabling practical implementation of any frequency-dependent unitaries through coupled-cavity arrays. The effectiveness of this approach is demonstrated through high fidelity performance metrics, achieving approximately 90% fidelity matching for systems with up to 100 modes with a triangular meshing, with potential for improvement through advances in high-Q factor integrated microring resonators.

Alternatively, in Subsection 3.3.3, the smooth single-mode decomposition method introduces a new different way to handle these frequency-dependent unitaries. Rather than allowing arbitrary frequency-dependent beam-splitter, this approach fixes their profile and implements arbitrary frequency dependence through frequency-dependant phase shifters. These can be implemented using chains of single-mode cavities. This allows to mapping of any frequency-dependent unitaries into a mesh 50:50 frequency beam splitter and empty cavity arrays.

This decomposition ensures smooth parameter variation across frequencies and establishes a new foundation for implementing frequency-dependent transformations in quantum optics. Looking ahead, several promising research directions emerge, including the development of more efficient algorithms for handling smooth-parameter matrix optimizations, exploration of more compact decomposition methods, more particularly using linear systems with feedback in order to compactly program any frequency functional dependence. Beyond that, we can work also the improvement of loss scaling through advances in integrated photonics. Additionally, investigation of alternative nulling orders could lead to better and more loss-resilient meshing. Finally, there is potential to extend the applicability of these techniques beyond their original context of IMEs, to scenarios requiring frequency-dependent transformations with smooth parameter variation.

Predictive criteria for hidden squeezing

In Section 3.2, we derive for the first time criteria to predict the presence (or not) of hidden squeezing in cavity-based quantum optical systems from the interactions solely. These hidden squeezing features, we have shown, are related to whether the spectral covariance matrix is real or complex.

The nature of this spectral covariance matrix characterizing the output quantum state of the system plays a crucial role in determining appropriate measurement strategies. This work establishes the first comprehensive theoretical framework for predicting hidden squeezing directly from system parameters, without requiring complete state reconstruction.

We derived precise mathematical conditions under which the output spectral covariance matrix $\sigma_{\text{out}}(\omega)$ of a cavity-based optical quantum system, characterized by the most general quadratic Hamiltonian is constrained to be either real- or complex-valued. The framework reveals that beyond the trivial cases where $F = 0$ and \mathcal{M} is diagonal, the spectral covariance matrix remains real only under two specific conditions:

- The system exhibits mode-independent damping rates.
- The product of the interaction matrices GF is symmetric.

When either condition fails, the spectral covariance matrix becomes complex, indicating hidden correlations that standard homodyne detection cannot fully characterize. Alternative detection methods such as resonator detection, synodyne detection, or interferometers with memory effect become necessary to fully capture all correlations. Furthermore, these criteria can enable the engineering of systems to either harness or avoid these complex correlations, providing a powerful tool for quantum state design and characterization. A promising future direction would be extending these criteria beyond cavity-based optical systems to generalize this theory to uncover potentially new predictive ways for new classes of systems to predict the presence of hidden correlations.

Publications

- [1] B. Dioum, S. Srivastava, M. Karpiński, G Patera, “Temporal cavities as temporal mode filters for optical information processing”, arXiv:2303.09155, hal-04031281, Physical Review A, vol. 111, p. 033704, Mar. 2025, DOI:10.1103/PhysRevA.111.033704
- [2] Bakhao Dioum, Virginia D’Auria, Alessandro Zavatta, Olivier Pfister, and Giuseppe Patera “Universal quantum frequency comb measurements by spectral mode-matching,” arXiv:2405.18454, hal-04600554, Optica Quantum **2**, 413 (2024), DOI: 10.1364/OPTICAQ.532232.
- [3] Bakhao Dioum, Virginia D’Auria, Giuseppe Patera, “Hidden quantum correlations in cavity-based quantum optics,” arXiv:2410.16479, hal-04747328, Submitted to Physical Review A.
- [4] B. Dioum and G. Patera, “Quantum Pulse Gate” in preparation (2025).

$$\begin{pmatrix} \hat{E}_k \\ \hat{E}_r \end{pmatrix} = \begin{pmatrix} t_1 & r_1 \\ -r_1 & t_1 \end{pmatrix} \begin{pmatrix} \hat{E}'_{c,k} \\ \hat{E}'_{in1,k} \end{pmatrix} \quad (\text{A.1})$$

$$\begin{pmatrix} \hat{E}_t \\ \hat{E}_{c,k}^{(0)} \end{pmatrix} = \begin{pmatrix} t_2 & r_2 \\ -r_2 & t_2 \end{pmatrix} \begin{pmatrix} \hat{E}'_k \\ \hat{E}'_{in2,k} \end{pmatrix} \quad (\text{A.2})$$

The general form of the electric field is:

$$\hat{E}_f^{(+)}(t, z) = e^{i(k_0 z - \omega_0 t)} \hat{A}_f(z, t) \quad (\text{A.3})$$

$$\text{with } \hat{A}_f(z, t) = \sum_{k=-\infty}^{+\infty} \sum_{m \in \mathbb{N}} \varepsilon_m \hat{a}_{f,m}^{(k)} u_m(t - k\tau, z) \quad (\text{A.4})$$

$$f = \{\text{in1, in2, } t, r\} \quad (\text{A.5})$$

A.0.1 Round Trip Analysis

For a single round trip between $(k-1)T$ and kT , the electric field is:

$$\hat{E}_{in1}^{(+)}(t) = e^{-i\omega_0 t} \sum_k \sum_m \hat{A}_{in1,m}^{(k)}(t) \quad (\text{A.6})$$

$$\text{with } \hat{A}_{in1,m}^{(k)}(t) = \varepsilon_m \hat{a}_{in1,m}^{(k)} u_m(t - k\tau, 0), \quad (\text{A.7})$$

where $u_m(t - k\tau, z)$ are the Hermite Gaussian modes defined as:

$$u_m(x, 0) = H_m \left(\frac{t}{\sigma_0} \right) \exp \left(-\frac{t^2}{2\sigma_0^2} \right). \quad (\text{A.8})$$

This input field can be expressed as:

$$\hat{E}_{in1}(t) = \sum_k E_{in,k}(t) \quad (\text{A.9})$$

where

$$\hat{E}_{in,k}(t) = e^{-i\omega_0 t} \sum_m \varepsilon_m \hat{a}_{in1,m}^{(k)} u_m(t - kT, 0) \quad (\text{A.10})$$

After the first beam splitter, the propagation writes:

$$\hat{E}_k(t) = t_1 \hat{E}_{in,k}(t) - r_1 \hat{E}'_{c,k}(t) \quad (\text{A.11})$$

We can express the cavity field $\hat{E}'_{ck}(t)$ in terms of $\hat{E}_{c,k}^{(0)}(t)$ after propagation of distance δ_1 :

$$\hat{E}_{ck}^{(0)}(t) = e^{-i\omega_0 t} \sum_m \varepsilon_m \hat{c}_m^{(k)} u_m(t - \delta_1/c - kT, 0) \quad (\text{A.12})$$

A.0.2 Propagation through D_1

Before propagation inside the dispersive media, we want to move in the moving frame. For that, we induce the following variable change at $z = \delta_1$: $\tau = t - \beta'_1 \delta_1$, we have:

$$\hat{E}_{c,k}^{(0)}(\tau) = e^{-i\omega_0 \tau} \sum_m \varepsilon_m \hat{c}_{m1}^k \hat{u}_m \left(\tau + \beta'_1 \delta_1 - \frac{\delta_1}{c} - kT, 0 \right) \quad (\text{A.13})$$

with:

$$\hat{c}_{m1}^{(k)} = -r_2 t_1 e^{ik'_0 \delta_1} \hat{a}_m^{(k-1)} + t_2 \hat{a}_{in2,m}^{(k)} \quad \text{and} \quad k'_{01} = k_0 - \beta'_1 \omega_0. \quad (\text{A.14})$$

For propagation through D_1 , represented by the ABCD matrix $\begin{pmatrix} 1 & D_1 \\ 0 & 1 \end{pmatrix}$, the complex q

parameter transforms as:

$$q^{(1)} = q^{(0)} + D_1 = D_1 + j\sigma_0^2 = \beta_1'' d_1 + j\sigma_0^2, \quad (\text{A.15})$$

and the field writes:

$$\hat{E}_{c,k}^{(1)}(\tau) = e^{-i\omega_0\tau} \sum_m \varepsilon_m \hat{c}_m^{(k)} u_m \left(\tau + \beta_1' \delta_1 - \frac{\delta_1}{c} - kT, d_1 \right) \quad (\text{A.16})$$

where:

$$\hat{c}_m^{(k)} = -r_2 t_1 e^{ik_0 \delta_1} \hat{a}_m^{(k-1)} + t_2 \hat{a}_{in2,m}^{(k)} \quad (\text{A.17})$$

$$u_m(x, d_1) = \frac{\sigma_0}{\sigma_1(d_1)} H_m \left(\frac{x}{\sigma_1(d_1)} \right) e^{-i \frac{x^2}{2q^{(1)}}} e^{-i(1/2+m)\psi_1(d_1)} \quad (\text{A.18})$$

$$\sigma(d_1) = \sigma_0 \left[1 + \left(\frac{\beta_1'' d_1}{\sigma_0^2} \right) \right]^{1/2} \quad (\text{A.19})$$

$$\psi_1(d_1) = A_1 \arctan \left(\frac{\beta_1'' d_1}{\sigma_0^2} \right) \quad (\text{A.20})$$

To come back to the initial frame of reference, we make the following variable change at $z = \delta_1 + d_1 : t = \tau + \beta_1'(\delta_1 + d_1)$, and the field writes:

$$\hat{E}_{c,k}^{(1)}(t) = e^{-i\omega_0(t-\beta_1' d_1)} \sum_m \varepsilon_m \hat{c}_m^{(k)} u_m \left(t - \beta_1' d_1 - \frac{\delta_1}{c} - kT, d_1 \right) \quad (\text{A.21})$$

A.0.3 Propagation through the time lens

First, we make a variable change at the time lens : $\tau = t - \beta_{TL}'(\delta_1 + d_1)$:

$$\begin{aligned} \hat{E}_{c,k}^{(1)}(\tau) &= e^{-i\omega_0[\tau + \beta_{TL}'(\delta_1 + d_1)]} \\ &\sum_m \varepsilon_m \hat{c}_{m,TL}^{(k)} u_m \left[\tau + \beta_{TL}'(\delta_1 + d_1) - \beta_1' d_1 - \frac{\delta_1}{c} - kT, d_1 \right] \end{aligned}$$

with:

$$\hat{c}_{m,TL}^{(k)} = -r_2 e^{ik'_{0,TL} \delta_1} \hat{a}_m^{(k-1)} + t_2 \hat{a}_{in2,m}^{(k)} \quad (\text{A.22})$$

and

$$k'_{0,TL} = k_0 - \beta'_{TL} \omega_0 \quad (\text{A.23})$$

The field during propagation through the TL is:

$$E_{c,k}^{(2)}(z) = e^{-i\omega_0[\tau + (\beta'_{TL} - \beta'_1)d_1]} \quad (\text{A.24})$$

$$\sum_m \varepsilon_m \hat{c}_{m,TL}^{(k)} u_m \left[\tau + \beta'_{TL}(\delta_1 + d_1) - \beta'_1 d_1 - \frac{\delta_1}{c} - kT, d_1 + d_{TL} \right] \quad (\text{A.25})$$

where:

$$u_m(x, d_1 + d_{TL}) = \frac{\sigma_0}{\sigma_1(d_1)} H_m \left(\frac{x}{\sigma_1(d_1)} \right) e^{-\frac{ix^2}{2q^{(2)}}} e^{-i(1/2+m)\psi_1(d_1)} \quad (\text{A.26})$$

$$\text{with } q^{(2)} = \frac{q^{(1)} + 1}{-\frac{1}{D_f} q^{(1)}} \quad (\text{A.27})$$

We end with a variable Change at the end of the TL to return to the initial frame of reference

$t = \tau + \beta'_{TL}(\delta_1 + d_1 + d_{TL})$:

$$\hat{E}_{c,k}^{(2)}(t) = e^{-i\omega_0(t - \beta'_1 d_1 - \beta'_{TL} d_{TL})} \quad (\text{A.28})$$

$$\sum_m \varepsilon_m \hat{c}_m^{(k)} u_m \left(t - \beta'_1 d_1 - \beta'_{TL} d_{TL} - \frac{\delta_1}{c} - kT, d_1 + d_{TL} \right) \quad (\text{A.29})$$

A.0.4 Propagation through D_2

First, we make a variable change inside D_2 : $\tau = t - \beta'_2(\delta_1 + d_1 + d_{TL})$:

$$\hat{E}'_{c,k}(\tau) = e^{-i\omega_0[\tau + \beta'_2(\delta_1 + d_1 + d_{TL}) - \beta'_1 d_1 - \beta'_{TL} d_{TL}]} \quad (\text{A.30})$$

$$\sum_m \varepsilon_m \hat{c}_{m,2}^{(k)} u_m \left[\tau + \beta'_2(\delta_1 + d_1 + d_{TL}) - \beta'_1 d_1 - \beta'_{TL} d_{TL} - \frac{\delta_1}{c} - kT, d_1 + d_{TL} \right] \quad (\text{A.31})$$

with:

$$\hat{c}_{m,2}^{(k)} = -r_2 e^{ik'_{02} \delta_1} \hat{a}_m^{(k-1)} + t_2 \hat{a}_{in2,m}^{(k)} \quad (\text{A.32})$$

$$k'_{02} = k_0 - \beta'_2 \omega_0 \quad (\text{A.33})$$

For propagation through D_2 with matrix $\begin{pmatrix} 1 & D_2 \\ 0 & 1 \end{pmatrix}$, we have:

$$q^{(3)} = q^{(2)} + D_2 = q_1^{(0)} = j\sigma_0^2 \quad (\text{A.34})$$

Note that parameters (D_1, D_2, D_f, z_0^2) are chosen such that we return to $q^{(0)}$ after every round-trip.

The field after propagation is:

$$\hat{E}'_{c,k}(\tau) = e^{-i\omega_0[\tau + \beta'_2(d_1 + d_{TL}) - \beta'_1 d_1 - \beta'_{TL} d_{TL}]} \quad (\text{A.35})$$

$$\sum_m \varepsilon_m \hat{c}_{m2}^{(k)} u_m \left[\tau + \beta'_2(\delta_1 + d_1 + d_{TL}) - \beta'_1 d_1 - \beta'_{TL} d_{TL} - \delta_1/c - kT, D_{tot} \right] \quad (\text{A.36})$$

where:

$$u_m(x, D_{tot}) = u_m(x, 0)e^{-i(m+1/2)\psi(D_{tot})} \quad (\text{A.37})$$

$$= H_m\left(\frac{x}{\sigma_0}\right) \exp\left(-\frac{x^2}{2\sigma_0^2}\right) e^{-i(m+1/2)\psi(D_{tot})} \quad (\text{A.38})$$

We then end with a variable Change at end of D_2 : $t = \tau + \beta'_2(\delta_1 + d_1 + d_{TL} + d_2)$:

$$\hat{E}'_{c,k}(t) = e^{i\omega_0(t - \beta'_1 d_1 - \beta'_{TL} d_{TL} - \beta'_2 d_2)} e^{-i(m+1/2)\psi(D_{tot})} \quad (\text{A.39})$$

$$\sum_m \varepsilon_m c_m^{(k)} u_m\left(t - \beta'_1 d_1 - \beta'_{TL} d_{TL} - \beta'_2 d_2 - \frac{\delta_1}{c} - kT, 0\right). \quad (\text{A.40})$$

A.0.5 Final Round Trip Analysis

After one complete round trip, we have:

$$\hat{E}_k(t) = t_1 \hat{E}_{in1,k}(t) - r_1 \hat{E}'_{ck}(t) \quad (\text{A.41})$$

where:

$$\hat{E}_{in1,k}(t) = e^{-i\omega_0 t} \sum_m \varepsilon_m \hat{a}_{in1,m}^{(k)} u_m(t - kT, 0) \quad (\text{A.42})$$

$$\hat{E}'_{c,k}(t) = e^{-i\omega_0(t - \beta'_1 d_1 - \beta'_{TL} d_{TL} - \beta'_2 d_2)} e^{-i(m+1/2)\psi(D_{tot})} \quad (\text{A.43})$$

$$\sum_m \varepsilon_m c_m^{(k)} u_m\left(t - \beta'_1 d_1 - \beta'_{TL} d_{TL} - \beta'_2 d_2 - \frac{\delta_1}{c} - kT, 0\right) \quad (\text{A.44})$$

A.0.6 Round Trip Condition

The round trip condition is:

$$T = \frac{\delta_1}{c} + \beta'_1 d_1 + \beta'_{TL} d_{TL} + \beta'_2 d_2 \quad (\text{A.45})$$

This leads to:

$$\hat{E}'_{c,k}(t) = e^{-i\omega_0(t-T)} e^{-i(m+1/2)\psi(D_{tot})} \quad (\text{A.46})$$

$$\sum_m \varepsilon_m [-r_2 t_1 \hat{a}_m^{(k-1)} + t_2 \hat{a}_{in2,m}^{(k)}] u_m(t - kT, 0) \quad (\text{A.47})$$

where:

$$e^{i\omega_0 T} = e^{i\omega_0 \left(\frac{L_{loop}}{c}\right)} = e^{ik_0 L_{loop}}. \quad (\text{A.48})$$

This comes back to exactly as if we were propagating pulse by pulse, as we mentioned in the main text.

Appendix B

Two-mode smooth decomposition algorithms

Algorithm 1 Transformation to nullify matrix element using element in the same column

```
1: procedure CREATECOLUMNELEMENTNULLIFIER( $U(\omega)$ ,  $c$ ,  $p$ ,  $h$ )
2:   Input: Matrix  $U(\omega)$ , column index  $c$ , position to nullify  $p$ , helper position  $h$ 
3:   Output: Special unitary transformation matrix  $T(\omega)$ 
4:   MatrixHeight  $\leftarrow$  number of rows in  $U(\omega)$ 
5:   ElementToBeNulled  $\leftarrow U_{p,c}(\omega)$ 
6:   HelperValue  $\leftarrow U_{h,c}(\omega)$ 
7:   NormalizationFactor  $\leftarrow \sqrt{|HelperValue(\omega)|^2 + |ElementToBeNulled(\omega)|^2}$ 
8:    $T(\omega) \leftarrow I_{MatrixHeight}$ 
9:   if NormalizationFactor = 0 then
10:      $T_{h,h}(\omega) \leftarrow 1$ 
11:      $T_{h,p}(\omega) \leftarrow 0$ 
12:      $T_{p,h}(\omega) \leftarrow 0$ 
13:      $T_{p,p}(\omega) \leftarrow 1$ 
14:   else
15:      $T_{h,h}(\omega) \leftarrow HelperValue^*(\omega)/NormalizationFactor$ 
16:      $T_{h,p}(\omega) \leftarrow ElementToBeNulled^*(\omega)/NormalizationFactor$ 
17:      $T_{p,h}(\omega) \leftarrow -ElementToBeNulled(\omega)/NormalizationFactor$ 
18:      $T_{p,p}(\omega) \leftarrow HelperValue(\omega)/NormalizationFactor$ 
19:   end if
20:   return  $T(\omega)$ 
21: end procedure
```

Algorithm 2 Transformation to nullify matrix element using element in the same row

```
1: procedure CREATEROWELEMENTNULLIFIER( $U(\omega)$ ,  $r$ ,  $p$ ,  $h$ )
2:   Input: Matrix  $U(\omega)$ , row index  $r$ , position to nullify  $p$ , helper position  $h$ 
3:   Output: Special unitary transformation matrix  $R(\omega)$ 
4:    $U^T(\omega) \leftarrow$  transpose of  $U(\omega)$ 
5:    $T(\omega) \leftarrow$  CreateColumnElementNullifier( $U^T(\omega)$ ,  $r$ ,  $p$ ,  $h$ )
6:    $R(\omega) \leftarrow T^T(\omega)$ 
7:   return  $R(\omega)$ 
8: end procedure
```

Algorithm 3 Smooth Triangular Decomposition of Unitary Matrix

```
1: procedure TRIANGULARDECOMPOSITION( $U(\omega)$ )
2:   Input: Unitary matrix  $U(\omega)$  of size  $n \times n$ 
3:   Output: List of transformations  $\{T_i(\omega)\}$  and diagonal matrix  $D(\omega)$ 
4:   MatrixSize  $\leftarrow n$ 
5:   NumTransformations  $\leftarrow \frac{\text{MatrixSize} \times (\text{MatrixSize} - 1)}{2}$ 
6:   TransformationMatrices  $\leftarrow$  empty list of size NumTransformations
7:   WorkingMatrix  $\leftarrow U(\omega)$ 
8:   LowerTrianglePositions  $\leftarrow \{(i, j) : i > j, \text{ for } i, j \in \{0, 1, \dots, \text{MatrixSize} - 1\}\}$ 
9:   SortedPositions  $\leftarrow$  Sort LowerTrianglePositions by column index (ascending), then row
   index (descending)
10:  CurrentIndex  $\leftarrow$  NumTransformations  $- 1$ 
11:  for each (RowIndex, ColumnIndex) in SortedPositions do
12:    Nullifier( $\omega$ )  $\leftarrow$  CreateColumnElementNullifier(WorkingMatrix( $\omega$ ), ColumnIndex,
   RowIndex, RowIndex  $- 1$ )
13:    WorkingMatrix( $\omega$ )  $\leftarrow$  Nullifier( $\omega$ )  $\times$  WorkingMatrix( $\omega$ )
14:    TransformationMatrices[CurrentIndex]( $\omega$ )  $\leftarrow$  Nullifier( $\omega$ )
15:    CurrentIndex  $\leftarrow$  CurrentIndex  $- 1$ 
16:  end for
17:  DiagonalMatrix( $\omega$ )  $\leftarrow$  TransformationMatrices( $\omega$ )
18:  for  $i \leftarrow 1$  to NumTransformations  $- 1$  do
19:    DiagonalMatrix( $\omega$ )  $\leftarrow$  DiagonalMatrix( $\omega$ )  $\times$  TransformationMatrices[ $i$ ]( $\omega$ )
20:  end for
21:  DiagonalMatrix( $\omega$ )  $\leftarrow$  DiagonalMatrix( $\omega$ )  $\times$   $U(\omega)$ 
22:  FinalDecomposition  $\leftarrow$  empty list of size NumTransformations
23:  for  $i \leftarrow 0$  to NumTransformations  $- 1$  do
24:    FinalDecomposition[ $i$ ]( $\omega$ )  $\leftarrow$  TransformationMatrices[NumTransformations  $- 1 - i$ ]( $\omega$ )†
25:  end for
26:  return FinalDecomposition( $\omega$ ), DiagonalMatrix( $\omega$ )
27: end procedure
```

Appendix C

Supplemental details on IME

C.1 Recycling IME cavities

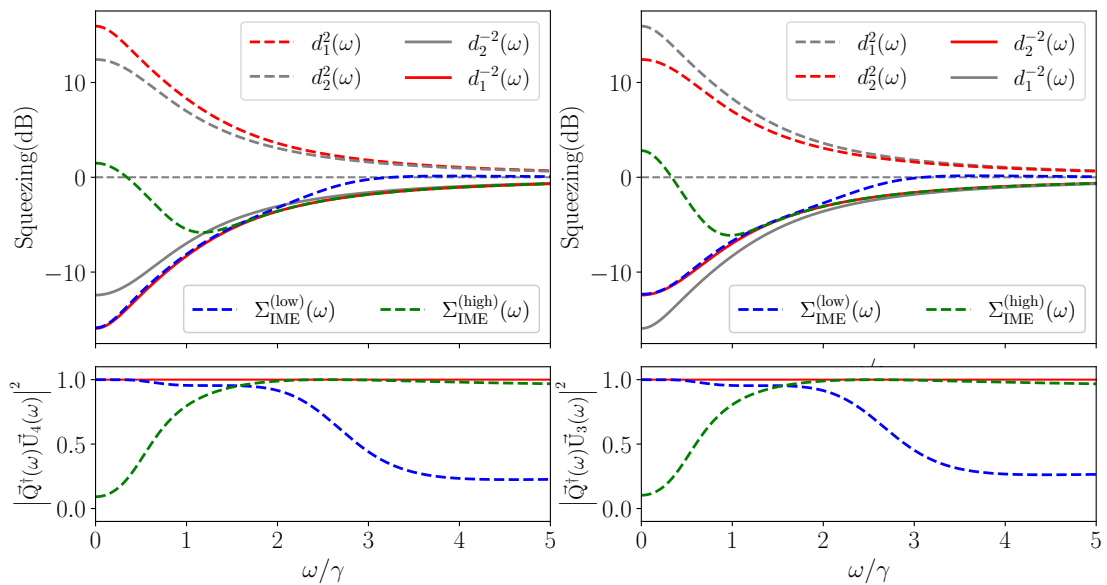


Figure C.1: Two-mode OPO recycling IME

In Section 3.4, we demonstrate that recovering each morphing supermode requires a minimum of one IME configuration per supermode profile. The complexity of certain supermodes often necessitates multiple IME configurations in a chain, as a single configuration may lack

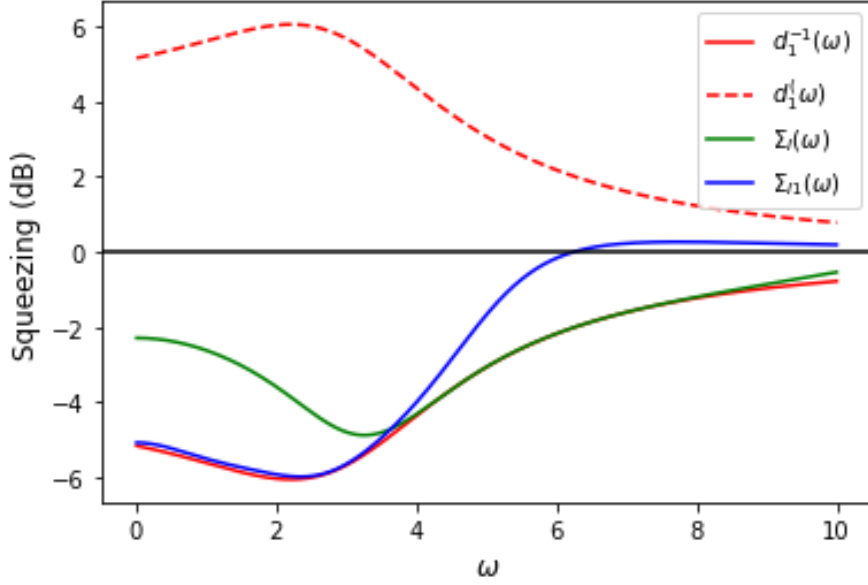


Figure C.2: Four-mode OPO recycling IME

sufficient complexity to accurately match the supermode profile. To minimize the number of required IME configurations, we show examples of two cavity recycling strategies:

- For the two-mode OPO operating at 43% below threshold (Fig C.1), we show an optimized approach using a single cavity configuration to access multiple squeezing spectra. By simply adjusting the local oscillator vector, we can target different spectral regions of interest. This efficient method requires only two cavity configurations to fully recover both squeezing spectra, whereas a traditional approach would have needed two chains of two IME configurations, totaling four cavities. The blue curve represents the first cavity: $\gamma_{\text{IME},1} = \gamma_{\text{IME},2} = 1.01\gamma_1$, $\Delta_1 = -1.51\gamma_1$, $\Delta_2 = -1.2\gamma_1$, $\theta_d = 1.21\gamma_1$ and $\phi_d = 4.32$. The LO vector to target $d_1^{-2}(\omega)$ is with $\theta_{\text{LO},1} = 4.46$ rad, $\theta_{\text{LO},2} = 1.01$ rad and $\theta_{\text{LO},3} = 0.6$ and to target $d_2^{-2}(\omega)$ is with $\theta_{\text{LO},1} = 3.40$ rad, $\theta_{\text{LO},2} = -0.49$ rad and $\theta_{\text{LO},3} = 2.25$. The green curve represents the second cavity: $\gamma_{\text{IME},1} = \gamma_{\text{IME},2} = 2.36\gamma_1$, $\Delta_1 = -4.45\gamma_1$, $\Delta_2 = -4.55\gamma_1$, $\theta_d = 4.01\gamma_1$ and $\phi_d = 0.44$. The LO vector to target $d_1^{-2}(\omega)$ is with $\theta_{\text{LO},1} = 4.29$ rad, $\theta_{\text{LO},2} = 3.66$ rad and $\theta_{\text{LO},3} = -0.94$ and to target $d_2^{-2}(\omega)$ is with $\theta_{\text{LO},1} = 5.87$ rad, $\theta_{\text{LO},2} = -5$ rad and $\theta_{\text{LO},3} = 0.39$.
- In Fig. C.2, we instead show an example for the four-mode case 100% below threshold

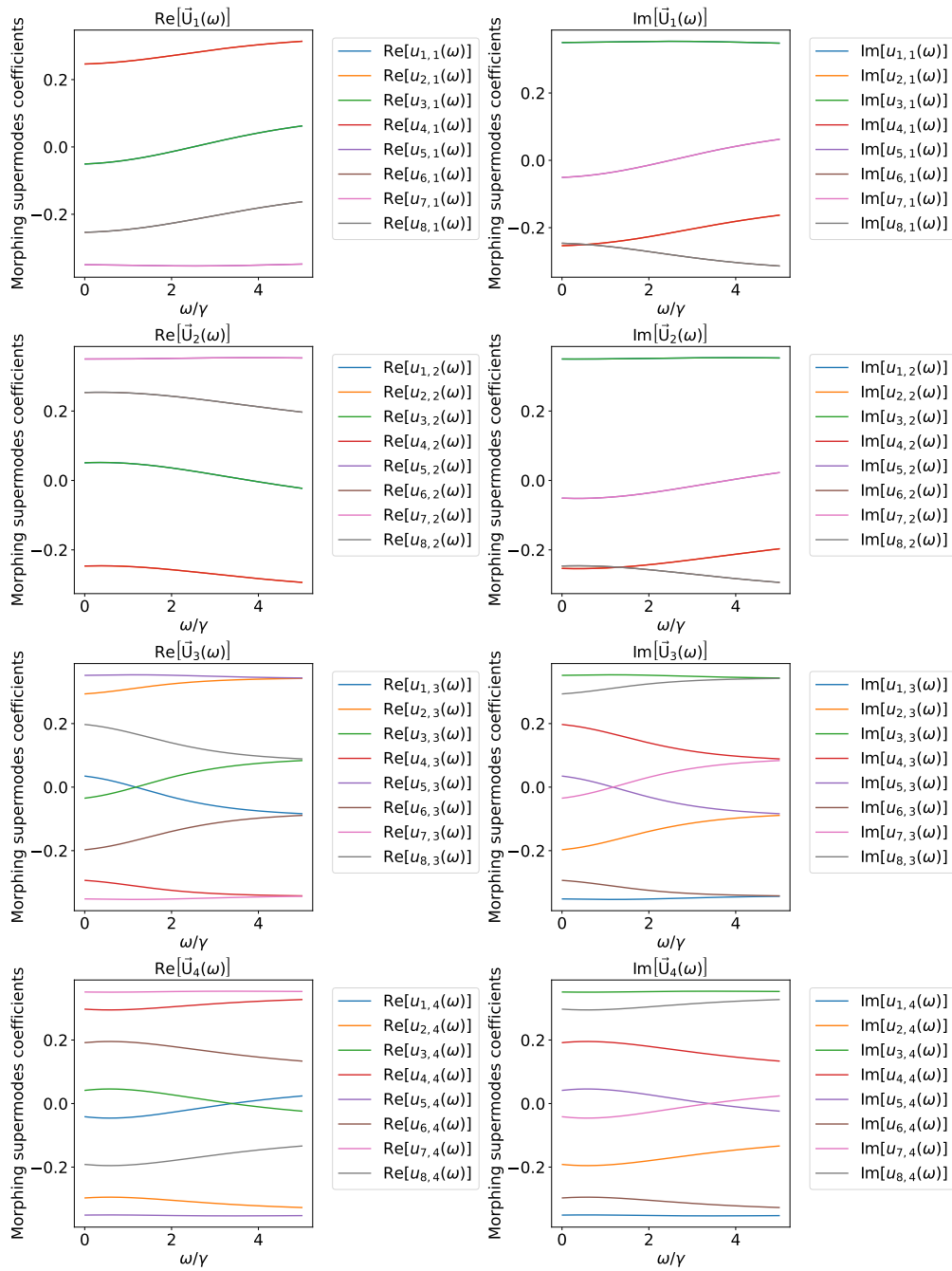


Figure C.3: **Morphing supermodes of the four modes OPO configuration at 7% below threshold.**

where we have used a single cavity to access different subsets of the spectrum, by tuning the LO. This allows to use of a single cavity configuration in two shots rather than a single

shot with two cavities, showing the flexibility of the IME.

C.2 Morphing supermodes of four mode OPOs

See Figs. C.3 and C.4.

C.3 Optimal parameters of the four modes OPOs

Here we give the optimal parameters of the four-mode OPO IME configuration we detailed in Subsection 3.150. For a much more compact notation, we give the mode-independent damping rate and the G_{IME} matrix (Eq. (3.104)) for each configuration. The local oscillator corresponds to 8-dimensional vector using Hopf coordinates with seven parameters:

$$\vec{Q} = \begin{pmatrix} \cos(\phi_1) \cos(\phi_2) \cos(\theta_1) \\ \cos(\phi_1) \sin(\phi_2) \cos(\theta_2) \\ \sin(\phi_1) \cos(\phi_3) \cos(\theta_3) \\ \sin(\phi_1) \sin(\phi_3) \cos(\theta_4) \\ \cos(\phi_1) \cos(\phi_2) \sin(\theta_1) \\ \cos(\phi_1) \sin(\phi_2) \sin(\theta_2) \\ \sin(\phi_1) \cos(\phi_3) \sin(\theta_3) \\ \sin(\phi_1) \sin(\phi_3) \sin(\theta_4) \end{pmatrix}$$

In Fig. 3.24a(top), four-mode OPO 7% below threshold. The optimal LO angles are

$$[10.36787653, 2.28592891, 8.29124352, 0.42999878, 5.3652864, 6.98168206, -0.72155864]$$

For the green curve, we have two chained IMEs. The first IME configuration: $\gamma = 3.09072292$ and

$$G_{IME} = \begin{pmatrix} 13.64901382 & 9.68357821 + 3.90796562i & 7.27426496 + 4.15164409i & 9.64666105 - 6.59743517i \\ 9.68357821 - 3.90796562i & 2.93151646 & 1.2977527 + 14.57394618i & 9.47857965 + 4.86421641i \\ 7.27426496 - 4.15164409i & 1.2977527 - 14.57394618i & 3.60846079 & 5.97543246 + 6.7542631i \\ 9.64666105 + 6.59743517i & 9.47857965 - 4.86421641i & 5.97543246 - 6.7542631i & 3.70753082 \end{pmatrix}.$$

C.3. OPTIMAL PARAMETERS OF THE FOUR MODES OPOS

For the second IME: $\gamma = 5.79188279$ and

$$G_{IME} = \begin{pmatrix} 11.12442739 & 0.38521244 + 5.60328544i & 4.55798192 + 9.35912584i & -2.972625 + 9.47472347i \\ 0.38521244 - 5.60328544i & 5.01951805 & 5.62419851 + 7.73797104i & -4.88985681 + 4.46810078i \\ 4.55798192 - 9.35912584i & 5.62419851 - 7.73797104i & 0.57689667 & 4.12218566 + 9.41048627i \\ -2.972625 - 9.47472347i & -4.88985681 - 4.46810078i & 4.12218566 - 9.41048627i & 12.51166411 \end{pmatrix}$$

In Fig. 3.24b(*top*), four-mode OPO 100% below threshold. The optimal LO angles are

$$[2.35232338, 6.54013581, 6.02511089, 3.31737623, 2.48870894, 0.17192804, 2.52132345]$$

. For the blue curve, a single IME configuration: $\gamma = 1.75850958$, and

$$G = \begin{pmatrix} 15.82457573 & 6.18998401 - 6.97100376i & -18.238298 + 0.07417626i & -4.83625725 + 5.44560892i \\ 6.18998401 + 6.97100376i & 22.40749605 & -4.54220266 - 4.83439314i & -25.46711041 + 0.08567452i \\ -18.238298 - 0.07417626i & -4.54220266 + 4.83439314i & 15.22993282 & 6.12443368 - 6.84385309i \\ -4.83625725 - 5.44560892i & -25.46711041 - 0.08567452i & 6.12443368 + 6.84385309i & 23.11438092 \end{pmatrix}$$

And for the green curve, we have two chained IMEs. The first IME configuration: $\gamma = 2.86678537$

and

$$G_{IME} = \begin{pmatrix} 13.68375504 & 9.60989996 + 4.08514038i & 7.0394004 + 4.3383497i & 9.60591485 - 6.88395985i \\ 9.60989996 - 4.08514038i & 2.94295262 & 1.21952955 + 14.3709342i & 9.47252503 + 4.94428653i \\ 7.0394004 - 4.3383497i & 1.21952955 - 14.3709342i & 3.51925546 & 5.92548114 + 6.56273251i \\ 9.60591485 + 6.88395985i & 9.47252503 - 4.94428653i & 5.92548114 - 6.56273251i & 3.61016669 \end{pmatrix}$$

For the second IME: $\gamma = 4.3810721$ and

$$G_{IME} = \begin{pmatrix} 10.67420969 & 0.3810942 + 6.39550373i & 4.0084575 + 9.59726411i & -2.90102179 + 9.35934225i \\ 0.3810942 - 6.39550373i & 4.81512163 & 5.27731404 + 7.32797531i & -4.51960162 + 4.79752595i \\ 4.0084575 - 9.59726411i & 5.27731404 - 7.32797531i & 0.62092378 & 3.52404066 + 8.83415614i \\ -2.90102179 - 9.35934225i & -4.51960162 - 4.79752595i & 3.52404066 - 8.83415614i & 13.61154344 \end{pmatrix}$$

C.3. OPTIMAL PARAMETERS OF THE FOUR MODES OPOS

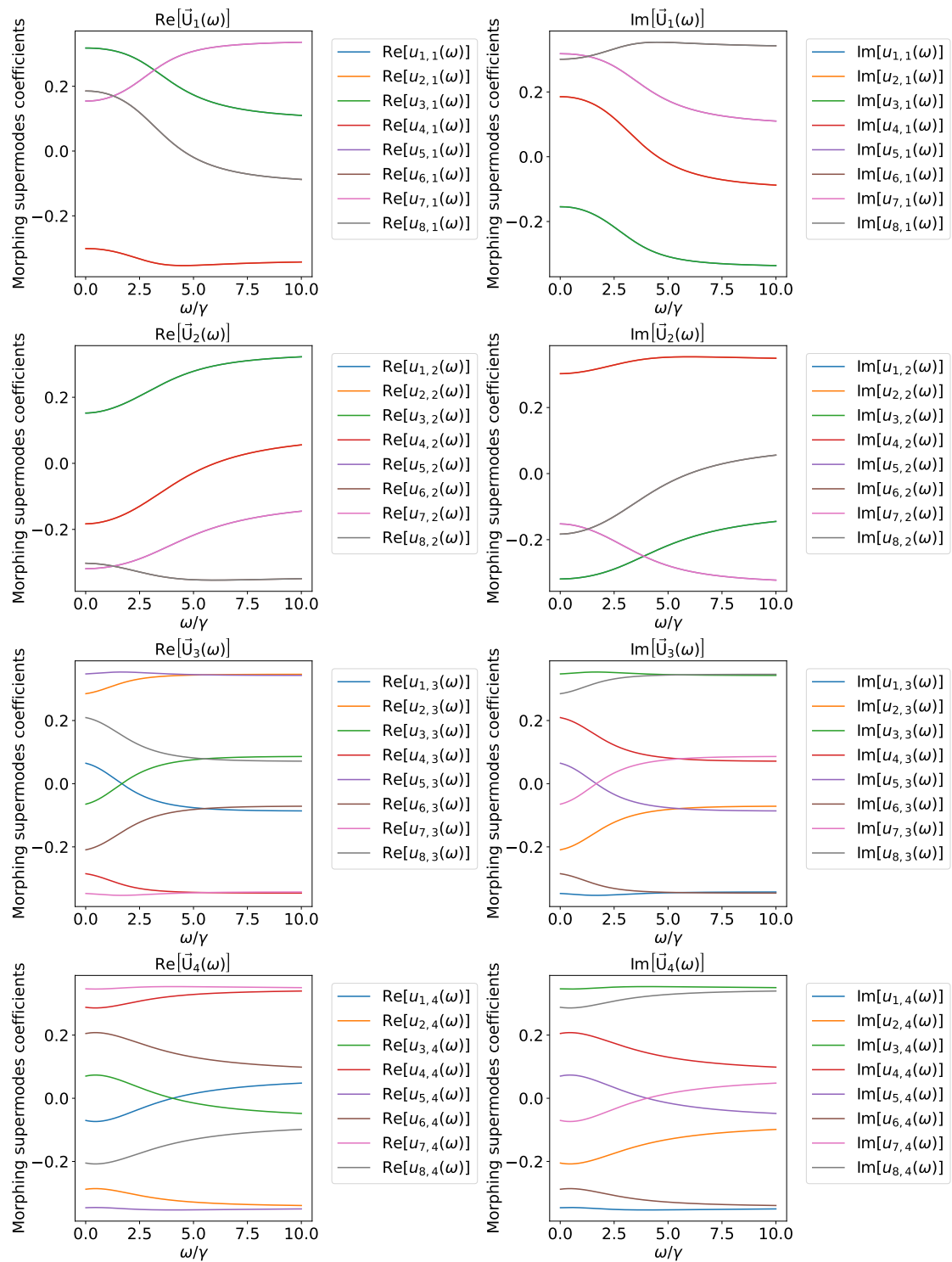


Figure C.4: Morphing supermodes of the four modes OPO configuration at 100% below threshold.

Bibliography

- [1] A. Einstein, B. Podolsky, and N. Rosen, "Can Quantum-Mechanical Description of Physical Reality Be Considered Complete?," *Physical Review*, vol. 47, pp. 777–780, May 1935. Publisher: American Physical Society.
- [2] J. S. Bell, "On the Einstein Podolsky Rosen paradox," *Physics Physique Fizika*, vol. 1, pp. 195–200, Nov. 1964.
- [3] A. Aspect, P. Grangier, and G. Roger, "Experimental Tests of Realistic Local Theories via Bell's Theorem," *Physical Review Letters*, vol. 47, pp. 460–463, Aug. 1981.
- [4] J. F. Clauser, M. A. Horne, A. Shimony, and R. A. Holt, "Proposed Experiment to Test Local Hidden-Variable Theories," *Physical Review Letters*, vol. 23, pp. 880–884, Oct. 1969.
- [5] J.-W. Pan, D. Bouwmeester, M. Daniell, H. Weinfurter, and A. Zeilinger, "Experimental test of quantum nonlocality in three-photon Greenberger–Horne–Zeilinger entanglement," *Nature*, vol. 403, pp. 515–519, Feb. 2000. Publisher: Nature Publishing Group.
- [6] L. S. Braunstein and P. Van Loock, "Quantum information with continuous variables," *Reviews of Modern Physics*, vol. 77, no. 2, pp. 513–577, 2005. arXiv: quant-ph/0410100.
- [7] G. Adesso, S. Ragy, and A. R. Lee, "Continuous variable quantum information: Gaussian states and beyond," *Open Systems and Information Dynamics*, vol. 21, Jan. 2014. arXiv: 1401.4679.
- [8] N. C. Menicucci, P. Van Loock, M. Gu, C. Weedbrook, T. C. Ralph, and M. A. Nielsen,

BIBLIOGRAPHY

- “Universal quantum computation with continuous-variable cluster states,” *Physical Review Letters*, vol. 97, no. 11, pp. 13–16, 2006. arXiv: quant-ph/0605198.
- [9] M. Gu, C. Weedbrook, N. C. Menicucci, T. C. Ralph, and P. Van Loock, “Quantum computing with continuous-variable clusters,” *Physical Review A - Atomic, Molecular, and Optical Physics*, vol. 79, no. 6, pp. 1–17, 2009. arXiv: 0903.3233.
- [10] V. Giovannetti, S. Lloyd, and L. Maccone, “Quantum-enhanced measurements: beating the standard quantum limit,” *Science*, vol. 306, pp. 1330–1336, Nov. 2004. arXiv: quant-ph/0412078.
- [11] A. Ferraro, S. Olivares, and M. G. A. Paris, *Gaussian states in continuous variable quantum information*. 2005. arXiv: quant-ph/0503237.
- [12] C. Weedbrook, S. Pirandola, R. García-Patrón, N. J. Cerf, T. C. Ralph, J. H. Shapiro, and S. Lloyd, “Gaussian quantum information,” *Reviews of Modern Physics*, vol. 84, no. 2, pp. 621–669, 2012. arXiv: 1110.3234.
- [13] A. Furusawa, J. L. Sørensen, S. L. Braunstein, C. A. Fuchs, H. J. Kimble, and E. S. Polzik, “Unconditional Quantum Teleportation,” *Science*, vol. 282, pp. 706–709, Oct. 1998. Publisher: American Association for the Advancement of Science.
- [14] F. Grosshans and P. Grangier, “Continuous Variable Quantum Cryptography Using Coherent States,” *Physical Review Letters*, vol. 88, p. 057902, Jan. 2002.
- [15] F. Grosshans, G. Van Assche, J. Wenger, R. Brouri, N. J. Cerf, and P. Grangier, “Quantum key distribution using gaussian-modulated coherent states,” *Nature*, vol. 421, pp. 238–241, Jan. 2003. Publisher: Nature Publishing Group.
- [16] M. Chen, N. C. Menicucci, and O. Pfister, “Experimental realization of multipartite entanglement of 60 modes of a quantum optical frequency comb,” *Physical Review Letters*, vol. 112, no. 12, pp. 1–19, 2013. arXiv: 1311.2957.
- [17] S. Yokoyama, R. Ukai, S. C. Armstrong, C. Sornphiphatphong, T. Kaji, S. Suzuki, J.-i. Yoshikawa, H. Yonezawa, N. C. Menicucci, and A. Furusawa, “Ultra-large-scale

BIBLIOGRAPHY

- continuous-variable cluster states multiplexed in the time domain,” *Nature Photonics*, vol. 7, pp. 982–986, Dec. 2013. Publisher: Nature Publishing Group.
- [18] J. F. Sherson, H. Krauter, R. K. Olsson, B. Julsgaard, K. Hammerer, I. Cirac, and E. S. Polzik, “Quantum teleportation between light and matter,” *Nature*, vol. 443, pp. 557–560, Oct. 2006. Publisher: Nature Publishing Group.
- [19] D. F. W. P. Meystre, *Nonclassical Effects in Quantum Optics*. New York: Springer, Oct. 1991.
- [20] H.-A. Bachor and T. C. Ralph, *A guide to experiments in quantum optics*. Weinheim, Germany: Wiley-VCH Verlag GmbH, third edition ed., 2019. OCLC: 1120067467.
- [21] H. J. Kimble, Y. Levin, A. B. Matsko, K. S. Thorne, and S. P. Vyatchanin, “Conversion of conventional gravitational-wave interferometers into quantum nondemolition interferometers by modifying their input and/or output optics,” *Physical Review D*, vol. 65, p. 022002, Dec. 2001. Publisher: American Physical Society.
- [22] H. Vahlbruch, S. Chelkowski, B. Hage, A. Franzen, K. Danzmann, and R. Schnabel, “Demonstration of a Squeezed-Light-Enhanced Power- and Signal-Recycled Michelson Interferometer,” *Physical Review Letters*, vol. 95, p. 211102, Nov. 2005. Publisher: American Physical Society.
- [23] K. Goda, O. Miyakawa, E. E. Mikhailov, S. Saraf, R. Adhikari, K. McKenzie, R. Ward, S. Vass, A. J. Weinstein, and N. Mavalvala, “A quantum-enhanced prototype gravitational-wave detector,” *Nature Physics*, vol. 4, pp. 472–476, June 2008. Publisher: Nature Publishing Group.
- [24] L. McCuller, C. Whittle, D. Ganapathy, K. Komori, M. Tse, A. Fernandez-Galiana, L. Barsotti, P. Fritschel, M. MacInnis, F. Matichard, K. Mason, N. Mavalvala, R. Mittleman, H. Yu, M. Zucker, and M. Evans, “Frequency-Dependent Squeezing for Advanced LIGO,” *Physical Review Letters*, vol. 124, p. 171102, Apr. 2020. Publisher: American Physical Society.
- [25] D. Tse and P. Kuppusamy, “Biocompatibility of Oxygen-Sensing Paramagnetic Implants,” *Cell Biochemistry and Biophysics*, vol. 77, pp. 197–202, Sept. 2019.

BIBLIOGRAPHY

- [26] N. Treps, U. Andersen, B. Buchler, P. K. Lam, A. Maître, H.-A. Bachor, and C. Fabre, “Surpassing the Standard Quantum Limit for Optical Imaging Using Nonclassical Multimode Light,” *Physical Review Letters*, vol. 88, p. 203601, May 2002. Publisher: American Physical Society.
- [27] N. Treps, N. Grosse, W. P. Bowen, M. T. L. Hsu, A. Maître, C. Fabre, H.-A. Bachor, and P. K. Lam, “Nano-displacement measurements using spatially multimode squeezed light,” *Journal of Optics B: Quantum and Semiclassical Optics*, vol. 6, p. S664, July 2004.
- [28] J. Huh, G. G. Guerreschi, B. Peropadre, J. R. McClean, and A. Aspuru-Guzik, “Boson sampling for molecular vibronic spectra,” *Nature Photonics*, vol. 9, pp. 615–620, Sept. 2015. Publisher: Nature Publishing Group.
- [29] J. M. Arrazola, T. Kalajdzievski, C. Weedbrook, and S. Lloyd, “Quantum algorithm for non-homogeneous linear partial differential equations,” *Physical Review A*, vol. 100, p. 032306, Sept. 2019. Publisher: American Physical Society.
- [30] T. R. Bromley, J. M. Arrazola, S. Jahangiri, J. Izaac, N. Quesada, A. D. Gran, M. Schuld, J. Swinarton, Z. Zabaneh, and N. Killoran, “Applications of near-term photonic quantum computers: software and algorithms,” *Quantum Science and Technology*, vol. 5, p. 034010, May 2020. Publisher: IOP Publishing.
- [31] P. van Loock and S. L. Braunstein, “Multipartite Entanglement for Continuous Variables: A Quantum Teleportation Network,” *Physical Review Letters*, vol. 84, pp. 3482–3485, Apr. 2000. Publisher: American Physical Society.
- [32] T. Steinmetz, T. Wilken, C. Araujo-Hauck, R. Holzwarth, T. W. Hänsch, and T. Udem, “Fabry–Pérot filter cavities for wide-spaced frequency combs with large spectral bandwidth,” *Applied Physics B*, vol. 96, pp. 251–256, Aug. 2009.
- [33] T. Wilken, G. L. Curto, R. A. Probst, T. Steinmetz, A. Manescau, L. Pasquini, J. I. González Hernández, R. Rebolo, T. W. Hänsch, T. Udem, and R. Holzwarth, “A spectrograph for exoplanet observations calibrated at the centimetre-per-second level,” *Nature*, vol. 485, pp. 611–614, May 2012. Publisher: Nature Publishing Group.

BIBLIOGRAPHY

- [34] U. M. Titulaer and R. J. Glauber, "Density Operators for Coherent Fields," *Physical Review*, vol. 145, pp. 1041–1050, May 1966. Publisher: American Physical Society.
- [35] G. J. de Valcárcel, G. Patera, N. Treps, and C. Fabre, "Multimode squeezing of frequency combs," *Physical Review A*, vol. 74, p. 061801, Dec. 2006. Publisher: American Physical Society.
- [36] B. Brecht, D. V. Reddy, C. Silberhorn, and M. G. Raymer, "Photon temporal modes: A complete framework for quantum information science," *Physical Review X*, vol. 5, no. 4, pp. 1–17, 2015. arXiv: 1504.06251.
- [37] B. Lamine, C. Fabre, and N. Treps, "Quantum improvement of time transfer between remote clocks," *Physical Review Letters*, vol. 101, no. 12, pp. 1–4, 2008. arXiv: 0804.1203.
- [38] J. M. Donohue, V. Ansari, J. Řeháček, Z. Hradil, B. Stoklasa, M. Paúr, L. L. Sánchez-Soto, and C. Silberhorn, "Quantum-Limited Time-Frequency Estimation through Mode-Selective Photon Measurement," *Physical Review Letters*, vol. 121, no. 9, pp. 1–6, 2018. arXiv: 1805.02491.
- [39] S. De, V. Thiel, J. Roslund, C. Fabre, and N. Treps, "Modal analysis for noise characterization and propagation in a femtosecond oscillator," *Optics Letters*, vol. 44, pp. 3992–3995, Aug. 2019. Publisher: Optica Publishing Group.
- [40] B. Brecht, A. Eckstein, A. Christ, H. Suche, and C. Silberhorn, "From quantum pulse gate to quantum pulse shaper - Engineered frequency conversion in nonlinear optical waveguides," *New Journal of Physics*, vol. 13, 2011. arXiv: 1101.6060.
- [41] A. Eckstein, B. Brecht, and C. Silberhorn, "A quantum pulse gate based on spectrally engineered sum frequency generation," *Optics Express*, vol. 19, no. 15, p. 13770, 2011. arXiv: 1007.3215.
- [42] D. V. Reddy, M. G. Raymer, and C. J. McKinstrie, "Sorting photon wave packets using temporal-mode interferometry based on multiple-stage quantum frequency conversion," *Physical Review A - Atomic, Molecular, and Optical Physics*, vol. 91, no. 1, pp. 1–12, 2015. arXiv: 1501.03216.

BIBLIOGRAPHY

- [43] D. V. Reddy and M. G. Raymer, “High-selectivity quantum pulse gating of photonic temporal modes using all-optical Ramsey interferometry,” *Optica*, vol. 5, no. 4, p. 423, 2018.
- [44] J. Ashby, V. Thiel, M. Allgaier, P. d’Ornellas, A. O. C. Davis, and B. J. Smith, “Temporal mode transformations by sequential time and frequency phase modulation for applications in quantum information science,” *Optics Express*, vol. 28, p. 38376, Dec. 2020. arXiv: 2009.07906 Publisher: The Optical Society.
- [45] L. Serino, J. Gil-Lopez, W. Ridder, R. Ricken, C. Eigner, B. Brecht, and C. Silberhorn, “High-dimensional temporal-mode decoding with a multi-output quantum pulse gate,” in *Quantum Information and Measurement VI 2021 (2021)*, paper F2B.4, p. F2B.4, Optica Publishing Group, Nov. 2021.
- [46] C. Joshi, B. M. Sparkes, A. Farsi, T. Gerrits, V. Verma, S. Ramelow, S. W. Nam, and A. L. Gaeta, “Picosecond-resolution single-photon time lens for temporal mode quantum processing,” *Optica*, vol. 9, no. 4, p. 364, 2022.
- [47] M. I. Kolobov and G. Patera, “Spatiotemporal multipartite entanglement,” *Physical Review A*, vol. 83, p. 050302, May 2011. Publisher: American Physical Society.
- [48] J. Laurat, L. Longchambon, C. Fabre, and T. Coudreau, “Experimental investigation of amplitude and phase quantum correlations in a type II optical parametric oscillator above threshold: from nondegenerate to degenerate operation,” *Optics Letters*, vol. 30, pp. 1177–1179, May 2005. Publisher: Optica Publishing Group.
- [49] V. D’Auria, S. Fornaro, A. Porzio, S. Solimeno, S. Olivares, and M. G. A. Paris, “Full Characterization of Gaussian Bipartite Entangled States by a Single Homodyne Detector,” *Physical Review Letters*, vol. 102, p. 020502, Jan. 2009. Publisher: American Physical Society.
- [50] Y. K. Chembo, “Quantum dynamics of Kerr optical frequency combs below and above threshold: Spontaneous four-wave mixing, entanglement, and squeezed states of light,” *Physical Review A*, vol. 93, p. 033820, Mar. 2016. arXiv: 1412.5700 Publisher: American Physical Society.

BIBLIOGRAPHY

- [51] C. Meng, G. A. Brawley, J. S. Bennett, M. R. Vanner, and W. P. Bowen, “Mechanical Squeezing via Fast Continuous Measurement,” *Physical Review Letters*, vol. 125, p. 043604, July 2020. Publisher: American Physical Society.
- [52] M. A. Guidry, D. M. Lukin, K. Y. Yang, R. Trivedi, and J. Vučković, “Quantum optics of soliton microcombs,” *Nature Photonics*, vol. 16, pp. 52–58, Jan. 2022. Publisher: Nature Publishing Group.
- [53] F. W. Isaksen and U. L. Andersen, “Mechanical cooling and squeezing using optimal control,” *Physical Review A*, vol. 107, p. 023512, Feb. 2023. Publisher: American Physical Society.
- [54] Gouzien, L. Labonté, J. Etesse, A. Zavatta, S. Tanzilli, V. D’Auria, and G. Patera, “Hidden and detectable squeezing from microresonators,” *Physical Review Research*, vol. 5, no. 2, pp. 1–11, 2023. arXiv: 2207.00360.
- [55] F. A. Barbosa, A. S. Coelho, K. N. Cassemiro, P. Nussenzveig, C. Fabre, A. S. Villar, and M. Martinelli, “Quantum state reconstruction of spectral field modes: Homodyne and resonator detection schemes,” *Physical Review A - Atomic, Molecular, and Optical Physics*, vol. 88, no. 5, pp. 1–16, 2013. arXiv: 1310.2427.
- [56] F. A. Barbosa, A. S. Coelho, K. N. Cassemiro, P. Nussenzveig, C. Fabre, M. Martinelli, and A. S. Villar, “Beyond spectral homodyne detection: Complete quantum measurement of spectral modes of light,” *Physical Review Letters*, vol. 111, no. 20, pp. 1–5, 2013. arXiv: 1308.5650.
- [57] Gouzien, S. Tanzilli, V. D’Auria, and G. Patera, “Morphing Supermodes: A Full Characterization for Enabling Multimode Quantum Optics,” *Physical Review Letters*, vol. 125, no. 10, pp. 1–6, 2020.
- [58] C. Fabre, E. Giacobino, A. Heidmann, and S. Reynaud, “Noise characteristics of a non-degenerate Optical Parametric Oscillator - Application to quantum noise reduction,” *Journal de Physique*, vol. 50, no. 10, pp. 1209–1225, 1989.

BIBLIOGRAPHY

- [59] C. Fabre, E. Giacobino, A. Heidmann, L. Lugiato, S. Reynaud, M. VDACCHINO, and W. KAIGE, "Squeezing in detuned degenerate optical parametric oscillators," *Quantum Optics: Journal of the European Optical Society Part B*, vol. 2, no. 2, pp. 159–187, 1990.
- [60] C. Fabre, M. PINARD, S. BOURZEIX, A. HEIDMANN, E. GIACOBINO, and S. REYNAUD, "Quantum-noise reduction using a cavity with a movable mirror," *Physical Review A*, vol. 49, no. 2, pp. 1337–1343, 1994.
- [61] S. Mancini and P. Tombesi, "Quantum noise reduction by radiation pressure," *Physical Review A*, vol. 49, no. 5, pp. 4055–4065, 1994.
- [62] M. Aspelmeyer, T. J. Kippenberg, and F. Marquardt, "Cavity optomechanics," *Reviews of Modern Physics*, vol. 86, no. 4, pp. 1391–1452, 2014. arXiv: 1303.0733.
- [63] B. Dioum, S. Srivastava, M. Karpiński, and G. Patera, "Temporal cavities as temporal mode filters for optical information processing," *Physical Review A*, vol. 111, p. 033704, Mar. 2025. Publisher: American Physical Society.
- [64] B. Kolner, "Space-time duality and the theory of temporal imaging," *IEEE Journal of Quantum Electronics*, vol. 30, pp. 1951–1963, Aug. 1994. Conference Name: IEEE Journal of Quantum Electronics.
- [65] M. Nakazawa, H. Kubota, A. Sahara, and K. Tamura, "Time-domain ABCD matrix formalism for laser mode-locking and optical pulse transmission," *IEEE Journal of Quantum Electronics*, vol. 34, no. 7, pp. 1075–1081, 1998.
- [66] J. Azana, N. Berger, B. Levit, and B. Fischer, "Spectro-temporal imaging of optical pulses with a single time lens," *IEEE Photonics Technology Letters*, vol. 16, pp. 882–884, Mar. 2004. Conference Name: IEEE Photonics Technology Letters.
- [67] M. Karpiński, M. Jachura, L. J. Wright, and B. J. Smith, "Bandwidth manipulation of quantum light by an electro-optic time lens," *Nature Photonics*, vol. 11, pp. 53–57, Jan. 2017. Publisher: Nature Publishing Group.

BIBLIOGRAPHY

- [68] F. Sośnicki, M. Mikołajczyk, A. Golestani, and M. Karpiński, “Aperiodic electro-optic time lens for spectral manipulation of single-photon pulses,” *Applied Physics Letters*, vol. 116, no. 23, p. 234003, 2020. arXiv: 2004.07195.
- [69] M. Karpiński, A. O. C. Davis, F. Sośnicki, V. Thiel, and B. J. Smith, “Control and Measurement of Quantum Light Pulses for Quantum Information Science and Technology,” *Advanced Quantum Technologies*, vol. 4, no. 9, p. 2000150, 2021. eprint: <https://onlinelibrary.wiley.com/doi/pdf/10.1002/qute.202000150>.
- [70] C. V. Bennett, R. P. Scott, and B. H. Kolner, “Temporal magnification and reversal of 100 Gb/s optical data with an up-conversion time microscope,” *Applied Physics Letters*, vol. 65, pp. 2513–2515, Nov. 1994.
- [71] C. V. Bennett and B. H. Kolner, “Upconversion time microscope demonstrating $10^3\times$ magnification of femtosecond waveforms,” *Optics Letters*, vol. 24, pp. 783–785, June 1999. Publisher: Optica Publishing Group.
- [72] M. A. Foster, R. Salem, D. F. Geraghty, A. C. Turner-Foster, M. Lipson, and A. L. Gaeta, “Silicon-chip-based ultrafast optical oscilloscope,” *Nature*, vol. 456, pp. 81–84, Nov. 2008. Publisher: Nature Publishing Group.
- [73] M. A. Foster, R. Salem, and A. L. Gaeta, “Ultra-high-Speed Optical Processing Using Space-Time Duality,” *Optics and Photonics News*, vol. 22, no. 5, p. 29, 2011.
- [74] Y. Okawachi, R. Salem, M. A. Foster, A. C. Turner-Foster, M. Lipson, and A. L. Gaeta, “High-resolution spectroscopy using a frequency magnifier,” *Optics Express*, vol. 17, pp. 5691–5697, Mar. 2009. Publisher: Optica Publishing Group.
- [75] O. Kuzucu, Y. Okawachi, R. Salem, M. A. Foster, A. C. Turner-Foster, M. Lipson, and A. L. Gaeta, “Spectral phase conjugation via temporal imaging,” *Optics Express*, vol. 17, pp. 20605–20614, Oct. 2009. Publisher: Optica Publishing Group.
- [76] Y. Zhu, J. Kim, and D. J. Gauthier, “Aberration-corrected quantum temporal imaging system,” *Physical Review A*, vol. 87, p. 043808, Apr. 2013. Publisher: American Physical Society.

BIBLIOGRAPHY

- [77] J. M. Donohue, M. D. Mazurek, and K. J. Resch, "Theory of high-efficiency sum-frequency generation for single-photon waveform conversion," *Physical Review A*, vol. 91, p. 033809, Mar. 2015. Publisher: American Physical Society.
- [78] S. Mittal, V. V. Orre, A. Restelli, R. Salem, E. A. Goldschmidt, and M. Hafezi, "Temporal and spectral manipulations of correlated photons using a time lens," *Physical Review A*, vol. 96, p. 043807, Oct. 2017. Publisher: American Physical Society.
- [79] F. Sośnicki and M. Karpiński, "Large-scale spectral bandwidth compression by complex electro-optic temporal phase modulation," *Optics Express*, vol. 26, p. 31307, Nov. 2018.
- [80] J. Shi, G. Patera, D. B. Horoshko, and M. I. Kolobov, "Quantum temporal imaging of antibunching," *JOSA B*, vol. 37, pp. 3741–3753, Dec. 2020. Publisher: Optica Publishing Group.
- [81] G. Patera and M. I. Kolobov, "Temporal imaging with squeezed light," *Optics Letters*, vol. 40, pp. 1125–1128, Mar. 2015. Publisher: Optica Publishing Group.
- [82] G. Patera, J. Shi, D. B. Horoshko, and M. I. Kolobov, "Quantum temporal imaging: application of a time lens to quantum optics," *Journal of Optics*, vol. 19, p. 054001, Mar. 2017. Publisher: IOP Publishing.
- [83] J. Shi, G. Patera, M. I. Kolobov, and S. Han, "Quantum temporal imaging by four-wave mixing," *Optics Letters*, vol. 42, pp. 3121–3124, Aug. 2017. Publisher: Optica Publishing Group.
- [84] G. Patera, D. B. Horoshko, and M. I. Kolobov, "Space-time duality and quantum temporal imaging," *Physical Review A*, vol. 98, p. 053815, Nov. 2018. Publisher: American Physical Society.
- [85] B. Dioum, V. D'Auria, A. Zavatta, O. Pfister, and G. Patera, "Universal quantum frequency comb measurements by spectral mode-matching," *Optica Quantum*, vol. 2, pp. 413–427, Dec. 2024. Publisher: Optica Publishing Group.
- [86] B. Dioum, V. D'Auria, and G. Patera, "Hidden quantum correlations in cavity-based quantum optics," Oct. 2024. arXiv:2410.16479.

BIBLIOGRAPHY

- [87] C. Navarrete-Benlloch, "Introduction to Quantum Optics," Mar. 2022. arXiv:2203.13206.
- [88] C. Navarrete-Benlloch, "Contributions to the Quantum Optics of Multi-mode Optical Parametric Oscillators," Apr. 2015. arXiv:1504.05917.
- [89] R. J. Glauber, "The quantum theory of optical coherence," *Physical Review*, vol. 130, no. 6, pp. 2529–2539, 1963.
- [90] A. Aspect, P. Grangier, and G. Roger, "Experimental Realization of Einstein-Podolsky-Rosen-Bohm *Gedankenexperiment* : A New Violation of Bell's Inequalities," *Physical Review Letters*, vol. 49, pp. 91–94, July 1982.
- [91] M. Redhead, *Incompleteness, Nonlocality, and Realism: A Prolegomenon to the Philosophy of Quantum Mechanics*. New York: Oxford University Press, 1987.
- [92] A. Steinberg, P. Kwiat, and R. Chiao, "Quantum Optical Tests of the Foundations of Physics," in *Springer Handbook of Atomic, Molecular, and Optical Physics* (G. Drake, ed.), pp. 1185–1213, New York, NY: Springer, 2006.
- [93] N. Treps and C. Fabre, "Criteria of quantum correlation in the measurement of continuous variables in optics," Nov. 2004. arXiv:quant-ph/0407214.
- [94] M. D. Reid, "Demonstration of the Einstein-Podolsky-Rosen paradox using nondegenerate parametric amplification," *Physical Review A*, vol. 40, pp. 913–923, July 1989. Publisher: American Physical Society.
- [95] D. F. Walls and G. J. Milburn, *Quantum Optics*. Berlin, Heidelberg: Springer, 1994.
- [96] C. Fabre and N. Treps, "Modes and states in quantum optics," *Reviews of Modern Physics*, vol. 92, no. 3, p. 35005, 2020. arXiv: 1912.09321 Publisher: American Physical Society.
- [97] J. C. Maxwell, "VIII. A dynamical theory of the electromagnetic field," *Philosophical Transactions of the Royal Society of London*, vol. 155, pp. 459–512, Dec. 1865. Publisher: Royal Society.

BIBLIOGRAPHY

- [98] H. Hertz, D. E. Jones (Daniel Evan), and Royal College of Physicians of Edinburgh, *Electric waves : being researches on the propagation of electric action with finite velocity through space*. London : Macmillan, 1893.
- [99] O. Heaviside, *Electrical papers*. New York and London : Macmillan and co., 1894.
- [100] B. E. A. Saleh and M. C. Teich, *Fundamentals of Photonics*. John Wiley & Sons, Feb. 2019. Google-Books-ID: rcqKDwAAQBAJ.
- [101] L. G. Gouy, *Sur une propriété nouvelle des ondes lumineuses*. Mélanges scientifiques, Paris: Gauthier-Villars, 1890. OCLC: 25595928.
- [102] G. H. Dos Santos, D. C. Salles, M. G. Damaceno, B. T. Menezes, C. Corso, M. Martinelli, P. H. Ribeiro, and R. M. De Araújo, "Decomposing Spatial Mode Superpositions with a Triangular Optical Cavity," *Physical Review Applied*, vol. 16, no. 3, pp. 1–9, 2021. arXiv: 2104.04635.
- [103] M. A. d. Gosson, *Symplectic Geometry and Quantum Mechanics*. Springer Science & Business Media, Aug. 2006. Google-Books-ID: q9SHRvay751C.
- [104] A. Serafini, *Quantum Continuous Variables*. 2017.
- [105] B. L. Schumaker, "Quantum mechanical pure states with gaussian wave functions," *Physics Reports*, vol. 135, pp. 317–408, Apr. 1986.
- [106] H. P. Robertson, "The Uncertainty Principle," *Physical Review*, vol. 34, pp. 163–164, July 1929. Publisher: American Physical Society.
- [107] A. Serafini, "Multimode Uncertainty Relations and Separability of Continuous Variable States," *Physical Review Letters*, vol. 96, p. 110402, Mar. 2006. Publisher: American Physical Society.
- [108] R. Simon, E. C. G. Sudarshan, and N. Mukunda, "Gaussian-Wigner distributions in quantum mechanics and optics," *Physical Review A*, vol. 36, pp. 3868–3880, Oct. 1987. Publisher: American Physical Society.

BIBLIOGRAPHY

- [109] R. Simon, N. Mukunda, and B. Dutta, “Quantum-noise matrix for multimode systems: $U(n)$ invariance, squeezing, and normal forms,” *Physical Review A*, vol. 49, pp. 1567–1583, Mar. 1994.
- [110] R. Berndt, *An Introduction to Symplectic Geometry*. American Mathematical Soc., 2001. Google-Books-ID: 5HbJJNYXoN0C.
- [111] Arvind, B. Dutta, N. Mukunda, and R. Simon, “The real symplectic groups in quantum mechanics and optics,” *Pramana*, vol. 45, no. 6, pp. 471–497, 1995. arXiv: quant-ph/9509002.
- [112] J. Williamson, “On the Algebraic Problem Concerning the Normal Forms of Linear Dynamical Systems,” *American Journal of Mathematics*, vol. 58, no. 1, pp. 141–163, 1936. Publisher: The Johns Hopkins University Press.
- [113] Arvind, B. Dutta, N. Mukunda, and R. Simon, “The real symplectic groups in quantum mechanics and optics,” *Pramana*, vol. 45, pp. 471–497, Dec. 1995.
- [114] S. L. Braunstein, “Squeezing as an irreducible resource,” *Physical Review A - Atomic, Molecular, and Optical Physics*, vol. 71, no. 5, pp. 1–4, 2005. arXiv: quant-ph/9904002.
- [115] T. Lipfert, D. B. Horoshko, G. Patera, and M. I. Kolobov, “Bloch-Messiah decomposition and Magnus expansion for parametric down-conversion with monochromatic pump,” *Physical Review A*, vol. 98, no. 1, 2018. arXiv: 1806.09384 Publisher: American Physical Society.
- [116] C. Bloch and A. Messiah, “The canonical form of an antisymmetric tensor and its application to the theory of superconductivity,” *Nuclear Physics*, vol. 39, pp. 95–106, Dec. 1962.
- [117] R. Balian, C. de Dominicis, and C. Itzykson, “Forme canonique des transformations de Bogoliubov pour les bosons et des transformations (pseudo) orthogonales,” *Nuclear Physics*, vol. 67, pp. 609–624, June 1965.

BIBLIOGRAPHY

- [118] G. Cariolaro and G. Pierobon, “Bloch-Messiah reduction of Gaussian unitaries by Takagi factorization,” *Physical Review A*, vol. 94, p. 062109, Dec. 2016. Publisher: American Physical Society.
- [119] A. M. Chebotarev and A. E. Teretenkov, “Singular value decomposition for the Takagi factorization of symmetric matrices,” *Applied Mathematics and Computation*, vol. 234, pp. 380–384, May 2014.
- [120] L. F. Muñoz-Martínez, F. A. S. Barbosa, A. S. Coelho, L. Ortiz-Gutiérrez, M. Martinelli, P. Nussenzveig, and A. S. Villar, “Exploring six modes of an optical parametric oscillator,” *Physical Review A*, vol. 98, no. 2, pp. 1–11, 2018. arXiv: 1710.02905.
- [121] B. R. Mollow, “Quantum Theory of Field Attenuation,” *Physical Review*, vol. 168, pp. 1896–1919, Apr. 1968. Publisher: American Physical Society.
- [122] W. H. Louisell, “Quantum statistical properties of radiation,” tech. rep., John Wiley and Sons, Inc., New York, Jan. 1973.
- [123] L. A. Krivitsky, U. L. Andersen, R. Dong, A. Huck, C. Wittmann, and G. Leuchs, “Electronic noise-free measurements of squeezed light,” *Optics Letters*, vol. 33, pp. 2395–2397, Oct. 2008. Publisher: Optica Publishing Group.
- [124] M. Martinelli, “From spectral matrix to sideband structure: exploring stereo multimodes,” *Journal of the Optical Society of America B*, vol. 40, p. 1277, May 2023.
- [125] G. Breitenbach, S. Schiller, and J. Mlynek, “Measurement of the quantum states of squeezed light,” *Nature*, vol. 387, pp. 471–475, May 1997. Publisher: Nature Publishing Group.
- [126] D. T. Smithey, M. Beck, J. Cooper, and M. G. Raymer, “Measurement of number-phase uncertainty relations of optical fields,” *Physical Review A*, vol. 48, pp. 3159–3167, Oct. 1993. Publisher: American Physical Society.
- [127] A. Ourjoumtsev, R. Tualle-Brouri, and P. Grangier, “Quantum Homodyne Tomography of a Two-Photon Fock State,” *Physical Review Letters*, vol. 96, p. 213601, June 2006. Publisher: American Physical Society.

BIBLIOGRAPHY

- [128] A. I. Lvovsky, B. C. Sanders, and W. Tittel, "Optical quantum memory," *Nature Photonics*, vol. 3, no. 12, pp. 706–714, 2009. arXiv: 1002.4659 Publisher: Nature Publishing Group.
- [129] A. Ourjoumtsev, H. Jeong, R. Tualle-Brouri, and P. Grangier, "Generation of optical 'Schrödinger cats' from photon number states," *Nature*, vol. 448, pp. 784–786, Aug. 2007. Publisher: Nature Publishing Group.
- [130] T. C. Ralph and P. K. Lam, "Teleportation with Bright Squeezed Light," *Physical Review Letters*, vol. 81, pp. 5668–5671, Dec. 1998. Publisher: American Physical Society.
- [131] N. Lee, H. Benichi, Y. Takeno, S. Takeda, J. Webb, E. Huntington, and A. Furusawa, "Teleportation of Nonclassical Wave Packets of Light," *Science*, vol. 332, pp. 330–333, Apr. 2011. Publisher: American Association for the Advancement of Science.
- [132] M. Pysher, *Towards Quantum Computing With Light*. PhD thesis, Jan. 2011. Publication Title: Ph.D. Thesis ADS Bibcode: 2011PhDT.....120P.
- [133] H. P. Yuen and V. W. Chan, "Noise in Homodyne and Heterodyne Detection.," vol. 8, no. 3, pp. 218–220, 1983.
- [134] B. L. Schumaker, "Noise in homodyne detection," *Optics Letters*, vol. 9, pp. 189–191, May 1984. Publisher: Optica Publishing Group.
- [135] G. J. Milburn, "Quantum measurement theory of optical heterodyne detection," *Physical Review A*, vol. 36, pp. 5271–5279, Dec. 1987.
- [136] M. Collett, R. Loudon, and C. Gardiner, "Quantum Theory of Optical Homodyne and Heterodyne Detection," *Journal of Modern Optics*, vol. 34, pp. 881–902, June 1987.
- [137] H. Yuen and J. Shapiro, "Optical communication with two-photon coherent states—Part III: Quantum measurements realizable with photoemissive detectors," *IEEE Transactions on Information Theory*, vol. 26, pp. 78–92, Jan. 1980. Conference Name: IEEE Transactions on Information Theory.
- [138] A. Buonanno, Y. Chen, and N. Mavalvala, "Quantum noise in laser-interferometer gravitational-wave detectors with a heterodyne readout scheme," *Physical Review D*, vol. 67, p. 122005, June 2003.

BIBLIOGRAPHY

- [139] L. F. Buchmann, S. Schreppler, J. Kohler, N. Spethmann, and D. M. Stamper-Kurn, “Complex Squeezing and Force Measurement beyond the Standard Quantum Limit,” *Physical Review Letters*, vol. 117, no. 3, pp. 1–6, 2016. arXiv: 1602.02141.
- [140] M. G. Raymer and K. Srinivasan, “Manipulating the color and shape of single photons,” *Physics Today*, vol. 65, pp. 32–37, Nov. 2012.
- [141] P. C. Humphreys, W. S. Kolthammer, J. Nunn, M. Barbieri, A. Datta, and I. A. Walmsley, “Continuous-Variable Quantum Computing in Optical Time-Frequency Modes Using Quantum Memories,” *Physical Review Letters*, vol. 113, p. 130502, Sept. 2014. Publisher: American Physical Society.
- [142] M. G. Raymer and I. A. Walmsley, “Temporal modes in quantum optics: Then and now,” *Physica Scripta*, vol. 95, no. 6, 2020. arXiv: 1911.06771 Publisher: IOP Publishing.
- [143] X. Wang, Y. Jia, X. Guo, J. Liu, S. Wang, W. Liu, F. Sun, J. Zou, and Y. Li, “Silicon photonics integrated dynamic polarization controller for continuous-variable quantum key distribution,” *Chinese Optics Letters*, vol. 20, no. 4, p. 041301, 2022. arXiv:2108.08428 [quant-ph].
- [144] G. Patera, C. Navarrete-Benlloch, G. de Valcárcel, and C. Fabre, “Quantum coherent control of highly multipartite continuous-variable entangled states by tailoring parametric interactions,” *The European Physical Journal D*, vol. 66, p. 241, Sept. 2012.
- [145] Y. Cai, J. Roslund, G. Ferrini, F. Arzani, X. Xu, C. Fabre, and N. Treps, “Multimode entanglement in reconfigurable graph states using optical frequency combs,” *Nature Communications*, vol. 8, p. 15645, June 2017. Publisher: Nature Publishing Group.
- [146] N. C. Menicucci, S. T. Flammia, H. Zaidi, and O. Pfister, “Ultracompact generation of continuous-variable cluster states,” *Physical Review A*, vol. 76, p. 010302, July 2007. Publisher: American Physical Society.
- [147] L. Serino, J. Gil-Lopez, M. Stefszky, R. Ricken, C. Eigner, B. Brecht, and C. Silberhorn, “Realization of a Multi-Output Quantum Pulse Gate for Decoding High-Dimensional Tem-

BIBLIOGRAPHY

- poral Modes of Single-Photon States,” *PRX Quantum*, vol. 4, p. 020306, Apr. 2023. Publisher: American Physical Society.
- [148] V. Torres-Company, J. Lancis, and P. Andrés, “Space-time analogies in optics,” in *Progress in Optics*, vol. 56, pp. 1–80, 2011. ISSN: 00796638.
- [149] R. Salem, M. A. Foster, and A. L. Gaeta, “Application of space–time duality to ultrahigh-speed optical signal processing,” *Advances in Optics and Photonics*, vol. 5, no. 3, p. 274, 2013. arXiv: 1303.6810 ISBN: 1943-8206.
- [150] B. H. Kolner and M. Nazarathy, “Temporal imaging with a time lens,” *Optics Letters*, vol. 14, pp. 630–632, June 1989. Publisher: Optica Publishing Group.
- [151] J. v. Howe and C. Xu, “Ultrafast Optical Signal Processing Based Upon Space-Time Dualities,” *Journal of Lightwave Technology*, vol. 24, p. 2649, July 2006. Publisher: IEEE.
- [152] P. Tournois, “Analogie optique de la compression d’impulsion,” *CR Acad. Sci*, vol. 258, no. 15, pp. 3839–3842, 1964.
- [153] P. Tournois, J. Vernet, and G. Biennu, “Sur l’analogie optique de certains montages électroniques: Formation d’images temporelles de signaux électriques,” *CR Acad. Sci*, vol. 267, pp. 375–378, 1968.
- [154] W. J. Caputi, “Stretch: A Time-Transformation Technique,” *IEEE Transactions on Aerospace and Electronic Systems*, vol. AES-7, pp. 269–278, Mar. 1971. Conference Name: IEEE Transactions on Aerospace and Electronic Systems.
- [155] S. Akhmanov, A. Sukhorukov, and A. Chirkin, “Nonstationary phenomena and space-time analogy in nonlinear optics,” *Soviet Physics–JETP [translation of Zhurnal Eksperimentalnoi i Teoreticheskoi Fiziki]*, vol. 28, no. 4, pp. 748–757, 1969.
- [156] E. B. Treacy, “MEASUREMENT OF PICOSECOND PULSE SUBSTRUCTURE USING COMPRESSION TECHNIQUES,” *Applied Physics Letters*, vol. 14, pp. 112–114, Feb. 1969.

BIBLIOGRAPHY

- [157] A. E. Siegman, *Lasers*. Mill Valley, California: University Science Book, 1986. OCLC: 638695687.
- [158] S. A. Collins, "Lens-System Diffraction Integral Written in Terms of Matrix Optics*," *Journal of the Optical Society of America*, vol. 60, no. 9, p. 1168, 1970.
- [159] C. Palma and V. Bagini, "Extension of the Fresnel transform to ABCD systems," *JOSA A*, vol. 14, pp. 1774–1779, Aug. 1997. Publisher: Optica Publishing Group.
- [160] S. Mookherjea and A. Yariv, "Analysis of optical pulse propagation with two-by-two (ABCD) matrices," *Physical Review E - Statistical Physics, Plasmas, Fluids, and Related Interdisciplinary Topics*, vol. 64, no. 1, p. 10, 2001.
- [161] D. Strickland and G. Mourou, "Compression of amplified chirped optical pulses," *Optics Communications*, vol. 56, pp. 219–221, Dec. 1985.
- [162] O. E. Martinez, "3000 times grating compressor with positive group velocity dispersion: Application to fiber compensation in 1.3-1.6 m region," *IEEE Journal of Quantum Electronics*, vol. 23, no. 1, pp. 59–64, 1987.
- [163] Y. Zhang, H.-P. Lo, A. Mink, T. Ikuta, T. Honjo, H. Takesue, and W. J. Munro, "A simple low-latency real-time certifiable quantum random number generator," *Nature Communications*, vol. 12, p. 1056, Feb. 2021. Publisher: Nature Publishing Group.
- [164] M. Karpiński, A. O. Davis, F. Sośnicki, V. Thiel, and B. J. Smith, "Control and Measurement of Quantum Light Pulses for Quantum Information Science and Technology," *Advanced Quantum Technologies*, vol. 4, no. 9, 2021.
- [165] F. Sośnicki, M. Mikołajczyk, A. Golestani, and M. Karpiński, "Aperiodic electro-optic time lens for spectral manipulation of single-photon pulses," *Applied Physics Letters*, vol. 116, p. 234003, June 2020.
- [166] N. Matsuda, "Deterministic reshaping of single-photon spectra using cross-phase modulation," *Science Advances*, vol. 2, no. 3, 2016.

BIBLIOGRAPHY

- [167] T. Hirooka and M. Nakazawa, “All-optical 40-GHz time-domain Fourier transformation using XPM with a dark parabolic pulse,” *IEEE Photonics Technology Letters*, vol. 20, no. 22, pp. 1869–1871, 2008.
- [168] F. Sośnicki, M. Mikołajczyk, A. Golestani, and M. Karpiński, “Interface between picosecond and nanosecond quantum light pulses,” *Nature Photonics*, vol. 17, pp. 761–766, Sept. 2023. Publisher: Nature Publishing Group.
- [169] M. Yu, D. Barton III, R. Cheng, C. Reimer, P. Kharel, L. He, L. Shao, D. Zhu, Y. Hu, H. R. Grant, L. Johansson, Y. Okawachi, A. L. Gaeta, M. Zhang, and M. Lončar, “Integrated femtosecond pulse generator on thin-film lithium niobate,” *Nature*, vol. 612, pp. 252–258, Dec. 2022. Publisher: Nature Publishing Group.
- [170] D. Zhu, C. Chen, M. Yu, L. Shao, Y. Hu, C. J. Xin, M. Yeh, S. Ghosh, L. He, C. Reimer, N. Sinclair, F. N. C. Wong, M. Zhang, and M. Lončar, “Spectral control of nonclassical light pulses using an integrated thin-film lithium niobate modulator,” *Light: Science & Applications*, vol. 11, p. 327, Nov. 2022. Publisher: Nature Publishing Group.
- [171] J. M. Arrazola, V. Bergholm, K. Brádler, T. R. Bromley, M. J. Collins, I. Dhand, A. Fumagalli, T. Gerrits, A. Goussev, L. G. Helt, J. Hundal, T. Isacsson, R. B. Israel, J. Izaac, S. Jangiri, R. Janik, N. Killoran, S. P. Kumar, J. Lavoie, A. E. Lita, D. H. Mahler, M. Menotti, B. Morrison, S. W. Nam, L. Neuhaus, H. Y. Qi, N. Quesada, A. Repeatingon, K. K. Sabapathy, M. Schuld, D. Su, J. Swinerton, A. Száva, K. Tan, P. Tan, V. D. Vaidya, Z. Vernon, Z. Zabaneh, and Y. Zhang, “Quantum circuits with many photons on a programmable nanophotonic chip,” *Nature*, vol. 591, no. 7848, pp. 54–60, 2021. arXiv: 2103.02109 ISBN: 4158602103202.
- [172] D. Oser, S. Tanzilli, F. Mazeas, C. Alonso-Ramos, X. Le Roux, G. Sauder, X. Hua, O. Alibert, L. Vivien, Cassan, and L. Labonté, “High-quality photonic entanglement out of a stand-alone silicon chip,” *npj Quantum Information*, vol. 6, pp. 1–6, Mar. 2020. Publisher: Nature Publishing Group.
- [173] P. Imany, J. A. Jaramillo-Villegas, O. D. Odele, K. Han, D. E. Leaird, J. M. Lukens, P. Lougovski, M. Qi, and A. M. Weiner, “50-GHz-spaced comb of high-dimensional

- frequency-bin entangled photons from an on-chip silicon nitride microresonator,” *Optics Express*, vol. 26, pp. 1825–1840, Jan. 2018. Publisher: Optica Publishing Group.
- [174] H. Mahmudlu, R. Johanning, A. van Rees, A. Khodadad Kashi, J. P. Epping, R. Haldar, K.-J. Boller, and M. Kues, “Fully on-chip photonic turnkey quantum source for entangled qubit/qudit state generation,” *Nature Photonics*, vol. 17, pp. 518–524, June 2023. Publisher: Nature Publishing Group.
- [175] Gouzien, *Optique quantique multimode pour le traitement de l’information quantique*. These de doctorat, Université Côte d’Azur (ComUE), Dec. 2019.
- [176] G. Patera, N. Treps, C. Fabre, and G. J. De Valcárcel, “Quantum theory of synchronously pumped type I optical parametric oscillators: Characterization of the squeezed supermodes,” *European Physical Journal D*, vol. 56, no. 1, pp. 123–140, 2010. arXiv: 0907.4550.
- [177] A. Christ, B. Brecht, W. Mauerer, and C. Silberhorn, “Theory of quantum frequency conversion and type-II parametric down-conversion in the high-gain regime,” *New Journal of Physics*, vol. 15, 2013. arXiv: 1210.8342.
- [178] G. Patera, *Quantum properties of ultra-short pulses generated by SPOPOs: multi-mode squeezing and entanglement*. phdthesis, Université Pierre et Marie Curie - Paris VI, Nov. 2008.
- [179] G. Patera, N. Treps, C. Fabre, and G. J. de Valcárcel, “Quantum theory of synchronously pumped type I optical parametric oscillators: characterization of the squeezed supermodes,” *The European Physical Journal D*, vol. 56, pp. 123–140, Jan. 2010.
- [180] O. Pfister, S. Feng, G. Jennings, R. Pooser, and D. Xie, “Multipartite continuous-variable entanglement from concurrent nonlinearities,” *Physical Review A*, vol. 70, p. 020302, Aug. 2004. Publisher: American Physical Society.
- [181] J. Roslund, R. M. De Araújo, S. Jiang, C. Fabre, and N. Treps, “Wavelength-multiplexed quantum networks with ultrafast frequency combs,” *Nature Photonics*, vol. 8, no. 2, pp. 109–112, 2014. arXiv: 1307.1216.

BIBLIOGRAPHY

- [182] J. Junker, D. Wilken, N. Johny, D. Steinmeyer, and M. Heurs, “Frequency-Dependent Squeezing from a Detuned Squeezer,” *Physical Review Letters*, vol. 129, p. 033602, July 2022. Publisher: American Physical Society.
- [183] R. Yanagimoto, E. Ng, A. Yamamura, T. Onodera, L. G. Wright, M. Jankowski, M. M. Fejer, P. L. McMahon, and H. Mabuchi, “Onset of non-Gaussian quantum physics in pulsed squeezing with mesoscopic fields,” *Optica*, vol. 9, pp. 379–390, Apr. 2022. Publisher: Optica Publishing Group.
- [184] M. Jankowski, R. Yanagimoto, E. Ng, R. Hamerly, T. P. McKenna, H. Mabuchi, and M. M. Fejer, “Ultrafast second-order nonlinear photonics – from classical physics to non-Gaussian quantum dynamics,” Jan. 2024. arXiv:2401.06265.
- [185] J. Zhang and K. Mølmer, “Prediction and retrodiction with continuously monitored Gaussian states,” *Physical Review A*, vol. 96, p. 062131, Dec. 2017.
- [186] I. Brandão, D. Tandeitnik, and T. Guerreiro, “QuGIT: a numerical toolbox for Gaussian quantum states,” *Computer Physics Communications*, vol. 280, p. 108471, Nov. 2022. arXiv:2201.06368 [quant-ph].
- [187] M. A. Guidry, D. M. Lukin, K. Y. Yang, and J. Vučković, “Multimode squeezing in soliton crystal microcombs,” *Optica*, vol. 10, p. 694, June 2023.
- [188] H. Bacher and T. C. Ralph, *A Guide to Experiments in Quantum Optics*. 2019. Publication Title: A Guide to Experiments in Quantum Optics.
- [189] A. I. Lvovsky, R. Ghobadi, A. Chandra, A. S. Prasad, and C. Simon, “Observation of micro–macro entanglement of light,” *Nature Physics*, vol. 9, pp. 541–544, Sept. 2013. Publisher: Nature Publishing Group.
- [190] Y.-S. Ra, A. Dufour, M. Walschaers, C. Jacquard, T. Michel, C. Fabre, and N. Treps, “Non-Gaussian quantum states of a multimode light field,” *Nature Physics*, vol. 16, pp. 144–147, Feb. 2020. Publisher: Nature Publishing Group.
- [191] M. F. Melalkia, T. Gabbrielli, A. Petitjean, L. Brunel, A. Zavatta, S. Tanzilli, J. Etesse, and V. D’Auria, “Plug-and-play generation of non-Gaussian states of light at a telecom

BIBLIOGRAPHY

- wavelength,” *Optics Express*, vol. 30, pp. 45195–45201, Dec. 2022. Publisher: Optica Publishing Group.
- [192] N. C. Menicucci, “Fault-Tolerant Measurement-Based Quantum Computing with Continuous-Variable Cluster States,” *Physical Review Letters*, vol. 112, p. 120504, Mar. 2014. Publisher: American Physical Society.
- [193] F. Arzani, C. Fabre, and N. Treps, “Versatile engineering of multimode squeezed states by optimizing the pump spectral profile in spontaneous parametric down-conversion,” *Physical Review A*, vol. 97, p. 033808, Mar. 2018. arXiv:1709.10055 [quant-ph].
- [194] V. D. Vaidya, B. Morrison, L. G. Helt, R. Shahrokshahi, D. H. Mahler, M. J. Collins, K. Tan, J. Lavoie, A. Repingon, M. Menotti, N. Quesada, R. C. Pooser, A. E. Lita, T. Gerrits, S. W. Nam, and Z. Vernon, “Broadband quadrature-squeezed vacuum and nonclassical photon number correlations from a nanophotonic device,” *Science Advances*, vol. 6, p. eaba9186, Sept. 2020. Publisher: American Association for the Advancement of Science.
- [195] H. Seifoory, Z. Vernon, D. H. Mahler, M. Menotti, Y. Zhang, and J. E. Sipe, “Degenerate squeezing in a dual-pumped integrated microresonator: Parasitic processes and their suppression,” *Physical Review A*, vol. 105, no. 3, pp. 1–14, 2022. arXiv: 2109.03298
Publisher: American Physical Society.
- [196] Y. Zhang, M. Menotti, K. Tan, V. D. Vaidya, D. H. Mahler, L. G. Helt, L. Zatti, M. Liscidini, B. Morrison, and Z. Vernon, “Squeezed light from a nanophotonic molecule,” *Nature Communications*, vol. 12, p. 2233, Apr. 2021.
- [197] C. K. Li, R. Roberts, and X. Yin, “Decomposition of unitary matrices and quantum gates,” *International Journal of Quantum Information*, vol. 11, no. 1, pp. 1–8, 2013. arXiv: 1210.7366.
- [198] H. Hu and L. K. Oxenløwe, “Chip-based optical frequency combs for high-capacity optical communications,” *Nanophotonics*, vol. 10, no. 5, pp. 1367–1385, 2021. ISBN: 0000000288590.

BIBLIOGRAPHY

- [199] H. H. Lu, J. M. Lukens, N. A. Peters, O. D. Odele, D. E. Leaird, A. M. Weiner, and P. Lougovski, “Electro-Optic Frequency Beam Splitters and Titters for High-Fidelity Photonic Quantum Information Processing,” *Physical Review Letters*, vol. 120, Jan. 2018. arXiv: 1712.03992 Publisher: American Physical Society.
- [200] M. Reck and A. Zeilinger, “Experimental Realization of Any Discrete Unitary Operator,” *Physical Review Letters*, vol. 73, no. 1, 1994.
- [201] W. R. Clements, P. C. Humphreys, B. J. Metcalf, W. S. Kolthammer, and I. A. Walsmley, “Supplementary Material : Optimal design for universal multiport interferometers,” *Optica*, vol. 3, no. 12, p. 1460, 2016. arXiv: 1603.08788.
- [202] I. R. Petersen, “Cascade cavity realization for a class of complex transfer functions arising in coherent quantum feedback control,” *Automatica*, vol. 47, no. 8, pp. 1757–1763, 2011. Publisher: Elsevier Ltd.
- [203] H. I. Nurdin, M. R. James, and A. C. Doherty, “Network Synthesis of Linear Dynamical Quantum Stochastic Systems,” *SIAM Journal on Control and Optimization*, vol. 48, pp. 2686–2718, Jan. 2009. Publisher: Society for Industrial and Applied Mathematics.
- [204] L. Dieci and A. Pugliese, “SVD, joint-MVD, Berry phase, and generic loss of rank for a matrix valued function of 2 parameters,” *Linear Algebra and its Applications*, vol. 700, pp. 137–157, Nov. 2024.
- [205] A. Christ, B. Brecht, W. Mauerer, and C. Silberhorn, “Theory of quantum frequency conversion and type-II parametric down-conversion in the high-gain regime,” *New Journal of Physics*, vol. 15, 2013. arXiv: 1210.8342.
- [206] A. Bensemhoun, C. Gonzalez-Arciniegas, O. Pfister, L. Labonté, J. Etesse, A. Martin, S. Tanzilli, G. Patera, and V. D’Auria, “Multipartite entanglement in bright frequency combs out of microresonators,” *Physics Letters A*, vol. 493, p. 129272, Jan. 2024.
- [207] L. Labonté, O. Alibart, V. D’Auria, F. Dautre, J. Etesse, G. Sauder, A. Martin, Picholle, and S. Tanzilli, “Integrated Photonics for Quantum Communications and Metrology,” *PRX Quantum*, vol. 5, p. 010101, Feb. 2024.

BIBLIOGRAPHY

- [208] W. Bogaerts, P. de Heyn, T. van Vaerenbergh, K. de Vos, S. Kumar Selvaraja, T. Claes, P. Dumon, P. Bienstman, D. van Thourhout, and R. Baets, "Silicon microring resonators," *Laser and Photonics Reviews*, vol. 6, no. 1, pp. 47–73, 2012.
- [209] J. Heebner, R. Grover, and T. A. Ibrahim, *Optical Microresonators*. 2009.



CEMPI CENTRE EUROPÉEN
POUR LES MATHÉMATIQUES, LA PHYSIQUE ET
LEURS INTERACTIONS



Titre: Manipulation et Caractérisation de la Lumière Quantique Multimode dans les Systèmes Photoniques

Mots clés: cavité temporelle, interféromètre avec effet mémoire, états comprimés, morphings de supermodes

Résumé: Cette thèse fait progresser l'optique quantique multimode à travers deux contributions théoriques et pratiques majeures. Premièrement, nous introduisons les cavités temporelles comme une nouvelle approche pour le filtrage des modes temporels, en exploitant les principes de dualité espace-temps pour transposer les principes des cavités de nettoyage de modes spatiaux au domaine temporel. Contrairement aux approches existantes, cette opération de filtrage ne repose pas sur des interactions non linéaires ou sur l'accord de phase, préserve la fréquence porteuse et maintient intacte la structure des modes temporels. Nous démontrons la faisabilité d'une implémentation pratique utilisant des lentilles temporelles électro-optiques et des réseaux de diffraction, avec des stratégies complètes d'optimisation des paramètres pour les applications classiques

et quantiques. Deuxièmement, nous abordons les limitations fondamentales de la détection d'états quantiques à travers les interféromètres à effet mémoire (IME). Nous établissons de nouveaux critères pour prédire la compression cachée directement à partir des paramètres du système et développons de nouvelles méthodes de décomposition lisse pour implémenter des unitaires dépendant de la fréquence. Ces innovations permettent un appariement parfait des modes pour les états présentant des caractéristiques spectrales complexes et des morphing de supermodes, qui sont plus courants que précédemment reconnu dans les systèmes quantiques basés sur des cavités. L'efficacité de notre approche est démontrée par des études de cas détaillées de configurations d'oscillateurs paramétriques optiques.

Title: Manipulation and Characterization of Multimode Quantum Light in Photonic Systems

Keywords: temporal cavities, interferometer with memory effect, hidden squeezing, morphing supermodes

Abstract: This thesis advances multimode quantum optics through two major theoretical and practical contributions. First, we introduce temporal cavities as a novel approach to temporal mode filtering, leveraging space-time duality principles to translate spatial mode-cleaning cavity principles to the temporal domain. Unlike existing approaches, this filter operation does not rely on nonlinear interactions or phase matching, preserves the carrier frequency, and maintains the temporal mode structure intact. We demonstrate practical implementation feasibility using electro-optic time lenses and diffraction gratings, with comprehensive parameter optimization strategies for both classical and quantum applications. Second,

we address fundamental limitations in quantum state detection through interferometers with memory effect (IME). We establish new criteria for predicting hidden squeezing directly from system parameters and develop novel smooth decomposition methods for implementing frequency-dependent unitaries. These innovations enable perfect mode-matching for states exhibiting complex spectral features and morphing supermodes, which are more common than previously recognized in cavity-based quantum systems. The effectiveness of our approach is demonstrated through detailed case studies of optical parametric oscillator configurations.

Titre: Manipulation et Caractérisation de la Lumière Quantique Multimode dans les Systèmes Photoniques

Mots clés: cavité temporelle, interféromètre avec effet mémoire, états comprimés, morphings de supermodes

Résumé: Cette thèse fait progresser l'optique quantique multimode à travers deux contributions théoriques et pratiques majeures. Premièrement, nous introduisons les cavités temporelles comme une nouvelle approche pour le filtrage des modes temporels, en exploitant les principes de dualité espace-temps pour transposer les principes des cavités de nettoyage de modes spatiaux au domaine temporel. Contrairement aux approches existantes, cette opération de filtrage ne repose pas sur des interactions non linéaires ou sur l'accord de phase, préserve la fréquence porteuse et maintient intacte la structure des modes temporels. Nous démontrons la faisabilité d'une implémentation pratique utilisant des lentilles temporelles électro-optiques et des réseaux de diffraction, avec des stratégies complètes d'optimisation des paramètres pour les applications classiques

et quantiques. Deuxièmement, nous abordons les limitations fondamentales de la détection d'états quantiques à travers les interféromètres à effet mémoire (IME). Nous établissons de nouveaux critères pour prédire la compression cachée directement à partir des paramètres du système et développons de nouvelles méthodes de décomposition lisse pour implémenter des unitaires dépendant de la fréquence. Ces innovations permettent un appariement parfait des modes pour les états présentant des caractéristiques spectrales complexes et des morphing de supermodes, qui sont plus courants que précédemment reconnu dans les systèmes quantiques basés sur des cavités. L'efficacité de notre approche est démontrée par des études de cas détaillées de configurations d'oscillateurs paramétriques optiques.

Title: Manipulation and Characterization of Multimode Quantum Light in Photonic Systems

Keywords: temporal cavities, interferometer with memory effect, hidden squeezing, morphing supermodes

Abstract: This thesis advances multimode quantum optics through two major theoretical and practical contributions. First, we introduce temporal cavities as a novel approach to temporal mode filtering, leveraging space-time duality principles to translate spatial mode-cleaning cavity principles to the temporal domain. Unlike existing approaches, this filter operation does not rely on nonlinear interactions or phase matching, preserves the carrier frequency, and maintains the temporal mode structure intact. We demonstrate practical implementation feasibility using electro-optic time lenses and diffraction gratings, with comprehensive parameter optimization strategies for both classical and quantum applications. Second,

we address fundamental limitations in quantum state detection through interferometers with memory effect (IME). We establish new criteria for predicting hidden squeezing directly from system parameters and develop novel smooth decomposition methods for implementing frequency-dependent unitaries. These innovations enable perfect mode-matching for states exhibiting complex spectral features and morphing supermodes, which are more common than previously recognized in cavity-based quantum systems. The effectiveness of our approach is demonstrated through detailed case studies of optical parametric oscillator configurations.

